CRANFIELD UNIVERSITY

MUBARAK DANLADI MUHAMMAD

DEVELOPMENT OF A CASCADED LATENT HEAT STORAGE SYSTEM FOR PARABOLIC TROUGH SOLAR THERMAL POWER GENERATION

SCHOOL OF ENGINEERING

PhD THESIS

CRANFIELD UNIVERSITY

SCHOOL OF ENGINEERING

PhD THESIS

Academic Year 2013-2014

MUBARAK DANLADI MUHAMMAD

DEVELOPMENT OF A CASCADED LATENT HEAT STORAGE SYSTEM FOR PARABOLIC TROUGH SOLAR THERMAL POWER GENERATION

Supervisors: Dr. Ossama Badr
Prof. Hoi Yeung

September 2014

ABSTRACT

Concentrated solar power (CSP) has the potential of fulfilling the world's electricity needs. Parabolic-trough system using synthetic oil as the HTF with operating temperature between 300 and 400^{o}C, is the most matured CSP technology. A thermal storage system is required for the stable and cost effective operation of CSP plants. The current storage technology is the indirect two-tank system which is expensive and has high energy consumption due to the need to prevent the storage material from freezing. Latent heat storage (LHS) systems offer higher storage density translating into smaller storage size and higher performance but suitable phase change materials (PCMs) have low thermal conductivity, thus hindering the realization of their potential. The low thermal conductivity can be solved by heat transfer enhancement in the PCM. There is also lack of suitable commercially-available PCMs to cover the operating temperature range. In this study, a hybrid cascaded storage system (HCSS) consisting of a cascaded finned LHS and a high temperature sensible or concrete tube register (CTR) stages was proposed and analysed via modelling and simulation. Fluent CFD code and the Dymola simulation environment were employed.

A validated CFD phase change model was used in determining the heat transfer characteristics during charging and discharging of a finned and un-finned LHS shell-and-tube storage element. The effects of various fin configurations were investigated and heat transfer coefficients that can be used for predicting the performance of the system were obtained. A model of the HCSS was then developed in the Dymola simulation environment. Simulations were conducted considering the required boundary conditions of the system to develop the best design of a system having a capacity of 875 MWh_{th}, equivalent to 6 hours of full load operation of a 50 MW_e power plant.

The cascaded finned LHS section provided ~46% of the entire HCSS capacity. The HCSS and cascaded finned LHS section have volumetric specific capacities 9.3% and 54% greater than that of the two-tank system, respectively. It has been estimated that the capital cost of the system is ~12% greater than that of the two-tank system. Considering that the passive HCSS has lower operational and maintenance costs it will be more cost effective than the two-tank system considering the life cycle of the system. There is no requirement of keeping the storage material above its melting temperature always. The HCSS has also the potential of even lower capital cost at higher capacities (>6 hours of full load operation).

Keywords:

Phase change materials, Concrete, Fin, Thermal energy storage, Computational fluid dynamics,

ACKNOWLEDGEMENTS

I hereby extend my gratitude to Dr. O. Badr, my supervisor and teacher who guided me throughout the duration of this research work. Your support and encouragement and availability whenever I needed you kept me going. My appreciation also goes to my co-supervisor, Prof. H. Yeung for his valuable comments, suggestions and support.

I also want to thank all the staff and students of the Process System Engineering Group especially Sam Skears for hear help and advice throughout my stay in Cranfield University.

Special thanks to my parents, brothers, sister (Dr. Amina), my wife (Fatima), daughter, and my friends for their support, patience and prayers throughout the duration of this study. Sincere appreciation goes to all my friends in Cranfield especially, Aminu, Chet, Habeeb, Yahya, Adamu and Grema. Thank you for all your support.

To Suleiman and Binta, thank you for your support, advice and encouragement. I am indebted to the Federal Government of Nigeria for sponsoring my PhD through the Petroleum Technology Development Fund (PTDF), Nigeria.

Finally this thesis is dedicated to my parents and my wife Fatima Abdullahi.

.

TABLE OF CONTENTS

LIST OF FIGURES

LIST OF TABLES

LIST OF EQUATIONS

LIST OF ABBREVIATIONS

ACW	Asbestos containing waste
ANU	Australian National University
CESA	Central Electro-Solar de Almeria, Spain
CFD	Computational fluid dynamics
CNEG	Compressed naturally expanded graphite
CPC	Compound parabolic collector
CSP	Concentrated solar power
CTR	Concrete tube register
DISS	Direct solar steam
DISTOR	Energy Storage for Direct Steam Solar Power Plants
DLR	German Aerospace Centre
DNI	Direct normal insolation
DSG	Direct steam generation
EC	European Commission
ENG	Expanded natural graphite
EPRI	Electric Power Research Institute, USA
ERDA	Energy Research and Development Administration, USA
HCSS	Hybrid cascaded storage system
HTES	Heat transfer enhancement structure
HTF	Heat transfer fluid
IEA	International Energy Agency
ISCC	Integrated solar combine cycle
ISEGS	Ivanapha Solar Electricity Generating Station, USA
LCA	Life cycle assessment
LEC	Levelized electricity cost
LHS	Latent heat storage
LOS	Line of symmetry
NREL	National Renewable Energy Laboratory, US Department of Energy
PCM	Phase change material
PCS	Power conversion system
PSA	Plataforma Solar de Almería, Spain
RHS	Right hand side

RHTS	Reflux heat transfer storage
SCE	Southern California Edison, USA
SEGS	Solar Electric Generating Station, USA
SSPS	Small Solar Power Systems, Spain
TESS	Thermal energy storage system

NOMENCLATURE

A_o	Outer surface area of HTF-pipe	m^2
b	Fin thickness	m
C	Cost	$
c_p	Specific heat capacity	J/kgK
d_a	Storage element outer diameter	m
d_i	HTF-pipe inner diameter	m
dz	Height of segment	m
dr	Length of radial element	m
D	HTF pipe inner diameter	m
F	Liquid fraction	
g	Gravitational acceleration	m/s^2
H	Specific enthalpy of PCM	J/kg
h	Sensible specific enthalpy	J/kg
h	Heat transfer coefficient	W/m^2K
k	Thermal conductivity	W/mK
L	Length of storage element	m
m	Mass	kg
$\dot{m}$	Mass flow rate of HTF	kg/s
$\dot{q}$	Heat flux	W/m^2
$\dot{q}_w$	Heat flux at HTF-pipe wall	W/m^2
$\dot{Q}$	Heat transfer rate	W
r_a	Storage element outer radius	m
r_o	Outer radius of HTF-pipe	m
s	Phase change interface location, measured from the HTF-pipe wall	m
S	Source term	
t	Time	s
T	Average temperature	K or ^oC
T_{solid}	Temperature at beginning of melting of PCM	K or ^oC
T_{liquid}	Temperature at end of melting of PCM	K or ^oC
ΔT_m	Phase change temperature range	
u	Specific internal energy	J/kg

U	Overall heat transfer coefficient	W/m^2K
$\vec{v}$	Fluid velocity	m/s
W	Distance between fins	m

Greek symbols

α	Thermal diffusivity	m^2/s
β	Thermal expansion coefficient of PCM	1/K
λ	Latent heat of fusion of PCM	kJ/kg
μ	Dynamic viscosity	Pas
ρ	Density	kg/m^3

Subscripts

amb	Ambient
ave	Average
B	Bottom
conc	Concrete
eff	Effective
eq	Equivalent
fc	Forced convection
htf	Heat transfer fluid
H	Hot
in	Inlet
l	Liquid
m	Melting
o	Overheating
out	Outlet
pcm	Phase change material
qs	Quasi-steady
ref	Reference
s	Solid, solidification
w	Wall
wi	Inner surface of HTF-pipe wall
wo	Outer surface of HTF-pipe wall

Dimensionless Numbers

$Fo = \frac{\alpha t}{W^2}$	Fourier number
$Pr = \frac{c_p \mu}{k}$	Prandtl number
$Re = \frac{\rho v D}{\mu}$	Reynold's number
$Ste = \frac{c_p \Delta T}{\lambda}$	Stephan number

1 INTRODUCTION

1.1 Background

It has been estimated that the Earth surface receives about 1.36 x 10^6 YJ/year of solar energy [1], which is more than 4000 times the annual world energy consumption [2]. Solar energy is available in all habitable regions of the world, and thus represents a universal source of energy, not limited to small or specific region of the world.

Solar energy can be used for the production of electricity by one of two alternative technologies: solar thermal or concentrated solar power (CSP); and solar photovoltaic. CSP is of interest in this research. In order to generate electricity, direct solar radiation is intercepted, concentrated and used to heat a working fluid to high temperature for use in conventional power cycles (steam turbine or gas turbine) [3]. The amount of solar energy received in different parts of the world differs; as such, only places having annual direct insolation ≥ 2 MWh/m^2 are suitable for the utilization of CSP [1]. Figure 1.1 presents regions in the world with potential for the utilization of CSP. Such potential areas are available in all continents.

Different CSP technologies are employed for the production of electricity from solar energy. These include:

- The power-tower in which a large field of reflecting mirrors are used to concentrate solar radiation on to a central boiler for the production of heat.
- The parabolic-trough in which the solar radiation is concentrated using a trough shaped collector on to a linear receiver situated at the focal line of the trough. Heat produced from various receivers is then collected and sent into a Rankine cycle power block.
- The parabolic dish in which the collector is in the shape of a parabolic-dish and the solar radiation is concentrated on to the focal point of the dish for the production of heat.

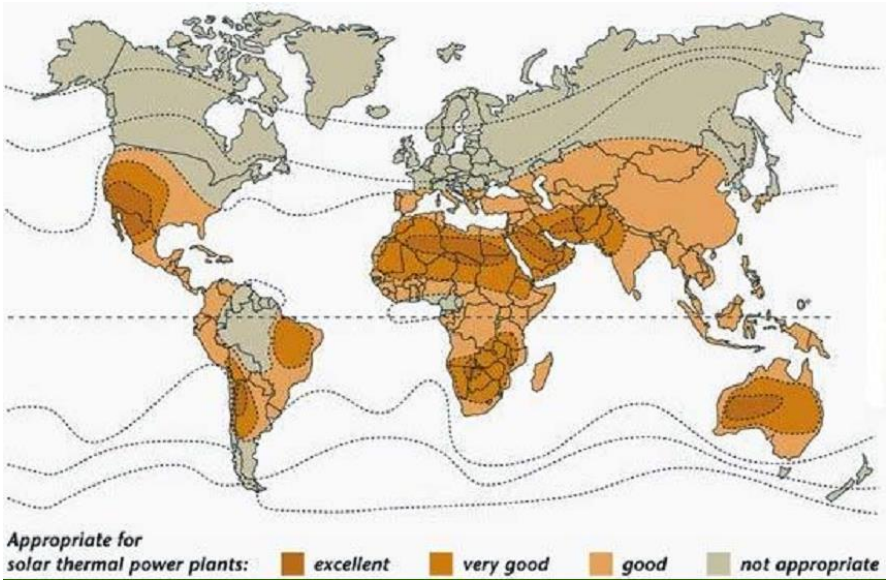

Figure 1.1 Regions of the world appropriate for CSP [1]

All these systems are advance and have been commercialized. Table 1.1 presents the key features of these technologies. The most matured of these technologies is the parabolic-trough with many commercial plants in operation and under construction. This is because of the experience gained through the operation of nine plants at Daggett, California called the SEGS plants with a total capacity of 354 MW for over 20 years [3; 4]. Although it has a lower solar to electricity conversion efficiency than the power-tower and parabolic-dish, it is still the most cost effective in the small and medium capacity range power plants (i.e capacities less than 200 MW).

Solar radiation intermittency makes the operation of solar thermal power plants to be limited to times when the energy from the Sun is sufficient for the turbine operation. A passing cloud can cause a sudden decrease in solar insolation and lead to undesirable transient operation of the turbine leading to grid instability, for grid connected plants. The plant has also to be shut down at night and it will be impossible for the plant to follow the demand for electricity except when the demand matches the solar insolation. Thus, for solar thermal power plants to function effectively, a backup thermal energy source is required.

Table 1.1 Key features of solar thermal power plants [5]

	Unit capacity (MW)	Concentration ratios	Peak solar efficiency (%)	Annual efficiency (%) (Solar to electricity)
Power Tower	10-500	300 – 1000	20(d) 35 (p)	8-10(d) 15-25(p)
Parabolic dish	0.01-1.5[1]	1000 – 3000	29(d)	16-18 (d) 18-23 (p)
Parabolic trough	10 – 360[1]	70 – 80	21 (d)	10 -15 (d) 17 – 18 (p)

(p) projected; (d) demonstrated

[1][6]

The use of a fossil-fired boiler for the production of thermal energy will be a good solution but leads to CO_2 emissions, thus making the system not completely renewable. The use of biomass or biofuel fired boiler can be a renewable option but this can be expensive due to the non-availability of feed stock since potential areas suitable for CSP are mostly desert areas.

To make solar thermal power plants a mainstream renewable power generation technology a thermal storage system is thus required which will store excess energy for use during periods of low or no insolation, also for shifting supply to match demand and avoiding transient operations of the turbine. Thermal energy storage systems can also increase the efficiency; annual solar contribution (capacity factor) and decrease the LEC of solar thermal power plants consequently increase their cost effectiveness.

Based on the storage media, thermal energy storage systems can be classified into: sensible, latent and chemical storage systems [7]. In chemical energy storage systems, thermal energy is stored using some reversible endothermic reactions. They have the advantage of high energy storage density and the thermal energy can be stored for indefinite time at near ambient conditions, but

their design is very complex. They are still in the research stage, very expensive and associated with environmental risks such as fire hazards and toxicity [8]. Sensible storage systems are the most extensively studied and the most advanced [9-13]. The two-tank thermal storage system has reached commercial status and is currently the state of the art in thermal energy storage [14]. It is still expensive and thus research is still geared towards the development of a more cost effective storage system. LHS systems have higher energy storage density and as such have the potential to provide smaller storage sizes than the sensible storage systems [15]. They also offer higher efficiency since they have a constant temperature of operation. They have the potential to reduce the cost of the storage system and improve the performance of the power block.

The main problem of LHS systems is their low utilization factor. This is caused by two factors:

- Suitable available PCMs have a very low thermal conductivity of about 0.5 W/mK [8; 15] making charging and discharging to be very slow.
- The large operating temperature range which is about 100^{o}C requires the use of many PCMs with different phase change temperature in series [8].

These have hindered the large-scale utilization of LHS systems [16]. In the operating temperature range of parabolic-trough power plants using synthetic oil as HTF, i.e. 291^{o}C to 391^{o}C [11], five PCM modules in cascade are required [17]. The inability of finding five suitable and commercially-available PCMs has limited experimental investigations on three PCM cascaded systems [17; 18].

The analysis of a five-stage cascaded LHS system using three commercially-available PCMs and two chosen from literature has shown that cascading of PCMs improves the performance of LHS system, but there is need for increasing the thermal conductivity of the PCMs to at least 2 W/mK [19; 20]. Thus, research over the years has focused on practical ways to increase the thermal conductivity of PCMs and develop cost effective LHS system for solar power generation applications [16; 21-29].

In summary, there is still need for ways to improve thermal conductivity of PCMs and also the need to find suitable PCMs for effective use in LHS systems for parabolic-trough power plants using synthetic oil as HTF. The lack of PCMs to cover the operating temperature range can be solved by combining LHS and sensible heat storage systems to form a hybrid system.

1.2 Aim and Objectives

In this study, a hybrid cascaded storage system (HCSS), consisting of a cascaded LHS system with HTES, incorporated with a high temperature sensible stage, for parabolic trough solar thermal power plants using synthetic oil as the HTF is proposed and analysed via modelling and simulation, to ascertain the technical and economic viability of the system.

This was achieved through the following objectives:

i. Selection of suitable and commercially-available PCMs for use in the operating temperature of the parabolic-trough plant using synthetic oil as the HTF.

ii. CFD modelling of practical size LHS using a validated phase change model to find the heat transfer characteristics during charging and discharging

iii. Determination of best HTES and configuration for use in the cascaded LHS system.

iv. Determination of heat transfer characteristics and coming up with correlations that can be used for the design of a LHS system with HTES.

v. Development and validation of models for a three-stage cascaded LHS with HTES and CTR (high temperature sensible stage) storage modules.

vi. Design of complete HCSS having a capacity for 6 hour full load turbine operation for a 50 MW_e plant via simulations and capital cost estimation.

The comprehensive validation of the Fluent® phase change model and the numerical modelling of the charging and discharging processes of a practical size LHS without HTES in order to determine the heat transfer characteristics during the processes have not appeared in the literature. The design of a LHS system with HTES requires the determination of the heat transfer enhancement produced by various configurations of the HTES in order to determine the best configuration for a particular application. The heat transfer coefficients that can be used to predict the performance of the system are also required. The study will present a validated model of the proposed HCSS consisting of cascaded LHS with HTES and a CTR sensible stage. Simulations will be conducted to come up with the best design and capital cost of the storage system. Thorough literature review has revealed that this configuration has not been studied.

1.3 The Storage System Configuration

The proposed storage system is the HCSS consisting of three LHS modules with HTES (each having a different PCM) and a CTR module (Figure 1.2a) connected in series with the CTR (as the last module). Each LHS module will be a vertical cylindrical enclosure consisting of a series of parallel tubes (Figure 1.2b) since cylindrical enclosures are more compact and have lower heat lost than rectangular enclosures [30]. The PCM and HTES occupy the space between the parallel tubes. The CTR module consists of arrays of tubes embedded in a casted concrete (Figure 1.2b).

A storage module can, thus, be considered to consist of storage elements (Figure 1.2c) placed in parallel. A cascaded LHS element can be formed by joining individual LHS elements and a HCSS element can be formed by joining the cascaded LHS element with the CTR element in series. Thus the performance of a whole storage module/system can be obtained by considering a single element.

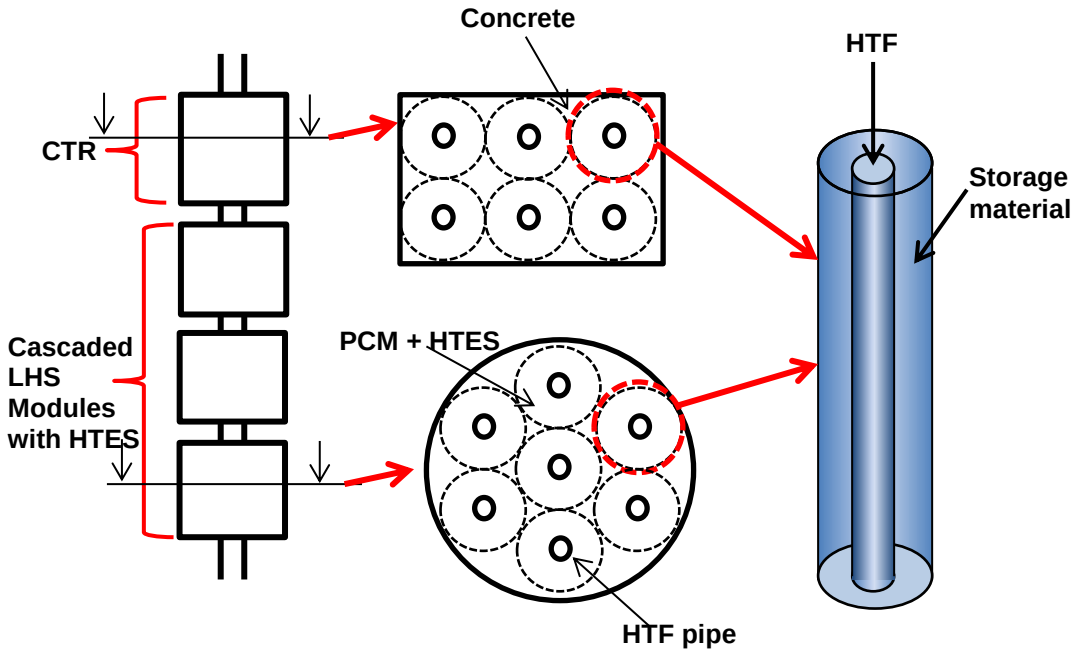

Figure 1.2 The proposed HCSS configuration (a) the system (b) cross-section of modules (c) single storage-element

1.4 Methodology and Tools for the Research

Suitable PCM for use in the operating temperature range were obtained from the literature. The existing melting and solidification model in Fluent® CFD code was rigorously validated for use in vertical cylindrical enclosures. It was then used for the simulation of the heat transfer characteristics in a single storage element with and without HTES and the determination of the best HTES configuration. Simulations were then conducted to find a correlation for the heat transfer coefficient for the charging and discharging using the best HTES configuration.

The obtained heat transfer coefficients from the CFD simulations were then used for the modelling and simulation of the HCSS using the Dymola®

simulation environment considering a single HCSS element. Results obtained from the simulation were then used for the design of a complete HCSS having a capacity suitable for 6 hour full load operation of a 50 MW_e parabolic-trough plant. The capital cost of the proposed HCSS was then obtained.

The Dymola® simulation environment which is a commercial software, based on the Modelica® object oriented language was used. This object oriented language was chosen because of its ability for the development of fully dynamic (highly discretized geometrical models) and a library called “TechThermo” has been developed based on this language [31]. The library consists of basic processes in technical thermodynamics and thus will reduce the development of trivial equations from scratch.

1.5 Thesis Structure

The thesis is organised into eight chapters as follows:

- Chapter 1 presents the introduction giving the background, aim and objectives and methodology used in the research.
- Chapter 2 presents the review on the different technologies that are used for the generation of electricity from solar energy. Emphasis was given to the commercialized technologies and their current status presented. The plants in operation and under construction were presented. The parabolic trough plant using synthetic oil as HTF was justified to be the most matured of all the technologies.
- In chapter 3, a review of all the methods used for the storage of thermal energy for solar power generation was conducted. The status of each method was presented and the state of the art in thermal storage for parabolic trough power plant and the challenges that need to be addressed were established.
- Chapter 4 presents the screening of various PCMs reported in the literature. The properties required for suitable PCM for use in LHS system was first presented. The most suitable commercially-available PCMs for use in parabolic-trough plants were found after considering their thermo physical properties.

- The comprehensive validation of the Fluent melting and solidification model using well controlled and documented experimental data and other models from the literature was presented in the first part of chapter 5. The model was then used for the simulation of the charging and discharging of a single practical size storage element without HTES in order to determine the heat transfer characteristics and establish the need for heat transfer enhancement.
- In Chapter 6, the CFD simulation of the performance of various fin (the best HTES) configurations in view of finding the best fin configuration and the heat transfer characteristics during charging and discharging of finned geometry were presented. A heat transfer coefficient for the best fin configuration was obtained that can be used in the HCSS model.
- Chapter 7 presents the design of the HCSS having a capacity of 875 MWh_{th}. Models for the finned LHS and CTR were first developed and validated. Simulations results were presented considering a single HCSS element and the design that will give the best performance was presented. A comparison of the capital cost of the obtained design with that of the state of the art (two-tank system) was also presented.
- Finally Chapter 8 presents the conclusions drawn from the research and recommendations for further work.

2 SOLAR THERMAL POWER GENERATION

2.1 Introduction

Over the years, various technologies have been developed for the production of electricity from solar energy. These technologies can be broadly classified into two:

I. Non-concentrating technologies in which the solar energy is not concentrated and thus operates at low temperatures. They have very low efficiencies and cannot be used as mainstream power generation systems. Systems under this category include [32; 33]:
    - Moving air systems in which the buoyancy force created due to the heating of ambient air is used to drive a turbine in a chimney.
    - The solar pond in which water at the bottom of a shallow pond which is heated by solar energy is prevented from moving up to the top by using varying salt concentration from the top to the bottom of the pond. This makes the water at the bottom to be heavier even though it is warmer. The upper layers serve as insulation. The heat can then be used for the production of electricity.

II. Concentrating technologies or concentrated solar power (CSP) in which direct solar radiation is intercepted by a solar collector and concentrated onto a receiver, where it is converted into useful thermal energy. A working fluid (HTF) passing through the receiver absorbs the concentrated solar thermal energy and transports it to a power cycle, where it is converted into mechanical energy and then to electricity. Due to the intermittency and the fact that solar radiation is not constant, some configurations can have a thermal storage system, in which some of the excess thermal energy produced can be stored for later use when the solar radiation is low or not available. Other configurations can have a backup boiler, for the production of thermal energy during periods of low insolation or at night (Figure 2.1). CSP systems include [3]:

- The parabolic-dish in which the collector is in the shape of a parabolic dish and the solar radiation is concentrated on to the focal point of the dish for the production of heat.
- The power-tower in which a large field of reflecting mirrors are used to concentrate solar radiation on to a central boiler for the production of heat.
- The parabolic-trough in which the solar radiation is concentrated using a trough shaped collector on to a linear receiver situated at the focal line of the trough. Heat produced from various receivers is then collected and sent into a Rankine-cycle power block.

CSP systems are of interest here. The three CSP technologies are advance and have been commercialized. Their development and current status are presented in the following sections.

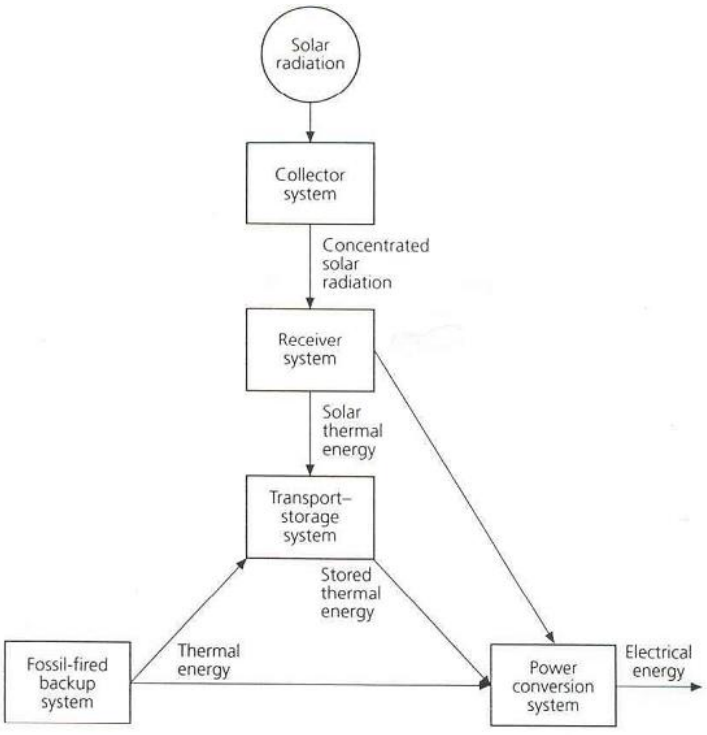

Figure 2.1 Schematic of a CSP system [3]

2.2 The Parabolic-Dish System

In this system, a two axis sun tracking parabolic-shaped concentrator is used to concentrate direct solar radiation onto a receiver situated at the focal point of the concentrator (Figure 2.2). The parabolic-dish system can be broadly classified into two: systems with centralized and decentralized PCS [3]:

2.2.1 Systems with Centralized Power Conversion System (PCS)

In this system a working fluid is circulated through many receivers situated at the focal point of the collectors and then sent to a centralized power-block for the production of electricity. This system has the advantage of easy thermal storage system integration but the circulation of HTF through the field pose a great challenge due to high thermal losses, pumping power and piping requirements [34]. Water/steam and air have been used in these systems.

2.2.1.1 Water/Steam System

Various studies and pilot plants in which water was used as the HTF and superheated steam produced from the receiver is sent to a conventional power block have been developed since the 1970s. These include [35]:

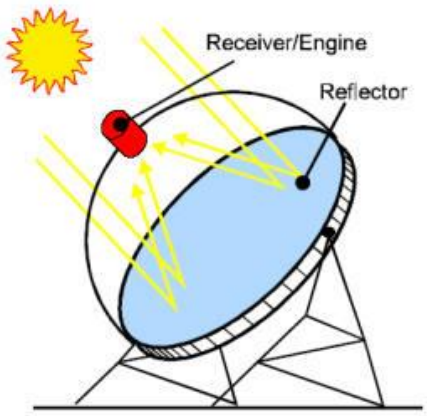

Figure 2.2 The parabolic-dish system

- The White Cliff 25 kW_e and 100 kW_{th} capacity CHP plant having 14, 5 m in diameter, parabolic-dish concentrators producing steam at 70 bar, 550^oC in a ‘semi cavity’ receiver. The plant started operation in 1983 and was shut down due to high cost leading to inability to compete with diesel engines.
- The 4.92 MW_e Solarplant I (Figure 2.3) in Warner Springs, California consisting of 600 stretched-membrane mirror dish collectors with a nitrate salt bath thermal storage in the receiver. The plant operated between 1984 and 1990 and was shut down due to high heat losses in the receiver and non-durability of the stretched membrane.

Figure 2.3 The 4.92 MW_e Solarplant 1 in Warner Spring, California

Two prototypes of the “Big dish” concentrators have successfully been tested [36; 37]: The first is the SG3 (Figure 2.4(a)) developed in 1994 in ANU, capable of producing superheated steam at 45 bar, 500^{o}C using a 100 g/s steam capacity mono-tube cavity receiver (Figure 2.4(b)) while the second was tested in the Ben Gurio University, Israel. Partnership between ANU and Wizard Power Pty led to the development of the SG4 prototype (Figure 2.4(c)) having 500 m^2 aperture area which was completed in 2009 [38]. The collector was made up of square mirror panel to optimize it for mass production.

(a)

(b)

(c)

Figure 2.4 Picture of the (a) 400 m^2 SG3 Dish (b) monotube cavity receiver (c) 500 m^2 SG4 Dish

The construction of a 40 MW_e solar thermal power plant in Whyalla, South Australia using 300 of the SG4 dish was expected to commence in late 2013. This is expected to be the first large scale commercial plant utilizing this technology.

2.2.1.2 Air Systems

The use of air as HTF in a volumetric receiver of a large parabolic dish with 500 m^2 aperture area was tested in 2007 by HelioFocus Ltd in Israel. The air is used in the production of steam for use in a fossil-fired power plant. In order to ensure low cost the collector is made flat with square mirrors arranged in a Fresnel-like way. The possibility of using a micro turbine is explored. A 320 m^2 prototype parabolic dish system also using air as HTF has been commissioned in 2011 using an 80 kW_e capacity micro turbine [35].

2.2.2 Systems with Decentralized Power Conversion System (PCS)

In these systems a coupled PCS is used at the focal point of each collector for the production of electricity. PCS used over the years include: steam and organic Rankine-cycle engines; Brayton-cycle engines; Stirling-cycle engines; and sodium-heat engine. Test in the 1970s and 1980s proved the unsuitability of steam and organic Rankine-cycle engines. This is due to weight and size limitations of using a high efficiency turbine expander and high maintenance cost for small steam Rankine-cycle engines; and the inefficiency and requirement of a big heat exchanger for organic Rankine-cycle engines. In sodium-heat engine the pressure differences caused by temperature differences is used to move sodium through an electrolyte and electrons produce useful work by passing through an external circuit. It has the advantage of not having any moving parts but is inefficient and there is need for further research on the technology [3; 35].

The Stirling-cycle engine is the most efficient CSP system with solar to electricity conversion efficiencies of up to 29.4%, concentration ratios ranging from 600 to 2000 suns and ability to produce temperatures in excess of 1500^oC [3; 4]. Although Brayton-cycle engines has been demonstrated in a dish system

[39], the Stirling-cycle engine is the most researched and used commercially. This is because of its high power density, high thermal to mechanical efficiency of about 40%, low-maintenance cost and high reliability for long term operation [3; 35]. The main disadvantage of decentralized-PCS dish system is that it requires many small components and a thermal storage system is difficult to incorporate.

2.2.2.1 Dish Stirling Engine System

Stirling engines are hot-gas machines with a closed thermodynamic process in which cyclic expansion and compression of a working gas due to the addition or removal of heat is used for the production of mechanical work. The Stirling engine requires the addition of heat from an external source as opposed to the Diesel and Otto cycles. This makes them very suitable for solar thermal applications. The Stirling engine basically consists of two cylinders: the working and the compression cylinders. Hydrogen or helium is used as working gas. Stirling engines can be divided into two [35]:

- The free piston Stirling engine in which there is no link between the two pistons.
- The kinematic Stirling engine in which a crank shaft is used for the transmission of power from the pistons to the generator.

2.2.2.1.1 Early Development

Various dish Stirling engine systems prototypes have been developed and tested in the 1980s with capacities ranging from 5 to 25 kW_e. These include [3; 35]:

- The Vanguard 1 (Figure 2.5(a)) in southern California with a capacity of 25 kW_e using the United Stirling 4-95 Mark II engine which started operation in 1984. Daily net average efficiency of 22.7% with a maximum net solar to electricity conversion efficiency of 29.4% was achieved for the 18 months operation of the plant with availability of 72%. This pilot plant gave a lot of insights in the operation and maintenance of the dish Stirling System.

(a) 25 kW_e Vanguard 1

(b) McDonnell Douglas/United Stirling

(c) 50 kW_e Schlaich Bergermann stretched-membrane system

(d) 10 kW_e Distal I, PSA

Figure 2.5 Pictures of various dish Stirling systems

The United Stirling 4-95 Mark II engine was also tested in three prototypes developed by McDonnell Douglas Corporation and United Stirling in Huntington Beach, California (Figure 2.5(b)) and result showed its high performance, and reliability. Further tests by the Southern California Edison

(SCE) between 1986 and 1988 gave net system efficiency of 28.4% and availabilities ranging from 50 to 87% [40].

- The feasibility of using stretched membrane concentrator was demonstrated using two 17 m diameter, grid-connected 50 kW_e dish Stirling systems (using a USAB model 4-275 Stirling engine) in Saudi Arabia by Schlaich Bergermann—Figure 2.5(c)—[41]. Overall system efficiency of 20% was achieved during the 3500 hours test. The use of stretched membrane was aimed at reducing the cost of the system. In 1989, a smaller stretched membrane collectors (Figure 2.5(d)) with diameters of 7.5 and 8.5 m coupled with the 10 kW_e SOLO V160 Stirling engine were field tested in PSA for more than 30,000 hours using azimuth elevation and polar tracking. Two advanced parabolic dish systems: a 7 kW_e and 25 kW_e for standalone and grid-connected power generation were developed by Cummins Power Generation in 1991 having a faceted stretched membrane concentrator made up polymer, tracking the sun using a polar axis drive. The Stirling engine type was the free-piston type [42]. The use of a heat pipe receiver using the liquid to gas phase change of sodium ensures high efficiency and even temperature distribution [43].

These activities in the 1980s have shown the potential of the dish Stirling system for standalone applications for capacities of up to 25 kW_e. Various initiatives have followed this initial interest in parabolic-dish but were cancelled due to one reason or the other. Most of the dish Stirling system built were standalone systems and thus were very expensive.

2.2.2.1.2 Current Initiatives

Various initiatives have followed the initial interest in order to commercialize the dish Stirling system. These include [35]:

- The Euro Dish project (Figure 2.6) in 1998, in which two 8.5 m diameter, 10 kW_e capacity, using a concentrator made up of fibre glass reinforced plastic shell and the SOLO Stirling 161 engine were initially built in PSA. Testing

was later conducted in many countries to gain operational experience in various climatic conditions.

- A 3.2 kW_e capacity system with a 4.7 m diameter concentrator having the free-piston type engine. The Stirling engine requires no maintenance for its whole life span. Testing has been conducted in various sites and a commercial installation of a plant in Yuma, Arizona, with 30 units was constructed in late 2010.
- A 1.5 MW plant (Tooele Army Depot project) with 430 parabolic-dish systems each having an aperture area of 35 m^2 is under construction in Tooele, Utah, USA [6].

2.3 The Power-Tower System

In this power generation technology, a large field of heliostats (reflecting mirrors) intercepts and concentrate solar radiation on to a central receiver situated on a tower. The concentrated solar radiation is absorbed by the HTF circulating in the receiver (i.e. receiver coolant) and the thermal energy is transported into a power conversion and storage unit.

Figure 2.6 The 10 kW_e EuroDish, PSA

Typical HTFs include: Liquid sodium, air, water/steam, thermal oils and molten salts. The heliostats are arranged in such a way that solar radiation striking them is reflected on the receiver at all times. For this to be possible the heliostats, track the sun along two-axes. Since a large field of heliostats concentrates solar radiation on-to a single receiver, very high concentration ratios up to 1500 can be achieved resulting in working fluid temperatures up to 1500^{o}C and can achieve average annual solar to electricity conversion efficiency of 20 to 35% [44]. Recently, Ho and Iverson [45] reported gross conversion efficiency of between 30 and 40% at operating temperatures of <600^{o}C. Typical operating temperature and size of the receiver depends on the thermo-physical properties of the HTF. Figure 2.7 is a configuration of a power-tower system in which the HTF is molten salt. The molten salt is pumped from the cold storage tank at 290^{o}C through the receiver (where it is heated to about 565^{o}C) to the hot storage tank. Steam is then produced in a heat exchanger by pumping the molten salt from the hot tank through the heat exchanger to the cold storage tank. The steam is then sent to a power block for the production of electricity [4].

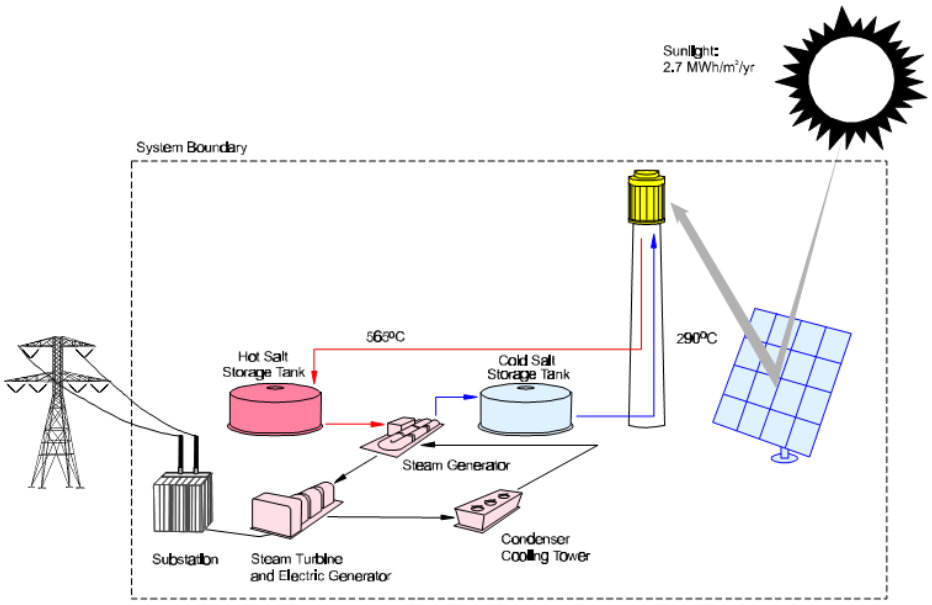

Figure 2.7 Configuration of a typical central receiver system [4]

2.3.1 Early Research and Development

In the late 1970s and early 1980s, development of the power-tower technology started, with many experimental plants in different countries such as the USA, France, Japan, Spain, Italy and Russia. In the initial stage these systems were designed for the production of thermal energy. In the USA research has been conducted on test facilities having thermal capacities of up to 5 MW. Some of the early plants tested in the world are presented in Table 2.1. These plants proved the feasibility for the generation of electricity using this technology [4; 46].

Although Liquid sodium has attractive properties for use as HTF such as high rate of heat transfer and low vapour pressure meaning smaller receiver; and operating temperature of 540^{o}C. It was only used in the SSPS plant in 1981 because it is an active metal and reacts rapidly with water or air. Thermal oils were also not used commercially due to their low maximum operating temperatures, flammability and are difficult to pump at low temperatures compared to other HTFs [32]. Thus research to date has concentrated on mainly three HTFs: Water/Steam, Molten Salts and Air. In the section that follow, the development of each was discussed to ascertain its current status.

Table 2.1 Early Central Receiver Experimental and Commercial Plants [4]

Project	Country	Power Output (MWe)	Heat Transfer Fluid	Storage Medium	Operation
SSPS	Spain	0.5	Liquid Sodium	Sodium	1981
EURELIOS	Italy	1	Steam	Nitrate Salt/Water	1981
SUNSHINE	Japan	1	Steam	Nitrate Salt/Water	1981
Solar One	USA	10	Steam	Oil/Rock	1982
CESA-1	Spain	1	Steam	Nitrate Salt	1983
MSEE/Cat B	USA	1	Molten Nitrate	Nitrate Salt	1984
THEMIS	France	2.5	Hi-Tec Salt	Hi-Tec Salt	1984
SPP-5	Russia	5	Steam	Water/Steam	1986
TSA	Spain	1	Air	Ceramic	1993
Solar Two	USA	10	Molten Nitrate Salt	Nitrate Salt	1996

2.3.2 Water/Steam Systems

The main advantage of using water/steam as HTF is that costly steam generator is not required since the steam is generated in the receiver. This has the potential of reducing the cost of the system.

The feasibility of using water/steam as HTF in power-tower on a large scale was first demonstrated in the 10 MW_e Solar One project. The plant consists of a total heliostat reflective area of 71,447.4 m^2, with each heliostat having a reflective area of 39.2 m^2. Steam is produced at a temperature of about 510^oC in an external cylindrical receiver (thermal capacity, 42 MW) situated 13.6 m high. A 182 MWh_{th} capacity, dual medium, rock/sand and oil (Caloria HT43) storage system was used for the storage of excess thermal energy [46; 47]. For the three years of operation, annual solar to electricity conversion efficiency of 4.1%, 5.8% and 5.7% were achieved respectively. A maximum efficiency of 8.7% was achieved in August 1985. Various challenges encountered hindered the performance of the system and showed that water/steam is not a good HTF and that a storage system is needed for the stable operation of such type of plants [46-48]. The main challenge was the inability of the receiver to produce superheated steam.

To solve this problem, saturated steam is produced in the receiver and a fossil-fired super heater can be used for the production of superheated steam. This was successfully tested in the CESA-1 facility in Spain. The use of saturated steam was demonstrated in commercial scale in the 11 MW_e PS10 plant in Spain. This plant has a total heliostat reflective area of 74,880 m^2 (approximately close to that of Solar One) with fewer and much bigger heliostats having reflective area of 120 m^2 each. A pressurized water tank was used as the storage system, which produces saturated steam temperatures of 250-255^oC at a pressure of 20 bar. The receiver tower has a height of 115 m and the semi-cylindrical cavity type receiver producing saturated steam at 240^oC with a maximum capacity of 55 MW was used [49; 50]. The use of cavity receivers meant increase in receiver efficiency since cavity receivers are generally more efficient than external receivers by about 10% [32]. PS10 has an

overall solar to electricity conversion efficiency of about 17% which is twice the maximum ever recorded by Solar One. The success of this plant lead to the construction of a similar plant (PS20) having a capacity of 20 MW_e in April 2009 [50; 51]. Figure 2.8 shows the configuration of the PS10. The disadvantage of using the cavity receiver was that, the heliostat field can only be in one side. A dual cavity receiver was thus developed and tested in the 5 MW Sierra Sun Tower plant in July 2009 with superheated steam produced at 60 bar and 440^{o}C [6; 52; 53]

A plant called the Ivanapha Solar Electricity Generating Station (ISEGS) having a total gross capacity of 392 MW using water/steam as HTF consisting of three units with capacities of 126, 133 and 133 MW respectively is under construction. The first unit started operation in 2013. They are expected to have a gross annual solar to electricity conversion efficiency of 28.72% with superheated steam produced in the receiver at a temperature of 565^{o}C [6; 54].

The power-tower using water as HTF is a matured technology that has already been commercialized. Over the years there has been an increase in annual solar to electricity conversion efficiency from about 5% in Solar One to 28.72% (this efficiency is projected not actual). This can partly be attributed to the increase in operating temperatures and pressures.

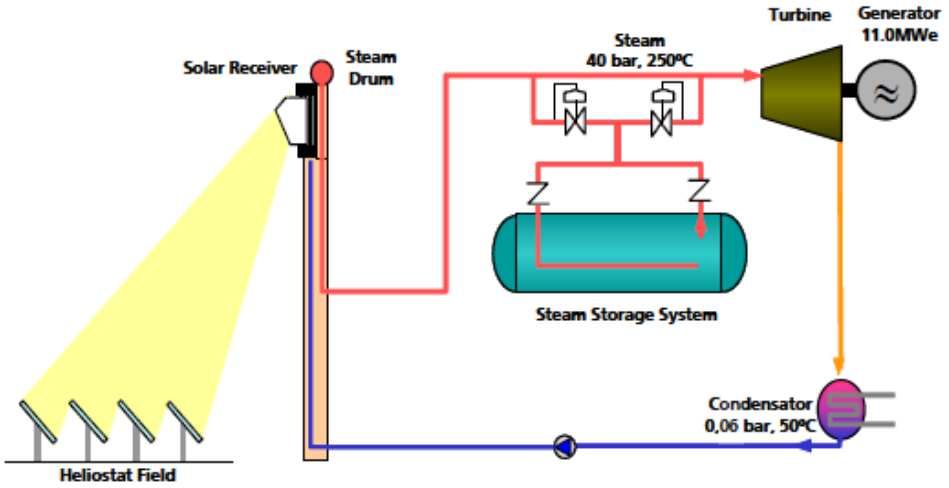

Figure 2.8 PS10 Schematic Diagram [49]

Table 2.2 presents the small plants in operation around the world using water/steam each with different kind of thermal storage system. Table 2.3 presents commercial plants under construction and development. Two out of the three plants have no thermal storage system while the third has a 2 hour saturated steam system. This is because the main challenge of using water/steam is finding a cost effective large scale thermal storage system. The use of pressurized steam which is the simplest option is very expensive and difficult for large scale applications.

Table 2.2 Small power-tower plants using water/steam in operation in the world [6]

Project Name	**Dahan Power Plant**	**Greenway CSP Mersin Tower Plant**	**Lake Cargelligo**
Developer	Institute of electrical engineering of Chinese Academy of science	Greenway CSP	Lloyd Energy Systems Pty Ltd
Location	Beijing, China	Mersin, Turkey	Cargelligo, Australia
Solar Field Configuration			
No. of Heliostats	100		620
Heliostat reflective area (m^2)	100		9.8
Tower height(m)	118		
Receiver Type	Cavity Receiver		Graphite Solar storage receiver
Receiver Inlet temperature(^oC)	104		200
Receiver outlet temperature(^oC)	400		500
Power Block			
Gross Turbine Capacity(MW)	1	1.4	3
Power Block cycle	Steam Rankine	Steam Rankine	Steam Rankine
Thermal Storage	Two stage saturated steam/oil	Molten salt. Single 3-phase tank, natural circulation, super steam junction design	Core graphite thermal storage technology
Thermal storage capacity (hr)	1	4 MW/hr	
Expected Electricity Generation (GWh/yr)			
Start Year of Operation	2012	2012	2011
Status	Operational	Operational	Operational

Table 2.3 Commercial power-tower plants using water/steam under construction or development [6]

Project Name	**Ashalim Thermal Solar Power Station**	**Khi Solar One**	**Palen Solar Electric Generating System**
Developer	Megalim Solar Power Ltd	Abengoa Solar-IDC	BrightSource Energy
Location	Ashalim, Israel	Upington, South Africa	Desert Centre, California
Solar Field Configuration			
No. of Heliostats		4,120	
Heliostat reflective area (m^2)		140	
Tower height(m)	240	200	
Receiver Type			
Receiver Inlet temperature(^oC)			
Receiver outlet temperature(^oC)			
Power Block			
Gross Turbine Capacity(MW)	121	50	500
Power Block cycle	Steam Rankine	Steam Rankine	Steam Rankine
Thermal Storage	None	Saturated Steam	None
Thermal storage capacity (hr)		2	
Expected Electricity Generation (GWh/yr)			
Start Year of Operation	2017	2014	2016
Status	Under development	Under construction	Under development

2.3.3 Molten Salt Systems

The low operating pressure and high specific heat capacity of molten salt meaning lighter piping make them attractive for use in power tower systems. Their main drawback is their high melting point, thus requiring freeze protection leading to higher parasitics.

The challenges encountered during the operation of the Solar One plant using water/steam and the conclusion to the unsuitability of using water as HTF, led to the modification of the plant to Solar Two using molten salt as HTF. The Solar Two is a 12 MW_e plant using molten nitrate salt (60% sodium nitrate and 40% potassium nitrate) with a two-tank direct thermal storage system capable of 3 hours full load operation. The heliostat field has a total reflective area of 81,707.4 m^2 [55]. The receiver, which is a cylindrical external type, can absorb 42 MW of thermal energy with an absorption efficiency of 95% at an average solar radiation flux of 430 kW/m^2 [56]. In the steam generator superheated steam is produced at 100 bar, 535^oC. The operation of the plant which ended in April 1999, proved the technical and economic feasibility for deployment of large commercial plants. Peak solar to electricity conversion efficiency of 15% was obtained [56]. This is much higher than that of Solar One.

The Solar Two operation encountered problems such as: blockage of receiver tubes leading to failures; failure of steam generator; receiver warpage due to lack of adequate allowance for thermal expansion. This alongside other financial problems led to the shutting down of the plant [54]. The law in Spain that all utility companies to buy electricity at 24 ¢/kWh for at least five years led to the development of the 15 MW_e Solar Tres plant in 2000 [56]. The plant has a total heliostat reflective area of 297,600 m^2 with large heliostats to reduce the number of drive mechanisms each having an area of 120 m^2. This led to reduction in cost of the heliostat field of 45% compared to Solar Two. A two-tank thermal storage system capable for 15 hour full load operation was used. The receiver is a 120 MW_{th} external cylindrical type similar to that of solar two and 3% more efficient, situated 120 m high. Other improvements were [57]: all equipment are placed above the storage system to allow easy draining of

molten salt; and the heat tracing was improved [10; 50]. This plant was later converted into the 19.9 MW_e Gemasolar Thermosolar plant (Figure 2.9) and this started operation in April 2011. Some of the changes made are the increase in the size of the heliostat field reflective area to 318,000 m^2 and the height of the tower to 140 m. The plants have proved the feasibility of 24 hours uninterrupted power production [6; 58]. Four plants having a combine capacity of 420 MW_e are under construction in the world using either direct or indirect TESS (Table 2.4).

Figure 2.9 The 19.9 MW Gemmasolar Themosolar plant in Spain

Table 2.4 Commercial solar tower plants using molten salt under construction in the world [6]

Project Name	**Crescent Dunes Solar Energy Project**	**Rice Solar Energy Project (RSEP)**	**Planta Solar Cerro Dominador**	**Supcon Solar Project**
Developer	SolarReserve's Tonopah Solar Energy, LLC	Solar Reserve's Rice Solar Energy, LLC	Abengoa Solar	SUPCON Solar
Location	Tonopah, Nevada	Rice, Mojave Desert, California	Calama, Chile	Delinga, China
Solar Field Configuration				
No. of Heliostats	17,170	17,170	10,600	217,440
Heliostat reflective area (m^2)	62.4	62.4	140	2
Tower height(m)	164.6	164.6	243	80
Receiver Type	Cylindrical-External	Cylindrical-External	External	
Receiver Inlet temperature(^oC)	288	288	300	
Receiver outlet temperature(^oC)	566	566	550	
Power Block				
Gross Turbine Capacity(MW)	110	150	110	50
Power Block cycle	Steam Rankine Cycle	Steam Rankine	Steam Rankine	Steam Rankine
Thermal Storage	Two tank direct	Two tank system	Two tank indirect	Two tank direct
Thermal storage capacity (hr)	10		17.5	2.5
Expected Electricity Generation (GWh/yr)	485	450		
Start Year of Operation	2013	2016	2018	
Status	Under construction	Under construction	Under construction	Under construction

2.3.4 Air Systems

Air as a receiver coolant has the advantage of being readily available, free, very low freezing point, and can be heated to any technically possible temperature meaning higher solar to electricity conversion efficiency. It can also be used in a gas turbine cycle directly (solar only) or used to pre-heat air before entering the combustor (hybrid). Up to 35% solar to electricity conversion efficiency is obtainable in solar only mode [59]. The hybrid operation mode has potential of increasing the solar to electricity conversion efficiency [60]. Using air as HTF can produce electricity more cost effectively than liquid sodium, nitrate salt or water/steam [61]. These make air an excellent candidate for solar thermal power generation. But air has a very low specific heat capacity and density and thus must be pressurized. This makes the sizes of air receivers and consequently cost to be higher than that of other HTF receivers. The main challenge of using air is the development of a suitable air receiver technology and thus research over the years has been geared toward developing air receivers.

Initial designs of air receivers in the 1980s led to overheating of the receiver tubes due to the very low specific heat capacity of air [5]. To solve this problem the volumetric air receiver having a wire mesh was developed. This new receiver technology with 2.5 MW_{th} capacity was tested at in the CESA-1 facility in Almeria, Spain and temperatures up to 800^{o}C were achieved. Another air receiver technology called the HiTRec developed by the DLR in Germany using a porous material as the heat absorbing medium instead of a wire mesh was successfully tested using a 3 MW_{th} capacity prototype. Test was conducted for over 200 hours in the PSA facility in Spain in a project called the SOLAir, achieving temperatures of up to 750^{o}C.[62]

The first attempt to use the air receiver on commercial scale was in a 30 MW_{e} solar/fossil fuel hybrid plant called the PHOEBUS project in Jordan. Grasse [63] and Meinecke et al. [64] have presented the details of the design of this plant. Technical, financial and the gulf war prevented the construction of this plant [65]. Attempts to commercialize this technology led to the construction of the 1.5

MW Jülich Solar Tower in 2006 to serve as demonstration for future deployment of commercial plants. The plant was designed to heat air to about 700^{o}C and used to produce steam in a steam generator at 100 bar, 500^{o}C and has a ceramic sensible storage system [66]. But during test steam was produced at 27 bar and 485^{o}C. The plant started operation in April 2009 delivering electricity to the grid [62]. Figure 2.10 shows the configuration of the plant.

The integration of volumetric air receivers with a gas turbine cycle was also tested (Figure 2.11) successfully in 2002 at the PSA facility in Spain using a plant of 230 kW_e capacity. Temperatures up to 930^{o}C were achieved [67].

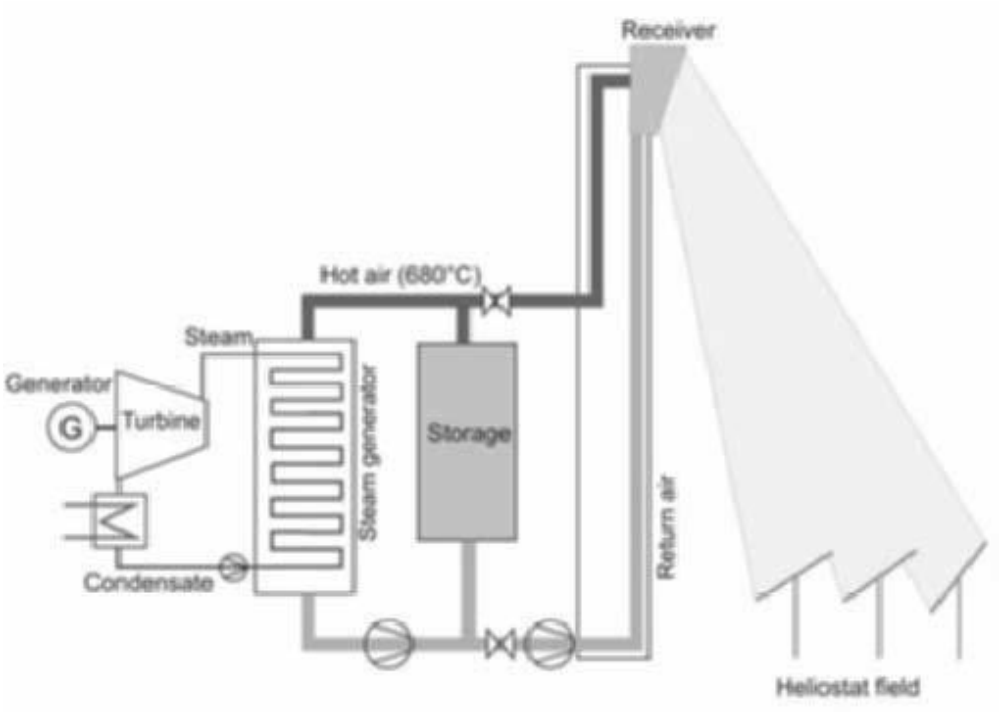

Figure 2.10 Schematic diagram of the Jülich power plant in Germany [66]

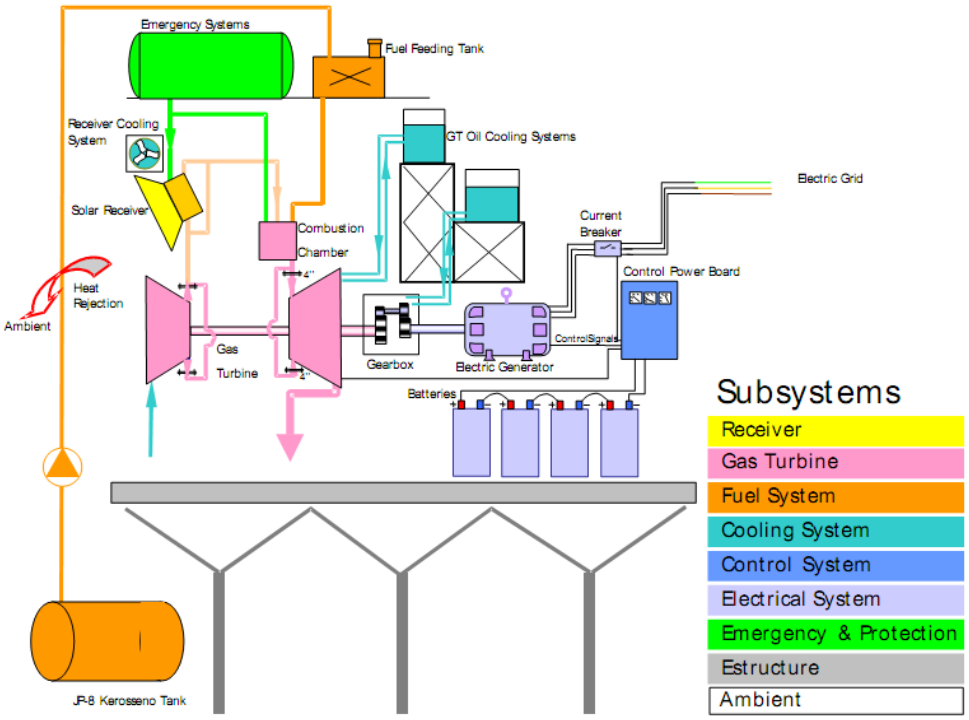

Figure 2.11 Schematic diagram of the SOLGATE hybrid plant [67]

Other researches were geared towards increasing the operating temperature meaning higher efficiencies. This led to the development of the beam down reflector concept [68]. In this concept a hyperboloidal reflector situated at the top of a tower collects concentrated radiation from the heliostat field and reflect it onto a compound parabolic collector (CPC) array situated below the tower. The CPC then further concentrates the radiation on to an annular pressurized receiver. High temperature suitable for use in a Brayton-cycle is obtainable. Figure 2.12 presents the concept. This concept has the advantage of a light weight tower since the receiver and the secondary concentrator are all situated near the ground level [69]. An Israeli consortium (ConSolar) have been involved in the development of the beam down reflector concept in which pressurized air at 20 bar can be heated up to 1200^{o}C using a compact volumetric receiver [70]. Another pilot plant (Figure 2.13) has been developed in Masdar Abu Dhabi consisting of 33 two axis heliostats reflecting solar radiation onto other set of mirrors at the top of a tower. The radiation is then sent to a concave receiver which heats water to generate steam [71].

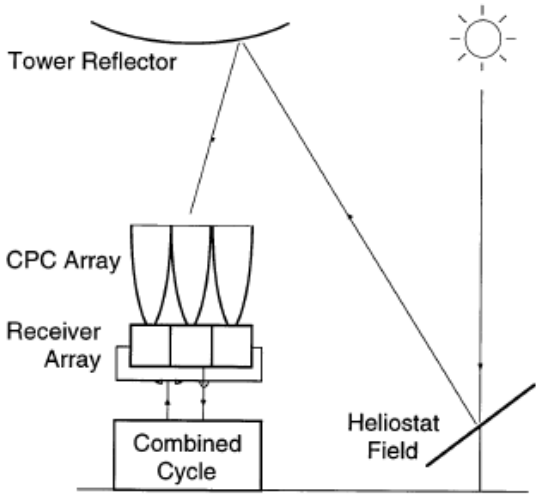

Figure 2.12 The Beam Down Reflector Concept [69]

Figure 2.13 The beam down reflector plant in Masdar, Abu Dhabi [71]

2.4 The Parabolic-Trough System

This system consists of a large field of collectors having a linear parabolic shape in the form of a trough. The collectors are aligned in rows tracking the sun in a single axis from east to west. The solar radiation received by each row of collectors is concentrated onto a tube like receiver which runs at the focal point of the trough. HTF is circulated through the receivers and the thermal energy is collected, transported and used to produce steam in a series of heat exchangers. The superheated steam which is at high pressure is used to generate electricity in a conventional Rankine-cycle power-block. In cases where the HTF is water/steam, a steam generator is not required and the steam from the collector is sent directly to the power-block. In some configurations a backup fossil fuel boiler and/or a thermal storage system is incorporated for thermal energy production when there is no sunshine or periods of low insolation (Figure 2.14).

The parabolic-trough can be integrated with conventional fossil fired power plant (combine cycle or coal fired). Parabolic trough integrated with combine cycle plants are called ISCC plants. In ISCC plants the solar field can either be used to produce high or low pressure steam for use in the high or low pressure stage of the turbine respectively (Figure 2.15). Other combinations include combining the solar field with an existing coal fired power plant (coal hybrid). These kinds of plants appear attractive and can aid the step wise and cost effective introduction of solar technology since there are already existing coal and combine cycle plants [4].

2.4.1 Early Development and Research Activities

The large scale development of parabolic-trough systems started in the USA, in the 1970s by the ERDA. These systems were basically intended for the production of industrial process heat at temperatures more than $500^{o}C$. Collector areas up to 5000 m^2 have been utilized at this time [4].

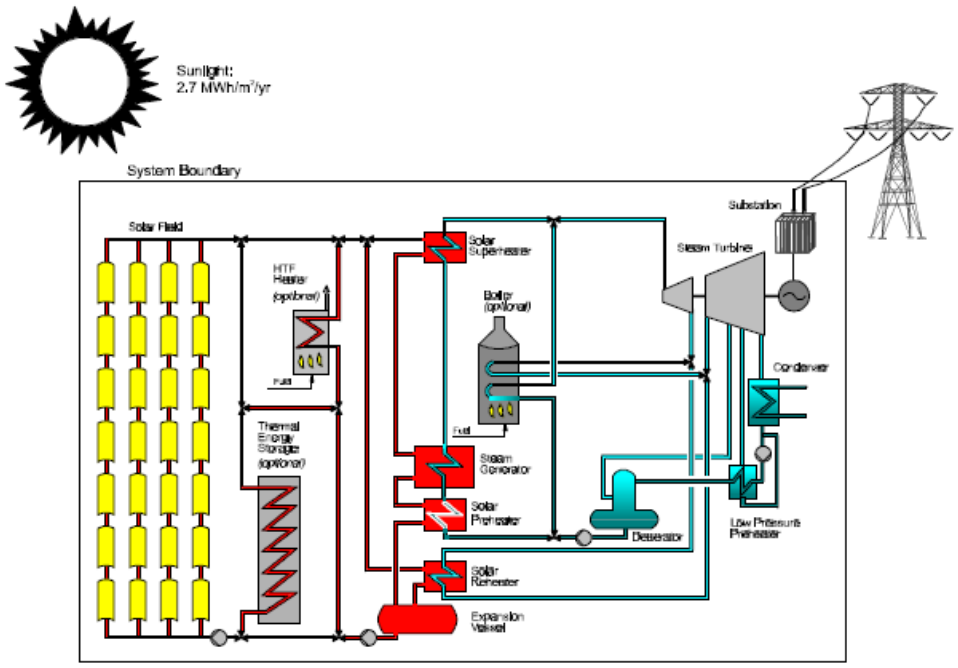

Figure 2.14 Schematic diagram of a typical parabolic-trough plant [4]

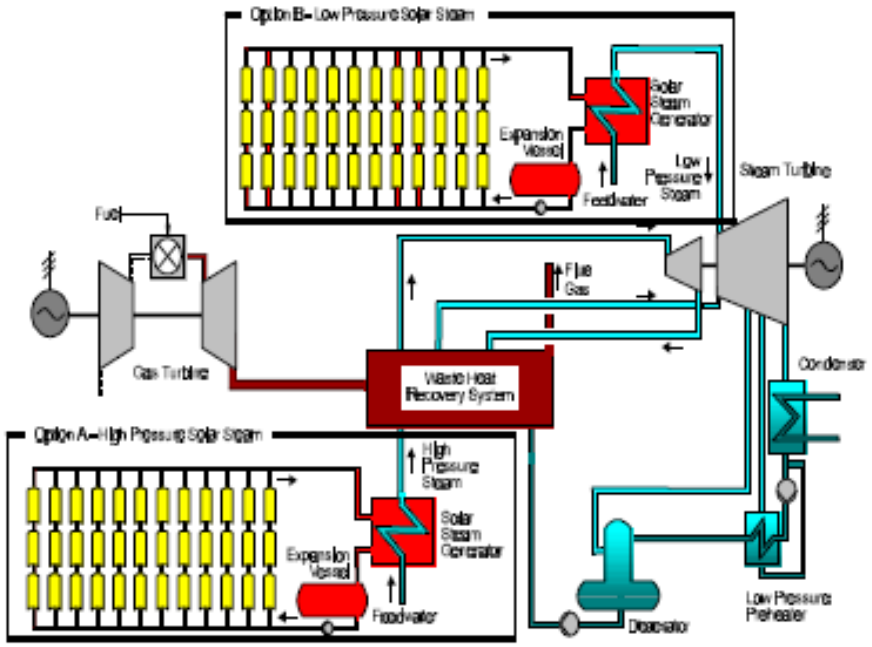

Figure 2.15 Schematic diagram of integrated solar combine cycle (ISCC) plant [4]

Similarly in the Europe, developments were taking place which in 1981 led to the construction of the SSPS/DCS (Small Solar Power Systems

Project/Distributed Collector System) in Spain with an electrical capacity of 0.5 MW and a total collector area of 7602 m^2 and a 5 MW_{th} capacity, cylindrical dual medium (thermal oil and cast iron slab) thermal storage system [4; 72-74]. The daily solar to electric conversion efficiency achieved was approximately 2.5% compared to the design value of 9% [3].

Many HTF have been used in parabolic-trough plants. The most studied are: Thermal oils, molten salt and water/steam. In the section that follow development and current status of each will be discussed.

2.4.2 Thermal Oil Systems

The first commercial parabolic-trough power plants were the SEGS I and II plants having capacities of 13.8 and 30 MW_e respectively and they started operation in 1984 and 1985 respectively. The success in operation of these plants led to the development of further six plants i.e. SEGS III to IX [3; 4; 74]. Table 2.5 presents the characteristics of these plants and Figure 2.16 shows their configuration. Initially in the SEG I plant (Figure 2.16a), mineral oil (Esso 500) was used as the HTF to produce saturated steam at 35.3 bar in a shell-and-tube heat exchanger. The saturated steam is then superheated to 415^oC by the natural-gas-fired super-heater. A two-tank direct system was used as the storage system. The maximum operating temperature of the HTF limited the production of superheated steam by the solar field in the SEG I plant. Thus 18% of the energy produced by the plant is provided by the fossil-fired super heater. In the SEG II plant a HTF (Therminol vp-1) with higher operating temperature was used making it possible for the production of superheated steam by the solar field. The cost of the HTF, which is a synthetic-oil, prohibits the use of the direct two-tank system and thus a natural gas fired boiler was used as a backup source [3].

Table 2.5 SEGS I-IX plant Characteristics [3; 4]

SEGS Plant	1st Year of operation	Net Output (MW_e)	Solar Field Outlet Temp. (^oC)	Solar Field Area (m^2)	Solar Turbine Efficiency (%)	Fossil Turbine Efficiency (%)	Annual Output (MWh)
I	1985	13.8	307	82,960	31.5	-	30,100
II	1986	30	321	190,338	29.4	37.3	80,500
III & IV	1987	30	349	230,300	30.6	37.4	92,780
V	1988	30	349	250,500	30.6	37.4	91,820
VI	1989	30	390	188,000	37.5	39.5	90,850
VII	1989	30	390	194,280	37.5	39.5	92,646
VIII	1990	80	390	464,340	37.6	37.6	252,750
IX	1991	80	390	483,960	37.6	37.6	256,125

Experience gained in these two plants led to the development of the SEG III-IX each with a capacity of 30 MW_e using Therminol vp-1 as HTF. Modifications made were: increase in the solar field optical efficiency by 9%; use of a re-heat turbine and increase in the solar field outlet temperature from 321^{o}C in SEG II to 349^{o}C in SEGS III-V and 390^{o}C in SEGS VI and VII. These led to increase in turbine efficiency from 29.4% in SEG II to 30.4% in SEGS III-V and 37.5% in SEGS VI and VII translating into the increase in power by 25% in SEGS III-VII. Solar to electricity conversion (annual) efficiencies of 11.5% and 14.5% were projected for SEGS III-V and SEGS VI-VIII respectively. In SEGS VIII and IX the turbine efficiency was increased to 37.6%. Steam conditions were also increased to 43.5 bar, 327^{o}C and 100 bar, 371^{o}C in SEGS III-V and SEGS VI-IX plants respectively [3; 4]. These plants have been in operation since then producing power to the grid. In 2002 it was estimated that the plants have produce 662 GWh of solar electricity and have offset 3800 tons of CO_2 emissions each year [14].

The continuous use of this technology will require reduction in cost. The main component that has the highest cost is the solar field. This led to the development of the Solargenix parabolic-trough in 2000.

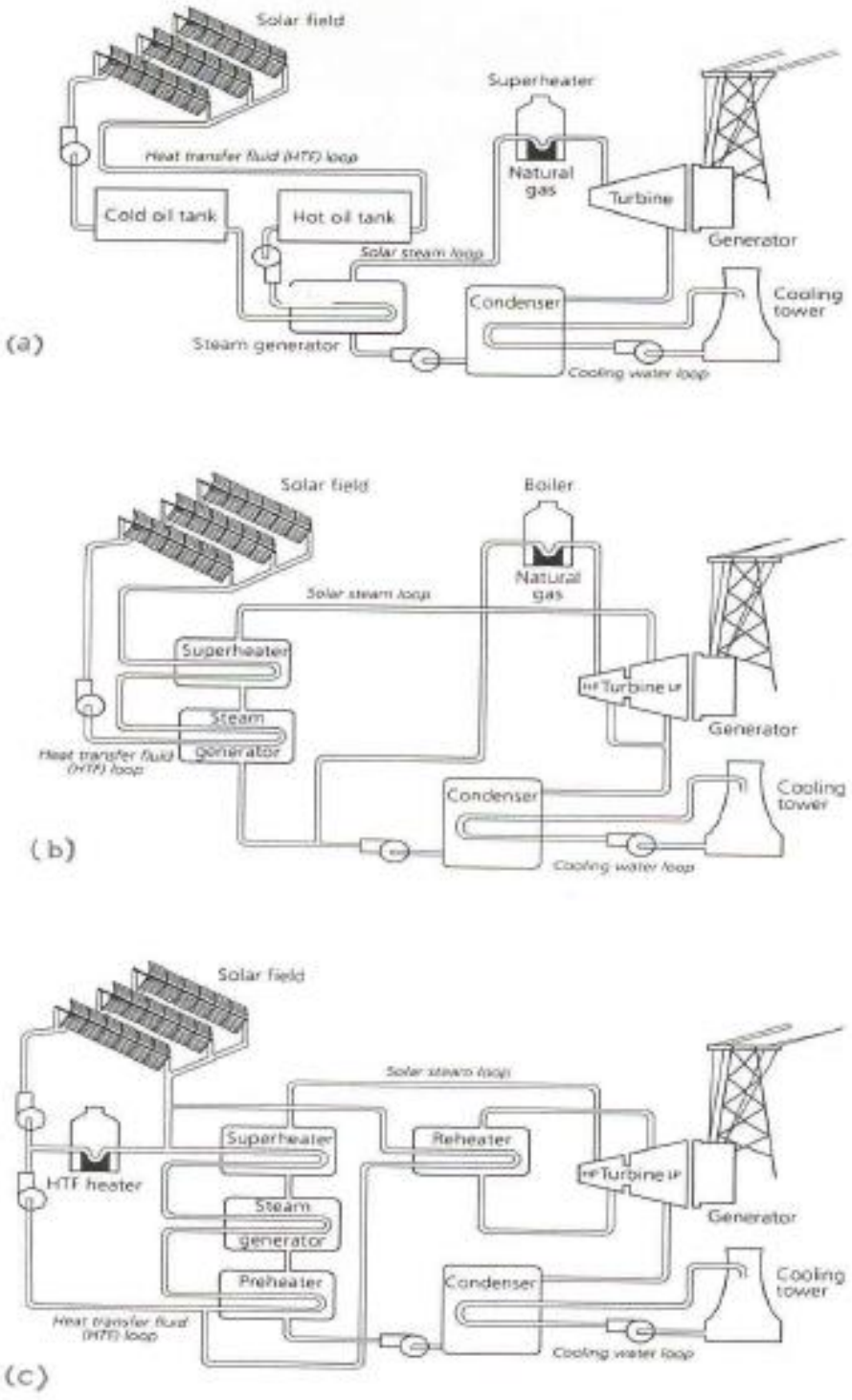

Figure 2.16 Schematic Diagram of the SEGS plants (a) SEGSI (b) SEGS III-V (c) SEGS VIII&IX.

This collector is light weight offering 10% performance increase and 18% reduction in installation cost and over 20% increase in cost compared to previous collectors [75]. The collector was used in the 1 MW_e pilot plant in Arizona, USA which started operation in 2006 using Xceltherm 600 as HTF. The HTF which is heated to 290^oC is sent to an organic Rankine-cycle using pentane as working fluid operating at a temperature of 205^oC. Annual solar to electricity conversion efficiencies of 12% were achieved [74; 76]. The success of this test led to the construction of the first commercial plant after the SEGS plants called the Nevada Solar One (Figure 2.17) having a capacity of 64 MW_e in Las Vegas, USA [14]. The plant is equipped with a small buffer thermal storage system capable of 30 mins full load operation and is expected to produce 129 GWh of electricity annually [77].

(a) The whole plant

(b) The solar field

(c) The power block

Figure 2.17 The 64 MWe Nevada Solar one plant, Nevada, USA

In Europe, the feed in tariff of up to 0.23 €/kWh for any company that construct a plant provided by the Spanish government [14], led to the development of the Andasol plants (Andasol I, II and III which started operation in 2008, 2009 and 2011 respectively)—Figure 2.18. Each plant has a capacity of 50 MW_e. A synthetic thermal oil called Dowtherm A which is similar to Therminol vp-1 was used as the HTF. It is heated to about 393^oC in the solar field and used to produce steam at 100 bar, 377^oC in a steam generator. The plant (Andasol I) is equipped with the two tank indirect thermal storage system having a capacity of 1,010 MWh_{th} (suitable for 7.5 hours full load operation). Molten salt was used as the storage medium. The plant is also equipped with a two 15 MW_{th} capacity fossil fired heaters to serve as backup and to prevent solidification of the molten salt. Annual solar to electricity conversion efficiency of the plant was 16% [74]. This is higher than that of the SEGS plants by 1.5%.

Figure 2.18 The Andasol 1 plant in Andalusia, Spain

These plants have proven the potential for the production of electricity from solar energy using parabolic-trough for 24 hours and serve as the state of the art in parabolic-trough power plants. Subsequent plants in Spain were built with similar configuration. Each of the Andasol plants consist of solar field aperture of 510,120 m^2 composed of 156 loops with 4 solar collector assemblies in each loop. Table 2.6 presents the commercial plants using thermal oil as HTF in operation in the world today. Those with thermal storage have a two-tank indirect storage system using molten salt with capacities ranging from 5 to 9 hours of full load operation.

Integrating of parabolic trough with existing coal fired or combined cycle plants have also been pursued. In Algeria, Solar Power Plant 1 (SPP1) started operation in 2009. This plant is an ISCC with total capacity of 150 MW_e out of which 25 MW_e output is produced by the solar field [74].

Other projects include [6]:

- The city of medicine Hat ISCC, in which parabolic trough provides 1.1 MW_e capacity of a 203 MW_e combine cycle plant in Medicine Hat, Canada which is under construction.

- The ISCC Ain Beni Mathar in Morrocco in which parabolic-trough provides 20 MW_e out of 470 MW_e capacity which started operation in 2010.

- The ISCC Kuraymat in Eqypt in which parabolic-trough provide 20 MW_e out of the 140 MW_e capacity. The plant started operation in 2011.

Finally Table 2.7 presents the plants using synthetic oil as HTF under construction or development in the world. Many of these plants are equipped with the two-tank storage system and are mostly in other countries other than Spain and the USA.

Table 2.6 Commercial parabolic trough plants using synthetic oil as HTF in the World [4; 6; 78]

Plant	Developer	Location	Capacity (MW)	Operation Start Year
Plants with two-tank thermal storage system				
La Florida	Renovables SAMCA	Badajoz, Spain	50	2010
Extressol I, II and III	ACS/Cobra Group	Badajoz, Spain	150	2010,2010,2013
Arcosol 50	Torresol	Cádiz, Spain	50	2011
Manchasol I and II	ACS/Cobra Group	Ciudad Real, Spain	100	2011
LaDahessa	Renovables SAMCA	Badajoz, Spain	50	2011
Termesol 50 (valle 2)	Torresol	Cádiz, Spain	50	2011
Aste 1A &1B	Elecnor/Aries/ABM AMRO	Ciudad Real, Spain	100	2012
Astexol II	Elecnor/Aries/ABM AMRO	Badajoz, Spain	50	2012
LaAfricana	Ortiz/TSK/Magtel	Córdoba, Spain	50	2012
Arenales	RREF/OHL	Sevilla, Spain	50	2013
Casablanca	ACS/Cobra Group	Badajoz, Spain	50	2013
Solana Generating Station	Abengoa Solar	Arizona, USA	280	2013
Termesol 1 and 2	NextEra, FPL	Badajoz, Spain	100	2013
Plants without thermal storage system				
La Risca	Acciona Energía	Badajoz, Spain	50	2009
Solnova I, III and IV	Abengoa Solar	Seville, Spain	150	2009
Ibersol Puertollano	Iberdrola Energia Solar	Ciudad Real	50	2009
Majadas I	Acciona Energía	Cáceres, Spain	50	2010
Martin Next Generation Solar Energy Centre	Florida Power & Light Co.	Florida, USA	75	2010

Table 2.6 continued

Plant	Developer	Location	Capacity (MW_e)	Operation Start Year
Palma del Río I and II	Acciona Energía	Córdoba, Spain	100	2010, 2011
Lebrija I	Solucia Renovables 1, S.L	Sevilla, Spain	50	2011
HelioEnergy 1 and 2	Abegoa Solar and EON	Sevilla, Spain	100	2011 and 2012
Hellios I and II	Helios I HYPERION Energy Investments	Ciudad, Real	100	2012
Morón	Ibereólica Solar	Sevilla, Spain	50	2012
Olivenza	Ibereólica Solar	Badajoz, Spain	50	2012
Orellana	Acciona	Badajoz, Spain	50	2012
Solacor 1 and 2	Abengoa Solar ; JGC	Córdoba, Spain	100	2012
Borges Termosolar	Abantia	Lleida, Spain	25	2012
Guzmán	FCC Energy	Palma del Rio, Spain	50	2012
Shams I	Masdar/Total/Abengoa Solar	Madinat Zayed, UAE	100	2013
Enerstar	FCC Energy	Alicante, Spain	50	2013
Godawari Solar Project	Godawari Green Energy Limited	Nokh. India	50	2013
Solaben 1, 2, 3 and 6	Abengoa	Cáceres, Spain	50	2013, 2012.2013,2013
Genesis Solar Energy Project	Genesis Solar and NextEra Energy Resources	Riverside, California	250	2014

Table 2.7 Commercial parabolic trough plants using synthetic oil as HTF under construction or development in the World [6]

Plant	Developer	Location	Capacity (MW_e)	Storage System	Expected Operation Start Year
Abhijeet Solar Project	Corporate Ispat Alloys Ltd.	Rajasthan, India	50	None	2013
Agua Prieta II	Abengoa Solar	Agua Prieta, Mexico	14	None	2014
Bokpoort	ACWA Power	Globershoop, South Africa	54.5	9.3 hrs 2-tank indirect	2015
Diwakar	Lanco Solar	Rajasthan, India	100	4 hrs 2-tank indirect	2013
Gujarat Solar One	Cargo Solar Power	Gujarat, India	28	9 hrs 2-tank indirect	2014
KaXu Solar One	Abengoa Solar - IDC	Poffader, South Africa	100	3 hrs 2-tank indirect	2015
KVK Energy Solar Project	KVK Energy Ventures Ltd	Rajasthan, India	100	4 hrs 2-tank indirect	2013
Megha Solar Plant	Megha Engineering and Infrastructure	Andhra Pradesh, India	50	None	2013
Mojave Solar Project	Mojave Solar, LLC ; Abengoa Solar, Inc.	Harper Dry Lake, California, USA	280	None	2014
Noor I	ACWA Power, Aries and TSK	Ouarzazate, Morrocco	160	3 hrs 2-tank indirect	2015
Pedro de Valdivia	Grupo Ibereolica	Maria Elena, Chile	360	10.5 hrs 2- tank indirect	2015
Xina Solar One	Abengoa Solar	Pofadder, South Africa	100	5 hrs 2-tank indirect	2016

2.4.3 Molten Salt Systems

The cost of synthetic thermal-oil prohibits its use as both a HTF and a thermal storage medium in a two-tank direct system. This necessitated the use of molten salt as the storage medium in the two-tank indirect thermal storage system in parabolic trough plants. A costly heat exchanger has to be used for the exchange of thermal energy between the HTF and the storage medium. A solution of doing away with the heat exchanger will thus be to use the molten salt as the HTF. Also when using thermal oil, operating temperature is limited to 400^{o}C, and increase in this temperature will increase plant efficiency.

In view of this the Archimede demonstration plant (Figure 2.19) was constructed in 2010 and then integrated with an existing 370 MW_e combine cycle plant, out of which 5 MW_e will be the solar share of electricity. A molten salt (mixture of 60% $NaNO_3$ and 40% KNO_3) was used as both the HTF and storage medium and is heated from 290^{o}C to 550^{o}C in the solar field. The thermal storage system has a capacity of 100 MWh_{th}, equivalent to 8 hours of operation. The annual solar to electricity conversion efficiency is 15.6% [6; 79; 80]. This plant is the only molten salt system existing.

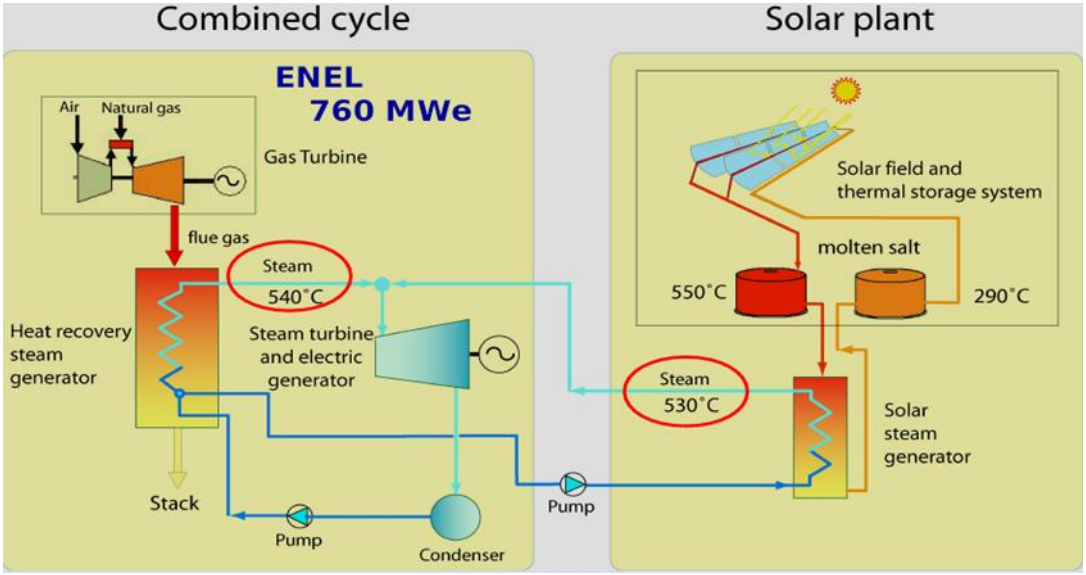

Figure 2.19 The Schematic diagram of the Archimede Demonstration Plant

2.4.4 Water/Steam Systems

The water/steam system do not require the use of a steam generator and have the potential of reducing capital cost by 15% [74] and LEC by 10% [81]. It also eradicates environmental problems associated with using oils/molten salts and higher temperatures can be achieved.

The concept of the possibility of producing steam directly from a parabolic trough field was first introduced by John Erricsson in 1870 [74]. In order to develop this technology the DISS project was initiated in the PSA test facility in Spain in 1995. A test facility having specifications as shown in Table 2.8 was constructed in 1998. This was used to test different methods in which steam can be produced directly from the solar field [82]. Methods tested where:

- Once through in which the pre-heated water will be passed through the solar field and steam will be produced at the required conditions at the exit of the collector (Figure 2.20(a)).
- The injection in which some of the water is by passed and injected at some points in the collector (Figure 2.20(b)).
- The Recirculation in which excess water is separated from the steam at some point in the collector. The excess water is recirculated back to the collector inlet. The steam collected by the separator is then superheated and delivered to the turbine (Figure 2.20(c)).

Table 2.8 Specification of the DISS experimental facility in 1998 [82]

No. of Parabolic trough modules	40
Module Aperture/ Length(m)	5.76/12
Length of a row (m)	550
Reflecting mirrors surface area(m^2)	3000
Tracking Axis orientation	North-South
Receiver pipe inner/outer diameter(mm)	50/70
Steam mass flow per row (kg/s)	0.8
Max. water recirculation rate	4
Max. Outlet steam temperature/pressure (^oC/bar)	400/100

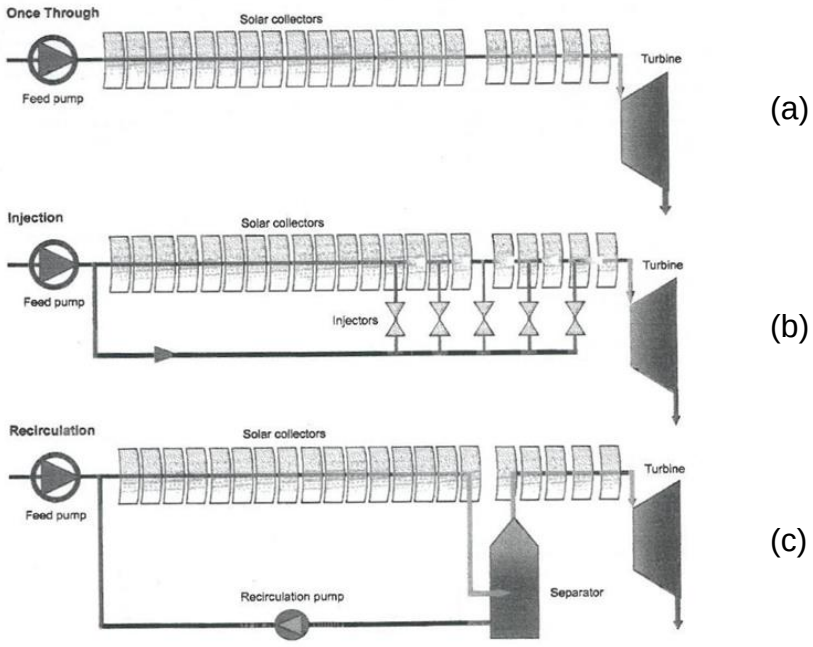

Figure 2.20 Three methods of DSG in parabolic trough (a) Once through (b) Injection (c) Recirculation [81]

The test proved the feasibility of DSG in parabolic-trough plants and showed that the recirculation concept is the best option. Tests conducted on the integration with regenerative Rankine power cycle gave overall efficiency of 23% for steam temperatures of 550^{o}C. This is higher than the efficiency for plants using molten salts with the same operating temperatures.

The success of the feasibility tests led to the development of the 5 MW_e INDITEP plant in which superheated steam is produced at 69.9 bar, 411^{o}C using the recirculation method in a field consisting of 70 Eurotrough collectors split into 7 rows. Each row consist of 10 collectors—Figure 2.21 [74; 83; 84]. Another 3 MW_e grid connected pre-commercial plant (Puertollano GDV) was constructed in Ciudad Real similar to the INITEP plant. The lay out of the plant and water/steam conditions at inlet and exit of the solar field are presented in Figure 2.22 [85; 86]. Construction started in 2009 [74].

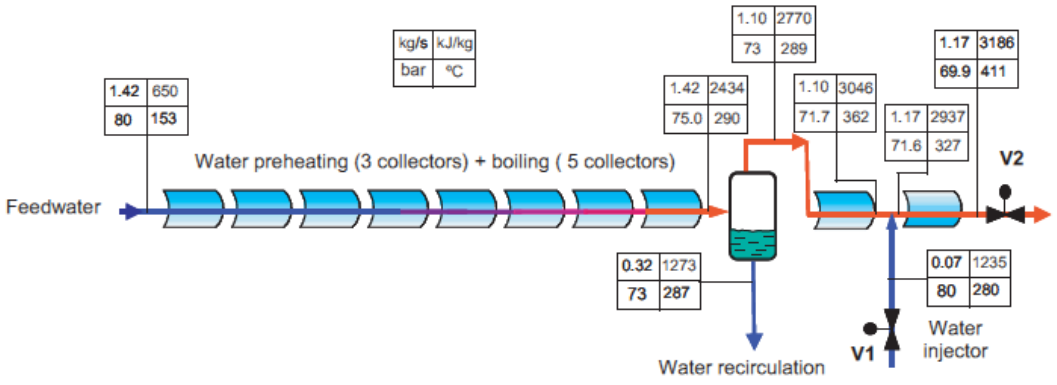

Figure 2.21 Schematic diagram of a row in the INDITEP project solar field [84]

.

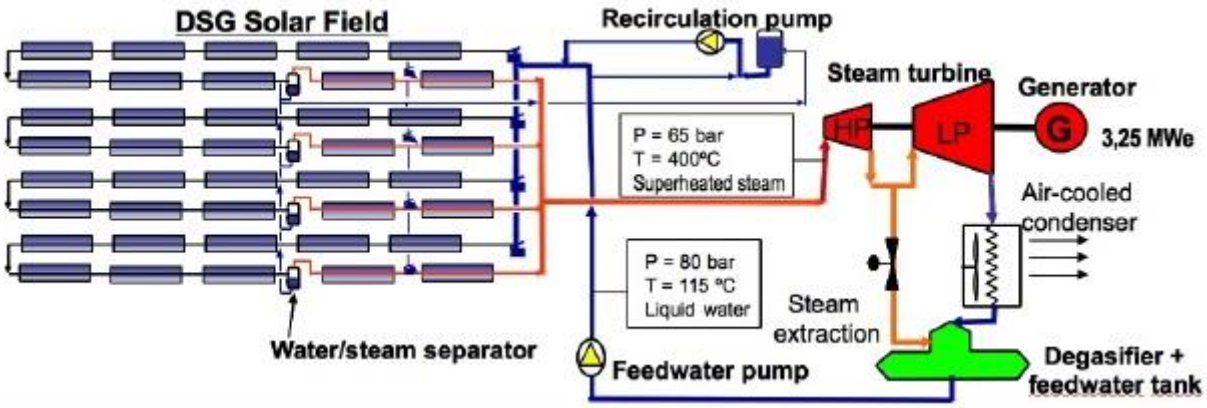

Figure 2.22 Layout of the INDTEP DSG solar thermal power plant

2.4.4.1 Linear Fresnel Reflector Concept

Due to efforts to reduce the cost of parabolic-trough field, a concept was developed in which various thin flat mirrors are arranged in a plane, in which each mirror concentrate solar radiation onto a linear receiver situated about 10 to 15 m above the ground (Figure 2.23). Although the mirrors are arranged in the same plane, they are oriented in such a way that they approximate a parabolic-trough. Since the receiver is not supported by the reflector, sun tracking becomes easier, more efficient and accurate. Mirrors used in this collector are much cheaper than the parabolic trough collector. The mirrors can

be designed to track the sun in either single or dual axis. The principle of energy collection, conversion and transportation is exactly the same as in the parabolic-trough.

One of the main issues with this reflector is shading by adjacent reflectors. This makes it occupy larger land area. This problem can be solved by the use of multiple receivers in which adjacent receiver that are situated further away from a receiver are oriented in such a way that they concentrate radiation on to different receivers (Figure 2.24). This design was developed at the Sydney University by Mills and Morrison [87]. The linear reflector power plants can use any working fluid that can be used in a parabolic-trough plant but water/steam has been adopted as the HTF on all plants developed.

The linear Fresnel collector was tested at the PSA DISS facility using water/steam as the HTF. A reflector field having a length of 100 m and width of 20 m was connected to the exiting power-block used for the DISS project. In the receiver pipe the water was heated and superheated steam was produced at a temperature greater than 400^{o}C at a pressure of about 100 bar. The capacity tested was about 1MW [88].

The CLFR has been tested in various demonstration projects which include:

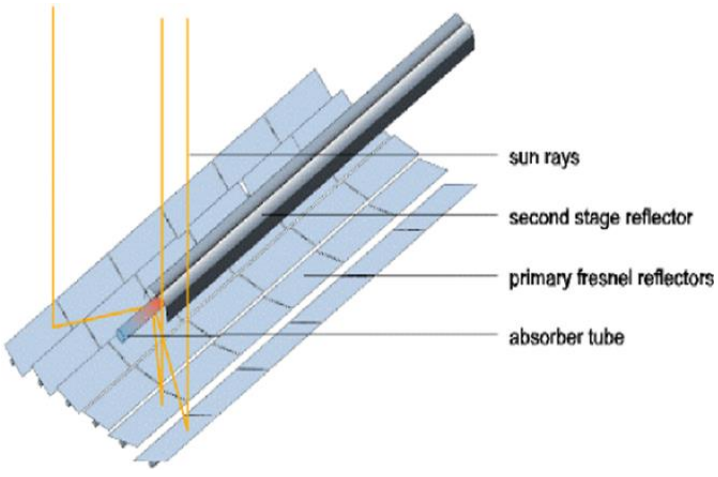

Figure 2.23 The linear Fresnel reflector concept

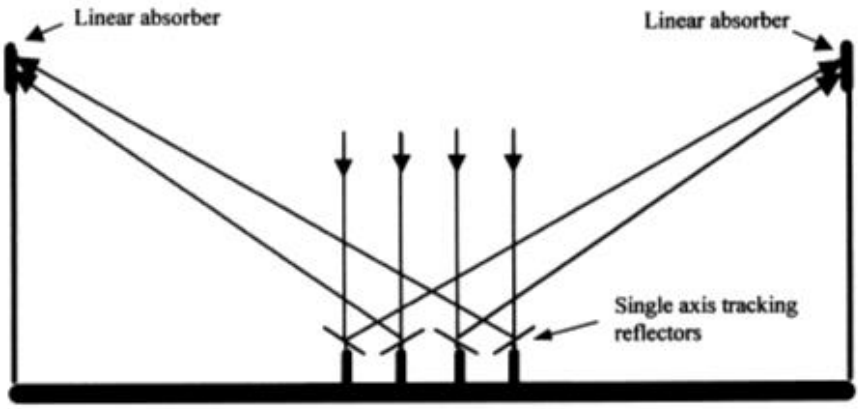

Figure 2.24 Multiple receiver Linear Fresnel reflector concept [87]

- Hybrid operation with the Liddel coal fired power plant in which the CLFR was used for the pre-heating of the coal fired boiler feed water with an estimated electricity share of 5 MWe [37]
- The Kimberlina Power plant in Bakersfield (Figure 2.25(a)), California in which the CLFR system produces 25 MW_{th} superheated steam which is equivalent to 5MW_e capacity contribution [6; 89].
- The 1.4 MW Puerto Errado 1 thermosolar plant (Figure 2.25(b)) in Calaspara, Spain which started operation in 2009. Steam is produced at 55 bar, 270^oC [6].
- The 0.25 MW_e Augustine Fresnel 1 plant in Targassonne, France which started operation in 2012.

The first and the only commercial plant using water/steam as HTF and the linear Fresnel collector is the 30 MW_e Puerto Errado 2 thermosolar plant (Figure 2.25(c)) in Calaspara, Spain which started operation in 2012. It is equipped with a 0.5 hour capacity single-tank thermocline storage system. Apart from other small scale plants under construction, two large scale commercial plants are under construction: The Kogan Creek Solar Boost in Chinchilla, Australia having a capacity of 44 MW_e and integrated with a coal fired power plant; and the 125 MW_e Dhursar plant in Dursar, India [6].

(a) 5 MW Kimberlina plant, USA

(b) 1.4 MW Puerto Errado 1 thermo solar plant, Spain

(c) 30 MW Puerto Errado 2 thermo solar plant, Spain

Figure 2.25 Linear-Fresnel reflector plants using water/steam HTF

2.5 Conclusions

Various technologies have been developed over the years for the production of electricity from solar energy. The most advanced are: The parabolic-dish, power-tower and parabolic-trough systems.

The parabolic dish technology has been studied extensively over the years. The use of water as HTF in centralized systems has been demonstrated with potential for commercial operation and plan for a 40 MW_e plant. The use of micro turbines is still in the research stage. Most systems developed are standalone systems. The Dish Stirling engine system is the most promising with capacities up to 25 kW_e. Currently only one plant having 30 units of 3.2 kW_e each exist in a commercial scale. Even though the parabolic-dish is the most efficient solar thermal power generation technology, it is only suitable for small scale or standalone applications. It is also the most expensive.

Three working fluids have been demonstrated successfully for use on power-tower plants. The use of water/steam has reached commercial status with various plants in operation and 671 MW_e capacities under construction. The use of pressurized water tank is the easiest storage system but is difficult for use in large scale. The main challenge remaining for this system to be able to be a mainstream power generation technology is the development of an alternate thermal storage system. The use of molten salt as HTF has also reached commercial status with three commercial plants in operation and a capacity of about 420 MW_e under construction. The two-tank direct or indirect system has been proven for use in these systems. They are thus capable of 24 hour uninterrupted power production. The air receiver technology has been demonstrated. It has various configurations but basically hot air produced from the receiver is either used for the production of steam in a Rankine-cycle or used in a Brayton-cycle in either solar only or hybrid mode. Apart from the 1.5 MW_e demonstration plant (Jülich Solar Tower) there is no other plant in operation. There is no commercial plant using air as HTF.

In the parabolic-trough systems, three working fluids have been used successfully over the years: Thermal oil, molten salt and water/steam. The use of molten salt has been demonstrated but there is no commercial plant in operation or under construction. Most plants (a total of more than 2.68 GW_e installed capacity) in operation use thermal oil as HTF with another 1.4 GW_e under construction. The use of water/steam and the linear Fresnel collector

which offers reduction in cost and increase in efficiency has reached commercial status with only one plant in operation and two others under construction. Even though the use of water/steam as HTF has shown a reduction of 11% in LEC compared to the thermal oil system for systems without storage [90], the LEC cost for system with integrated two-tank indirect storage system is higher [91]. In summary the parabolic-trough systems using thermal oil as HTF is the most matured solar thermal electricity generation technology.

3 THERMAL ENERGY STORAGE

The intermittency of solar radiation makes the amount of thermal energy captured to be more or less than that required by the power-block. In the former case the excess amount of energy is lost while in the latter case a backup boiler has to be used to compensate for the discrepancy. To effectively utilize solar energy a thermal storage system is thus required to store excess energy for later use. At night when the solar insolation is zero, the plant has to be shut down or operated with a fossil-fired boiler. This kind of operation will lead to inefficient use of solar energy, increase in the cost of solar electricity and makes it not a sustainable source. Sometimes the supply of solar energy will not match the demand and as such the supply needs to be shifted. A passing cloud can also cause undesirable transient turbine operation. For grid connected solar thermal plants, a storage system is also mandatory in order to prevent grid instability due to frequency fluctuation [24].

For these reasons solar thermal power plants must be incorporated with a thermal storage system, which can perform one or more of the following functions [8]:

- To provide a small buffer than can be used to smooth out power output due to solar transients.
- To shift power production to times when needed or more expensive (3-6 hours)
- To extend power production for a longer period of time after sunset (3-12 hours)
- To average the annual electricity generated.

Thermal energy storage systems can increase the efficiency, annual solar contribution and decrease the LEC of solar thermal power plants. It can also increase the utilization factor of the power-block.

Thermal energy storage systems can be classified based on two main criteria [7]:

- Mechanism of storage (the storage media): Under this criterion storage system can be classified into sensible, latent or chemical storage systems.
- The way in which the system is integrated with the solar thermal power plant. Under this criterion a storage system can either be active (the storage medium flows during charging or discharging) or passive in which the storage medium does not flow during operation. Passive systems must have a secondary fluid that will transport the heat in and out of the storage medium and are sometimes termed dual-medium systems. An active storage system can be direct (the storage medium is the same as the heat transfer fluid in the solar field) or indirect in which the storage medium is not same as the HTF and as such a heat exchanger is required for the exchange of heat between the HTF and the storage medium

In this chapter the first criterion i.e. based on the storage media will be used as the main basis for the classification of storage systems.

Chemical storage systems involve the storage of thermal energy using reversible endothermic reactions. Advantages of chemical energy storage include: high energy storage density and the thermal energy can be stored for indefinite amount of time. The design of these systems is very complex and they are expensive and associated with environmental risks such as fire and toxicity [8]. They are still at initial research stage. This review will thus focus on the two advanced thermal storage systems (sensible and latent) with the aim of reviewing the progress made in the development of storage systems for use with parabolic trough solar thermal power plants using thermal oil as HTF.

3.1 Thermal Storage Operation

The operating temperature range of parabolic trough plants using synthetic oil as HTF is about 100^{o}C (from 293 to 393^{o}C) and a thermal storage system has two modes of operation: charging and discharging. During charging heated HTF from the solar field at about 393^{o}C enters the storage through the top and is

required to exit the storage at a maximum temperature of 330^{o}C to prevent overheating of the HTF in the solar field. During discharging HTF from the power block at a temperature of about 286^{o}C enters the thermal storage system from the bottom and is expected to be heated to a minimum of 350^{o}C.

3.2 Sensible Heat Storage Systems

Sensible heat is that form of energy when added to a material it causes increase in the temperature of the material. The energy is stored as internal energy and can be calculated using the product of the temperature change caused by the added heat, the specific heat capacity and the mass of the material. The amount of sensible heat that can be stored by a solid or liquid depends on the specific heat capacity of the material. High specific heat capacity means smaller amount of material for a particular storage capacity. The rate at which the heat can be transferred to and from the material depends on the thermal conductivity of the material. This plays an important role in the utilization factor of some sensible storage systems. The utilization factor is the ratio of the actual heat a storage material stores over a period of time to the theoretical amount of heat the material is capable of storing.

Thus a good sensible storage system should be composed of a sensible storage media with high specific heat capacity and thermal conductivity. Table 3.1 presents the thermo physical properties and cost of some potential media for sensible storage system with their applicable range of operation temperatures. The sensible storage systems can be further classified into solid, liquid and dual medium systems.

3.2.1 Solid Media Storage Systems

Solid media storage systems are passive systems in which a secondary HTF is used for thermal energy transport to and from the storage. Mostly the HTF in the solar field is used as the secondary fluid. Various solid media materials have been considered for use in thermal storage systems.

Table 3.1 Potential sensible storage media [17]

Medium	Temperature Range	Density (Average)	Thermal Conductivity (Average)	Heat Capacity (Average)	Volumetric Specific Heat Capacity	Cost	
	^{o}C	kg/m^3	W/mK	kJ/kgK	$kWhth/m^3$	$/kg	$/ kWh_{th}
SOLID MEDIA							
Sand-rock-mineral oil	200 - 300	1700	1.0	1.30	60	0.15	4.2
Reinforced Concrete	200 - 400	2200	1.5	0.85	100	0.05	1.0
NaCl (Solid)	200 - 500	2160	7.0	0.85	150	0.15	1.5
Cast Iron	200 - 400	7200	37.0	0.56	160	1.00	32.0
Cast Steel	200 - 700	7800	40.0	0.60	450	5.00	60.0
Silica fire bricks	200 - 700	1820	1.5	1.00	150	1.00	7.0
Magnesia fire bricks	200 - 1200	3000	5.0	1.15	600	2.00	6.0
LIQUID MEDIA							
Mineral Oil	200 - 300	770	0.12	2.6	55	0.30	4.2
Synthetic Oil	250 - 350	900	0.11	2.3	57	3.00	43.0
Silicone Oil	300 - 400	900	0.10	2.1	52	5.00	80.0
Nitrite Salts	250 - 450	1825	0.57	1.5	152	1.00	12.0
Nitrate Salts	265 - 565	1870	0.52	1.6	250	0.70	5.2
Carbonate Salts	450 - 850	2100	2.0	1.8	430	2.40	11.0
Liquid Sodium	270 - 530	850	71.0	1.3	80	2.00	21.0

These include: solid salt, steel and concrete. The use of steel is too expensive and solid salt requires air tight steel casing to prevent contact with ambient air and the HTF-pipe [17]. This, thus, leaves concrete as the most promising option since it does not require any casing. Concrete storage systems are called CTR. In CTR, tubes through which the HTF passes are embedded in a cast concrete (Figure 3.1). Concrete has the potential for a low cost thermal storage system. The main problem with concrete is its low thermal conductivity. Research over the years has thus focused on developing a cost effective CTR system.

3.2.1.1 The Concrete Tube Register (CTR) System

The concept of CTR was first investigated by Dinter et al. (1991) for a 200 MW_{th} capacity. Between 1991 and 1994 the Solar Energy and Hydrogen Research Centre in Germany constructed two modules (prototypes) and performance of the modules obtained were similar to those predicted by Dinter et al. [17]. CTR is attractive because it offer lower cost in terms of investment and maintenance, availability of the aggregates of the concrete in all places of the world and that the materials pose no environmental risk [13].

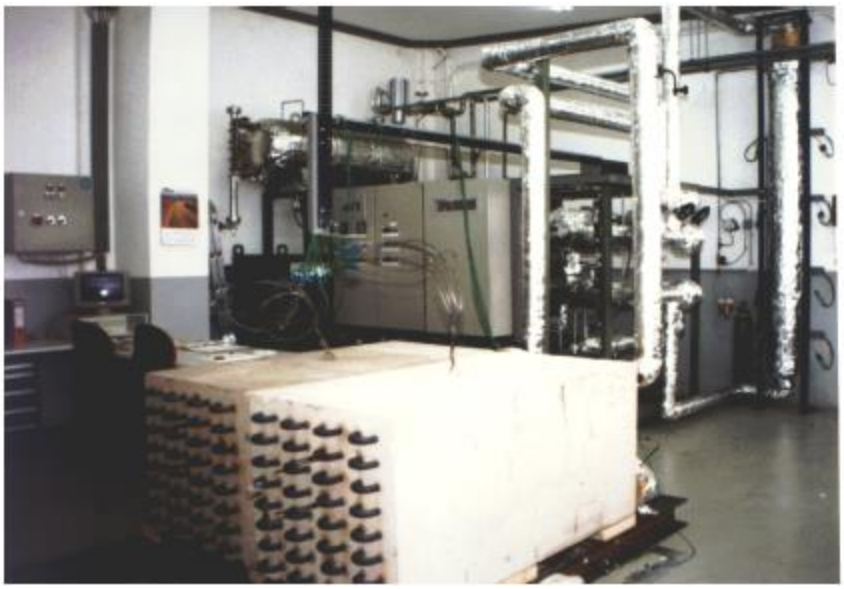

Figure 3.1 Concrete/tube register storage modules [8]

The thermal conductivity of the concrete plays a very important role in the performance of CTR storage system. Increasing the thermal conductivity will increase the utilization factor of the medium and the dynamics of the thermal storage system. Increasing the volumetric heat capacity will reduce the size of the storage system for the same capacity [92]. Other factors to consider are: the coefficient of thermal expansion of the concrete must be the same as that of the material of the tube (steel) and the concrete must be able to withstand thousand numbers of charging and discharging cycles. Researches on the development of this system have concentrated on finding ways to increase the utilization factor of the storage module and reducing the cost of the storage module. Methods reported in the literature can be classified into:

- Increasing effective thermal conductivity of the storage material by using suitable aggregates.
- Increasing the surface area of the tube register.

Based on these two ways the works that has been done over the years were presented in the following sections.

3.2.1.1.1 Increasing Effective Thermal Conductivity of Storage Material

One option of increasing the thermal conductivity of the storage media is by putting very small pieces of high thermal conductivity materials such as metals in the concrete mixture. The mixing of concrete aggregates with 75 kg of steel needles per cubic meter of concrete was found to increase the average thermal conductivity of the storage medium by 30% with only a 2.6% increase in cost [17]. Laing et al. [93] has considered two material splinters for use in concrete mixture: graphite and metal. The use of splinters of metal does not yield positive result because material handling limits the amount of metal splinters to 2.5% while the use of 10% by mass of graphite splinters made from expanded graphite increased the thermal conductivity by about 15%. Cost of graphite makes the storage media cost to be very high and thus over shadows the increase in performance. The use of high conductivity materials does not result into a cost effective system even though it increases the overall thermal conductivity.

The enhancement of the properties of the concrete by using aggregates that will result into higher thermal conductivity or specific capacity has also been considered. The use of calcium and basalt aggregates was not a viable option because their thermal expansion does not match that of the tube material (Steel). Tamme et al. [94] considered many concrete aggregate mixture and two concrete media were found to have good storage properties: high temperature concrete which composed of cement as the binder, Iron oxide and flue ash as the main aggregates with other auxiliary materials; and castable ceramic which is composed of Al_2O_3 as the binder and Iron oxides as the main aggregate and auxiliary materials. The auxiliary materials are added in both storage materials in order to ease the handling of the materials by serving as either viscosity reducers or accelerators. The use of Iron oxide as the main concrete aggregate resulted in increased density which increased the specific capacity of the media and reduce the cost since less tube material will be required [93]. Modules of these two materials were produced with the tubes embedded in the materials and a good contact between the tube and the materials were obtained. Table 3.2 presents the thermo physical properties of these two materials. The castable ceramic has higher density and thermal conductivity meaning higher capacity (20% higher) and dynamics respectively than the high temperature concrete. Test of each of these modules with dimensions of 0.48 x 0.48 x 23 using a 480 kW maximum capacity parabolic trough collector (Figure 3.2) for storage temperatures up to 325^{o}C showed no degradation in heat transfer for many charging and discharging cycles [93; 95].

Even though the castable ceramic has higher specific capacity and thermal conductivity, the high temperature concrete was chosen because it is stronger and easier to handle. More than 370 charging and discharging cycles have been conducted by the end of December, 2010 for temperature difference between charging and discharging ranging from 40 K to 120 K [13]. The stability of concrete up to storage temperatures of 400^{o}C [96] and 500^{o}C [13] have been achieved. This means that high temperature concrete is the most suitable material in terms of potential cost reduction for use in CTR system.

Table 3.2 Thermo physical properties of materials developed by Laing et al. [95]

Property		Material	
		High temperature concrete	Castable Ceramics
Density	kg/m^3	2750	3500
Specific heat capacity at 350°C	J/kgK	916	866
Thermal Conductivity at 350°C	W/mK	1.0	1.35
Thermal expansion coefficient at 350°C	$10^{-6}/K$	9.3	11.8
Initiation of Crack		Many Cracks	No cracks

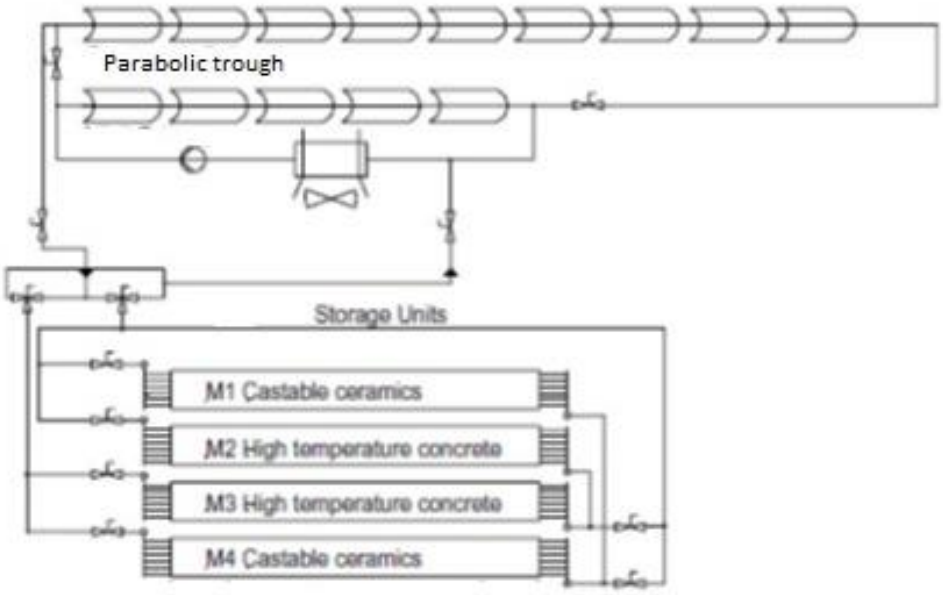

Figure 3.2 Test units for high temperature concrete and castable ceramic modules

It has been shown that 46% reduction in the amount of steel required for a thermal storage system can be obtained by increasing the thermal conductivity of the concrete from 1 to 1.8 W/mK [96] even though this increase does not produce any significant benefit in performance [97].

3.2.1.1.2 Increasing Surface Area of the Tube Register

Increasing the surface area of the tube register can improve the rate of heat transfer in and out of the storage module thereby increasing the dynamics and utilization factor of the storage system. The surface area can be increased by either increasing the tube diameter, using fins or by reducing the distance between tubes. Increasing the tube diameter was found to increase the heat transfer but with no cost benefit since the major cost of the CTR is the steel material [17; 97]. Dinter et al. (1991) reported that the use of fins is also not cost effective. To optimize the CTR different tube diameters and distance between tube centres were investigated. It was found out that the tube diameter of 20 mm and distance between tubes of 70 mm gives the highest utilization factor. The effect of reducing the distance between tube centres from 40 mm to 160 mm was investigated by Tamme et al. [97] using simulations. Result showed that distance between tube centres of more than 80 mm resulted into the existence of a radial temperature gradient in the storage medium and the rate of power into the storage during charging decreases with increasing tube distance.

The use of axial and radial fins and reinforcement grid in order to improve the heat transfer in CTR was also studied by Laing et al. [93] using FEM. The same distance between tubes was used for all the four configurations including the one without fins. Preliminary result showed that these structures improve the heat transfer. Even though the number of pipes has reduced but the amount of steel required (the tube plus fins) is almost equal to that without the fins and as such no cost benefit (Table 3.3). This result is in conformity with that reported by Dinter et al. (1991), that the use of fins made of steel does not provide any cost benefit.

The use of extended surfaces made of steel enhances the thermal performance of the CTR with a cost penalty. As such for the CTR to be cost effective a way of reducing the amount of steel material has to be found since the tube register forms majority of the cost. Laing et al. [93] has investigated ways of eliminating the steel tube by making use of pre-stressed and pre-fabricated concrete with holes through which the

Table 3.3 Material and cost reduction potential of using heat transfer structures in a CTR [93]

Configuration	Relative number of tubes/m^3 (%)	Relative cost of heat exchanger material (%)
Basic (without fins)	100	100
Reinforcement grids	88	96
Radial fins	82	96
Axial fins	65	91

HTF will flow without using a steel tube. The concrete absorbs some of the HTF and also it is very difficult to make a sealed joint in the interface between the storage and the pipe from the solar field. Other method proposed is the use of preformed units of concrete through which the HTF flows in a tank. This was also not a viable option because of the difficulty in making the concrete units impermeable.

It is now evident that to reduce the cost of the CTR system, the amount of tube material (steel) must be reduced. The use of other materials as HTES will help in achieving this. The use of horizontal aluminium sheets or graphite foils in a pre-cast concrete module (as shown in Figure 3.3) was found to reduce the amount of steel required for a similar storage system without the HTES by 47%. About 60% reduction in the amount of steel required was obtained with vertical and horizontal plates [13]

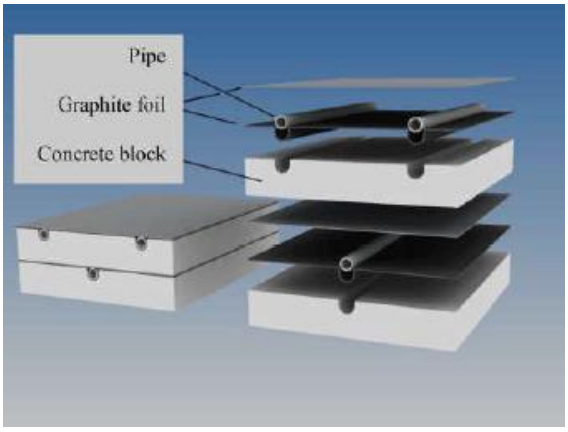

Figure 3.3 Pre-cast concrete slabs with horizontal graphite sheets [13]

3.2.1.2 Integration with Parabolic-Trough Plant

A CTR system is integrated into parabolic trough power plants as a passive system. During charging the HTF from the solar field is passed through series of tubes embedded in the concrete. Thermal energy is transferred from the HTF to the concrete. During discharging the HTF is passed through the medium in the reverse direction and thermal energy is extracted from the concrete medium (Figure 3.4). The performance (charging and discharging) and design of CTR for a complete plant must consider the boundary conditions of the parabolic-trough plant. During charging the inlet solar field HTF temperature must not exceed 315^{o}C in order to avoid the overheating of the HTF (oil) and during discharging the minimum HTF outlet temperature 350^{o}C is required for the operation of the power-block.

Tamme et. al. [97] developed a physical model of a CTR system (Figure 3.5) and a simulation environment called “StorageTechThermo” was developed in the Modelica Language. A CTR storage element with HTF-pipe internal and external diameter of 20 and 22 mm respectively and distance between pipe centres of 80 mm and length of 500 m were used. The boundary conditions of inlet HTF temperature of 265^{o}C, minimum HTF outlet temperature of 350^{o}C (the minimum required by the power block) during discharging and inlet HTF temperature of 390^{o}C, maximum HTF outlet temperature of 315^{o}C during charging were used. These temperature boundaries were used to determine the mass flow rates. Thermo-physical properties of concrete used are: specific heat capacity of 1000 J/kgK , thermal conductivity of 1.2 W/mk and density of 2200 kg/m^{3}. Results from the simulation gave insights into the behaviour of the CTR system and points out to the need for careful selection of distance between tubes to avoid exergy destruction.

The design of a CTR system for a 50 MW_e parabolic trough plant using performance results obtained from experiments resulted in CTR volume of 50,000 m^{3} for a CTR having a capacity of 1100 MWh_{th} [96]. In order to reduce the size of the storage other researches considered using operation strategies to increase the performance of the system.

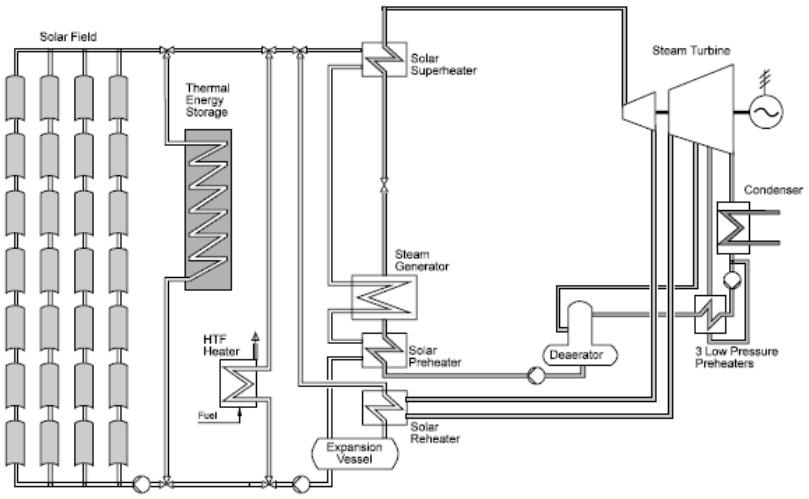

Figure 3.4 Integration of concrete/tube register storage system to parabolic trough plants [17]

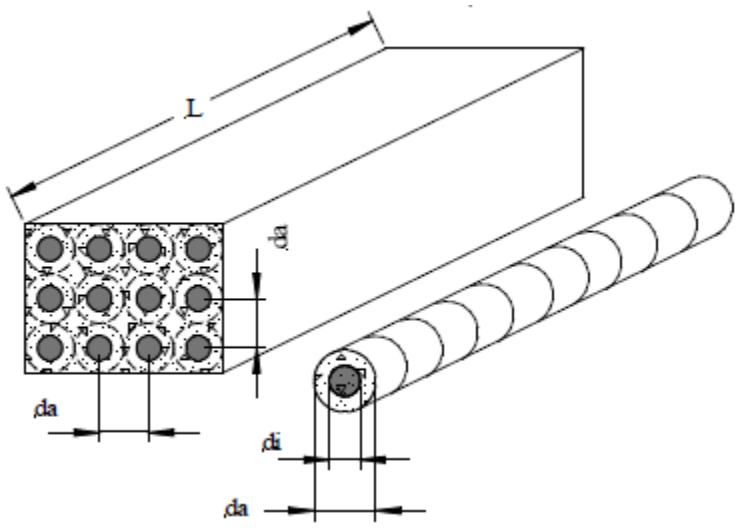

Figure 3.5 Model of the concrete/tube register developed by Tamme et al. [97]

In the power cycle a re-heat Rankine cycle with operating pressure of 100 bar corresponding to 311^{o}C is usually employed. This means about 88.4% of the thermal energy is used for pre-heating and evaporation of water at temperatures ≤311^{o}C. In the conventional configuration of storage integration, the HTF from the storage system is used to produce steam in a steam generator. The minimum discharge temperature is limited to 350^{o}C (the

minimum allowed by the Rankine cycle). This makes the maximum temperature difference during charging and discharging in the thermal storage system to be 40^{o}C. Increasing the temperature difference can thus increase the storage capacity of a CTR. In view of this, operation strategies for increasing the temperature difference were devised [97]. Since during discharging the minimum HTF outlet temperature is 350^{o}C, the solar field can be divided into two and the maximum HTF inlet temperature to the solar field can be increased from 315^{o}C to 350^{o}C. This will increase the average storage temperature thus increasing the performance and is called modular charging (Figure 3.6). Also the discharging process can also be made to match the Rankine-cycle characteristics by using different CTR modules for different temperature levels. Thus HTF with temperature below 350^{o}C can be used for the pre-heating of water and/or evaporation. This is called modular discharging (Figure 3.7) and it lowers the average storage temperature thus increasing the temperature difference and thus capacity. Modular charging and discharging can also be combined thus increasing the temperature difference in the storage. These concepts were investigated and results showed that each of these produced more electrical power in the following order of increasing power: conventional configuration, modular discharging, modular charging, modular charging and discharging. Finally a 200% increase in capacity is obtainable in the storage system with modular charging and discharging [97].

The concept of modular charging and discharging was simulated using Modelica language for a minimum discharge temperature of 350^{o}C for a 50 MWe capacity power-block by Laing et al. [93]. Table 3.4 shows the amount of storage capacity produced, specific cost of storage excluding the cost of additional components and LEC including the cost of additional components required by each integration concept for a similar size plant. This shows that for the same storage size more electrical power is produced. An increase of up to 115% on performance can be obtained by using modular charging and discharging compared to the conventional method.

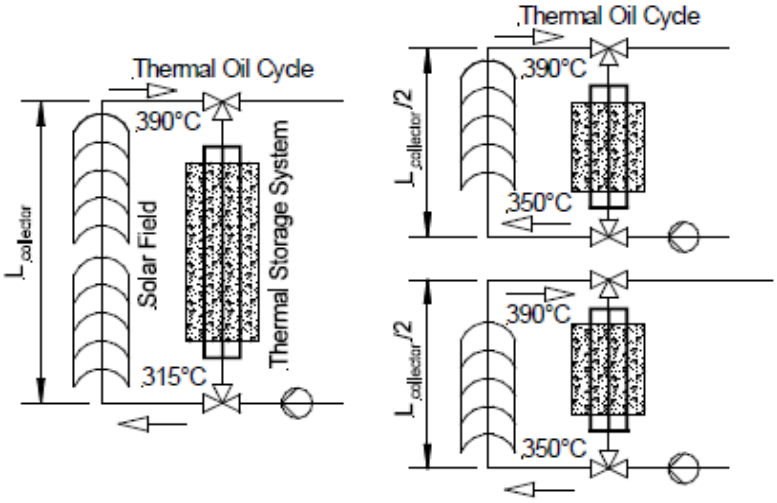

Figure 3.6 (a) Conventional concept (b) Modular charging concept

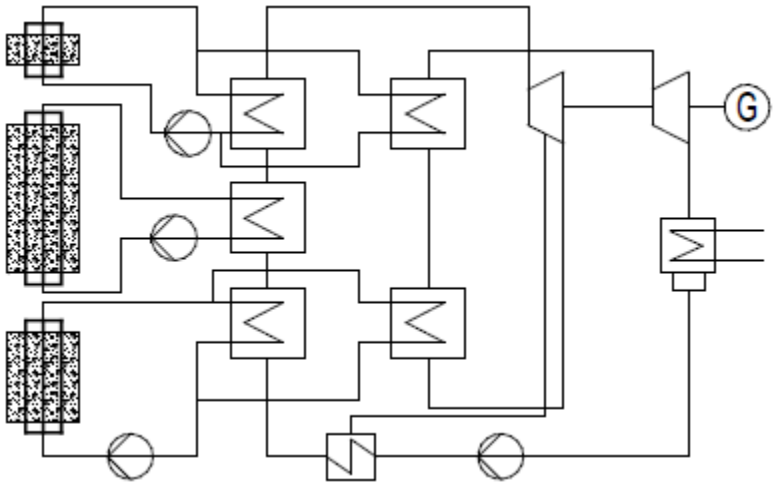

Figure 3.7 Modular discharging concept

Table 3.4 Performance and economic comparison of modular charging and discharging concepts [93; 98]

Concept	Total electricity produced for a similar size storage (MWh_e)	Specific cost of storage (€/kWh)	LEC (€/KWh)
Conventional	130	30.4	0.2
Modular charging	190	20.5	0.198
Modular discharging	210	19.1	0.197
Modular charging and discharging	280	14.1	0.195

Also a large reduction in the specific cost of storage was obtained without considering the cost of additional components. The cost of additional components was found to be very high and as such leads to little reduction in the levelized electricity cost to about 2%. LCA of a 50 MW_e Andasol type plant with a CTR instead of the two tank system shows a decrease in environmental impact; and emissions caused by the construction of the plants of about 7% and 9.5% respectively compared to the two-tank system using molten salt [98]. Other ways that will provide increase in the capacity of concrete storage system are sequential charging and discharging and the pre-heating of water using the storage.

The annual electric power generated by 50 MW_e plant similar to the Andasol plant integrated with a 1100 MWh_{th} capacity concrete storage module was simulated using Dymola environment by Laing et al. [13]. The Solar insolation data of Guadix, Spain for 2005 was used. A maximum HTF storage outlet temperature of 330^oC during charging and a minimum HTF outlet temperature of 350^oC during discharging were applied as the boundary conditions. Two operation strategies were considered: reference case in which the storage mass flow rate is not controlled during charging and a second case in which the mass flow rate is controlled so that the charging time can be increased. It was found out that the plant produces 175 GWh_e/yr which is equivalent to 3500 hr/year full load operation out of which 30% is produced by the storage system. The controlled mass flow rate operation strategy increases the amount of energy stored and annual electricity produced by 2.5% and 8.4% respectively compared to the reference case. This clearly shows the influence of operation strategy on the performance of a storage system.

In summary the CTR has been extensively analysed for use as a storage system in parabolic-trough plant. It provides a low cost storage system. Various pilot systems have been tested successfully but there is no plan for the commercial deployment of a CTR system in a commercial plant.

3.2.2 Liquid Media Storage Systems

Liquid media storage systems offers higher heat transfer rates (dynamics) than the solid media due to convection heat transfer. Liquid media storage systems can either be active direct or indirect systems. Two tanks (one for hot and the other for cold) or single tank thermocline can be utilized.

3.2.2.1 Liquid Storage Media

Table 3.1 presents suitable liquid storage media. In the operating temperature range of the parabolic trough plants (i.e. 293 - 393^{o}C) carbonate salts and mineral oil are not suitable. Nitrites salts are associated with corrosion problems. Although silicone oils are not hazardous to the environment, they are very expensive. Synthetic oils are very expensive [8]. Out of all these liquid media, inorganic mixtures of nitrate molten salts have been preferred by researchers and are the most studied. This is because they offer good thermo physical properties (specific heat = 1500 J/kgK, density=1880 kg/m^{3}, vapour pressure of less than 0.01 Pa) and they are cheap with cost range of 0.4 to 0.9 $/kg [9]. In order to obtain required properties, nitrate salts are mixed to form eutectic mixtures. Table 3.5 presents the principal mixture of molten salts for use as liquid media in storage systems for parabolic trough plants with their melting temperatures. One of the main disadvantage of molten salt media is their high melting point and as such heat tracing must be employed to prevent the solidification of the salt. Hitec XL salt is stable up to 500^{o}C with freezing point of about 120^{o}C and solar salt is stable up to 600 [99].

Table 3.5 Candidate inorganic molten salt mixtures for thermal storage in parabolic trough

Salt name	Type of mixture	Salt Constituents	Melting temperature (^{o}C)
Hitec	Tenary salt	$NaNO_3$, $NaNO_2$, KNO_3	120
Hitec XL®	Tenary salt	$Ca(NO_3)_2$, $NaNO_3$, KNO_3	130
Solar Salt	Binary	$NaNO_3$, KNO_3	220

3.2.2.2 Direct Two-Tank Storage System

In the direct two-tank system (Figure 3.8), the HTF in the solar field is used as the storage medium. This system has the advantage that it does not require a costly HTF/molten salt heat exchanger. During charging hot fluid from cold storage tank is pumped through the solar field where it is heated and then stored in the hot tank. During discharging the hot fluid is pumped from the hot storage tank through the steam generator where superheated steam is produced and then back to the cold storage tank.

This system has been used commercially in the 13.8 MWe SEGS I plant using mineral oil as the HTF and storage medium and a capacity of 120 MWh_{th} with a cold and hot tank volume of 4160 and 4540 m^3 respectively. This system offers utilization factor of up to 100% since there is no need for a heat exchanger. This system was not possible in the later SEGS plants using synthetic oil as HTF because of the cost of synthetic oil which is almost eight times that of mineral oil and its higher vapour pressure which will require pressurized tanks. The cost of oil accounts for about 42% of the investment cost [8; 17]. This system was not suitable for use in parabolic-trough systems using synthetic oil as HTF, but has been utilized in the power-tower system (Figure 2.7) in which the HTF is molten salt [4; 10].

3.2.2.3 Indirect Two-Tank Storage System

The high cost of synthetic oil which limited its use as storage media led to the development of the indirect two-tank system by INITEC of Spain [17]. In this system a another fluid (molten inorganic salt) different from the HTF in the solar field is used as the storage medium and a heat exchanger is required in order to transfer heat between the HTF and the storage medium.

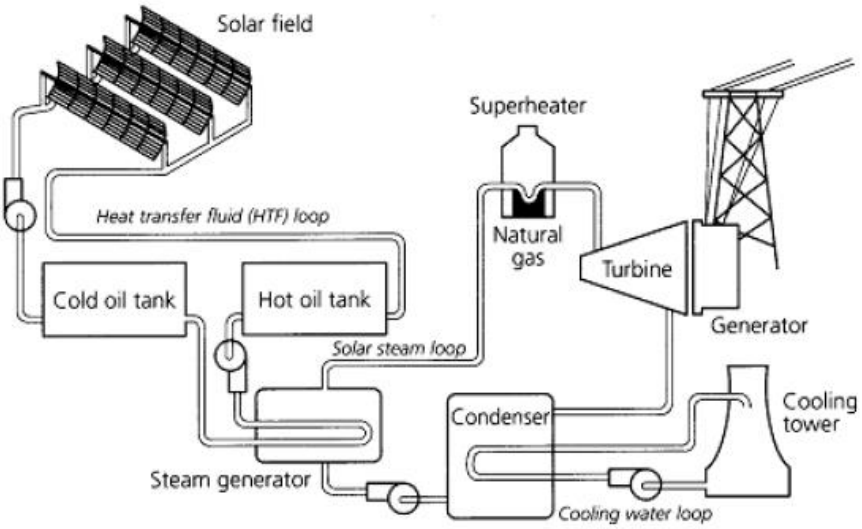

Figure 3.8 Two tank direct system for SEGS I Plant [3]

INITEC proposed two configurations of system using Hitec molten-salt (54% KNO_3, 40% $NaNO_2$ and 7% $NaNO_3$) having a melting temperature of 142^{o}C. In the first configuration, during charging, the molten salt is heated by the HTF from the solar field in a heat exchanger and then stored in the hot tank. During discharging, the molten salt from the hot tank is pumped through the heat exchanger to the cold tank and in the process heating the HTF. The heated HTF is then used to produce steam in a steam generator (Figure 3.9(a)). This is referred to as HTF charging and discharging. In the second configuration, the HTF is used to heat the molten-salt using the heat exchanger during charging. During discharging the molten salt is pumped directly to the steam generator for the production of steam. This is called HTF-charging and salt-discharging. In this way the rate of heat transfer is thus increased since the HTF/salt heat exchanger has been eliminated during discharging (Figure 3.9(b)). The advantage of this configuration is potential for cost reduction since the molten salt/steam generator is more compact than HTF/steam generator. Comparison of the two configurations using a 200 MWh_{th} capacity system showed that the

capital cost of the salt/steam generator system is 43.4 $/kWh$_{th}$, which is less than the HTF/steam generator system by 5.1 $/kWh$_{th}$ (11.8%) [17]. Although the HTF-charging and salt discharging provides lower cost of storage, the high melting temperature of the salt limited its further use.

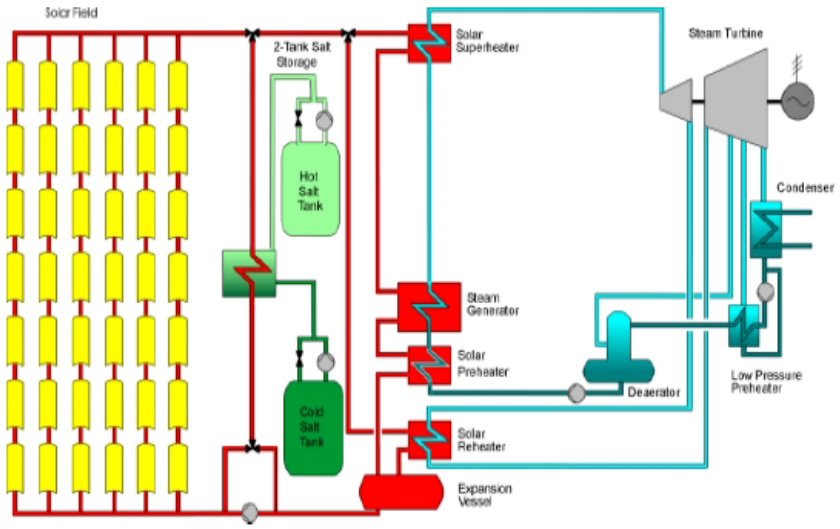

(a)

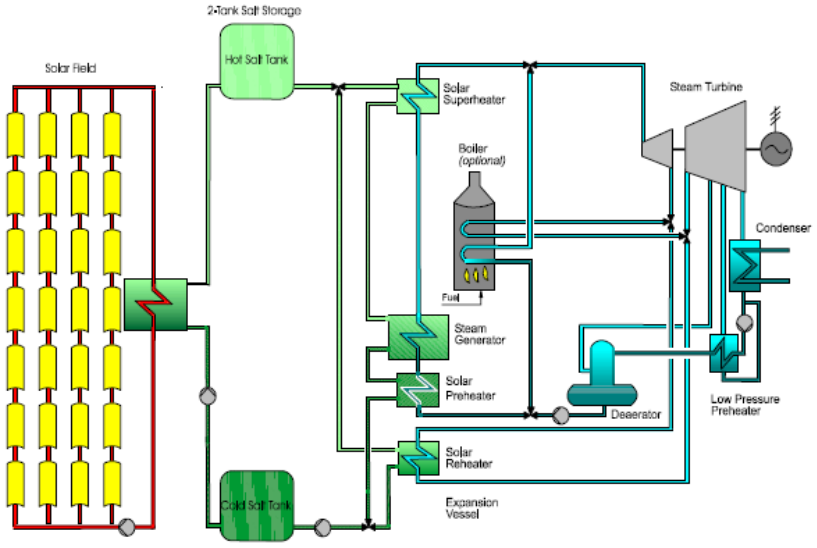

(b)

Figure 3.9 The Indirect two-tank configurations (a) HTF charging and discharging (b) HTF charging and steam discharging [100]

The technical and economic feasibility of the two-tank indirect system for use in a 50 MW_e capacity plant was investigated by Herrmann et al. [9] considering storage capacities up to 15 hours full load operation. A capital cost for the storage system ranging from 65.63 \$/kWh_{th} to 31.00 \$/kWh_{th} was obtained for capacities from 1-15 hours of full load operation respectively, neglecting the cost of construction management, procurement, engineering and interest. It was found out that for storage capacity of less than three hours the LEC is higher than the reference plant (plant without storage) and storage with 12 hours of capacity gives the lowest LEC which is 10% lower than the reference plant. In order to develop the technology into commercial status Kelly et al. [11] conducted a rigorous optimization study of the complete solar thermal plant integrated with the storage system. The study is different to that of Herrmann et al. [9] in the sense that it considers: the effect of changing the approach temperatures of the HTF/salt heat exchanger from 2^oC to 15^oC; two Rankine-cycle pressures of 101 bar and 66 bar were considered. About 144 configurations were studied. The study found out that the storage system with the lowest capital cost does not result in lower LEC. The storage system with Rankine steam pressure of 66 bar gave lower capital cost but the LEC is higher due to lower efficiencies in the Rankine-cycle at 66 bar.

The indirect two-tank system is currently the most matured thermal storage system for parabolic-trough plants and has reached commercial status with most commercial plants in operation using it. As such it serves as the benchmark for comparison with other storage concepts that are being developed.

3.2.2.4 Water/Steam Accumulators

In these systems sensible heat is stored in pressurized water at saturation point since water has a high specific heat capacity of 4.2 kJ/kgK. During discharge, the pressure of the saturated water is reduced to produce saturated steam. So during discharge the steam pressure reduces with time. The water/steam accumulator can be charged by either condensing the superheated steam in the

pressurized water, in this case the temperature of the water increases or by maintaining a constant temperature in the accumulator by the addition of more water. Another method of charging the accumulator in which the HTF is not water is to use a heat exchanger [101].

Water/steam accumulators are more suited for buffer storage so that unexpected transients can be compensated. This storage concept has fast reaction times and as such can give room for the extended reaction time of backup and storage systems. Water/steam accumulators are well suited for solar thermal plants that utilize water/steam as the HTF.

Steam accumulators have been utilized for the storage of thermal energy in industrial applications that require process heat and high storage capacities in the range of 20-30 kWh/m^3 are obtainable. The main problem associated with steam accumulators is that steam cannot be produced at constant pressure and only saturated steam can be produced [24]. A 20 MWh_{th} capacity (Figure 3.10) has been utilized in the PS10 power tower plant in Spain [49].

Figure 3.10 Steam tanks for PS10 power-tower plant

3.2.3 Single Tank Thermocline Systems (Dual Medium)

One of the methods that the cost of the two-tank system can be reduced is the use of a single tank. This can be achieved by using a single tank thermocline system in which the difference in density between the hot and cold fluid is utilized. The hot fluid can thus be stored at the top while the cold can stored at the bottom of the tank thus effectively using one tank for both the hot and cold medium. The hot and cold fluids are separated by a layer called the thermocline. The single tank can be used as either a direct or indirect system. Figure 3.11 shows the configuration of the single tank indirect system coupled to a parabolic-trough power plant. The main challenges of single tank thermocline system are: the design of the thermocline so that mixing does not occur between the hot and cold fluid is complex; and charging and discharging must be done in a controlled way in order to maintain the thermocline region (stratification between hot and cold fluid). In order to maintain the thermocline and reduce the amount of liquid media, low cost filler materials (solid media) such as rocks or sand are used in the tanks. In this situation the solid media and the storage fluid serve as the storage media and thus can be termed a dual storage system. Even though the solid media serve as the primary storage media [7].

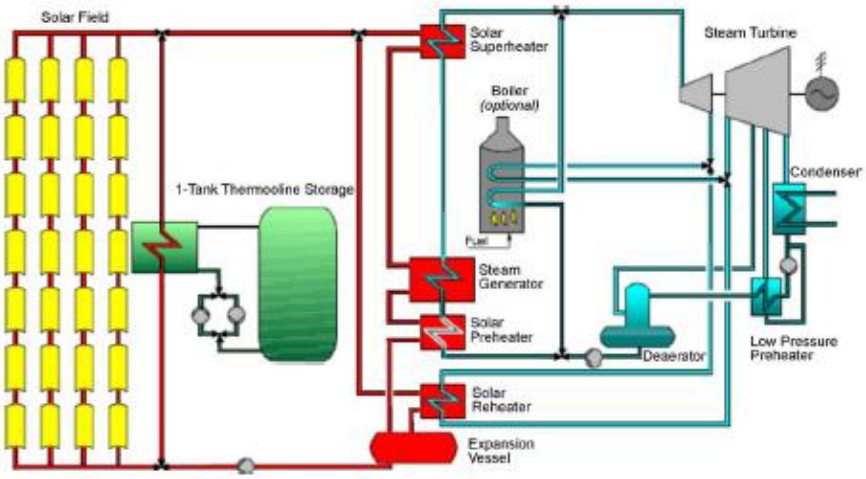

Figure 3.11 Single tank thermocline system [100]

The single tank thermocline system has been utilized successfully in the Solar one power-tower plant using a capacity of 182 MWh_{th} with 906 m^3 mineral oil (caloria) and 6170 tonnes of rocks and sand as the storage media (Figure 3.12). A good stratification was achieved in the single tank during operation with operating temperatures of between 218 and 302^oC [99; 102].

Molten salts are the most suitable liquid media for storage systems and thus to develop a single tank thermocline system, the compatibility of the low cost filler material in the molten salt environment has to be determined first. Also the filler material should also have the following properties: availability, high specific heat capacity; be non-hazardous and small void fraction so that the amount of liquid medium required will be small [99]. In a previous study [103], Taconite (pellets of iron ore) was found to withstand the molten salt environment for several years at 550^oC while granite rock dissolves in the molten nitrate salts. Pacheco et al. [99] has considered several materials as candidate filler material and chose seventeen for testing. These were: Witherite, Taconite, Scheelite, Quartzite, Marble, Magnesite, 2 types of Limestone (one from New mexico and the other from Kansas), Illmenite, Hydroxyapatite, Fluoropatite, Corrundum, Cassiterite, Carborumdum, Bauxite, Barite and Anhydrite. These materials were

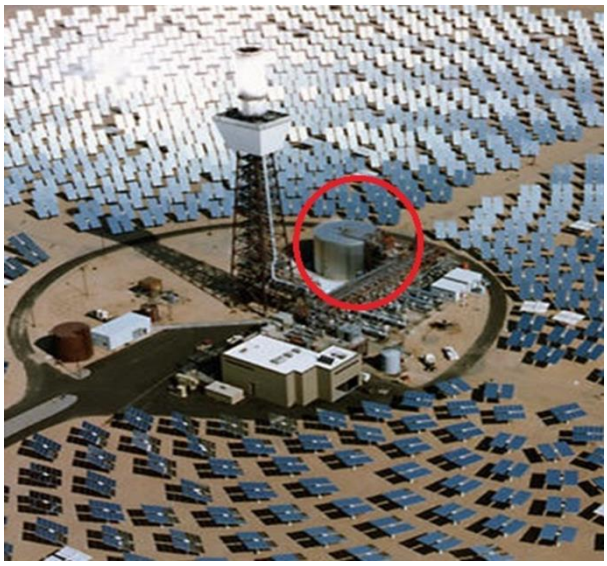

Figure 3.12 The 182 MWh_{th} single tank thermocline system in Solar one plant

tested for corrosion by immersing them in Hitec XL® salt (42% $Ca(NO_3)_2$, 15% $NaNO_3$, 43% KNO_3 by weight) and observing them after 10, 100 and 1000 hours. Result showed that only Cassiterite, Scheelite, corundum, apatite, marble, taconite, quartzite and limestone from New Mexico shows good compatibility with the Hitec XL salt environment. Test on compatibility of marble, taconite, quartzite and limestone from New Mexico were also conducted with Solar salt (60% $NaNO_3$, 40% KNO_3 by weight) for 400 hours immersion time. Thermal cycling test were conducted on four filler materials (marble, taconite, quartzite and limestone from New Mexico) because of their availability and cost. Experiments were conducted using a cylindrical container having a diameter of 10 cm and height of 30 cm filled with each of these materials and filter sand in order to reduce the void fraction in the tank. Results showed that only Taconite and Quartzite withstand the thermal cycling test in Hitec XL salt temperatures between 290 and 400^oC. As such Quartzite-rock/Silica-filter-sand was selected as the first candidate for use in thermocline tanks because of their performance in the test and is more available than taconite.

Brosseau et al. [102] conducted extended isothermal and thermal cycling tests on Quartzite-rocks/Silica-filter-sand for extended period of time in molten salt environment (Hitec XL) in order to find the durability of the filler in the longer term. The Isothermal testing was done by immersing the filler material in hot molten salt at temperatures between 450 and 500^oC for a period of one year. For the thermal cycling test a tank of 10.2 cm diameter and 25.4cm height was used and the operating temperatures were same as that of Pacheco et al. [99] and 10,000 cycles were completed. Results showed that the filler materials can withstand the environment of molten salt even on the long term. This has thus confirmed that Quartzite rock/Silica-filter-sand can be used in molten salt thermocline tanks and thus a cheap filler material has been obtained.

3.2.3.1 Design and Performance Evaluation of Thermocline Tanks

Design of a thermocline tank entails finding the parameters such as tank diameter, height that will provide a very good performance. Pacheco et al. [99] evaluated the performance and economics of a single tank thermocline system

by lab scale experiments and simulations. A 2.3 MWh_{th} capacity tank was designed and constructed using Quartzite and silica-filter-sand in the ratio of 2:1 respectively (since it was found to be the best filler) with an actual void fraction of 0.22. A tank with diameter of 3 m and height of 6.1 m made up of carbon steel was used. 49.9 tonne and 21.9 tonne of quartzite and silica filter sand were used respectively. Eutectic mixture 50% $NaNO_3$ and 50% KNO_3 was used as the liquid media. The actual heat capacity of the storage, shape and size of the thermocline, change in shape of the thermocline temperature profile after sometime and the heat lost were studied. These were compared with results of a model developed.

A thermocline tank with a capacity of 688 MWh_{th} was simulated using the model developed and result showed that the thermocline region requires a certain tank height to maintain stratification and as such the capacity of a thermocline tank depends on the height of the tank. The theoretical capacity utilization of thermocline tanks was about 68% compared to 85% for the two-tank system. The thermocline tanks resulted in about 35% decrease in cost compared to a two-tank system for the 688 MWh_{th} capacity. The study therefore proved the feasibility of thermocline tanks for use in parabolic-trough plants.

In order to have a greater understanding of the efficiency and thermal characteristics of a thermocline tank during charging and discharging, Yang and Garimella [104] developed a model. Hitec salt (7%$NaNO_3$, 40%$NaNO_2$, 53% KNO_3) with melting temperature of 149^oC stable up to 538^oC and Quartzite rock was used as the filler material. The model was developed using Fluent CFD code and validated with the result of Pacheco et al. [99]. Procedure for the design of thermocline tanks were developed and result showed that the discharge efficiency increases with the height of the tank and reduces with increasing Reynolds number. The size of the filler material also affects the discharge efficiency inversely (the smaller the size the larger the discharge efficiency). Design procedure for designing a thermocline tank for a pre-defined power and useful thermal capacity were produced.

Preliminary design work conducted by EPRI [105] for a single tank thermocline storage system (indirect) for different operating temperatures and capacities ranging from 100 to 3500 MWh_{th} for use with parabolic-trough showed that the capital cost of single tank is always lower than that of the two-tank system at all capacities and that the cost reduction was caused by the salt inventory requirement of each. The cost reduction for thermocline capacity ≥500 MWh_{th} is ≥ 20%. The single tank requires about half the amount of salt of the two-tank system. A capacity of 1500 MW_{th} resulted in minimum capital cost per kWh_{th} for the single tank thermocline system. On the annual performance aspect, the single tank thermocline system is only comparable to the two-tank system when the single tank is operated by sliding pressure during discharge to provide a minimum amount of super-heat.

From the capital cost point of view single tank offers cost reduction potentials of about 33% [99; 105]. It is expected that this reduction in cost will lead to reduced LEC for parabolic trough plants. In view of this Kolb [12] compared the annual performance of the single tank thermocline system with the two-tank system using the TRNSYS software using the Andasol plant as reference plant. The weather data for Tucumcari, New Mexico with a time step of 3 minutes was used for the simulations because the annual DNI for this place is similar to that of Spain (2.3 MWh/m^2). Sliding pressure operation was employed in the Rankine-cycle to maintain 50^oC of super-heat. The Rankine-cycle was designed to operate up to 90^oC below the design temperature of 390^oC. Using this allowable reduction in temperature the model produced a predicted annual gross output of 152 GWh for the two-tank system and 149 GWh for the single tank system. This shows that allowing for a HTF temperature difference of 90^oC during discharge makes the thermocline storage system performance similar to the two-tank system.

The only challenge hindering the utilization of the potential of the single tank thermocline is thermal ratcheting. Thermal ratcheting occurs due to the expansion and contraction of the tank. During expansion the filler materials move down and during contraction they can’t move up and thus stresses are

exerted on the walls of the tank which can lead to bursting of the tank. Also performance and cost analysis of the optimum storage capacity for use in commercial plants needs to be conducted.

3.3 Latent Heat Storage (LHS) Systems

When materials undergo phase change, energy is absorbed or released. The phase change from solid to liquid is used. Solid to liquid phase change is preferred to liquid to vapour phase change since in the latter changes of pressure occurs making the system complex.

LHS systems offer higher efficiency since thermal energy is transferred at constant temperature thus minimizing the temperature difference between the HTF and the PCM. During charging, thermal energy is stored as latent heat (the material changes from solid to liquid). During discharging the energy is released by solidifying the material. The temperature of the PCM is chosen in such a way that it is between the charging and discharging temperatures of the HTF. The storage capacity per unit volume of LHS systems is about 2.5 times greater than that of the sensible heat storage systems. LHS systems thus offer smaller size storage. To completely charge and discharge a LHS system using a HTF such as the one used in parabolic-trough power plants the PCM must be superheated and sub-cooled respectively due to the wide operating temperature range [15; 17].

Although PCMs have high storage density theoretically, the large operating temperature (about $100^{o}C$) in parabolic trough plants makes their utilization factor to be very low because discharging ceases once there is no enough temperature difference between the PCM and the HTF. To illustrate this, Figure 3.13(a) presents the temperature profile of a LHS system at the end of charging and discharging using a single PCM at a melting temperature of about $307^{o}C$. It will be observed that large portion of the PCM is in the liquid form at the end of discharging because there is no temperature difference to drive heat transfer between the HTF and the PCM. In order to increase the utilization factor of LHS systems the melting temperature of the PCMs must always be greater than that of the HTF during discharging and lower during charging.

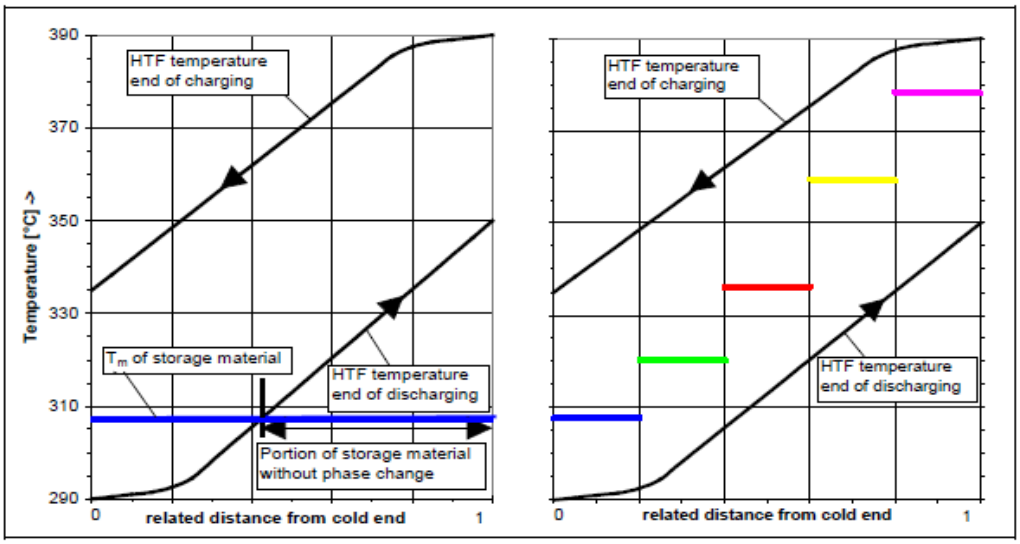

(a) (b)

Figure 3.13 Temperature profile of a single and cascaded LHSS for parabolic-trough plant [17]

This can be achieved by cascading many PCMs with different melting temperatures [8]. Michels and Hahne [18] asserted that for a fully optimized system five PCMs modules are required. Figure 3.13(b) shows an illustration of the temperature profile for a cascaded storage system at the end of discharging using five PCMs in the operating temperature range. Five suitable PCMs are required to fully utilize LHS for parabolic-trough plants.

3.3.1 Research on Cascaded Latent Heat Storage (LHS) Systems

Cascading of LHS system is one way of increases their utilization factor since it avoids sub-cooling and super-heating of PCM and also offers faster charging/discharging and increase in exergy efficiency [16]. The use of multiple PCMs in LHS systems have been extensively investigated for low temperature applications [106-110]. For parabolic trough plants, In the 1990s, LUZ international, INITEC and SGR conducted studies on cascaded LHS systems with 5 PCMs. LUZ international considers five PCMs ($NaNO_3$, KCl-KNO_3, KNO_3,

KOH, $MgCl_2$-KCl-NACl) and INITEC also considered five PCMs (NaOH-NaCl, KOH, KNO_3-KCl, $NaNO_3$ and $NaNO_2$). Results showed that due to the very low thermal conductivity of the PCMs, it is difficult to utilize the full theoretical capacity of the storage during charging and discharging. One way of enhancing the thermal conductivity in the PCM is to increase the surface area of the HTF pipe by reducing the distance between the HTF-pipes in the storage module. This led to an optimum distance between tubes of 60 mm. Also obtaining suitable five PCMs was not possible at the time and thus only three materials were obtained. This led to the proposal of using three PCMs in cascade from the colder end of the storage system and a concrete storage module on the high temperature side by SGR [17].

Michels and Hahne [18] conducted laboratory tests using three different PCM ($NANO_3$, KNO_3/KCL and KNO_3) having melting points of 308, 320 and 336^oC respectively in cascade and thermal energy is supplied using electric heaters. Figure 3.14 shows the laboratory schematic of the system. The results obtained showed that utilization factor is increased by cascading. The study also showed that the heat transfer characteristics of a single shell and tube (annular HX) and an array of tubes in a single cylindrical tank are similar. This means that simplifying the analysis of an array of tubes to a single shell and tube is a valid assumption.

Michels and Pitz-Paal [20] conducted experiments using three PCMs: KNO_3, KNO_3/KCL and $NaNO_3$ having 335^oC, 320^oC and 306^oC melting temperatures and heat of fusion of 95, 74 and 172 kJ/kg respectively. The experiment was conducted with a shell-and-tube heat exchanger with the HTF flowing in the tube of 0.012 outer diameter and the PCM occupies the shell section having 0.13 inner diameter. Experimental result showed that cascading offer higher actual storage capacity. A model was developed in Dymola and validated using the experimental data. Five PCMs were used (Table 3.6) and optimization studies on the size of each stage was conducted. An optimized thermal storage having a capacity of 875 MWh_{th} (capacity for 6 hours full load operation of a 50 MW_e parabolic trough plant) was designed.

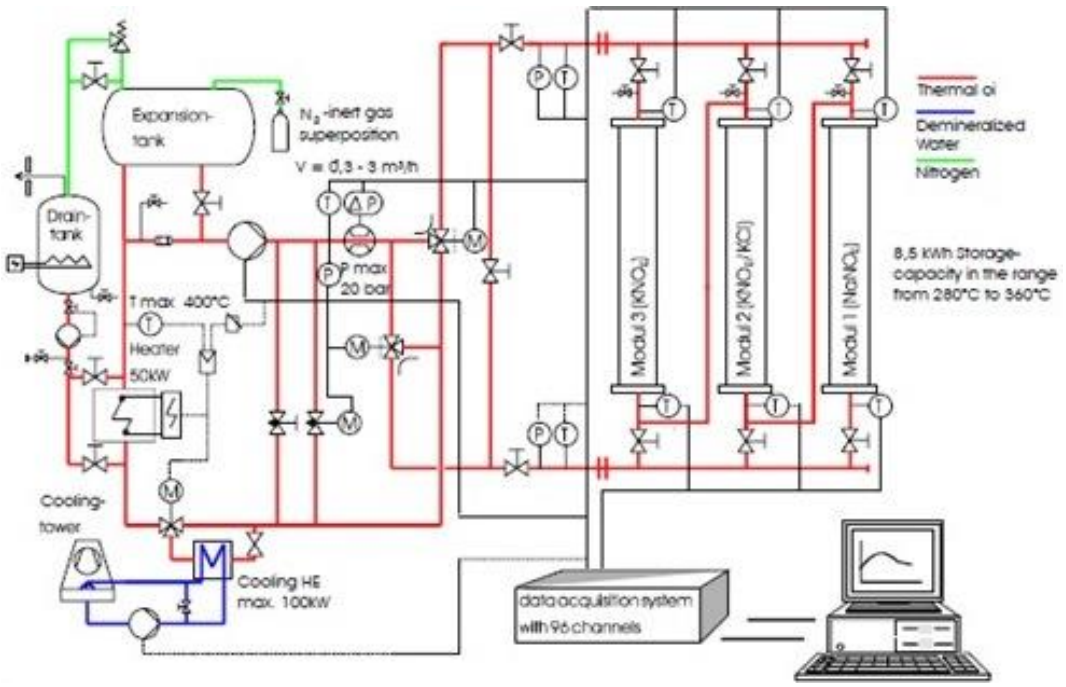

Figure 3.14 Schematic Diagram of a cascaded PCM test Module [18]

Table 3.6 Thermo physical properties of five possible PCMs [20]

Medium	Ratio of constituents (by mass)	Temperature range °C	Latent heat of fusion kJ/kg	Density (Average) kg/m^3	Thermal Conductivity W/mK	Heat Capacity kJ/kgK
$NaNO_3$		306	172	2261	0.5	1.10
KNO_3/KCl	95.5/4.5	320	74	2100	0.5	1.21
KNO_3		335	95	2109	0.5	0.953
KOH		360	134	2040	0.5	1.34
$MgCl_2$/KCl/NaCl	60/20.4/19.6	380	400	1800	n/a	0.96

The resulting storage obtained requires higher amount of molten salt than the two-tank system. This is because of the low thermal conductivity of the PCMs. Increasing the thermal conductivity of the PCMs from 0.5 to 2 W/mK was found to greatly reduce the amount of PCM to be less than that of the two-tank system by 4,000 tonne.

Shabgard et al. [16], conducted an exergy and heat transfer analysis of a commercial scale three stage cascaded LHS system in which thermo-syphon tubes were used in each module in order to enhance the thermal conductivity of the PCM. A thermal resistance network model developed by Shabgard et al. [29] was used in the analysis. The three PCMs used are eutectic mixtures of (percentages by mass): NaOH-NaCl(26.7%); KCl (22.9%)-$MnCl_2$(60.6%)-NaCl; and NaOH(66.2%)-NaCl(20%)-Na_2CO_3(14.8%) with melting temperatures of 370^{o}C, 350^{o}C and 318^{o}C respectively. Operating temperatures typical for the parabolic-trough plants using synthetic oil of between 280^{o}C and 390^{o}C were used. Comparison of the three stage system with a single PCM storage were done and results showed that cascading increases the exergy efficiency compared to non-cascaded systems and that the PCM stage with the lowest melting temperature resulted in the highest exergy efficiency. Also it was found out that the design of an efficient system using thermo-syphon pipes for solar thermal plants is dependent on the length of the charging and discharging cycles. For a charging time of less than 10.5 hours the single PCM system with the smallest melting temperature has higher exergetic efficiency.

Although cascading increases the utilization factor of PCM storage modules, the low thermal conductivity is still hindering the performance and cost effectiveness of these systems. As such thermal conductivity of PCM must be enhanced.

3.4 Conclusions

The stable and sustainable operation of any solar thermal power plant requires a thermal storage system. There are basically three methods of storing thermal energy: chemical, sensible and latent. Chemical storage is at the developmental stage and very expensive. The sensible and latent heat storage methods are the most considered for parabolic trough plants. Three technologies have been researched over the years under the sensible storage methods: CTR, two-tank system and the single tank thermocline. The two-tank indirect system is the most matured technology and currently the state of the art. The challenge with

this technology is it is expensive due to high storage material requirement, the use of two tanks and has high parasitics.

The use of single tank thermocline system offers lower cost and reduced storage material inventory. This technology has been demonstrated on small scale and simulations of commercial scale systems have shown its capability of producing a smaller and more cost effective storage system. The main challenge of the single tank thermocline system is thermal ratcheting. There is also need for a complete optimization of the storage system integrated with commercial scale solar thermal plant to determine the storage size and capacity that will give the minimum capital cost and LEC.

The availability and low cost of concrete prompted the development of the CTR in order produce a more cost effective system. Various pilot plants were tested and the feasibility of developing a commercial scale system has been conducted successfully. The main issue with CTR is their high volume.

The use of LHS system offers smaller storage volume and high efficiency. The low thermal conductivity of potential PCMs and the lack of PCMs to cover the operating temperature range have hindered the capability of producing a more cost effective system than the two-tank system.

4 PCM SCREENING

Many researchers have used arbitrary chosen PCMs in the analysis of LHS systems. To develop a practical LHS system, commercially-available PCMs having suitable properties must be obtained. This must be done first since the thermo-physical properties of the PCM influence the performance of the system as a whole. In this chapter screening of various PCMs was conducted in order to come up with suitable commercially-available PCMs for use in LHS system for parabolic trough plants using synthetic oil as HTF. In LHS systems phase transition from solid to liquid and vice versa are preferred because the latent heat of fusion is higher than that of evaporation, smaller density change and technically simpler because of smaller pressure changes [111].

The first most important property to consider in selecting a suitable PCM is that its melting temperature must be in the operating temperature range of the parabolic-trough plant using synthetic oil as the HTF. Thus suitable PCMs must have melting temperatures between 300 and 400^{o}C. Other properties required for a suitable PCM apart from melting temperature are presented in Table 4.1 alongside the function of each [15]. In selecting a PCM three of these properties must be considered critically because they determine the usability of the material even if it has other favourable properties. These are: reversible phase change, negligible sub-cooling and super-cooling and compatibility with other materials of the system. In general candidate commercially-available PCMs are either made up of a single material; eutectic mixture of two or more materials or metals and alloys.

4.1 Single Component PCMs

Potential single component PCMs having melting temperatures in the operating temperature range are limited to low melting point metals such as tin and lead, metallic alloys and inorganic salts [15; 112; 113]. Low melting point metals and alloys are relatively very expensive even though they have high thermal conductivity [114]. Table 4.2 presents potential materials suitable in the operating temperature range from the literature.

Table 4.1 Properties of suitable PCM

Physical requirements	
High latent heat of fusion	Smaller storage size for a given capacity compared to sensible heat storage.
High thermal conductivity	To increases the dynamics in the system (rate of heat transfer).
Reversible Phase change	For cyclic operation.
Negligible sub-cooling and super-cooling	This is to make sure that the freezing and melting takes place at the same temperature.
High Density	Smaller storage size
Technical Requirements	
Small density change	To reduce the amount of unfilled space in the PCM container.
Low vapour pressure	To eliminate the need for pressurized container.
Chemical stability and compatibility with other materials of the system	To ensure the long term use of the system.
Economic requirements	
Low specific cost and availability Non-toxic and recyclable	To ensure it will be cost effective.

Only few single materials are available in this temperature range. $RbNO_3$, CsOH and $PbBr_2$ have low latent heat of fusion and thus are not suitable. MgH_2 is not safe since it reacts violently with air and InBr does not have a completely reversible phase change process [115]. Chlorides have high hygroscopicity, high vapour pressure and corrode steel which is the material used in most components of the storage system [22; 116]. Strong bases such as (Sodium hydroxide and potassium hydroxides) attacks aluminium and cannot be used with heat exchanger having aluminium fins [117; 118]. This thus leaves nitrates of sodium and potassium which are alkali nitrates.

Table 4.2 Potential single component PCMs for parabolic trough plant using synthetic oil as HTF [20; 24; 119; 120]

Material	Melting Temperature (average) ^{o}C	Latent Heat of Fusion kJ/kg	Density (at room temperature) kg/m^3	Thermal Conductivity (W/mK) Solid	Liquid
$NaNO_2$	270	180	1810	0.67-1.25	0.53-0.67
$ZnCl_2$	280	75	2907	0.5	
InBr	297	133			
$RbNO_3$	305	38	2519		
$NaNO_3$	307	176	1900	0.59	0.51-0.57
NaOH	323	165	2130	0.92	
TlF	326	62	8300		
MgH_2	327	532	1450		
KNO_3	337	100	1865		0.42-0.50
CsOH	342	52	1720		
KOH	360	134	2040		
$PbBr_2$	371	45	5730		

4.1.1 Alkali Nitrates

Alkali nitrate salts have very favourable characteristics in comparison with other materials due to their low rates of corrosion (< 0.01 mm/year), their stability, low vapour pressures, availability and they are relatively cheap making them the most promising [121].

Sodium nitrate is the most extensively studied PCM for high temperature LHS systems. One of the reasons is that its melting point coincides with saturated steam temperature of water at 100 bar. This condition is suitable for DSG in parabolic-trough plants. The melting and latent heat of fusion of $NaNO_3$ reported in the literature ranges from 306 - 310^{o}C and 172 - 200 kJ/kg respectively [122; 123]. Discrepancies can be attributed to the fact that impurities cause reduction in the melting temperature and broaden the melting range [124].

Bauer et al. [125] has conducted an experimental study on the suitability of sodium nitrate as a high temperature PCM. $NaNO_3$ has a melting temperature of 306^oC and an average heat of fusion of 177 kJ/kg. $NaNO_3$ is stable up to 450^oC, above which it start to form sodium nitrite and oxygen. It has an average percentage change in volume during melting of 9.7%. Thermal stability at 350^oC for long time has been tested in DLR with small production of nitrite. It attacks graphite and as such cannot be used with graphite fins [125]. $NaNO_3$ has been tested in an 8.51 kWh theoretical capacity experimental LHS system having aluminium fins for about 172 cycle's equivalent to about 4000 hours of operation without any problem [126].

Potassium nitrate has a reported melting temperature range of 333 –337^oC and latent heat of fusion ranging from 91 – 98.9 kJ/kg in the literature [15; 24; 127; 128]. Geyer [129] reported a latent heat of fusion of 266 kJ/kg. This value is different from all the values reported in the literature. Experiments conducted using DSC gave a latent heat of fusion of 97.25 kJ/kg and a melting temperature of 335.32^oC [116]. This is close to what has been reported in most literatures. KNO_3 being an alkali nitrate will have corrosion, compatibility and thermal stability properties similar to $NaNO_3$. It has a volume expansion of 3.3% which is very good since small volume change is good for LHS system. Overall $NaNO_3$ and KNO_3 are suitable for use as PCMs since they are thermally stable, compatible with other materials of the system and are not expensive.

4.2 Multi-component PCMs

From Section 4.1, it can be concluded that there are very few suitable single component PCMs for use in LHS system and thus eutectic mixtures of two or more salts to produce a suitable PCM are required. Multi-component mixtures of salts tend to have higher latent heat of fusion than single component PCMs [114]. They have the potential of smaller and cheaper system than the single component PCMs. The main challenge of eutectic salt mixtures is finding the eutectic composition and thermal properties of the mixture especially the melting temperature and latent heat of fusion [113]. Tables 4.3 and 4.4 present composition and available thermo-physical properties of eutectic mixtures of

salts suitable for the operating temperature range. Properties presented in Table 4.3 were obtained using either the FactSage 6.2 thermochemistry software or the phase change diagram of the mixture by Gomez [113]. The materials presented in Table 4.4 were obtained from literature data since 1960 compiled by Kenisarin [128]. These properties must be confirmed by experiments since some composition and properties reported in the literature do not agree with that obtained using thermo-chemistry software or phase change diagrams.

Experiments conducted by Gomez [113] using a DSC confirms the presence of discrepancies in the reported composition, melting point and latent heat. One of such discrepancy is the nonexistence of the melting temperature of 342^{o}C for the eutectic mixture of KNO_3 (80.69), KBr (11.87) and KCl (7.44) % by mass and latent heat of fusion of 140 kJ/kg. Experiments confirm that the mixture melt over a range of temperature which is in conformity with the result from FactSage 6.0 software and phase diagram.

4.2.1 Experimental Investigation of Eutectic Mixtures

In this section the multicomponent PCMs that have been investigated or used successfully for LHS systems will be discussed in order to come up with the most suitable commercially-available PCMs that can be used in the LHS system.

4.2.1.1 KNO_3/KCl

Dinter et al. [17] reported an eutectic mixture of KNO_3/KCl (6% by mol, 4.5% by mass) having a melting temperature and latent heat of fusion of 320^{o}C and 150 kJ/kg respectively. From Table 4.3 an eutectic mixture with 7.18% by mass KCl was reported to have a melting temperature and latent heat of fusion of 307.87^{o}C and 150.63 kJ/kg respectively using FactStage software [113].

Table 4.3 Potential eutectic salt mixtures for parabolic trough plants using synthetic oil as HTF obtained using FactSage software and phase equilibrium diagram

Composition of salt mixture (by mass%)			T_m (^oC)	ΔH kJ/kg	Cp, J/gK	
					Solid	Liquid
Binary Mixtures						
KNO_3 (92.82)	KCl (7.18)		307.87	105.63	1.156	1.177
KNO_3 (65.31)	K_2CO_3(34.69)		325.73	71.58	0.812	0.823
LiBr (52.26)	KBr (47.74)		327.8	333.05	0.562	0.672
KNO_3(91.15)	KBr (8.85)		329.84	100.93	1.161	1.161
$FeCl_2$(52.08)	KCl (47.92)		350	133.91	0.706	0.938
KCl (54.75)	LiCl (45.25)		352.53	267.96	1.009	1.279
K_2CO_3 (22.05)	KOH (77.95)		365.5	164.35	1.332	1.394
K_2SO_4 (16.54)	KOH (83.46)		376	174.09	1.329	1.408
$FeCl_2$ (63.02)	NaCl (36.98)		376	249.54	0.768	0.983
Ternary Mixtures						
$MgCl_2$ (42.05)	KCl (39.07)	NaCl (18.88)	331.31	198.45	0.857	1.031
$MgCl_2$ (46.23)	KCl (39.90)	NaC l(22.87)	331.87	207.14	0.859	1.033
NaCl (22.24)	KCl (28.80)	$FeCl_2$ (48.96)	332.55	308.88	1.326	1.695
$CaCl_2$(10.37)	KCl (53.11)	LiCl (36.52)	338.36	241.24	0.950	1.200
$MgCl_2$(42.90)	KCl (48.14)	NaCl (8.96)	380.95	177.27	0.752	0.946
KCl (57.2)	LiCl (36.5)	LiSO4 (6.3)*	324			
KF (54.0)	AlF_3 (6.2)	ZrF_4 (39.8)*	380			
Na_2SO_4 (28.4)	K2SO_4 (17.4)	$ZnSO_4$ (54.2)*	385			

*Percentage by Mol.

Table 4.4 Potential eutectic salt mixtures of from the literature since the 1960s [128]

Composition of salt mixture (mol%)				T_m (^oC)	ΔH J/g
Binary Mixtures					
LiCl (59.15)	$Ca(NO_3)_2$ (40.85)			270	167
LiOH (65.5)	LiCl (34.5)			274	339
$NaNO_3$ (93.6)	NaCl (6.4)			284	171
$NaNO_2$(54.8)	KNO_3(45.2)			285	152
KNO_3 (13)	$Ba(NO_3)_2$ (87)			290	124
KNO_3 (33)	$RbNO_3$ (67)			292	
NaF (3.5)	$NaNO_3$ (96.5)			304	
NaCl (6.3)	NaOH (93.7)			314	
LiOH (40)	KOH (60)			314	341
KNO_3 (94)	KCl (6)			320	150
LiCl (58)	KCl (42)			348	170
Ternary Mixtures					
LiOH (62)	LiCl (36.5)	KCl (1.5)		282	300
NaOH (85.8)	NaCl (7.8)	Na2CO_3 (6.4)		282	316
Na_2SO_4 (5.3)	NaCl (8.4)	$NaNO_3$(86.3)		287	176
NaCl (8)	NaF(5)	$NaNO_3$ (87)		288	224
LiCl (54.2)	$BaCl_2$ (6.4)	KCl (39.4)		320	170
KNO_3 (80)	KBr (10)	KCl (10)		342	140
NaCl (33)	KCl (24)	LiCl (43)		346	281
KCl (28.7)	$MgCl_2$ (45)	NaCl (26.3)		350	215
Quaternary Mixture					
LiF (7)	LiCl (41.5)	$LiVO_3$ (16.4)	Li_2CrO_4 (35.1)	340	177

Experiment conducted by Michels [19] using DSC showed that an eutectic mixture with 4.5% (by mass) KCl has a melting temperature and latent heat of fusion of 320^{o}C and 74.4 kJ/kg respectively. Also Glatzmaier et al. [116] obtained a melting temperature of ~320^{o}C and latent heat of fusion of about 82.86 kJ/kg using DSC and showed that it is the best candidate PCM for temperature bucket around 320^{o}C after considering various eutectic mixtures. This confirms the correct properties and clears the discrepancy. Since this

eutectic mixture has 96.5% by mass KNO_3, it will thus be expected to have similar characteristics thus proving its suitability for LHS systems. The difference in the latent heat of fusion of 74.4 kJ/kg and 82.86 kJ/kg may be due to impurities and experimental errors.

4.2.1.2 Mixture of KNO_3, KBr and KCl

SERI [112] has presented an eutectic composition of 80.69% KNO_3, 11.87% KBr and 7.44% KCl (percentages by mass) having a melting temperature of 342^{o}C and latent heat of fusion of 140 J/g. From the FactSage software and phase diagrams for ceramist, Gomez [113] reported that this mixture does not have a particular melting temperature but melts at a range of temperature. Experiments conducted proved this and the mixture has a melting temperature ranging from 326.58^{o}C to 412.99^{o}C with a latent heat of fusion (average) of 75.89 J/g which is not same as that reported by SERI [112]. This mixture cannot be used as a PCM.

4.2.1.3 Mixture of NaCl, KCl and LiCl

From the literature this has an eutectic mixture with a composition of 34.81% NaCl, 32.29% KCl and 32.90% LiCl (% by mass) having a melting temperature of 346^{o}C and latent heat of fusion of 281 J/g [112]. Experimental investigation on corrosion at 500^{o}C showed that this mixture corrodes stainless steel (SS316L) and attacks aluminium [113]. Experimental investigations [113] showed that the mixture has an average melting point of 351.36^{o}C with average super cooling of 1.20^{o}C. This is about 5^{o}C higher than that reported by SERI [112] and may be due to the purity or method employed in making of the mixture. A value of latent heat of fusion (average) of 131.96 J/g with a standard deviation of 9.32 was obtained and a latent heat of solidification of 123.71 J/g with a standard deviation of 0.86 was obtained. Even though the standard deviation for the latent heat during melting is very high and brings doubt to the accuracy of the result the value is much less than that reported in SERI [112]. This result has to be collaborated with other experimental result in order to confirm the exact latent heat.

4.2.1.4 Mixture of $MgCl_2$, KCl and NaCl

From literature this has an eutectic composition of 60% $MgCl_2$, 20.4% KCl and 19.6% NaCl (% by mass) with melting temperature of 380^{o}C and latent heat of fusion of 400 J/g [17]. This mixture was found to highly corrode stainless steel (SS316L) and attack aluminium metal. Investigation of the of the properties of the mixture resulted in an average melting temperature of 381.47^{o}C with a standard deviation of 0.79 and an average heat of fusion of 198.55 J/g. This shows that the value for the melting point presented in the literature was correct but the latent heat of fusion reported was too high which is about double the actual value [113].

4.3 Conclusions

There are very few materials having melting temperature in the operating temperature range of the parabolic trough plants using synthetic oil as HTF. Alkali nitrates and nitrate are the most suitable PCMs for use in LHS systems. Many eutectic mixtures of materials have potential for use but the main challenge with eutectic mixture is the correctness of the melting temperature and latent heat of fusion reported in the literature. Thus properties of material must be confirmed using experiments before a PCM can be termed suitable. Many of the potential eutectic mixtures are chlorides and hydroxides both of which corrode steel, hydroxides attack aluminium and chlorides have high vapour pressure. This has limited their suitability.

In view of this only three commercially-available PCMs are suitable in the operating temperature range whose properties have been confirmed experimentally. Table 4.5 presents the thermo-physical properties of these materials. These will be used in this study. Finally there is need in finding other PCMs with high latent heat of fusion preferably mixtures containing more of nitrates since they are the most suitable.

Table 4.5 Thermo-physical properties of suitable PCMs [19]

	$NaNO_3$		**KNO_3/KCl (4.5% by mass)**		**KNO_3**	
	Solid @ 20 ^oC	Liquid @ melting	Solid @ 20 ^oC	Liquid @ melting	Solid @ 20^oC	Liquid @ melting
Melting temperature (^oC)		306		320		335
Latent heat of fusion (kJ/kg)		171.8		74.4		95.2
Density (kg/m^3)	2261	1910	2100	1850	2109	1870
Specific heat capacity (kJ/kgK)	1.096	1.823	1.21	1.21	953	1342
Thermal conductivity (W/mK)	0.495	0.565	0.48	0.48	0.5	0.459
Dynamic viscosity (kg/ms)		$3.02x10^{-3}$				$2.97x10^{-3}$
Thermal expansion coefficient (1/K)		$3.65x10^{-4}$				$4.16x10^{-3}$
Volume expansion (%)		10.7		14.1		3.3

5 CFD MODELLING AND SIMULATION OF LATENT HEAT STORAGE (LHS) SYSTEM

The modelling of melting (charging) and solidification (discharging) in vertical cylindrical enclosures have been studied both experimentally [18; 20; 121; 130-134] and numerically [133; 135-140]. Most of these studies are limited to either the melting or solidification only. Sparrow et al. [135] modelled the melting in a vertical cylindrical enclosure with length-to-outer radius (L/r_o) ratios of 4 and 10, showing the effect of natural convection during melting. Due to the effect of natural convection in the melt, the heat transfer rate during melting in vertical cylindrical enclosures depends on the geometrical configuration. Wang et al. [140] developed correlations for the heat transfer coefficient in vertical cylinders with length-to-outer radius (L/r_o) ratios of ≤10 that can be used for design. Ismaila and Melo [137] investigated the effect of varying the geometrical configuration of the system on the heat transfer rate and developed correlations for L/r_o of up to 12 and r_a/r_o of up to 5. The results of Ismaila and Melo [137] and those of Wang et al. [140] are not in good agreement.

Most of previous studies on the numerical investigation of melting and solidification in cylindrical enclosures are for aspect ratios (L/r_o) of less than 20 and for low temperature applications (i.e. <100^oC). In practice, especially for solar thermal power generation applications, very large aspect ratios are used. The geometrical configuration and the properties of the PCM employed also affect the thermal performance of the system. In this chapter the modelling and simulation of an un-finned storage element was done using the melting and solidification model in the commercial CFD software, Fluent. The CFD melting and solidification model was first validated using experimental data and results from other models in the literature.

5.1 Modelling of Heat Transfer with Phase Change

The modelling of phase change phenomenon is complex, because of the non-uniform movement of the phase change interface; the presence of motion driven by buoyancy in the liquid region; volume expansion and the conjugate

heat transfer between the PCM and the HTF [141]. Stefan was the first to publish the mathematical solution of phase change in 1891 in a study to determine the thickness of ice in the polar region [142]. This solution is only applicable to simple geometries and boundary conditions; one dimensional problems of semi or infinite layer of PCM; and constant thermo-physical properties. Also the effect of buoyancy driven natural convection is neglected. Numerical methods must be employed to the solution of the governing equations during phase change.

5.1.1 Numerical Formulation

For any numerical method for the solution of phase change problem to be stable, it must accommodate the difference in the thermal properties of the PCM in the liquid and solid regions. Numerical approaches for solving heat transfer in phase change can be categorized into two:

- Moving grid temperature-based method
- Fixed grid enthalpy-based method

5.1.1.1 Moving Grid Temperature Based Method

This method is based on the Stefan formulation in which two governing equations based on one-dimensional conduction (one for each phase) and an interface equation (5.1) are solved numerically. Energy balance (equation (5.1)) must be satisfied at the phase front explicitly and as such requires the tracking of the phase change interface [141].

$$\lambda\rho_{pcm}\left(\frac{ds(t)}{dt}\right) = k_s\left(\frac{\partial T_s}{\partial t}\right) - k_l\left(\frac{\partial T_l}{\partial t}\right) \tag{5.1}$$

In the solution, the phase change interface is assumed to be stationary at each time step and the energy balance equations for each phase is solved. The temperature gradient in both the solid and liquid interface are computed and then used in the interface equation to determine the position of the phase change interface.

The advantage of this method is that the phase change interface position and flow structure are better predicted than in the fixed-grid enthalpy based method and requires less computing resources [141; 143].

The disadvantages of this method include [141; 144]:

- In order to obtain a numerical solution deforming (moving) grids or a transformed co-ordinate system has to be used to take care of the moving phase front. This makes its implementation more complex.
- It can only be used for phase change processes that occur in a single temperature (Isothermal) i.e. for pure substances.
- It may also be inappropriate for engineering applications in which the phase change process is just one of many components in the system.
- Difficult to extend to three dimensions.

5.1.1.2 Fixed Grid Enthalpy Based Method

The enthalpy approach was first proposed by Eyres et al.[145] in 1946, for the solution of the non-linearity encountered in the governing equations involving heat transfer [146]. The solution of phase change problem requires satisfying the non-linear evolution of the latent heat at the phase change interface. In this method the latent heat of fusion is accounted for, by using an enthalpy function in the governing equation. This means one equation is used for both the solid and liquid phases. This removes the need for satisfying the heat transfer conditions at the vicinity of the phase interface and as such a fixed grid can be used in the solution domain. The fixed grid method predicts the phase change interface and temperature distribution very well but the temperature at a grid point over time may oscillate [147]. In this method the phase change is assumed to occur over a small temperature range.

The enthalpy formulation of the governing equation for a conduction controlled solid to liquid phase change with constant thermo physical properties will thus be:

$$\frac{\partial \rho_{pcm} H(T)}{\partial t} = \nabla(k \nabla T) \tag{5.2}$$

$H(T)$ is the enthalpy representing the sensible and latent heat.

The advantages of the enthalpy method include [144; 148; 149]:

- It avoid discontinuities which can lead to numerical instability
- Fixed grid can be used as there is no need of tracking the phase front since the equation are based on the enthalpy not the temperature and the phase interface is implicitly considered (accounted for) in the equations.
- It can handle both single temperature (isothermal) and temperature range (mushy zone) phase changes.
- It can easily be extended to three dimensional problems.
- This method is easier to implement in existing software packages [150]

The enthalpy $H(T)$ from equation (5.2) can be obtained and implemented using two methods [151]:

- The equivalent heat capacity method
- The enthalpy function (Source based) method

5.1.1.2.1 The Equivalent Heat Capacity Method

In this method the latent heat of fusion during phase change is accounted for by using a modified specific heat which is calculated from the sensible specific heat and latent heat of fusion. Various methods of finding the modified specific heat have been proposed by many researchers. One of these is [147]:

$$c_{p,eq} = \begin{cases} c_{p,s} & if\ T < T_{solid} \\ \dfrac{\lambda}{T_{liquid} - T_{solid}} + \dfrac{c_{p,s} + c_{p,l}}{2} & if\ T_{solid} < T < T_{liquid} \\ c_{p,l} & if\ T > T_{liquid} \end{cases}$$

Thus the enthalpy is represented by:

$$H(T) = c_{p,eq}\partial T$$

The programming of this method is simple but care must be taken in choosing the mesh size, time step and the phase change temperature range to obtain a stable numerical solution.

5.1.1.2.2 Use of Enthalpy Function (Source Term Method)

The latent heat of fusion is accounted for, by using an enthalpy function representing both the sensible and latent heat, given by:

$$H(T) = h(T) + F\lambda \tag{5.3}$$

Where $h(T) = \int \ c_p \delta T$ is the sensible specific enthalpy and the liquid fraction (F) is given by:

$$F = \begin{cases} 0 & if\ T < T_{solid} \\ 1 & if\ T > T_{liquid} \\ \dfrac{T - T_{solid}}{T_{liquid} - T_{solid}} & if\ T_{solid} < T < T_{liquid} \end{cases} \tag{5.4}$$

Substituting equation (5.3) in the governing equation of heat transfer (equation (5.2)), the following is obtained (assuming that the density does not change with time):

$$\frac{\partial h_{pcm}(T)}{\partial t} = \nabla\left(\alpha \nabla h_{pcm}\right) - \rho_{pcm}\lambda \frac{\partial F}{\partial t}$$

The effect of the latent heat (λ) is represented as a source term in the governing equation. That is why this method is sometimes referred to as source based method.

5.1.2 Approaches to Modelling Latent Heat Storage (LHS) Systems

The approach that can be used for solving any phase change problem depends on the complexity and validity of assumptions that can be made. In some cases the effect of natural convection can be neglected and the solution is reduced to a conduction only problem. In systems where the effect of natural convection

cannot be neglected, two methods can be used to account for the convection effect in the liquid region [152; 153]:

- **Empirical**

  In this method, the problem is treated as a diffusion problem (assuming only conduction) and the effect of natural convection on the heat transfer in the liquid region is taken into account by use of an increased thermal conductivity in the governing equations.

- **Classical**

  This is by taking the full account of the convection in the liquid. This may involve deriving suitable governing equations for heat and mass transfer and development of a suitable numerical scheme.

In this chapter the classical method was used for the modelling and simulation of an un-finned storage element.

5.2 CFD Modelling, Verification and Validation

In this section, the melting and solidification model in the Fluent software was employed for the modelling of melting in vertical cylindrical enclosure and the results validated with the available experimental data of Jones et al. [139] and numerical results of Wang et al. [140] and Jones et al. [139].

5.2.1 The CFD Numerical model

The melting and solidification model in Fluent is based on the fixed-grid based enthalpy formulation (described in section 5.1.1.2) in which there is no need of tracking the phase change front explicitly. The phase change interface is represented by a mushy zone. This zone is modelled as a pseudo porous zone with the liquid fraction (porosity) varying from 0 to 1; zero is pure solid while 1 represents pure liquid.

The enthalpy formulation of the energy equation solved is:

$$\frac{\partial(\rho H)}{\partial t} + \nabla.(\rho \vec{v} H) = \nabla.(k \nabla T) + S \tag{5.5}$$

The specific enthalpy of the system is defined as the sum of the sensible specific enthalpy h, and latent specific enthalpy ΔH at any point:

$$H = h + \Delta H$$

ΔH has a value of zero when PCM is solid and the latent heat of fusion, λ when the PCM is completely liquid. During the melting process in the mushy zone, ΔH is defined as:

$$\Delta H = F\lambda$$

Where F has been defined in equation (5.4).

For substances in which the phase-change occurs at a particular temperature the equivalent heat capacity method (this has been described in section 5.1.1.2.1) developed by Voller and Prakash [152] is employed. Full details of the mathematical formulation of the melting and solidification model have been presented in Fluent [154].

5.2.1.1 The Bousinesq Approximation

The modelling of buoyancy driven flows require specification of density as a function of temperature. In order to increase the speed of convergence the Bousinesq approximation [154] is often used. In this approximation, a constant density is used in all the governing equations except in the buoyancy term (left hand side of equation (5.6)). This is approximated by the term in the right hand side in which the density is obtained by using the coefficient of thermal expansion and the temperature difference.

$$\left(\rho - \rho_{ref}\right)g \approx -\rho_{ref}\beta\left(T - T_{ref}\right)g \tag{5.6}$$

ρ_{ref} is the constant density and T_{ref} is the corresponding reference temperature. Thus the variable density ρ is eliminated from the buoyancy term. This approximation is valid for:

$$\beta\left(T - T_{ref}\right) \ll 1$$

5.2.2 The Experimental Set-up

Figure 5.1 shows the geometry and the boundary condition for the inward melting of the PCM in a cylindrical enclosure used by Jones et al. [139]. This was used for the validation of the CFD melting and solidification model in Fluent. The experimental set-up consists of a transparent hollow cylinder made of polycarbonate, in which the PCM (n-eicosane) fills the cylinder. The base and top are made up of acrylic. The need of transparency and removal of expanded melt prohibits the complete insulation of the top. A constant temperature boundary condition of 70^{o}C (T_H) was imposed on the exterior wall of the cylinder using a water bath; the bottom wall is kept at a temperature of 32^{o}C (T_B) and the initial temperature of PCM of ~23^{o}C. Table 5.1 presents the properties of the PCM (n-eicosane) and Table 5.2 presents the thermo-physical properties of the acrylic (bottom wall) and the polycarbonate walls (cylinder wall) used in the experiment.

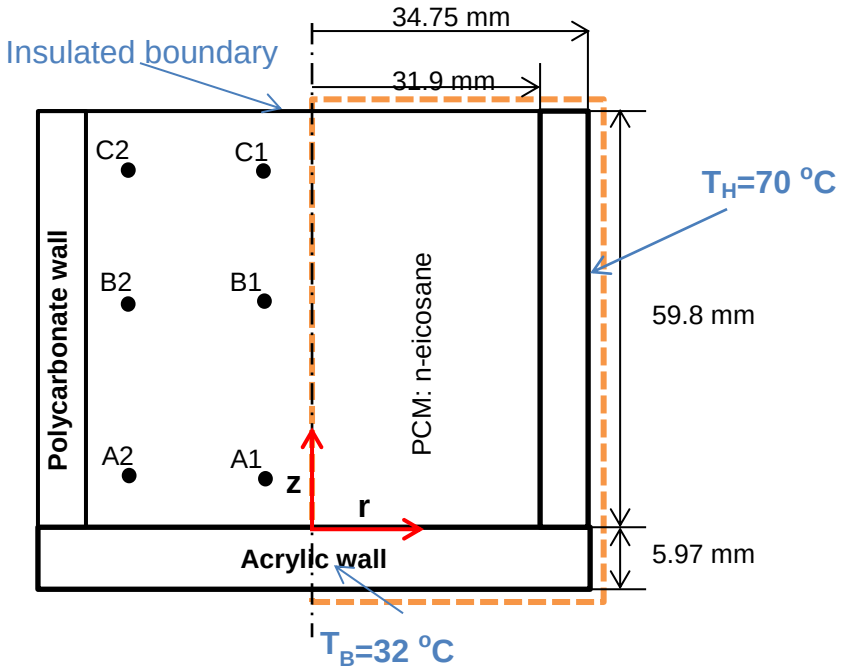

Figure 5.1 Geometry and boundary conditions for the experimental set-up for inward melting conducted by Jones et al. (2006)

Table 5.1 Thermo-physical properties of n-eicosane [155-158]

	Solid (25 ^{o}C)	Liquid (50 ^{o}C)
Density ρ (kg/m^3)	910	769
Thermal Conductivity k (W/mK)	0.423	0.146
Specific heat capacity c_p (J/kgK)	1926	2400
Thermal expansion coefficient β (1/K)	-	8.161 x 10^{-4}
Reference temperature T_{ref} (^{o}C)	-	50
Melting point T_m (^{o}C)	36.4	
Latent heat of fusion λ (kJ/kg)	248	

Table 5.2 Thermophysical properties of wall materials [139]

	Density (kg/m^3)	Thermal conductivity (W/mK)	Specific heat capacity (J/kgK)
Polycarbonate	1200	0.19	1260
Acrylic	1188	0.193	1420

Thermocouples were placed at various points in the phase change material. Table 5.3 presents the position of these thermocouples with reference to the cylindrical coordinate system presented in Figure 5.1.

5.2.3 CFD Set-up and Verification

5.2.3.1 CFD Set-up

The axisymmetric domain denoted by the dashed line in Figure 5.1 was considered. The PCM section was drawn and meshed. The thermal resistance in the walls was modelled assuming 1D conduction through the walls. This is implemented in Fluent by specifying a wall thickness and thermo-physical properties of the walls in the boundary conditions dialog box. A constant temperature boundary condition was specified at the cylinder and bottom walls.

Table 5.3 Thermocouple positions

	A1	B1	C1	A2	B2	C2
r (mm)	3.2	3.1	3.1	21.3	21.8	21.9
z (mm)	13.6	34.7	54.9	14	35.3	44.8

The top wall was assumed to be well insulated even though small heat loss is expected since in the experiment it was not possible to insulate the top properly. The second order upwind scheme was used for the transient discretisation; semi-implicit pressure-linked equations (SIMPLE) algorithm for pressure-velocity coupling and PRESTO for pressure correction. The density of the PCM was assumed to be constant (the liquid density at 50^{o}C was used) and the buoyancy effect was taking into consideration using the Boussinesq approximation, with a reference temperature of 50^{o}C. Fluent allow the specification of thermo-physical properties as functions of temperature. In this case, there is discontinuity in these properties from solid to liquid at the melting point. These discontinuities can cause numerical instabilities. In order to be able to specify different properties, it is assumed that during melting (i.e. in the mushy zone), the change of a property is linear (Figure 5.2). The thermo-physical properties of the PCM (n-eicosane) presented in Table 5.1 was used. The dynamic viscosity (in Pas) which is a strong function of temperature was modelled using the equation [157]:

$$\mu_{PCM} = (9 \times 10^{-4}T^2 - 0.6529T + 119.94) \times 10^{-3} \quad (5.7)$$

The numerical model requires that the melting occurs at a range of temperature. For pure substances the phase change occurs at a particular temperature. Therefore, a very small temperature difference between the start and end of melting, across the mushy zone thickness of 0.1 K was used.

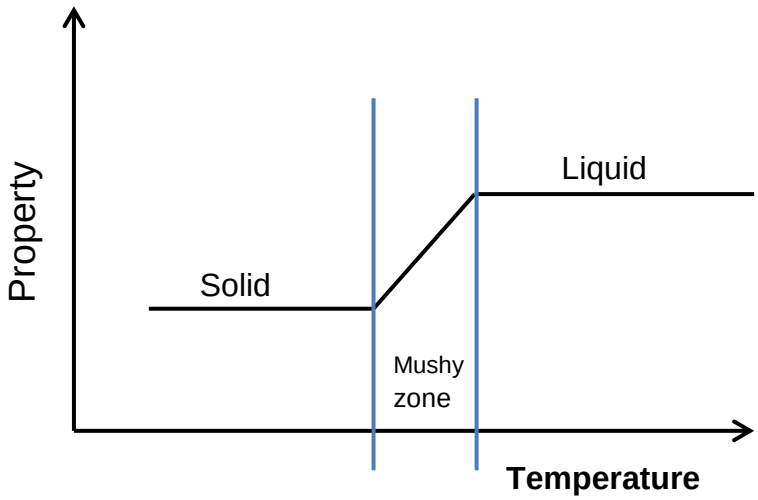

Figure 5.2 Variation of PCM thermo-physical property with temperature

5.2.3.2 Mesh Dependency Study

In order to determine the mesh size that will give accurate enough result with the least computational time, five meshes having 25 x 50 (1250 cells), 50 x 100 (5000 cells), 50 x 150 (7500 cells), 75 x 150 (11250 cells) and 100 x 200 (20000 cells) divisions in the radial and axial directions, respectively, were drawn. A time step of 0.05 s was used. Figure 5.3 presents the liquid fraction (ratio of the mass of melt to the total mass of the PCM in the domain) against time for four mesh sizes. It will clearly be seen the result becomes independent of the mesh from a mesh size of 11,250 cells.

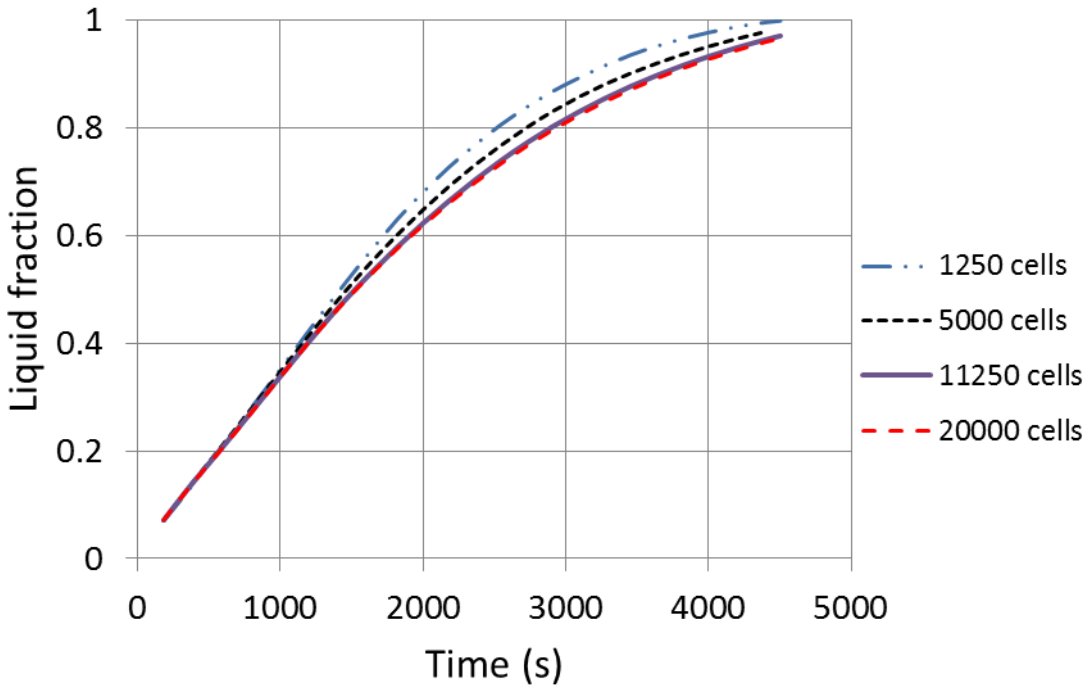

Figure 5.3 Liquid fraction as a function of time for different meshes

5.2.3.3 Time Step Convergence

Three time steps of 0.01, 0.05 and 0.1s were simulated in order to determine the effect of time step on the result and to know the best time step to use in order to have the least computational time that will give accurate enough results. Figure 5.4 presents the liquid fraction for the three time steps. The discrepancy in the three results is negligible and as such a time step of up to 0.1 s was found to be appropriate.

5.2.3.4 Transient Formulation

Comparison was made between first and second order implicit transient formulation in the solution of the governing equation. This is to know whether it is worth using second order in the simulation. Figure 5.5 shows the comparison and as such the use of the second order transient formulation does not produce any noticeable improvement in the result. Thus the first order transient formulation is sufficient.

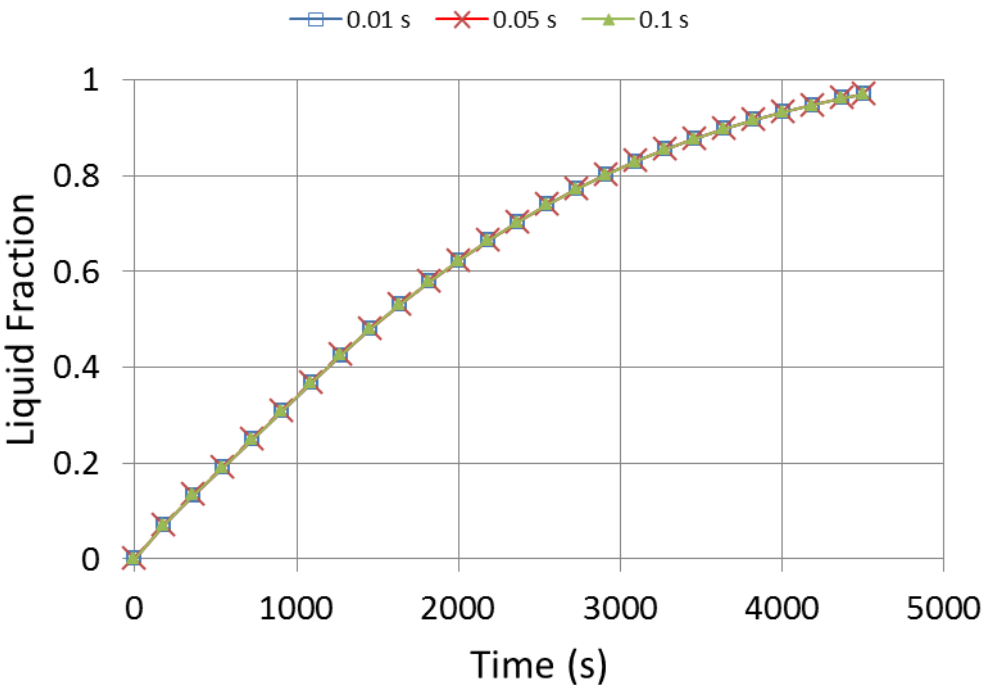

Figure 5.4 Time step convergence

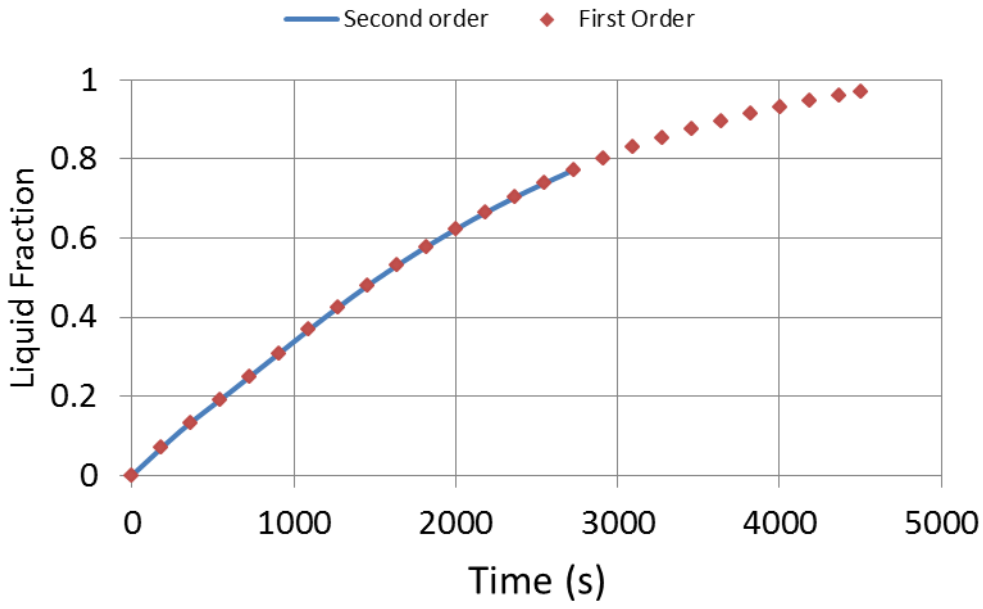

Figure 5.5 Comparison of first and second order transient formulation

5.2.4 CFD Validation

5.2.4.1 Validation with Experimental Results

Simulations were conducted using the mesh size of 11,250 cells, time step of 0.05 s and first order transient formulation. Figure 5.6 presents the comparison of the liquid fraction between the simulation and the experimental results. The maximum discrepancy between the predicted melt fraction and those obtained in the experiment is 7.5 %. Figure 5.7 presents the temperatures at the selected locations of the domain presented in Figure 5.1 and Table 5.3. The predicted temperatures when the PCM is solid (i.e. when conduction is the main mode of heat transfer) are higher than those obtained experimentally. This is because in the simulation, the liquid density of the PCM was used throughout. Since the solid density is higher than the liquid density, the heat capacity of the solid PCM is lower and thus the higher rise in temperature.

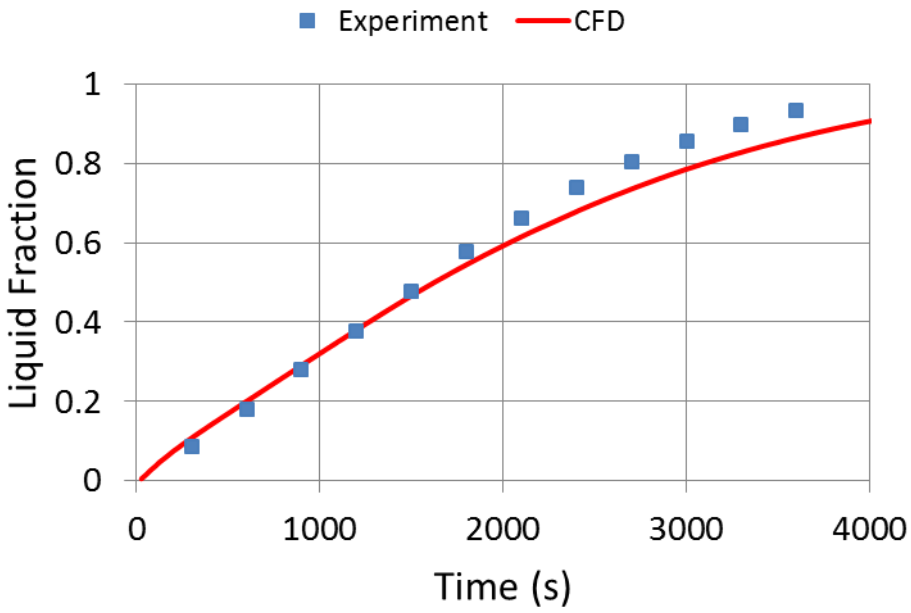

Figure 5.6 Liquid fraction comparison of CFD (using varying thermal conductivity and specific heat capacity) and experimental results

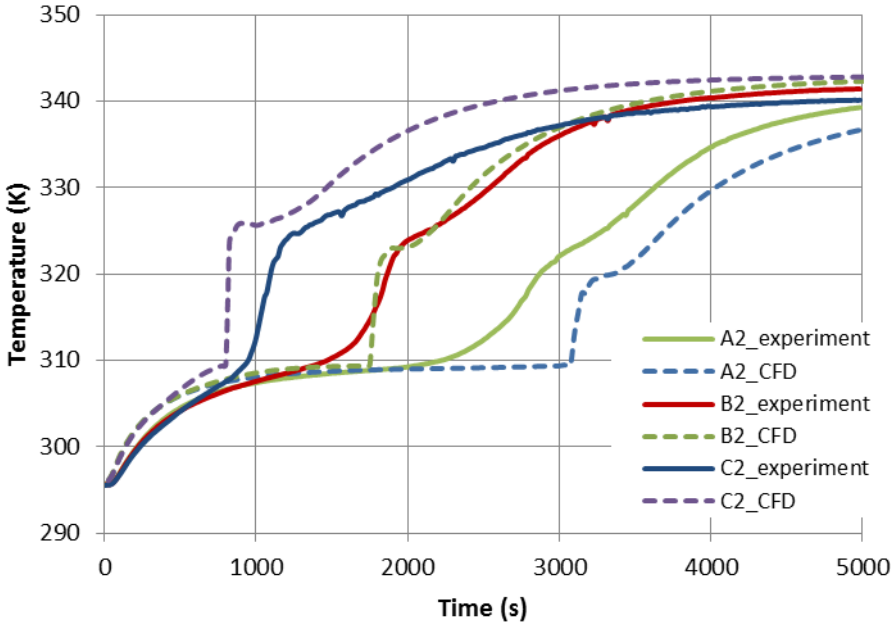

(a)

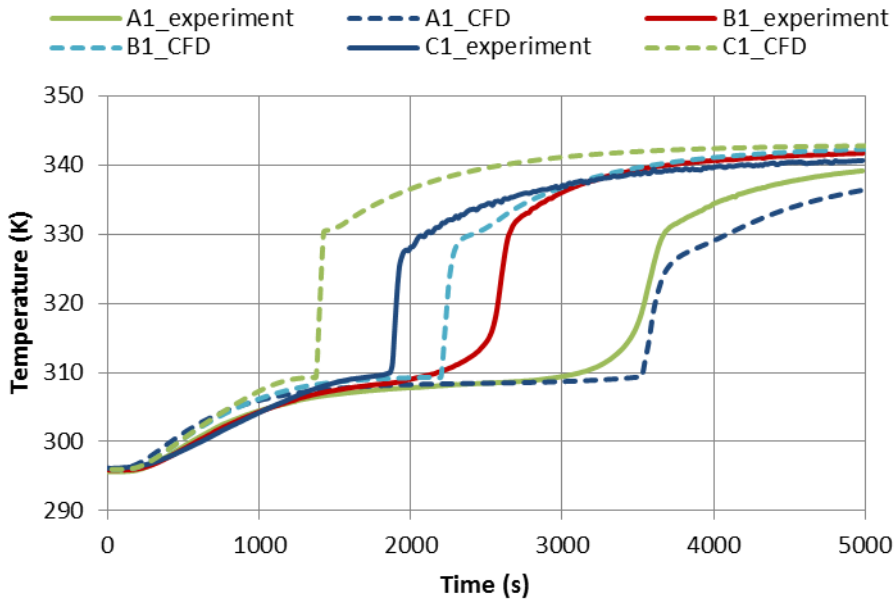

(b)

Figure 5.7 Temperature profile at selected locations for CFD and experiment (a) near to cylinder wall (b) near the centreline

In the Boussinesq model, the constant density of the liquid has to be used in order to appropriately predict the buoyancy effects in the fluid. In order to compensate for the smaller heat capacity of the solid PCM, Wang et al. [140] proposed the use of an effective specific heat $c_{p,eff}$ in the solid region defined by:

$$c_{p,eff} = \frac{\rho_s c_{p,s}}{\rho_l} \tag{5.8}$$

This was used to conduct simulations and the results are presented in Figures 5.8 and 5.9. Figure 5.8 indicates that there is no much difference in the predicted liquid fraction of the CFD simulations with actual and effective specific heats. This is expected since the specific heat only affects the solid region. Figure 5.9, however, shows that the use of effective specific heat predicts the temperature profile in the solid region more accurately.

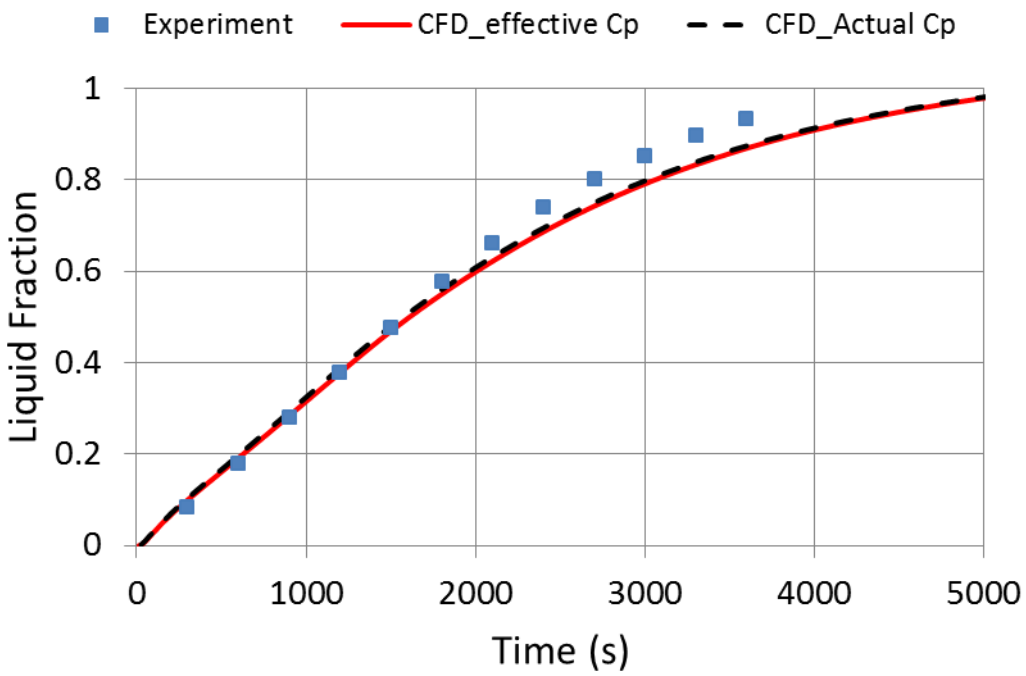

Figure 5.8 Effect of using effective specific heat on the predicted liquid fraction

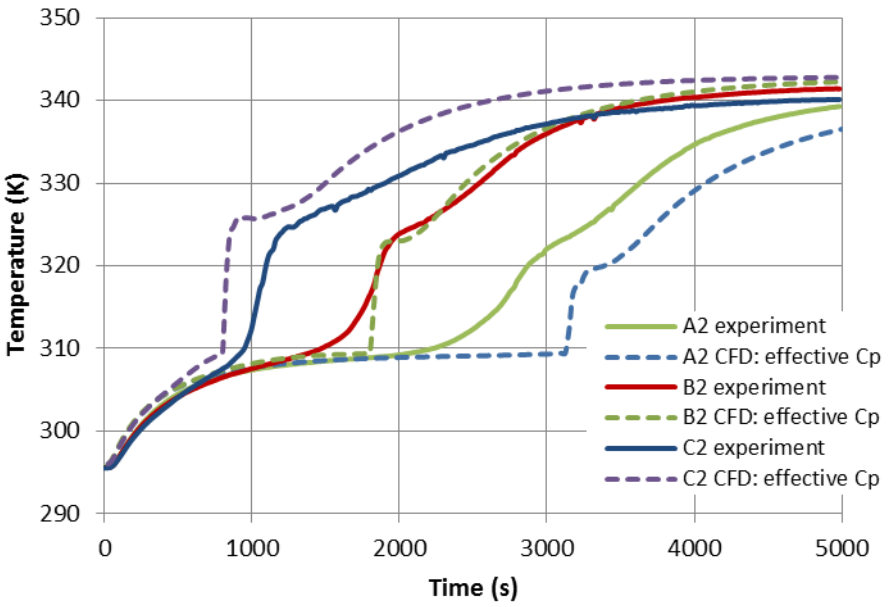

(a)

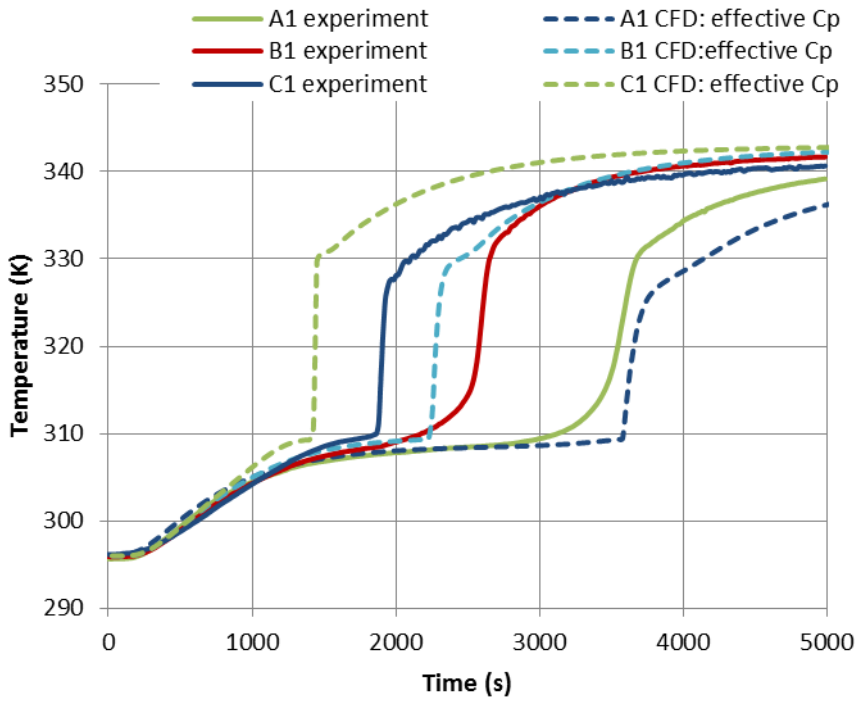

(b)

Figure 5.9 Comparison of Temperature profile at selected locations for CFD with effective specific heat and the experiment (a) near to cylinder wall (b) near the centre line

Figure 5.10 presents the melting interface comparison between the CFD modelling and experiment at three selected times. Since in the experiment the top wall was not insulated, heat will be lost through this wall, and, as such, it should be expected that the numerical liquid fraction will be higher than the experimental values. However, as the liquid fraction increases, air embedded in the solid PCM will be released and collected at the top forming a layer which will reduce considerably the rate of heat loss through the top —see Figure 5.10 (b) and (c).

The discrepancies in the liquid region which lead to lower liquid fraction when compared to the experimental results are due to:

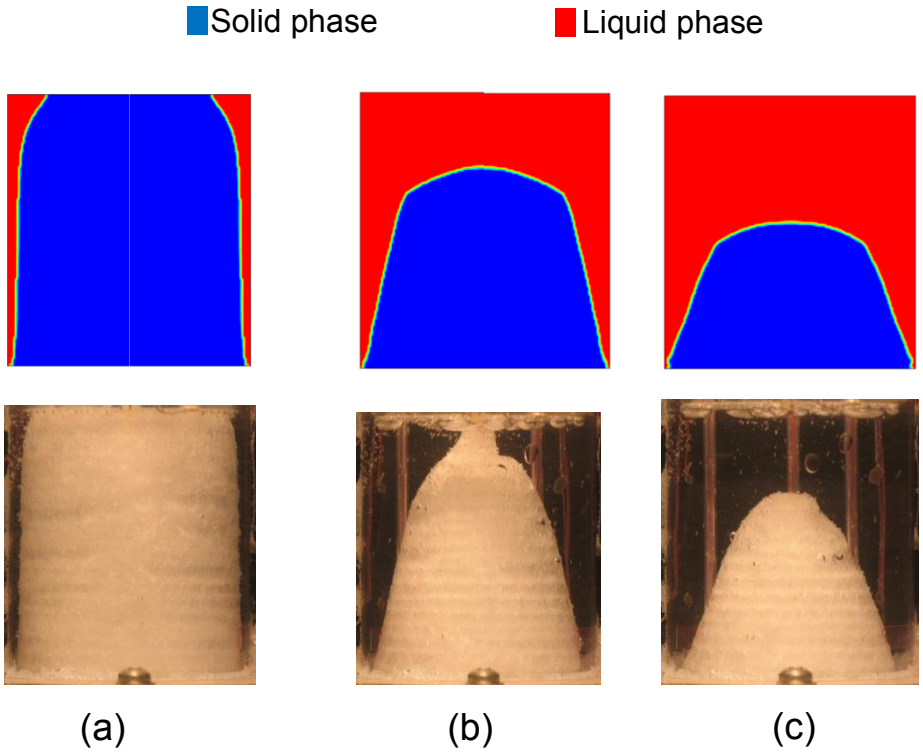

Figure 5.10 Comparison of melt Interface for the CFD and experiment at (a) 600 s (b) 1800 s and (c) 2400 s

- The assumptions made in the numerical modelling, especially the use of the Bousinesq approximation which assumes density to be constant in the energy equation. Refer to section 5.2.1.1 for details of the Bousinesq approximation.
- Difficulty in the imposition of an insulated boundary condition at the top and errors in the experiment; and the fact that the numerical results presents temperatures at specific points while the thermocouple may represent average temperature of many surrounding points.
- During the experiments, there was a net decrease in the mass of the PCM in the cylinder since the expanded melt was removed [139].
- The presence of air bubbles in the solid PCM which was confirmed visually and the fact that 8% increase in volume was obtained in the experiment even though the PCM (n-eicosane) has 18% volume change during phase change [158].

Finally, it can be concluded that the phase change model in Fluent is accurate enough for the modelling of melting and solidification in cylindrical geometries.

5.2.4.2 Comparison with other Numerical Simulations

Jones et al. [139] and Wang et al. [140] developed numerical models using the enthalpy based approach to the numerical formulation of phase change problems. They both validate their model results with the experimental values of Jones et al. [139]. In this section, a comparison of result obtained from the current CFD simulation and those obtained in these studies was conducted in order to compare the accuracy of the CFD model with the two numerical models.

Figure 5.11 shows the liquid fraction comparison between those obtained numerically from this work and the other two results. The maximum discrepancy in the predicted liquid fraction between this work and that of Jones et al. [139] and Wang et al. [140] is 2.2% and 5.7% respectively.

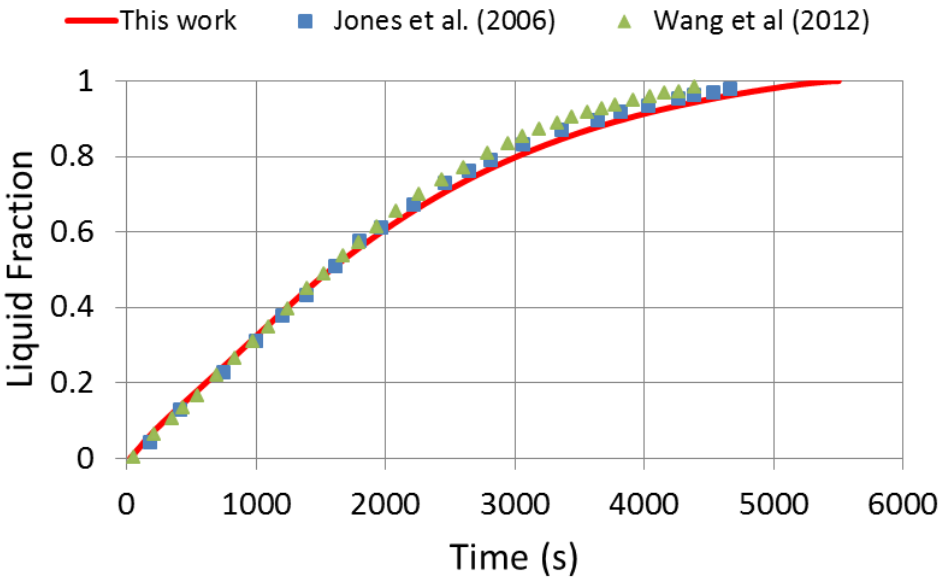

Figure 5.11 Liquid fraction comparison for numerical predictions of Jones et al. (2006), Wang et al. (2012) and this work

Figure 5.12 shows that the temperature distribution in the domain obtained from this work is in close agreement with those obtained by Wang et al. [140]. This thus shows that the result obtained from the Fluent CFD code closely agree with other numerical simulations produced by other researchers.

5.3 CFD Modelling of Single Storage Element

A single storage element is a shell-and-tube in which the HTF passes through the tube and the PCM is placed in the shell. In this section the modelling of the charging and discharging of a practical size storage element with aspect ratio (L/r_o) of 153 using sodium nitrate as the PCM and Therminol vp-1 as the HTF flowing inside the tube was conducted. The storage element has a HTF pipe outer radius (r_o) of 0.006 m, element outer radius (r_a) of 0.0325 m and length of 0.92 m. Thermo-physical properties of the PCM (sodium nitrate) and the HTF are presented in Tables 4.5 and 5.4 respectively.

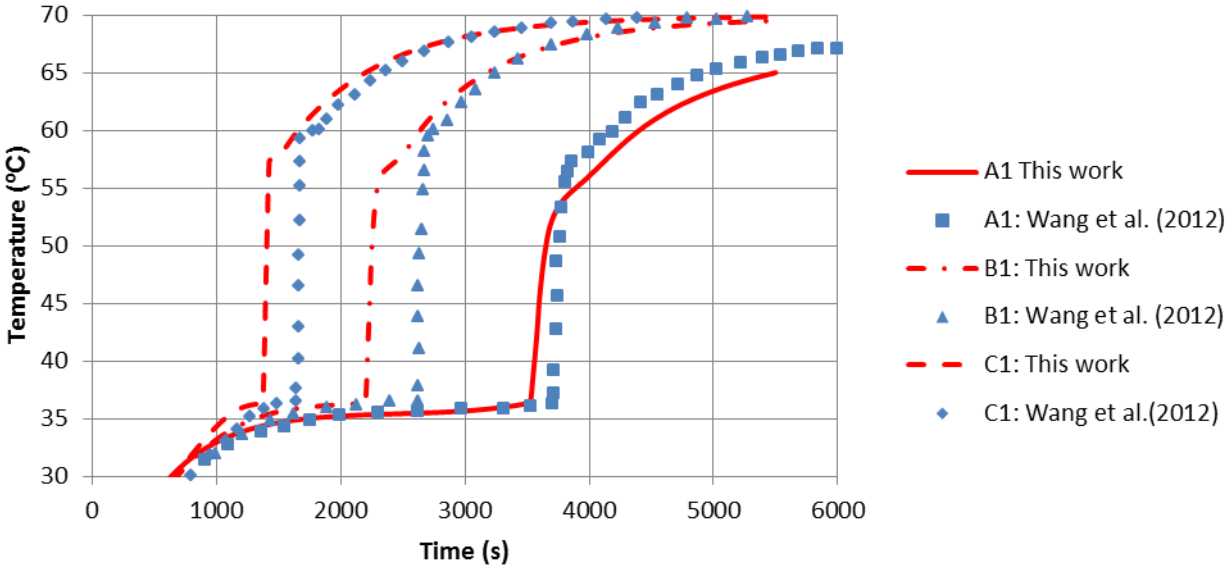

(a)

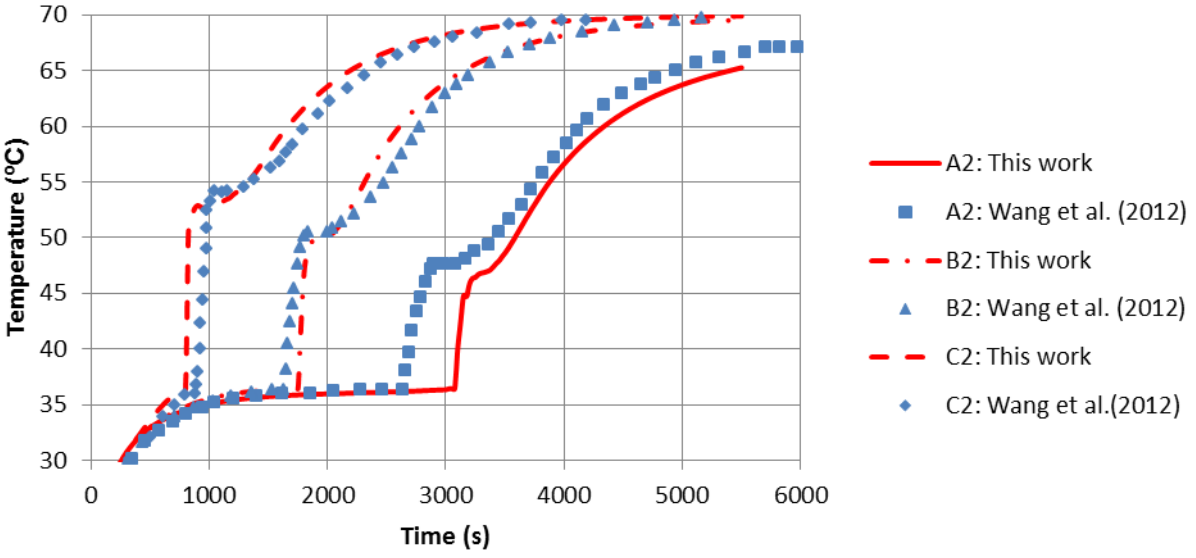

(b)

Figure 5.12 Comparison of temperatures at selected locations in the domain between the numerical result of Wang et al. [140] and this work.

Table 5.4 Thermophysical properties of Therminol VP-1 [159]

	@ **250 °C**	@ **400 °C**
Density (kg/m^3)	867	694
Specific heat (kJ/kgK)	2.181	2.628
Thermal conductivity (W/mK)	0.106	0.076
Dynamic viscosity (kg/ms)	2.88 x 10^{-4}	1.46 x 10^{-4}

5.3.1 Simulation Set-up

The single shell-and-tube element was modelled as an axisymmetric domain as shown in Figure 5.13. Figure 5.14 shows part of the meshed geometry. The thickness of the high thermal conductivity HTF pipe wall was neglected. The HTF inlet was divided into 30 cells so as to have a very fine mesh and the PCM section (annular gap) is meshed with square cells having a side length of 0.4 mm equal to that obtained in the model verification. This thus makes a total of about 151,800 and 66,700 cells in the PCM and HTF domains, respectively.

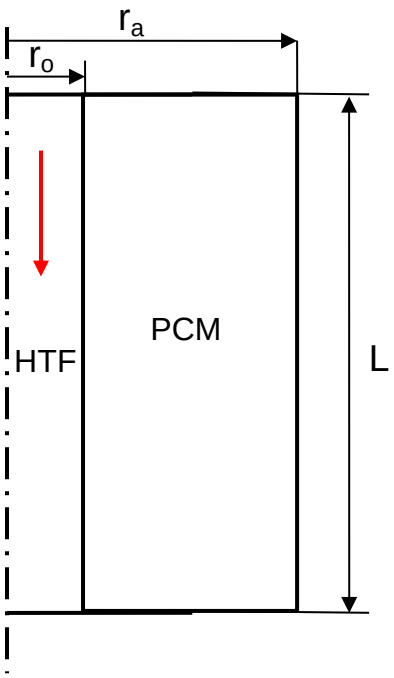

Figure 5.13 Geometry of the single shell and tube storage element

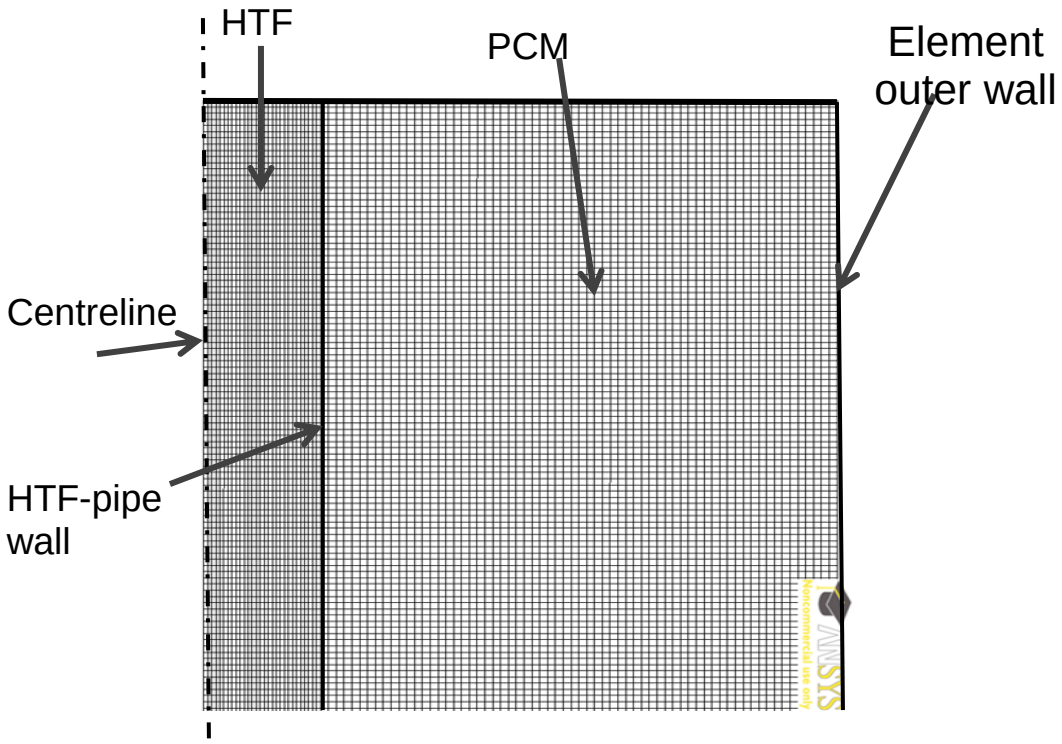

Figure 5.14 Part of the meshed axisymetrical domain

A constant HTF fluid density of 823 kg/m^3 was used and the viscosity, specific heat and thermal conductivity were assumed to vary linearly with temperature from 250^{o}C to 400^{o}C. The density of PCM (sodium nitrate) was assumed constant (the liquid density at melting point was used). Buoyancy effects in the momentum equation were taking care of using the Bousinesq approximation. The effective specific heat was used for the PCM in the solid phase. A mushy zone constant of 10^5 kg/m^{3}s was used. Initial PCM temperatures of 559.5 K and 600 K were used for the charging and discharging, respectively. The HTF inlet temperatures of 600 K and 559.5 K were considered for the charging and discharging processes, respectively. A relatively high HTF velocity of 1.0 m/s was used in order to guarantee a nearly constant temperature along the length of the HTF-pipe wall.

5.3.2 Charging (Melting)

5.3.2.1 Shell and Tube with Constant Wall Temperature

The use of a relatively high HTF velocity ensures an almost constant wall temperature. Simulations were conducted with the HTF flowing from top to bottom of the storage element.

By using a scaling analysis, Jany and Bejan [160] showed that four regimes exist during the melting of PCMs with Prandtl numbers >1.0 in rectangular enclosures:

- Pure conduction regime
- Conduction/ convection regime
- Pure convection regime
- Solid shrinking regime.

The existence of these four regimes has been shown experimentally by Jones et al. [139] for short cylindrical enclosures. Figure 5.15 presents a plot of the heat flux at the surface of the HTF-pipe as a function of time and Figure 5.16 presents the liquid fraction distribution in the annular gap at selected times. At the start of melting, the PCM in contact with the wall of the pipe, carrying the HTF, is solid at a temperature below the melting point and is heated up to the melting point and start melting. The distance between the wall and the phase-change interface is very small and thus there is no convection current in the melt. Thus, the mode of heat transfer between the pipe wall and the PCM is pure conduction. This makes the movement of the phase-change interface at this regime to be parallel to the HTF pipe wall. As the interface moves away from the wall of the HTF pipe, the heat flux decreases rapidly due to the increase in the melt thickness and the reduction of the driving temperature difference between the HTF and the PCM. A melt thickness is reached at which convection starts to take part due to the buoyancy-generated movement in the melt. At this stage, the heated liquid PCM moves to the top and transfers its thermal energy to the solid PCM causing deformation of the melt interface at the top (Figure 5.16a).

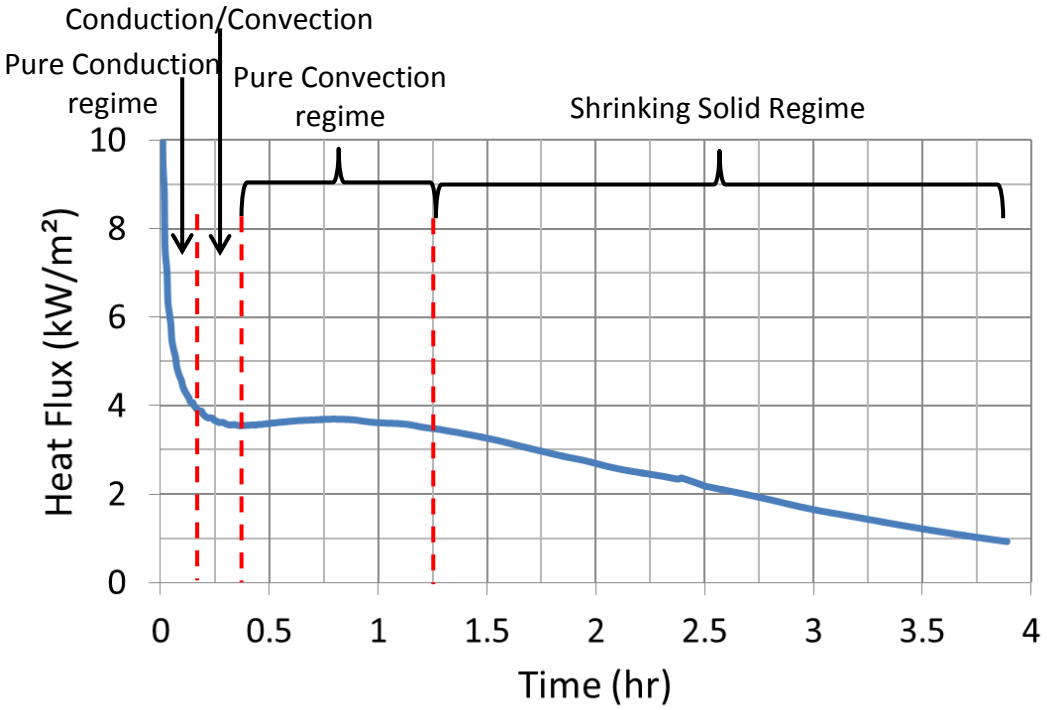

Figure 5.15 Variation of heat flux with time for melting in a single storage element with HTF velocity of 1.0 m/s and inlet HTF temperature of 600 K.

However, along most of the length of the pipe the interface is parallel to the pipe wall, indicating that conduction still plays a role and signifying a conduction/convection regime [160; 161]. The start of convection arrests the rapid decrease in the heat flux (Figure 5.15). With the domination of the convection mode of heat transfer, the heat flux then becomes almost constant and the interface deforms along the entire length of the HTF pipe (i.e. throughout the length of the storage) –Figure 5.16(b). This stage is termed the quasi-stationary melting [121; 130; 131]. It should be noted, however, that at this stage the heat flux increases slightly to a maximum and then decreases. The increase is caused by the increase in the buoyancy-driven currents due to the increase in the melt thickness.

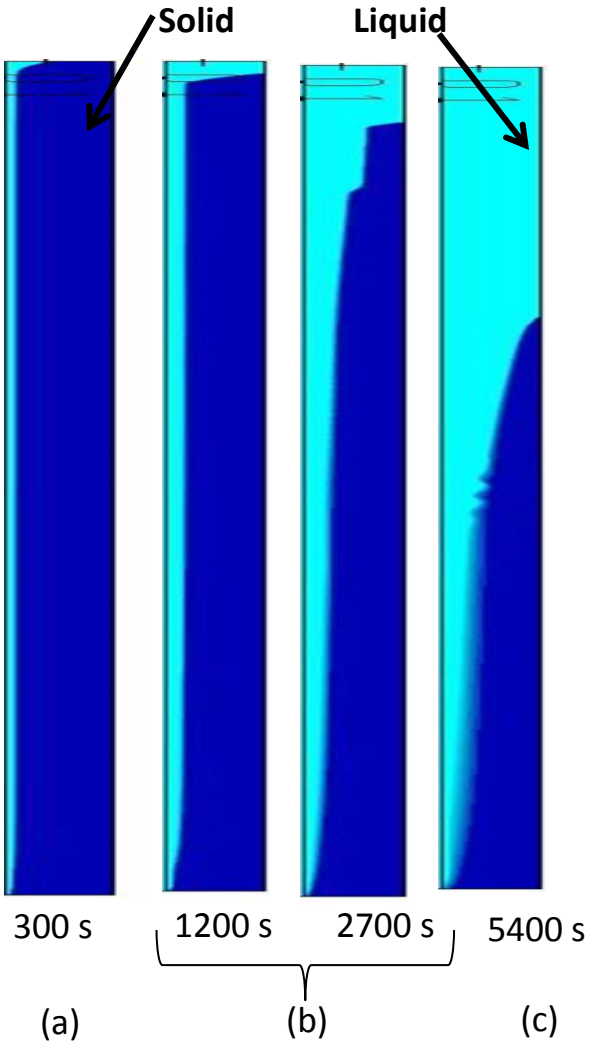

Figure 5.16 Heat transfer regimes during melting in cylindrical annular gap (a) mixed conduction/convection (b) pure convection (c) solid shrinking

The boundary layer thickness adjacent to the HTF pipe wall is very small. When the melt thickness reaches a certain critical value, the velocity of the convection current reduces and the boundary layer thickness adjacent to the HTF pipe wall increases. The decrease in the velocity of the convection current is caused by the reduction in the temperature gradient in the liquid PCM and the more resistance the convection current meet due to more exposed top and outer walls. These caused the decrease in the heat flux.

Once the end of the quasi-stationary melting regime is reached, the heat flux decreases continuously as the melt interface moves from top to bottom in an inclined way –Figure 5.16(c). This is because as the process proceeds, the top of the annular gap becomes filled with liquid PCM and the heat collected at the wall is first used for the overheating of the already melted PCM (much of which is at the top of the annular gap). This reduces the radial temperature gradient at the top of the storage element thus leading to reduction in the total heat transfer to the PCM. This is called the shrinking solid regime [160].

Figure 5.17 presents the predicted variation of the average temperature of the HTF pipe wall and the outlet temperature of the HTF with time during the charging process. The average HTF-pipe wall and outlet temperature are almost constant during the convection regime. Since the melting temperature is also constant this means that the heat transfer coefficient is constant and also further proves the existence of quasi stationary melting. Figure 5.18 presents the variation of the liquid fraction with time during the charging process showing that after 3 hours 80% of the PCM has already melted.

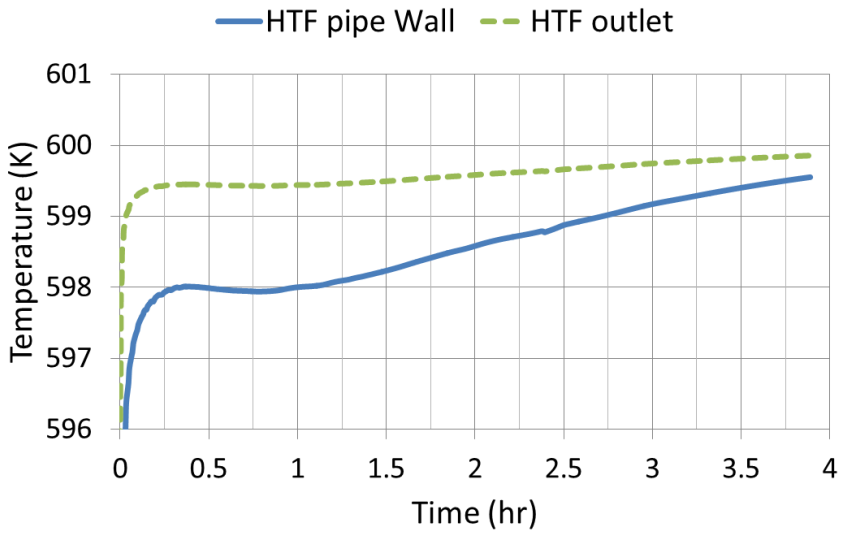

Figure 5.17 Variation of average temperature of the wall of the HTF pipe and outlet temperature of the HTF with time for melting in a single storage element with HTF velocity of 1.0 m/s and inlet HTF temperature of 600 K.

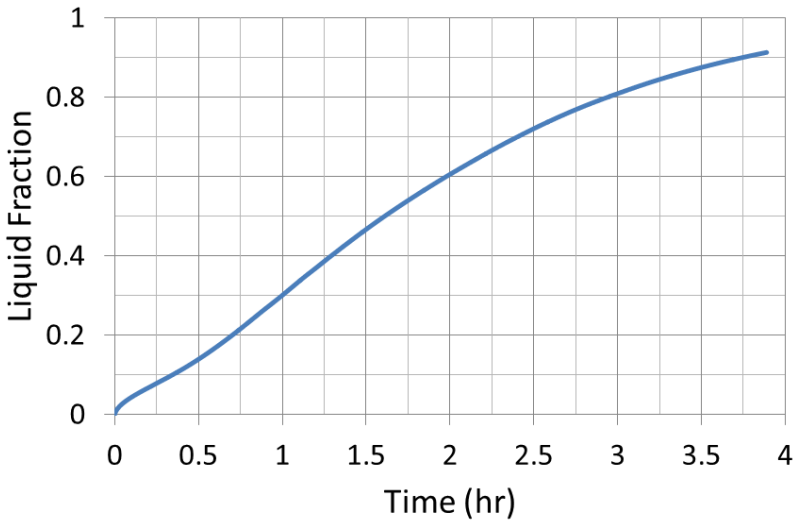

Figure 5.18 Variation of liquid fraction for melting in a single storage element with HTF flow velocity of 1.0 m/s, inlet HTF temperature of 600 K.

Attempts have been made by various researchers [20; 121; 137; 140; 162; 163] to develop correlations for the heat transfer coefficient during the quasi-stationary melting regime that can be used in the design of phase change storage systems. Most of these studies try to represent the Nusselt number (i.e. the dimensionless heat-transfer coefficient) as a function of other dimensionless parameters such as the Rayleigh number, Stephan number, Prandtl number and the geometrical configuration of the system. For a specific PCM, the heat-transfer coefficient and the heat flux during the melting process in a cylindrical annulus depends on the height, L, of the storage module (i.e. the length of the HTF pipe); the ratio of the annular gap radii, r_a/r_o; the HTF pipe outer radius, r_o, and the initial degree of sub cooling of the solid PCM. Such dependence on so many geometric parameters limits the applications of highly-empirical correlations developed.

5.3.2.2 Effect of the Driving Temperature Difference on the Quasi Stationary Heat Transfer Coefficient

In Section 5.3.2.1, the simulation was conducted with a very high HTF flow velocity (i.e. 1.0 m/s) in order to have an almost constant wall temperature along the HTF pipe length. This is not practical as it will lead to excessive pressure drop. In this section a realistic HTF flow velocity of 0.25 m/s was used in order to investigate the performance of the storage element and the effect of the driving temperature difference (i.e. difference between the average HTF temperature along the length of the HTF pipe and the PCM melting temperature). Three simulations (cases 1, 2 and 3) with driving temperature differences, during quasi stationary melting, of 25.44, 30.48 and 36.34 K, respectively, were conducted. Figure 5.19(a) present the variation of the average temperature of the HTF with time for each case. The average temperature of HTF is constant during quasi stationary melting. The higher the HTF average temperature, the higher the quasi-stationary heat flux —Figure 5.19(b), and the duration of the quasi-stationary melting reduces with the increase in driving temperature difference due to the increase in the rate of melting.

In order to see whether the heat transfer coefficient depends on the driving temperature difference, the overall heat transfer coefficient during the quasi-stationary melting for each case was calculated using the equation:

$$U_{qs} = \frac{q_{ave,qs}}{\Delta T} \tag{5.9}$$

Where $\Delta T = T_{htf} - T_m$

The results are presented in Table 5.5. The obtained overall heat transfer coefficient's dependence on the temperature difference, ΔT, is in agreement with the correlation developed by Michels and Pitz-paal [20].

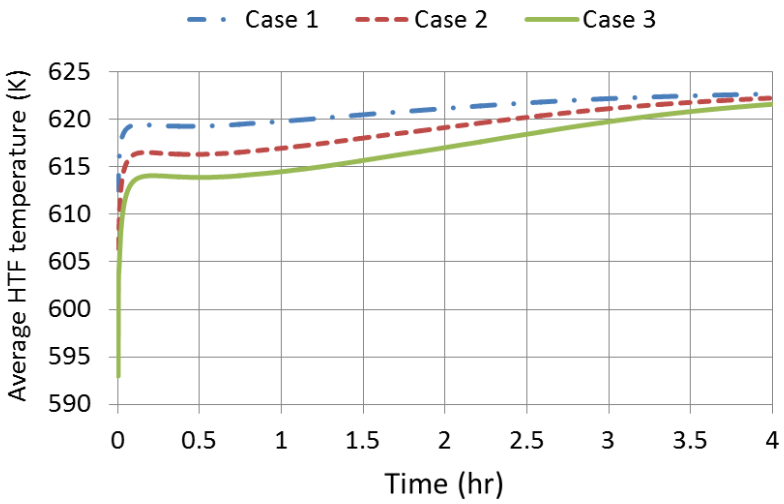

(a)

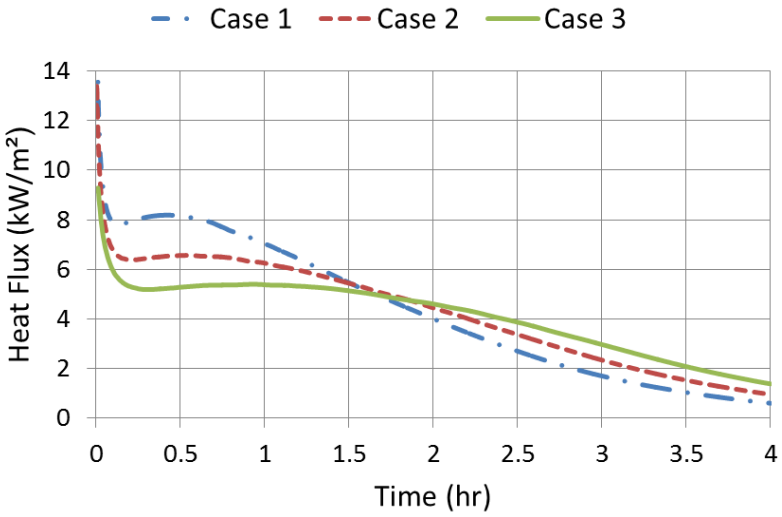

(b)

Figure 5.19 Variation of (a) HTF average temperature (b) heat flux, with time for single storage element with HTF flow velocity of 0.25 m/s.

Table 5.5 Heat transfer coefficient comparison during quasi-stationary melting

Case	Temperature difference (ΔT) (K)	Average heat transfer rate during quasi stationary melting (W/m^2)	Overall heat transfer coefficient (W/m^2K)
1	36.34	7834	216
2	30.48	6471	212
3	25.44	5290	208

5.3.3 Discharging (Solidification)

Simulations were conducted with simulation set-up presented in section 5.3.1 for the discharging of the storage. The HTF flows from the bottom to the top with flow velocity of 1.0 m/s to ensure an almost constant wall temperature.

Two cases of the discharging process were simulated: In the first one, the effect of buoyancy-driven motion in the liquid phase was considered (convection) and in the second, conduction was assumed to be the only mode of heat transfer. Figure 5.20 presents a comparison between the heat fluxes at the wall of the HTF pipe, the amounts of heat discharged and liquid fractions for the two cases. Figure 5.20(a) indicates that the heat flux for the conduction only case initially decreases faster than when the effect of buoyancy is included, suggesting that convection plays a role at this stage. But as the phase-change interface moves away from the HTF pipe wall (i.e. solid layer thickness increases), the effect of convection dies out and the heat fluxes for the two cases are almost the same, indicating that conduction is the main mode of heat transfer. Therefore, convection plays a role only at the initial stage when the solid layer thickness is very small. But as the solid layer thickness increases, the effect of convection vanishes. The difference between the amounts of heat discharged after three hours is only 46.9 kJ; the heat discharged with conduction only simulation is 6% less than that that when convection was taken into account (Figure 5.20(b)). Thus convection can be neglected during discharging of the thermal store.

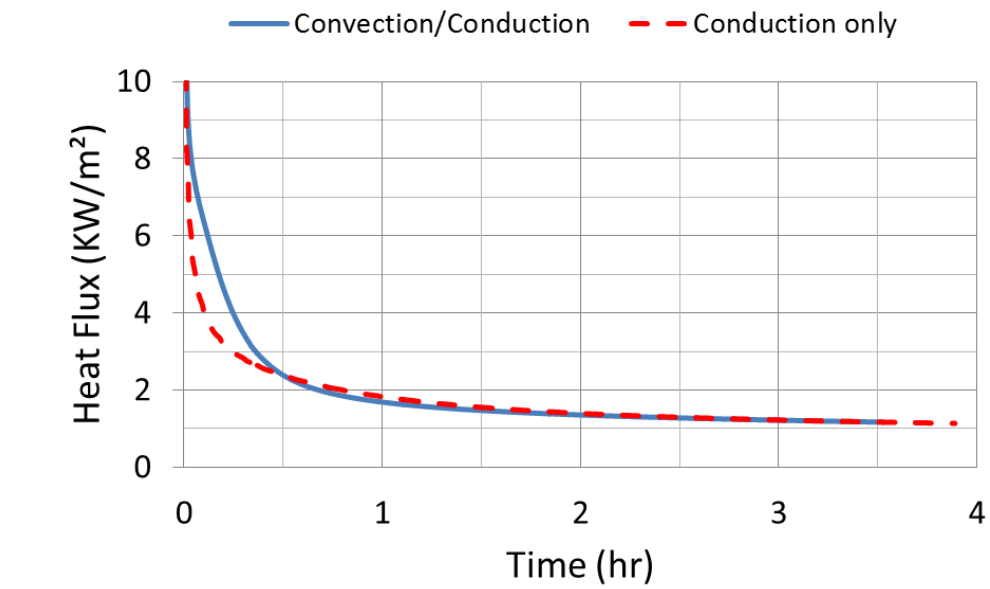

(a)

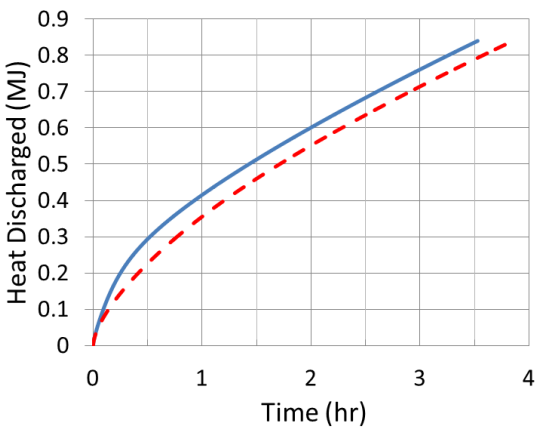

(b)

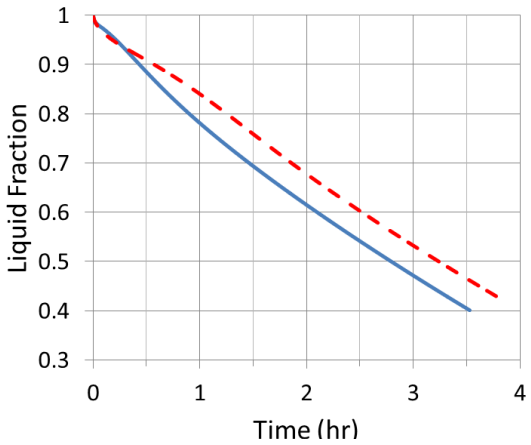

(c)

Figure 5.20 Variation of (a) liquid fraction (b) heat discharged and (c) heat flux with time for the discharging of a single storage element using HTF flow velocity of 1.0 m/s

5.3.4 Charging and Discharging Performance Comparison

Figure 5.20(c), indicates that 47.15% of the liquid PCM has not change phase after three hours of discharging. In comparison, in the charging process (Figure 5.18), about 80% of the PCM has changed phase after 3 hours. The charging is a lot faster than the discharging due to the fact that during charging (melting of PCM) convection enhances heat transfer and during discharging (solidification of PCM), convection has a very little effect and the heat flux reduces due to the increase in the thickness of the solid layer.

5.4 Conclusions

The Fluent CFD melting and solidification model was validated using the well-controlled experiments and documented experimental results available in the literature for the melting of n-eicosane paraffin in a vertical cylinder. Maximum deviation of the predicted melt fraction of 7.5% was obtained, which is smaller than those obtained by Shmueli et al. [164] by 4.5%. Comparison of temperatures at various locations and the melt interface shape at various times in the domain gave reasonable agreements with experimental data. The results obtained compared reasonably well with those obtained using other numerical codes. This shows that the Fluent melting and solidification model is capable of producing accurate results in the modelling of phase change in vertical cylinders. The use of effective heat capacity proposed by Wang et al. [140] was found to increase the accuracy of the predicted temperature distribution below melting point but has a negligible effect on the melt fraction.

The dependency of the dimensionless heat transfer coefficient on various geometrical parameters has limited the practical application of developed correlations in the literature. The numerical simulations for the charging and discharging of a practical size single shell-and-tube storage element, with a height L of 0.92 m and an outer radius r_a of 0.0325 m, has been conducted. During charging (melting) the presence of the four heat transfer regimes classified by Jany and Bejan, [160] for rectangular enclosures were also observed for cylindrical annular enclosure. The effect of natural convection cannot be neglected during melting. The utilization factor (i.e. the percentage of

PCM that undergoes phase change) during a specified time interval, which is a measure of the actual capacity of the LHS system, is lower during discharging and thus design of such system must be based on the discharging process. During discharging, conduction is the main mode of heat transfer and thus models that neglect the effect of convection can predict the amount of heat discharged with a maximum discrepancy of 6%.

6 CFD MODELLING AND SIMULATION OF FINNED LATENT HEAT STORAGE (LHS) SYSTEM

This chapter begins by first reviewing the heat transfer enhancement methods suitable for use in the temperature range of the parabolic-trough solar power-generation plants and justifying the selection of the use of finned systems. Considering the slower discharging process, the heat transfer enhancement produced by different fin configurations was obtained in order to determine the best fin configuration. For the selected fin configuration correlations for the heat transfer coefficient that can be used for the design of finned LHS systems were developed.

6.1 Heat Transfer Enhancement in Latent Heat Storage Systems

During discharging, in a LHS system, a solid layer of the PCM forms around the HTF pipes which insulates the pipe leading to decrease in heat transfer. Michels and Pitz-Paal [20] demonstrated that increasing the thermal conductivity of the PCM in both phases from 0.5 to 2 W/mK reduced the amount of PCM required in a five stage cascade ($NANO_3$, KNO_3/KCl, KNO_3, KOH and $MgCl_2$/KCl/NaCl) by ~40% and makes the amount of storage material required for an 875 MWh_{th} capacity storage system to be 15% less than that of a molten-salt two-tank system in the Andasol 1 plant. The amount of the storage material forms part of the major cost of the two-tank system. The increase in thermal conductivity will also reduce the number steel HTF-pipes required. Steinmann et al. [22] demonstrated that ~50% reduction in the number of pipes required is obtainable, if the thermal conductivity in both phases of the PCM is increased from 1 W/mK to 10 W/mK.

Various methods can be used to increase the thermal conductivity of PCMs. These can be broadly classified into three:

- Use of composite materials also known as micro encapsulation
- Use of extended surfaces
- Use of thermo syphon pipes

These methods have been studied extensively for low temperature applications [165; 166]. In the following sections, these methods of heat transfer enhancement for high temperature applications were discussed.

6.1.1 Composite Materials (Micro Encapsulation)

This entails mixing the PCM with a material having very high thermal conductivity to form a composite material with higher thermal conductivity than the original PCM. In a typical storage module the composite is produced as a solid with holes through which the HTF pipes will pass (Figure 6.1). This method does not require an encapsulation container.

Various methods can be used for the production of PCM composites:

- Infiltration or impregnation in which the PCM is absorbed into the pores of a porous high conductivity material such as expanded graphite to form a composite [167; 168].
- Dispersion which involves mechanically mixing the solid PCM with powder of a high conductivity material and then melting it to form a composite or dispersing the high conductivity material powder in melted PCM [25; 169; 170].
- Electro-spinning involves the production of nano/micro fibres of a PCM metal composite by using electromagnetic field [171].
- Cold compression involves compressing a mixture of the solid PCM with the high thermal conductivity material powder at ambient temperature to form a solid composite. This method do not require thermal energy during production and there is no corrosion of equipment [25]

The infiltration method is the most widely used technique and the most suitable high conductivity material for use is expanded graphite since it is chemically stable, have high thermal conductivity and high porosity [15].

Figure 6.1 Micro encapsulated PCM [23]

The production of PCM composites for high temperature applications have been conducted by various researchers. Morisson et al. [172] produced PCM/CNEG composites using an eutectic mixture of KNO_3/$NaNO_3$ as PCM by using the infiltration method without any significant loss in latent heat of the PCM. Table 6.1 presents the axial and radial thermal conductivities obtained for different percentage mass of CNEG in the composite. The use of 3.96% by mass of expanded graphite resulted in 74% reduction in the number of steel HTF-pipes required, compared with a similar storage using the pure PCM.

Table 6.1 Thermal conductivities of PCM/Graphite composites produced by Morrisson et al. [172]

Composite composition (% CEG)	Thermal conductivity (W/mK)	
	Axial direction	Radial direction
0	0.8	0.8
3.96	1.6	4.1
5.27	2.6	5.65
7.35	2.8	8.2

Pincemin et al. [26] used the infiltration method for the production of a $NaNO_3/KNO_3$-ENG composite by soaking of the graphite matrix in the melted PCM under atmospheric and vacuum conditions, at industrial and lab scale. After 15 hours of soaking, ~40% by volume of the graphite pores is empty. This thus shows the inefficiency of the infiltration method. Similarly, Steinmann et al. [21] asserted that it is impossible to infiltrate graphite with inorganic-salt PCM.

The cold compression method has also been used in the development of composite material using $KNO_3/NaNO_3$ as PCM and expanded graphite by Pincemin et al. [25] and Steinmann et al. [21]. Pincemin et al. [25] result showed that a composite with 20% ENG has a radial thermal conductivity of 40 W/mK and 22 W/mK at 47^oC and 200^oC respectively. This is about 31 times increase in the thermal conductivity at 200^oC compared to that of the pure PCM. Reduction in the specific latent heat was also observed. Steinmann et al. [21] tests showed that separation between the graphite and the salt (PCM) occurs during cyclic operation. This may be due to salt expansion; moisture and impurities in the PCM; and good wettability of the PCM with metals meaning high propensity for the occurrence of creeping.

The dispersion method has also been tried by putting graphite flakes of different sizes in molten $KNO_3/NaNO_3$ [26]. Axial thermal conductivities ranging from 3.5 to 9 W/mK were obtained for 20% by weight of graphite corresponding to a 14 times increase at room temperature. The difference in thermal conductivity was due to the size of the flakes. Reduction in the latent heat of between 5% and 28% depending on the flake size was also observed. The thermal conductivity were found to reduce with increasing temperature by 2.25 %/^oC. Thus at 220^oC which is the melting point of the PCM, the thermal conductivity was 6 W/mK for 20% by weight graphite.

In summary, the infiltration, cold compression and dispersion methods have all been tested and results clearly showed that the use of graphite to form PCM composites improves the thermal conductivity of the resulting composite. The higher the graphite content, the higher the thermal conductivity of the composite. There is a reduction in the thermal conductivity with increase in

temperature leading to requirement of higher amount of graphite (more than 10%). For cost effective composite material, the mass fraction of graphite is limited to 5% [21; 23]. Reduction in the specific latent heat was observed and separation of the PCM from the graphite occurred during cyclic operation. Thus the use of micro encapsulation with nitrate-salt PCM is not a viable heat transfer enhancement method in high temperature LHS system.

6.1.2 Extended Surfaces

6.1.2.1 Macro encapsulation

Macro encapsulation involves enclosing the PCM in small casings which can either be spherical or cylindrical in shape. Cylindrical containers are easier to manufacture. These small casings are then arranged in a vessel filled with pressurized water/steam or the HTF. Characteristic diameters of these casings range from 5 to 20 mm. To ensure that these capsules can survive the corrosion by the PCM for at least 10 years, a minimum of 1 mm wall thickness casings must be used. Since the PCM expands during melting by about 10%, space must be provided for this expansion by adding gas to the capsule. Cylindrical capsules of 0.5 m length and 7.5-12.5 mm radius range, using a mixture of KNO_3-$NaNO_3$ as the PCM, have been prepared and tested in DLR under the DISTOR project (Figure 6.2). Many charging and discharging cycles were achieved showing the feasibility of the method. It was found out that a lot of steel material (almost equal to the mass of the PCM) is required, manufacturing the capsules is complex and the proportion of PCM in the system is <40%. This makes it very expensive and not a promising option [21; 23].

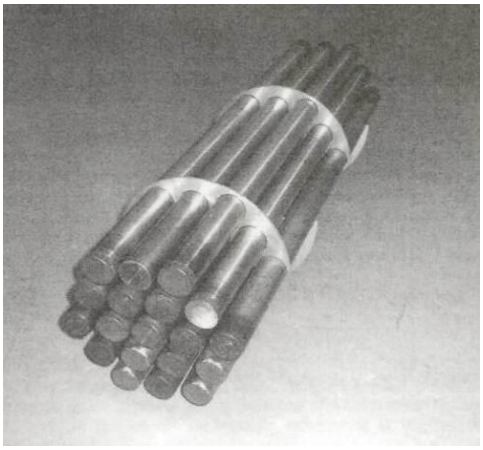

Figure 6.2 Macro encapsulation of PCM [23]

6.1.2.2 Sandwich Concept

The use of fins, which is referred to as the sandwich concept, is the most promising option of all the heat transfer enhancement methods for temperatures >200^{o}C [21; 126]. The common configuration of circumferential fins mounted on the HTF pipes is employed. Various materials with high thermal conductivity have been considered for the fin material, such as stainless and carbon steel, graphite, copper and aluminium. Graphite and aluminium are regarded as the best options out of these because of their high thermal conductivity and low specific cost [23]. Graphite is chemically stable for temperatures up to 250^{o}C in nitrate and nitrite salts and when in contact with steel pipes galvanic corrosion does not occur [22; 23]. Three experiments have been conducted in the DISTOR I, PROSPER and DISTOR II projects using fins made up expanded graphite foil for thermal storage capacities of 3.5, 7 and 55 kWh_{th}, respectively. Table 6.2 presents the details of the three storage units. Many charging and discharging cycles were achieved without any graphite degradation, thus proving the feasibility of the concept [22]. In the PROSPER a storage temperature of 155^{o}C was used for heating of saturated water from 125^{o}C to superheated steam at 145^{o}C (at the beginning of discharging) and saturated steam at 125^{o}C (at the end of discharging).

Table 6.2 Test storage modules using graphite fins [22]

Project	Maximum Power (kW)	Capacity (kWh)	PCM	PCM Mass (kg)	Melting temperature (^oC)	HTF
DISTOR I	2	3.5	$KNO_3/NaNO_3$	130	225	Thermal oil
PROSPER	15	7	$KNO_3/NaNO_2/NaNO_3$	400	145	Steam from test facility
DISTOR II	100	55	$KNO_3/NaNO_3$	2000	225	Steam from parabolic trough

Thermal power of ~8 kW_{th} was achieved for most part of the process. In the DISTOR II, average power of 90 kW_{th} and 35 kW_{th} were obtained over a period of 1 hour for the charging and discharging respectively [21].

Laboratory test have also been conducted at DLR in 2008 with a 37 MJ capacity module having seven finned HTF-pipes with a height of 1.4 m and diameter of 0.308 m using sodium nitrate, having melting temperature of 306^oC (Table 6.3). Aluminium fins were used since graphite is not compatible with the nitrate salt. The module was tested for more than 4000 hours corresponding to 168 charging/discharging cycles (3.5 hours charging and 2.5 hours discharging) for temperatures between 290 and 330^oC [22]. In a typical cycle, 7.87 kWh_{th} and 7.20 kWh_{th} were stored and discharged respectively. During discharging an average specific power of 42.5 kW_{th}/m^3 was achieved. Degradation in melting temperature was not observed and the aluminium fins did not show any sign of degradation [22; 126]. Thus Aluminium is chemically stable in nitrites and nitrates for temperatures up to 330^oC. A 700 kWh_{th} capacity LHS module using $NaNO_3$ as PCM and aluminium fins has been constructed and tested successfully in a three stage storage system suitable for DSG plants [173; 174].

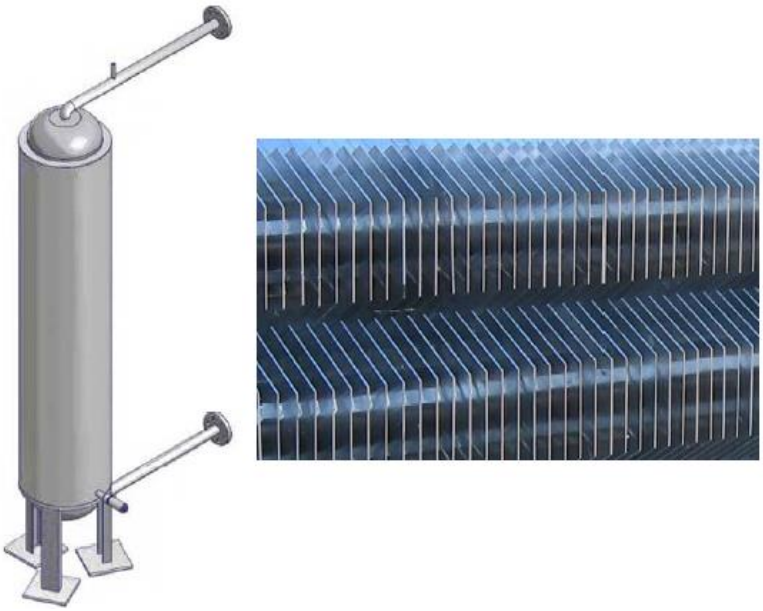

Figure 6.3 Test storage module using $NaNO_3$ PCM showing the full module and the fins [126]

It can be concluded that the sandwich concept using graphite fins at temperatures below 250^{o} and aluminium fins in the temperature range of 250-330^{o}C is a feasible way of solving the problem of the low thermal conductivity of PCM.

6.1.3 Heat Pipe/Thermo syphon

Heat pipe consist of a tube closed at both ends with a small amount of working fluid inside the tube. The interior of the tube is lined with a wick that transfers liquid due to capillary action. Figure 6.4 presents a schematic diagram showing the working principle of a vertical heat pipe. The end of the tube where heat is applied is called the evaporator and when heated the working fluid vaporizes and moves to the other end of the tube. At this end of the heat pipe, the heat of vaporization is released through the tube wall causing the working fluid to condense into liquid. The wick then transports the liquid back to the evaporator and the cycle is repeated. For vertical tubes the liquid can also be transported by gravity (there is no need of a wick). Since latent heat of evaporation is used, high heat transfer rates can be achieved using a small temperature difference

(almost isothermal). Heat transfer rates improvements of up to 90 times greater than bare copper tubes have been obtained for copper-water heat pipes in cooling of electronic devices [175].

Heat pipes have been applied in LHS systems for low temperature (<100^{o}C) applications [176-178]. By employing a thermal network model, Shabgard et al. [29] showed that heat pipe has the potential of enhancing the heat transfer rates in large-scale LHS system for parabolic-trough plants using synthetic oil as HTF. Economic analysis conducted by Robak et al. [28] showed that 15% potential decrease in capital cost is obtainable compared to the commercially available two-tank system. However, there is still the need for the demonstration of the real feasibility of such system and the long term corrosion and stability of the welded heat pipes.

Using the principle of thermo syphon Adinberg et al. [179] developed a novel concept called the RHTS concept in which a secondary-HTF just like the

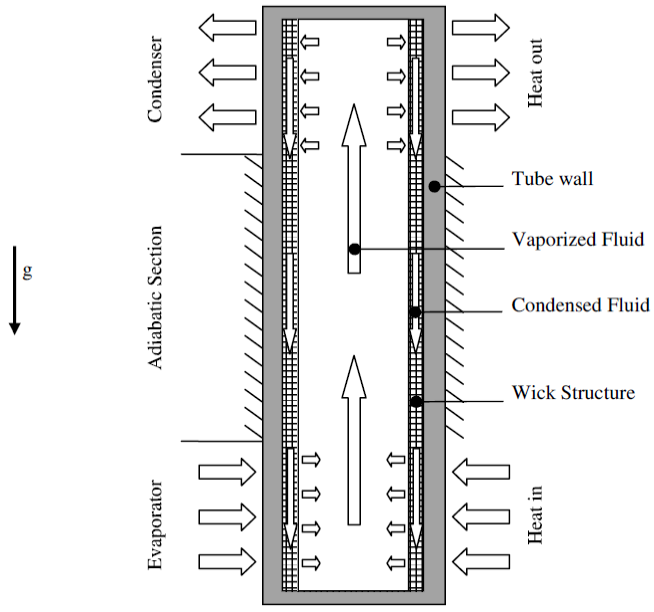

Figure 6.4 Heat pipe working principle [178]

working fluid in the thermo syphon is used for the exchange of thermal energy between the PCM and the HTF (water) for the production of superheated-steam in the 350-400^{o}C temperature range. Zinc-tin alloy with a melting temperature of 370^{o}C was used as the PCM. Figure 6.5 presents the schematic diagram of the RHTS system consisting of two heat exchangers for charging and discharging. The PCM is situated at the middle with embedded vertical channels linking the bottom with the top. During charging, steam is passed through the bottom heat exchanger with is situated in a pool of the secondary HTF, thus boiling the secondary-HTF leading to its evaporation through the channels in the thermal storage compartment. As the secondary-HTF pass through the compartment, the solid PCM is heated and it melts leading to the condensation of the secondary HTF back into the pool. During discharging, water is converted to steam in the top heat exchanger (steam generator) by evaporation of the secondary-HTF by the already heated PCM. The chemical stability and thermal cycling of the HTF and Therminol VP-1 (secondary-HTF) has been tested successfully and simulation of a 12 MW_e pilot plant with integrated storage showed the feasibility of the system. The proposed PCM (Zn-Sn alloy) is very expensive compared to inorganic salts.

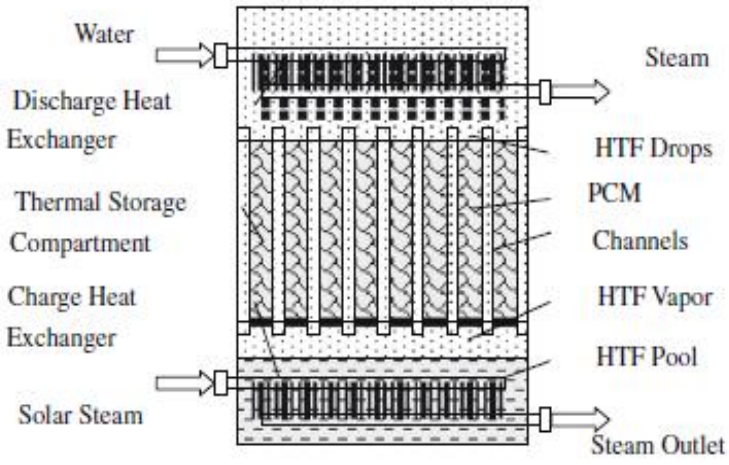

Figure 6.5 The novel reflux heat transfer storage (RHTS) system concept [179]

6.1.4 Summary

In summary, the use of aluminium fins is the most promising method for heat transfer enhancement in the 250-330^{o}C temperature range since it has successfully been tested in various lab and industrial scale experiments. The design of finned-LHS system requires the determination of the best fin configuration (i.e fin height, thickness and pitch). There is the need for evaluating the heat transfer rate for the charging and discharging processes for the design of the storage system and its integration with other components of the solar thermal power plants. Although the effect of fin pitch, fin thickness, HTF pipe radius on the performance of a finned-LHS module, using aluminium fins and eutectic mixture of KNO_3 and $NaNO_3$ with melting point of 220^{o}C, have been investigated numerically by Guo and Zang [180], their study considered only the discharging process and a constant HTF pipe wall temperature. The assumption of a constant HTF wall temperature does not consider the forced convection heat transfer in the HTF pipe. The study therefore, did not give a realistic quantitative performance results that can be used for design. It only presents times for complete discharging as functions of the geometrical parameters considered.

6.2 The Finned Storage Geometry

Figure 6.6(a) shows the configuration of a finned storage element with circumferential fins. The HTF flows from top to bottom during charging and from bottom to top during discharging. The PCM is embedded between adjacent fins. This storage element can be considered to consist of many finned segments (Figure 6.6(b)) connected axially to form the whole element. Thus the performance and heat transfer characteristics will be the same for each finned segment. The best geometrical configuration and the heat transfer characteristics in a storage element can thus be determined considering a single finned segment. The validated melting and solidification model in the Fluent commercial CFD code was used for the modelling and simulation.

6.3 CFD Set-up

The domain enclosed by the red dotted rectangle in Figure 6.6(b) was considered as the CFD domain and was drawn and meshed with a mesh size same or smaller than 0.4 mm (size obtained in the mesh dependency studies). The HTF-pipe wall thickness was neglected. The top and bottom centre lines of the adjacent fins forms the top and bottom boundaries of the domain respectively and were assumed to be insulated. The right-side boundary was assumed to be insulated since it is the point adjacent elements meet. The heat transfer due to the flow of the HTF through the pipe was considered by imposing a forced convection heat transfer in tubes boundary condition. The forced convection heat transfer coefficient was calculated using the Dittus Boetler correlation [181]:

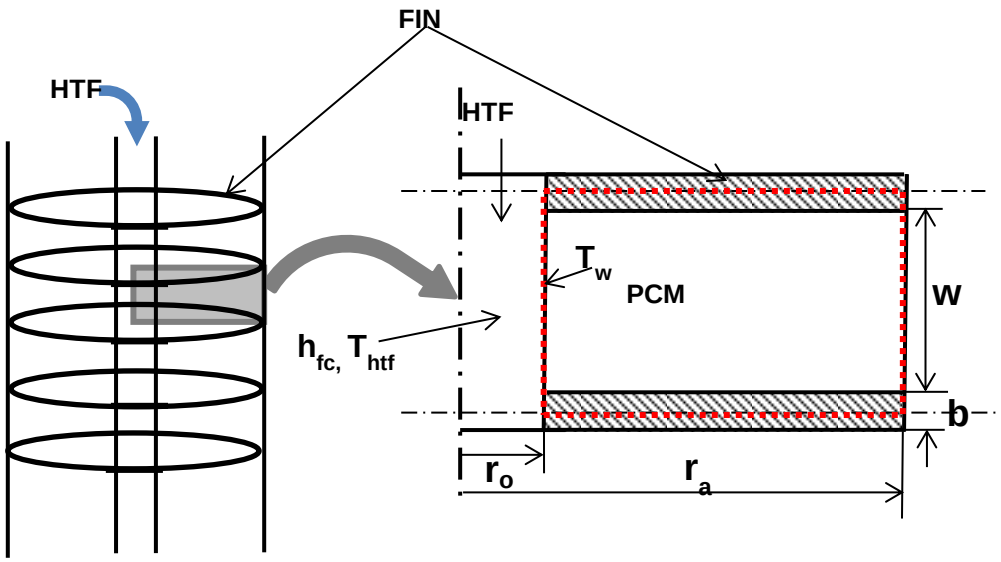

(a) (b)

Figure 6.6 Finned storage geometry

$$Nu_D = 0.023 Re_D^{\frac{4}{5}} Pr^n = \frac{h_{fc} D}{k_{htf}} \quad (6.1)$$

$$n = 0.4 \; for \; heating \; (discharging)$$
$$n = 0.3 \; for \; cooling \; (charging)$$

6.4 Determination of Storage Segment Configuration

The discharging (solidification) process of LHS is slower than the charging (melting) process because natural convection plays a significant role during the charging process. Thus, the best geometrical configuration of the storage element will be obtained considering the solidification process. In Chapter 5, it has already been established that the main mode of heat transfer for an un-finned storage element is pure conduction. Fins are added in order to increase the heat flux thus increasing the utilization factor of the storage system. The dimensions of the fin that will increase the heat flux and use the least amount of fin and tube material is required.

In the following sections CFD simulations were conducted considering the CFD set-up described in section 6.3 to find the best outer radius (r_a), distance between fins (w) and fin thickness (b). The HTF-pipe outer radius r_o of 0.006 m was used. A small HTF-pipe radius was selected since the smaller the pipe radius the more the surface are to volume ratio, thus the higher the heat transfer rate per unit volume of HTF. A segment with r_a=32.5 mm, w=10 mm and b=1 mm was selected as the base case configuration.

Sodium nitrate was used as the PCM whose thermo-physical properties have been presented in Table 4.5. The mean temperature of the HTF of 559.5 K (~20^{o}C below the melting point of the PCM), HTF mass flow rate of 0.09387 kg/s (corresponding to HTF velocity of 1 m/s) and initial PCM temperature of 600 K (i.e. ~20^{o}C above the melting point) were used. The thermo-physical properties of the HTF (Therminol VP-1) were obtained at the average HTF temperature of 559.5^{o}C [159].

6.4.1 Selection of Fin Thickness

In order to determine the effect of fin thickness, CFD simulations for a single finned segment were conducted using three fin thicknesses: 1 mm, 1.5 mm and 2 mm. All other operating and geometrical parameters were the same. Figure 6.7 presents the heat flux at the HTF pipe wall, cumulative heat discharged and liquid fraction variation during the discharge process for the three fin thicknesses. As the fin thickness increases the heat flux increases, especially at the initial stage of discharging. But the doubling of the fin thickness from 1 mm to 2 mm does not result in doubling of the heat flux or halving the time for complete discharge (Figure 6.7(b) and (c)). Thus a thinner fin is more advantageous considering performance and fin material amount. But the thinner the fin the less strong it will be and as such 1 mm fin thickness was selected as a compromise.

6.4.2 Determination of the Best Fin Configuration

In this section, the fin configuration (distance between fins and fin outer radius) that will give the best heat flux was determined. The distance between fins (w) was varied from 10 mm to 20 mm. For each distance between fins, the fin outer radius (r_a) was varied from 16.3 mm to 65 mm.

Figure 6.8 presents the heat flux variation with liquid fraction for the fin configurations studied. Initially the heat flux is very high due to contact of the liquid PCM with the HTF pipe wall and the temperature difference between the liquid PCM and the HTF. The heat flux reduces significantly with time due to the solidification of the PCM adjacent to the HTF pipe wall, creating a solid layer of PCM around the HTF pipe. The higher the fin outer radius (r_a), the smaller the variation of the heat fluxes during most part of the discharging process. For the fin outer radius of 16.3 mm, the heat flux reduces significantly as the discharging progresses. This is due to the increase in the thickness of the solid layer of PCM (solidification thickness) and the insufficient performance of the fin. For fin outer radius from >32.5 mm, the variation of the heat flux during the solidification process is small. This variation reduces with increasing fin outer radius (r_a) and decreasing distance between fins (w).

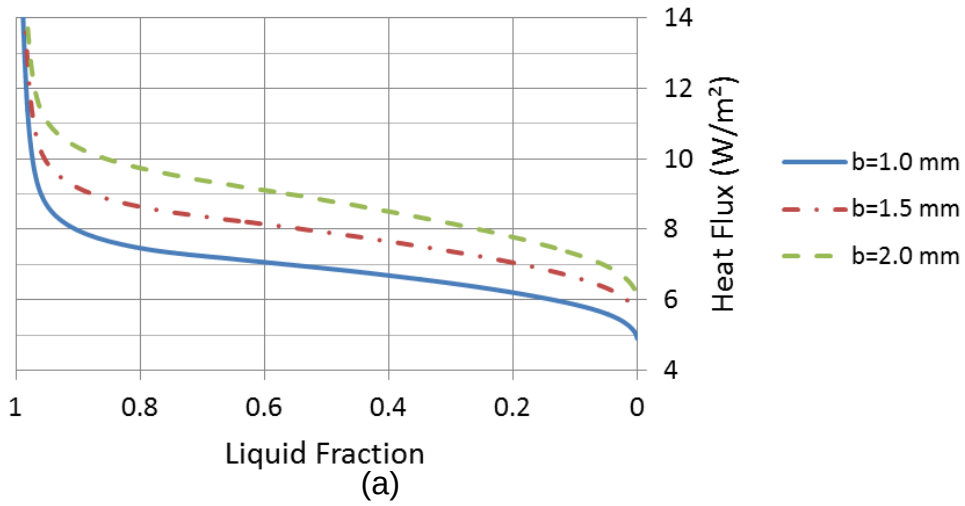

(a)

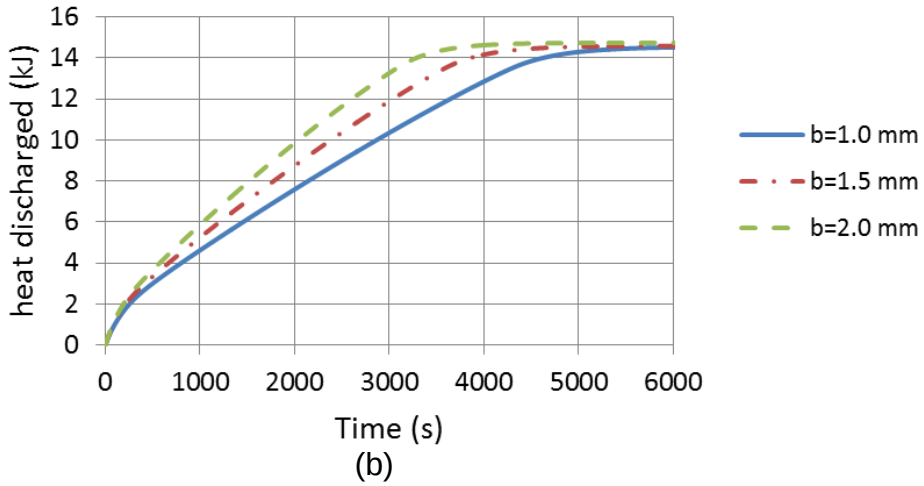

(b)

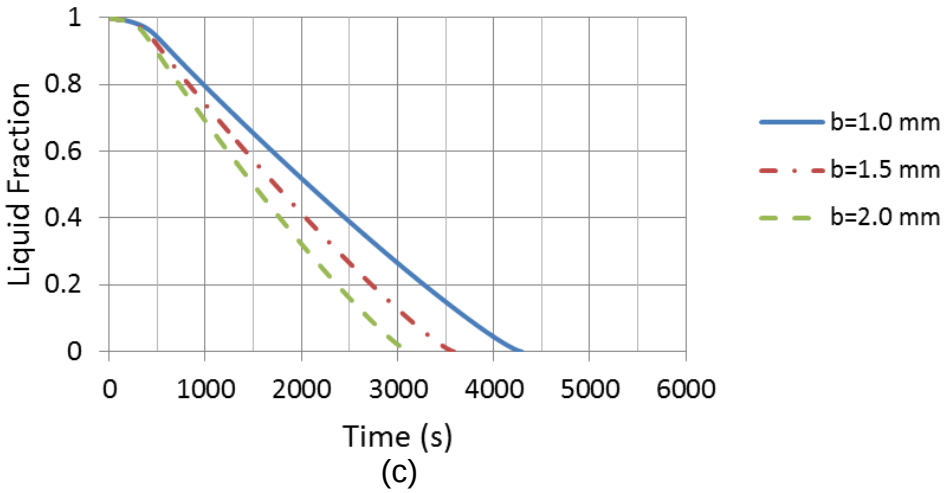

(c)

Figure 6.7 Variation of (a) heat flux with liquid fraction (b) Heat discharged with time (c) liquid fraction with time for different fin thicknesses

The more constant (stable) the heat flux the better it is for the thermal storage system. Thus the fin outer radius (r_a) of 48.8 mm was selected as its heat flux variation is very close to that of 65 mm.

Figure 6.9 presents the variation of the heat flux for the selected fin outer radius (r_a=48.8 m), with the distance between fins (w). The smaller the distance between the fins, the higher the heat flux. Thus the distance between fins of 10 mm was selected since using a smaller distance between fins will result into smaller percentage volume of PCM in the storage system and allowing for ≤10% volume of fin.

Finally the storage element configuration with HTF-pipe inner radius of 6 mm, fin outer radius of 48.8 mm, fin thickness of 1 mm and distance between fins of 10 mm is the best configuration.

6.5 Comparison with other Phase Change Materials (PCMs)

In section's 6.4 analyses, sodium nitrate was used as the PCM. The effect of the PCM's thermo-physical properties on the thermal performance of the discharging process was investigated here. Simulation using the best selected configuration was conducted with the same set-up but with potassium nitrate (KNO_3) as the PCM (properties presented in Table 4.5).

Figure 6.10 presents the comparison of the heat flux and the heat discharged for $NaNO_3$ and KNO_3 PCMs. The difference in the heat flux is very small. This is because the thermal conductivities of the PCMs are very close (refer to Table 4.5) and the main mode of heat transfer is pure conduction during the discharging process. But from Figure 6.10(b) the amount of heat discharged is different since the latent heat of fusion of $NaNO_3$ is almost double that of KNO_3.

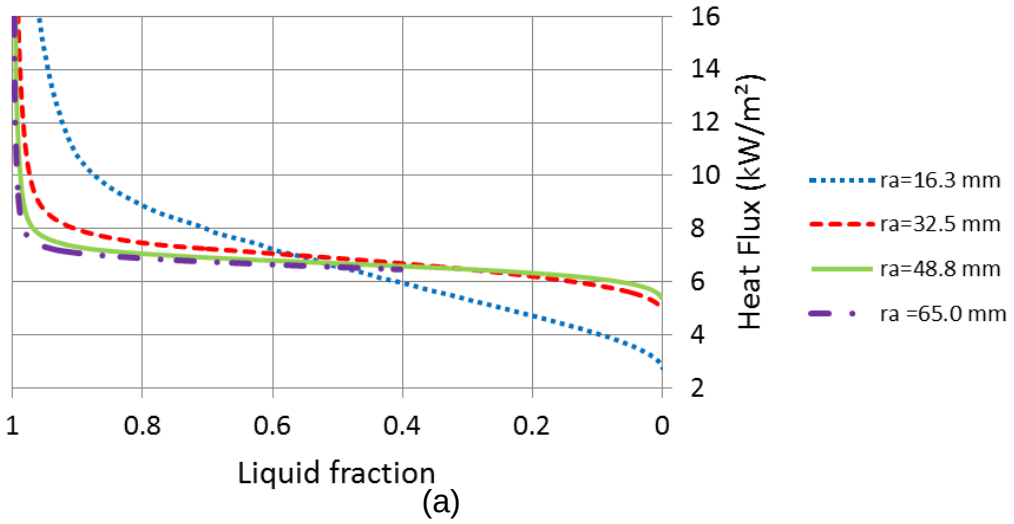

(a)

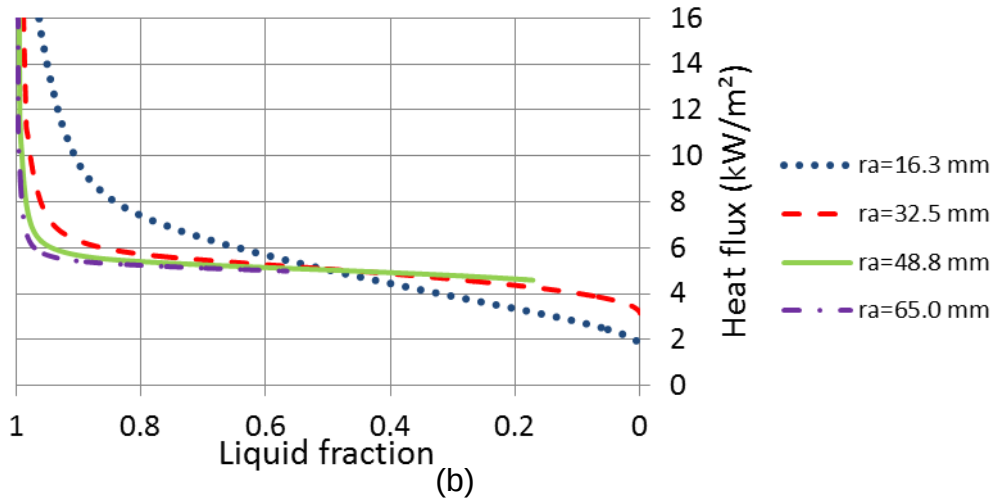

(b)

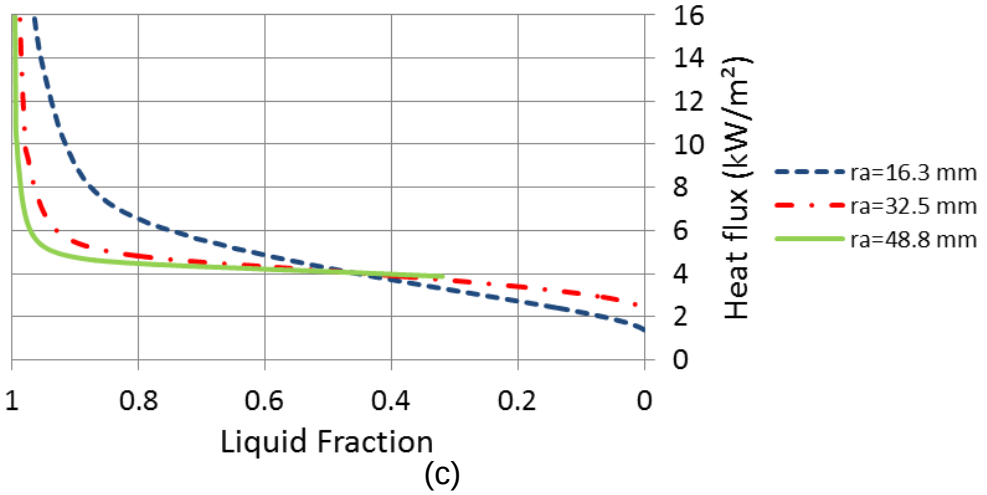

(c)

Figure 6.8 Variation of heat flux with liquid fraction for distance between fins (w) of (a) 10 (b) 15 and (c) 20 mm, for the discharging of a single finned storage segment.

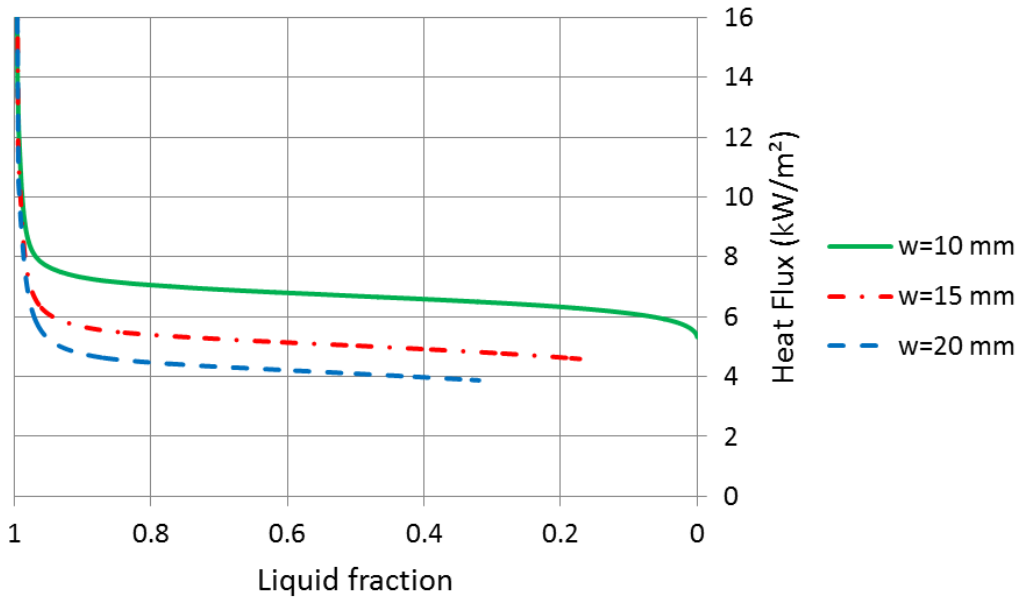

Figure 6.9 Variation of heat flux with liquid fraction for the discharging of a single finned LHS segment with fin outer radius of 48.8 mm

6.6 Heat Transfer Characteristics in the Selected Configuration

In this section the heat transfer characteristics during the charging and the discharging process in the selected configuration was determined in order to come up with heat transfer coefficients that can be used for the design of a finned LHS system. This was determined by considering the single finned segment (Figure 6.6b). The heat transfer in the HTF-pipe is forced convection and thus can be modelled by specifying a forced convection heat transfer coefficient and a mean HTF temperature. The heat transfer in the PCM may depend on the HTF mass flow rate and the mean HTF temperature. This was investigated in this section and heat transfer correlations for the charging and discharging process were obtained.

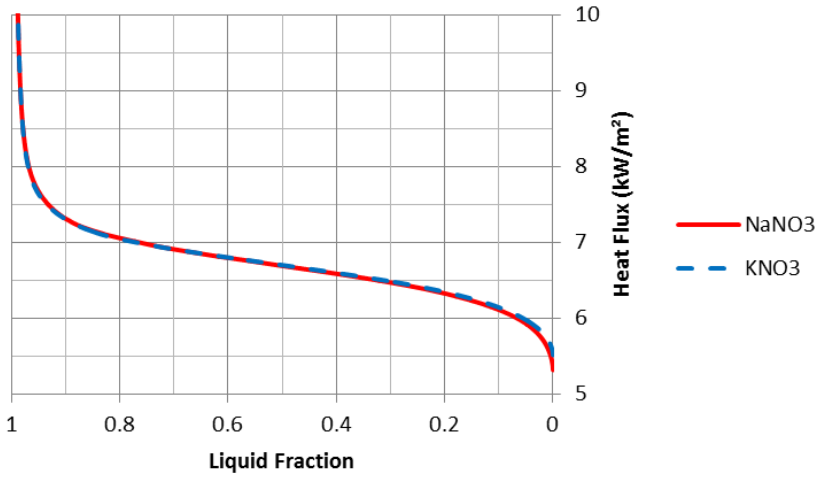

(a)

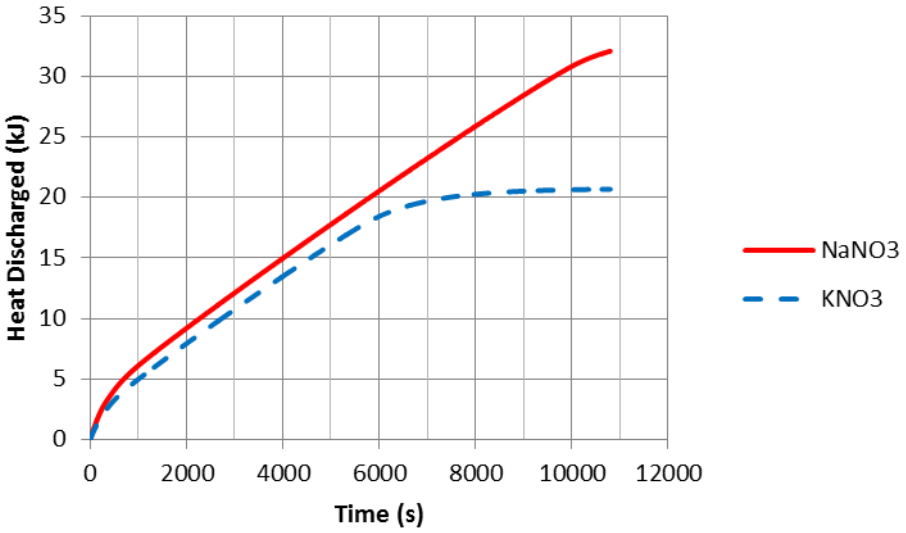

(b)

Figure 6.10 Comparison of variation of (a) Heat flux (b) Heat discharged with time for the discharging in a single finned segment using sodium and potassium nitrate PCM's

6.6.1 Charging

During the charging process the PCM melts and thus convection plays a role in the heat transfer process. This means that the heat transfer characteristics during charging will be dependent on the thermo-physical properties of the PCM.

Simulations were conducted with initial PCM temperature of ~20 K below the melting point of each PCM (see Table 4.5). For each PCM, HTF mass flow rates presented in Table 6.3 were considered. For each HTF mass flow rate, the average temperatures of HTF of 20, 15, 10, and 5 K above the melting point of the PCM were considered. The corresponding forced heat transfer coefficients were calculated using equation (6.1) with properties evaluated at the mean temperature of the HTF for each case. Thus for each PCM, 16 simulations were conducted.

6.6.1.1 Characteristic of the Process

In order to see the behaviour of the melting process simulations for HTF mass flow rate of 0.09387 kg/s for the different average HTF temperatures were considered using sodium nitrate PCM with melting temperature of 579 K. Figure 6.11 presents the variation of the average heat flux through the wall and the average HTF pipe wall temperature as a function of the dimensionless time at the different average HTF temperatures (above melting point). The shape of the graphs shows that natural convection plays a role in the heat transfer.

Table 6.3 HTF velocity and mass flow rate considered for the determination of heat transfer coefficient

HTF velocity (m/s)	HTF mass flow rate (kg/s)
1	0.09387
0.75	0.07040
0.50	0.04694
0.25	0.02347

The four regimes of melting can be seen as explained in section 5.3.2.1. The average HTF-pipe wall temperature (Figure 6.11b) is constant during much part of the melting process. This shows that there exist quasi-stationary melting and thus the heat flux is almost constant during the melting process. A heat transfer coefficient can be obtained that can be used in predicting the heat transfer during melting.

To further understand the melting process in the finned segment, Figure 6.12 presents the liquid fraction distribution in the domain at some selected times and Figure 6.13 presents the velocity vectors in the domain showing the movement of the PCM during the process. At the beginning of melting the heat transfer is by conduction since the PCM is completely solid and the heat flux is very high due to contact of the PCM with the HTF-pipe wall and the temperature difference between the PCM and the HTF (since initial temperature of the PCM in ~20 K below the melting point). From Figure 6.12(a) and (b), the melting starts at the centre of the wall. This is because at the beginning of the process, the PCM and the fins are at the same temperature and since the thermal conductivity of the fin is much higher than that of the PCM, most of the heat at the end will be transferred to the fin making the PCM at the centre to receive more heat and thus forcing melting to start at the centre. Initially the heat transferred to the fin will be used in increasing the fins temperature before being transferred to the PCM. From Figure 6.13(a) and (b) it will be observed that there is small liquid movement but at this stage the main mode of heat transfer is by conduction. As the process continues the effect of convection becomes more pronounced with the movement of the liquid from the bottom to the top. This causes the deformation of the melt interface at the top (Figure 6.12c). This is the mixed conduction and convection point. The convection soon takes over the process (Figure 6.12d) and the heat flux rises reaching a maximum and start falling slowly. This is the quasi-stationary regime. From Figure 6.12(d)-(f), heat is also transferred through the bottom fin on to the PCM. Nonetheless even with the fins, convection is still the main mode of heat transfer during the charging process.

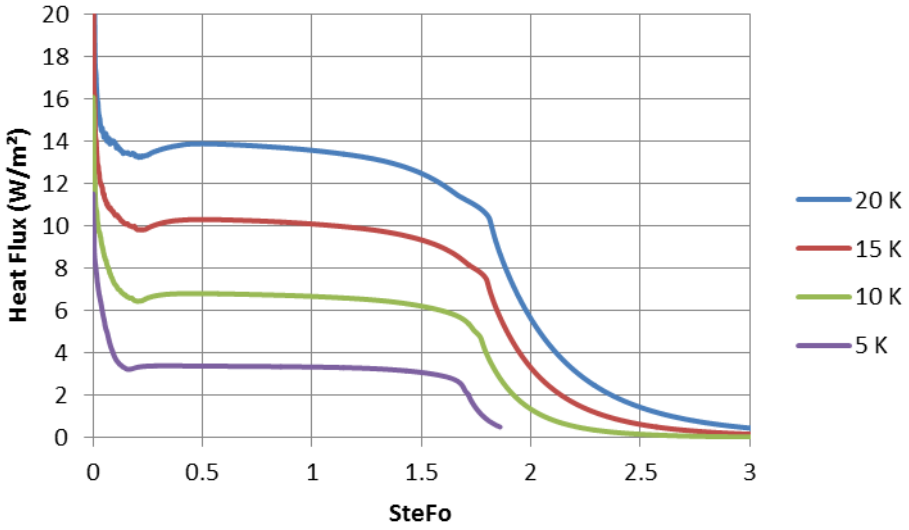

(a)

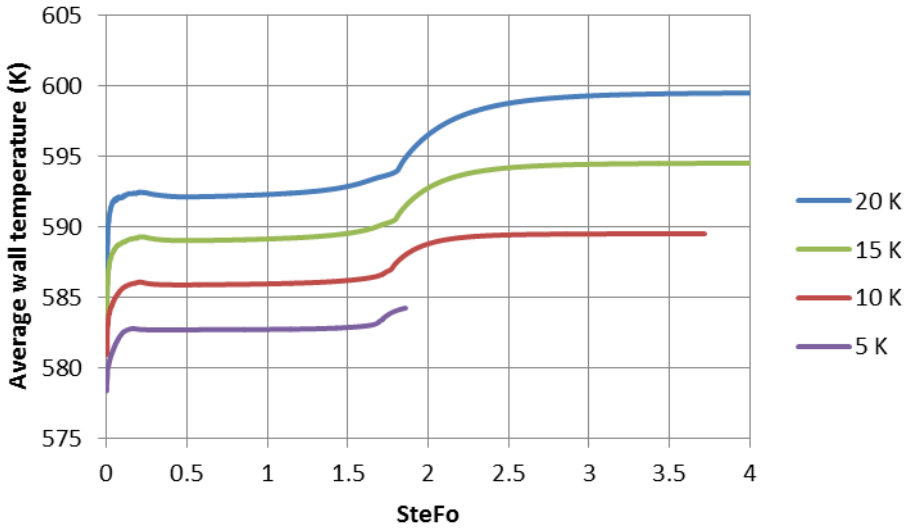

(b)

Figure 6.11 (a) Average heat flux at the HTF pipe wall (b) Average HTF pipe wall temperature, at different HTF average temperatures for HTF velocity of 1.0 m/s for $NaNO_3$ PCM.

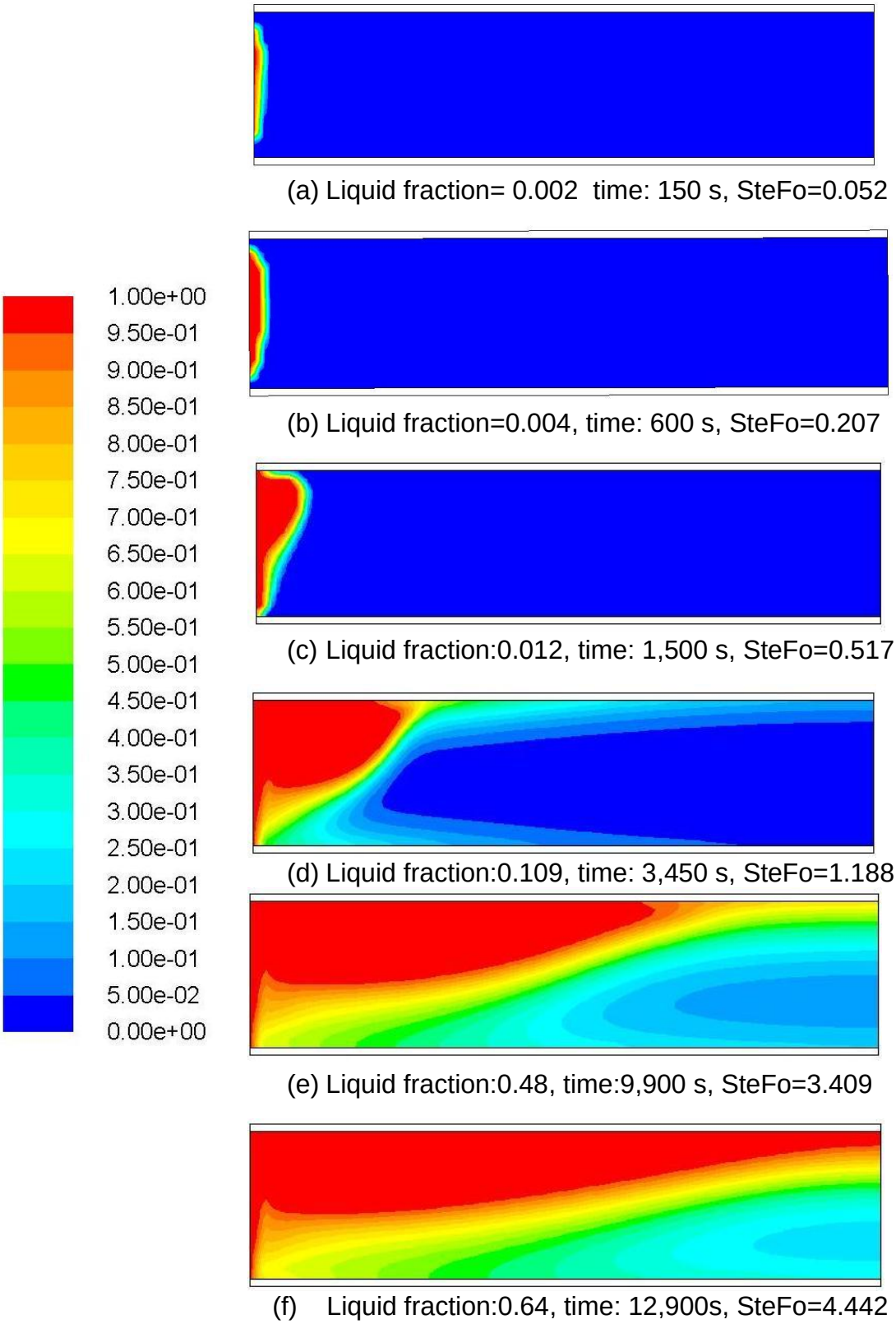

(a) Liquid fraction= 0.002 time: 150 s, SteFo=0.052

(b) Liquid fraction=0.004, time: 600 s, SteFo=0.207

(c) Liquid fraction:0.012, time: 1,500 s, SteFo=0.517

(d) Liquid fraction:0.109, time: 3,450 s, SteFo=1.188

(e) Liquid fraction:0.48, time:9,900 s, SteFo=3.409

(f) Liquid fraction:0.64, time: 12,900s, SteFo=4.442

Figure 6.12 Contours of liquid fraction in a finned segment for HTF velocity of 1.0 m/s and HTF average temperature of 5 K above the melting temperature using $NaNO_3$ PCM.

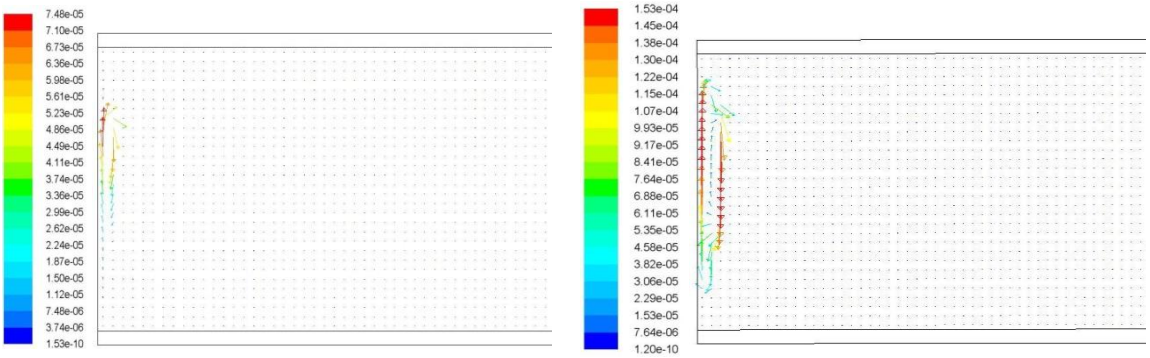

(a) 150 s, SteFo=0.052

(b) 600 s, SteFo=0.207

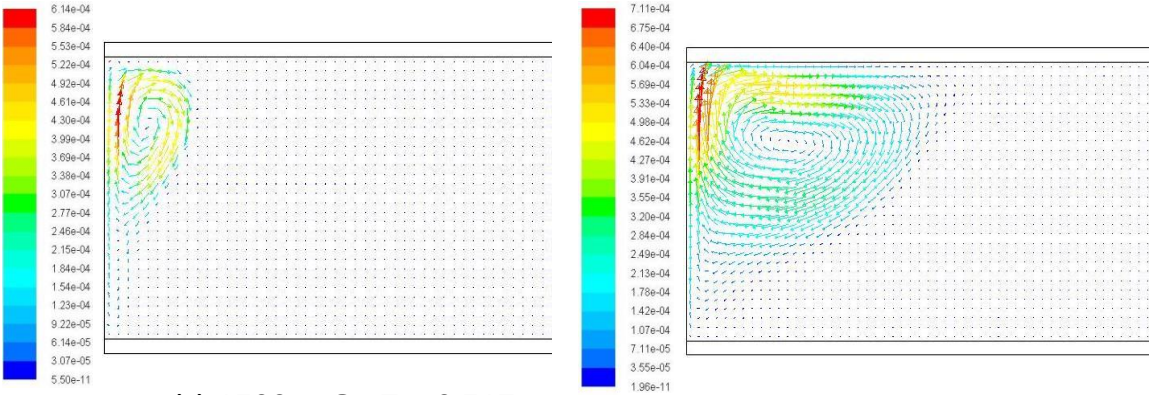

(c) 1500 s, SteFo=0.517

(d) 3450 s, SteFo=1.188

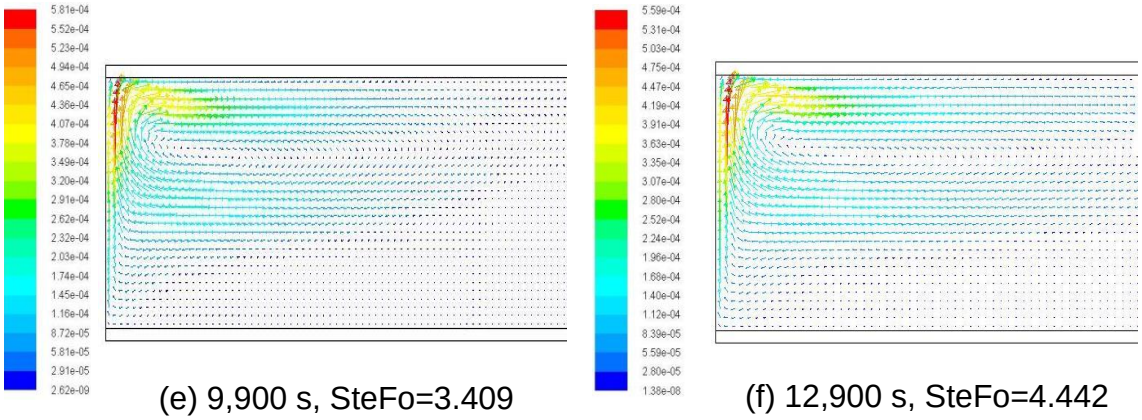

(e) 9,900 s, SteFo=3.409

(f) 12,900 s, SteFo=4.442

Figure 6.13 Contours of velocity in the PCM for HTF velocity of 1.0 m/s and mean temperature of 5 K above the melting temperature using $NaNO_3$ PCM

Thus the heat transfer rates during the charging process can be predicted by determining the heat transfer coefficient during quasi-stationary melting and that during over heating of the PCM since when all the PCM has melted natural convection will still be the mode of heat transfer until the there is no driving temperature difference.

6.6.1.2 Heat Transfer Coefficient during Melting

In this section the heat transfer coefficient during the melting of the PCM was determined for each of the cases simulated and PCM considered. The melting temperature of the PCM and the mean HTF temperature are known variables. Using the average heat flux through the wall during quasi-stationary melting obtained from the CFD simulation, the overall heat transfer coefficient (U_{ave}) during melting can be obtained by using the following equation:

$$U_{ave} = \frac{q_{ave,qs}}{T_{htf} - T_m} \tag{6.2}$$

Figure 6.14 presents the plot of the overall heat transfer coefficient (U_{ave}) against the temperature difference for the different mass flow rates of HTF considered for the $NaNO_3$ PCM. The overall heat transfer coefficient is not a strong function of the temperature difference. This may be due to the fact that even though natural convection is present it does not depend on the temperature difference since the distance between fins is small (0.01m). Thus the overall heat transfer coefficient (U_{ave}) depends only on the HTF mass flow rate in almost a linear fashion. Using the average overall heat transfer coefficient at each HTF mass flow rate the heat transfer coefficient, (h_m) during melting in the PCM side can be obtained using:

$$\frac{1}{h_m} = \frac{1}{U_{ave}} - \frac{1}{h_{fc}} \tag{6.3}$$

Figure 6.15 presents the heat transfer coefficient plotted against the HTF mass flow rate and can be represented by a linear function:

$$h_{m,NaNO_3} = 1391.6\left(\dot{m}_{htf}\right) + 933.64 \tag{6.4}$$

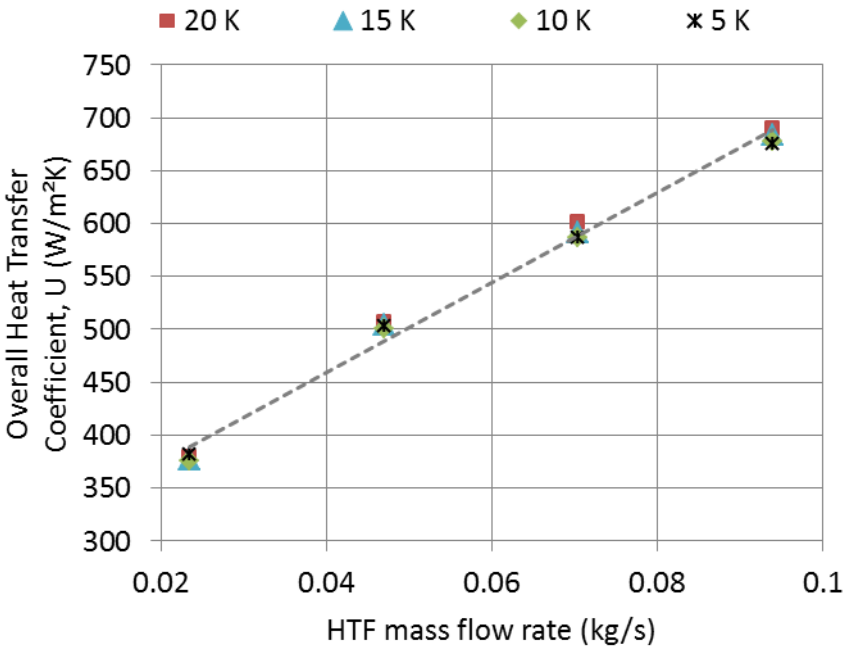

Figure 6.14 Overall heat transfer coefficient as a function of HTF mass flow rate for different temperature difference between HTF and PCM melting temperature using $NaNO_3$ PCM

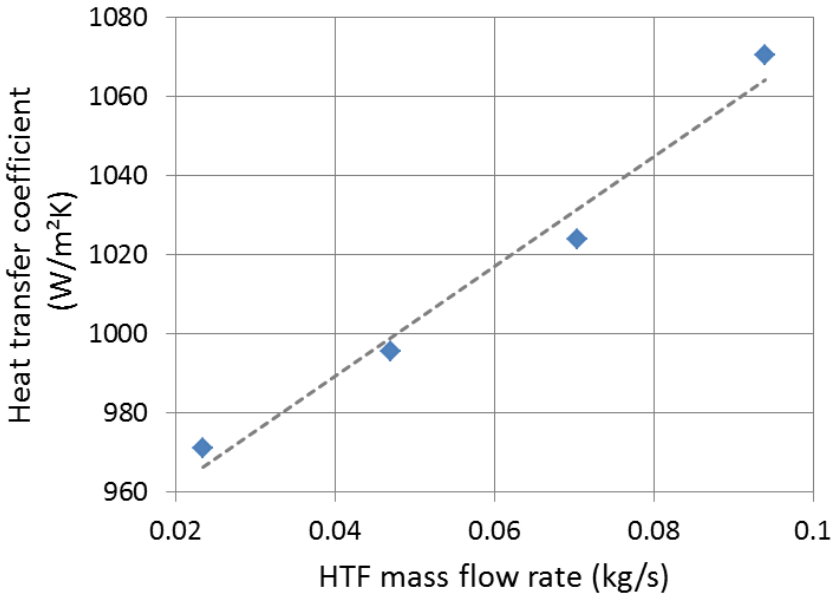

Figure 6.15 Heat transfer coefficient as a function of HTF mass flow rate during melting in a finned LHS segment for $NaNO_3$ PCM

Using similar method the overall heat transfer coefficient and the heat transfer coefficient in the other two PCMs (KNO_3/KCl and KNO_3) were also determined. Since the overall heat transfer rate does not depend on the temperature difference the simulations for these PCMs were conducted with only the 20 K temperature difference. Figure 6.16 presents the variation of the overall heat transfer coefficient during quasi stationary melting for KNO_3/KCl and KNO_3 PCMs while Figure 6.17 presents the heat transfer coefficient during the melting process for both PCMs. It will be seen that the overall heat transfer for the two PCMs is very close. This is because of the closeness of the thermo physical properties of the two PCM owing to the fact that the eutectic mixture of KNO_3/KCl is composed of mostly KNO_3. Equation (6.5) and (6.6) present a linear function for the heat transfer coefficient for the KNO_3/KCl and KNO_3 PCMs respectively.

$$h_{m,KNO_3/KCl} = 1363.6\left(\dot{m}_{htf}\right) + 744.51 \tag{6.5}$$

$$h_{m,KNO_3} = 1409.4\left(\dot{m}_{htf}\right) + 715.93 \tag{6.6}$$

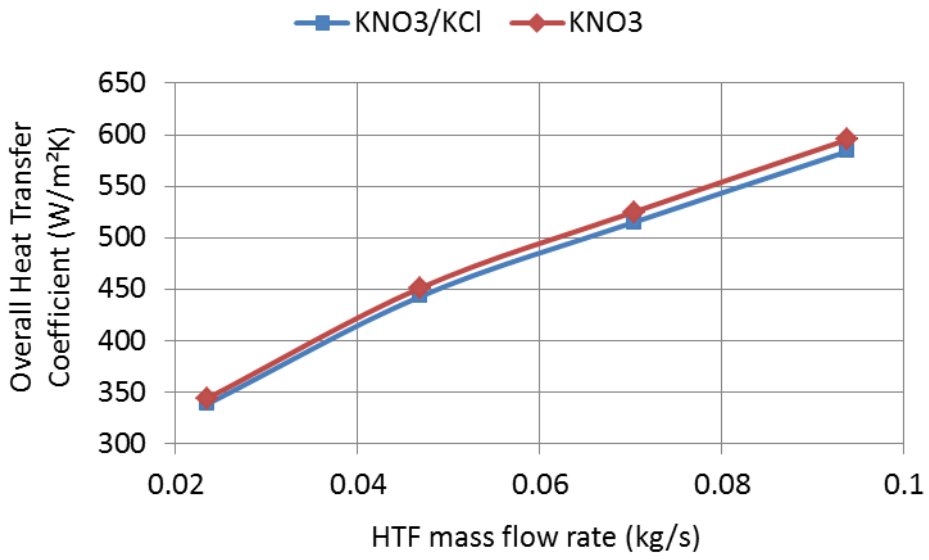

Figure 6.16 Overall heat transfer coefficient during melting in finned segment for KNO_3/KCl and KNO_3 PCMs

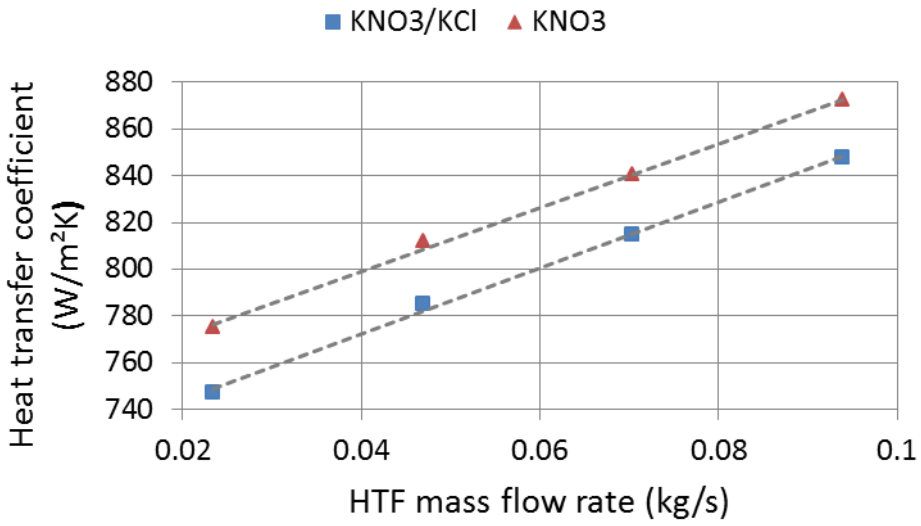

Figure 6.17 Heat transfer coefficient during melting in finned segment for KNO_3/KCl and KNO_3 PCMs

6.6.1.3 Heat Transfer Coefficient during Overheating

At the end of melting, heat transfer by natural convection continues in the PCM causing an increase in the temperature of the PCM until there is no driving temperature difference. In order to obtain the heat transfer coefficient during overheating, the heat transfer characteristic after all the PCM has melted was studied. The heat transfer coefficient was then calculated by dividing the average heat flux at the wall with the temperature difference between the average HTF-pipe wall temperature (T_w) and the average PCM temperature (T_{pcm}). Figure 6.18 presents the heat transfer coefficient as a function of the temperature difference for each HTF mass flow rate for the three PCMs. The heat transfer coefficient is a strong function of the temperature difference and the HTF mass flow rate. From these charts a function for the heat transfer coefficient during overheating can be obtained. Appendix A.1 presents how this can be obtained.

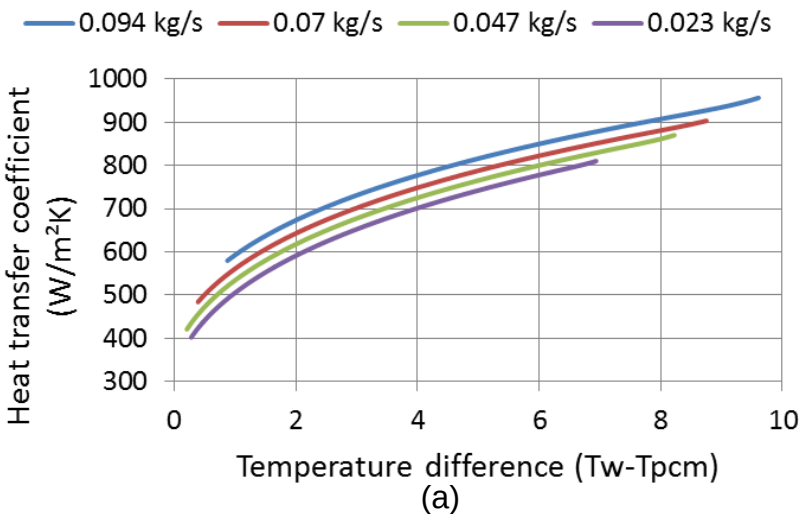

(a)

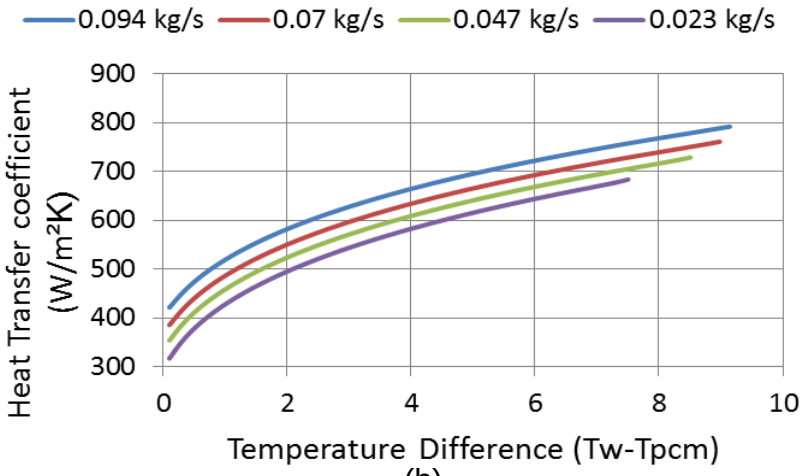

(b)

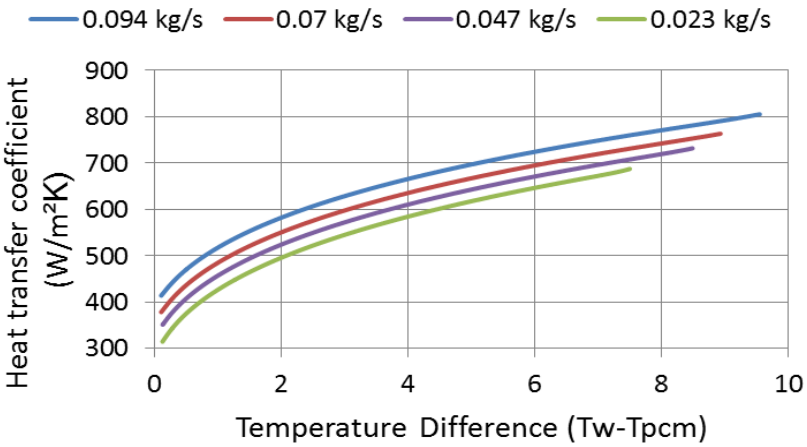

(c)

Figure 6.18 Heat transfer coefficient for the over-heating process during charging for (a) $NaNO_3$ (b) KNO_3/KCl (c) KNO_3 PCMs

6.6.2 Discharging

It has already been established that during the discharging (solidification) pure conduction is the main mode of heat transfer and the heat transfer characteristics is independent of the PCM. Thus in this section $NaNO_3$ PCM was used for the determination of the heat transfer coefficient during discharging. Simulations were conducted with initial PCM temperature of ~20 K above the melting point of the PCM (which is 306^{o}C) and average HTF temperatures of 20, 15, 10, and 5 K below the melting point were used. All other set-up and boundary conditions were same as that of the charging process.

6.6.2.1 Characteristics of the Process

In order to understand the heat transfer behaviour during the discharging process Figure 6.19(a) presents the variation of the heat flux with the dimensionless time for HTF mass flow rate of 0.09387 kg/s (velocity of 1 m/s) and different average HTF temperatures and Figure 6.19(b) presents the average PCM and HTF-pipe wall temperature variation with time for HTF average temperature of 559 K (20 K below the melting point). It will be seen that the heat flux varies during the solidification process and the average HTF-pipe wall temperature is almost constant during the solidification. The decrease in the heat flux during solidification is thus caused by the moving solid interface.

This will be fully understood considering the liquid fraction and velocity distribution at various times during the process as shown in Figures 6.20 and 6.21 respectively. At the start of the process the PCM is totally liquid at a temperature above the melting temperature and the HTF-pipe wall temperature is lower than the melting temperature. This will cause heat transfer from the PCM into the HTF. Since the liquid is directly in contact with the wall the heat transfer rate will be very high at the beginning. Also since the thermal conductivity of the fins is much higher than the PCM more heat will be transferred through the fins to the HTF-pipe wall. Natural convection is then started due to the cooling of the PCM at the top (Figure 6.21(a)) making the solidification of the PCM to start from point at the bottom where the fin meets the HTF-pipe (Figure 6.20(a)).

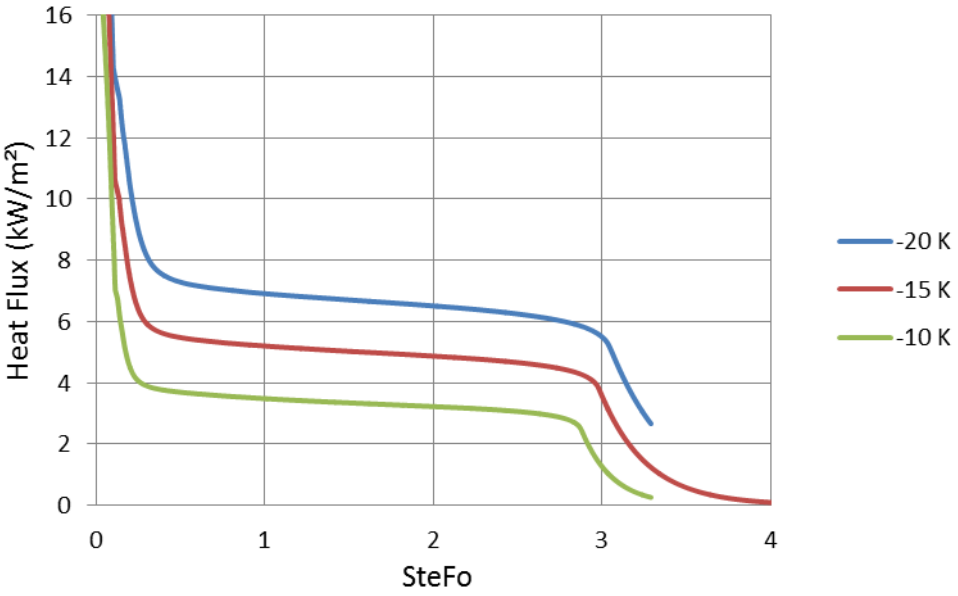

(a)

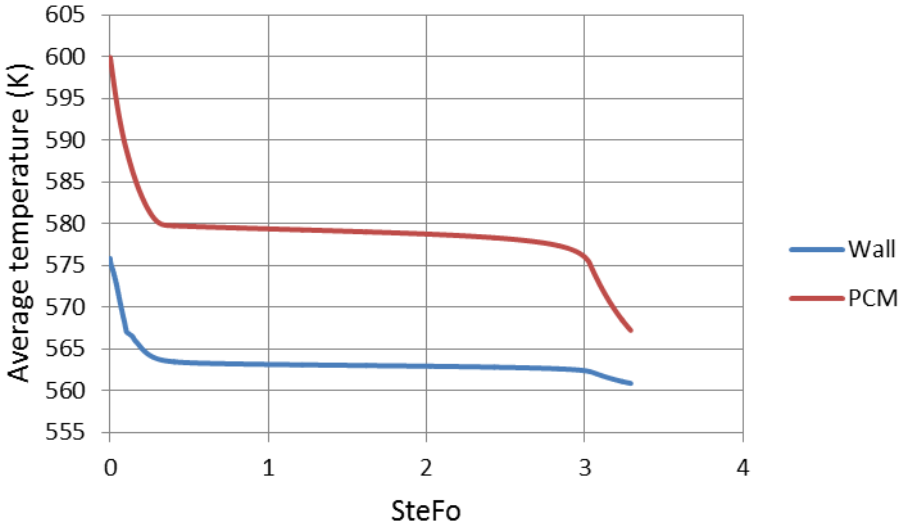

(b)

Figure 6.19 Dimensionless time wise variation of (a) Heat Flux at different HTF average temperatures (b) Average HTF-pipe wall and PCM temperatures for HTF average temperature of 559 K (-20 K), for discharging of a finned segment, using HTF velocity of 1 m/s for $NaNO_3$ PCM.

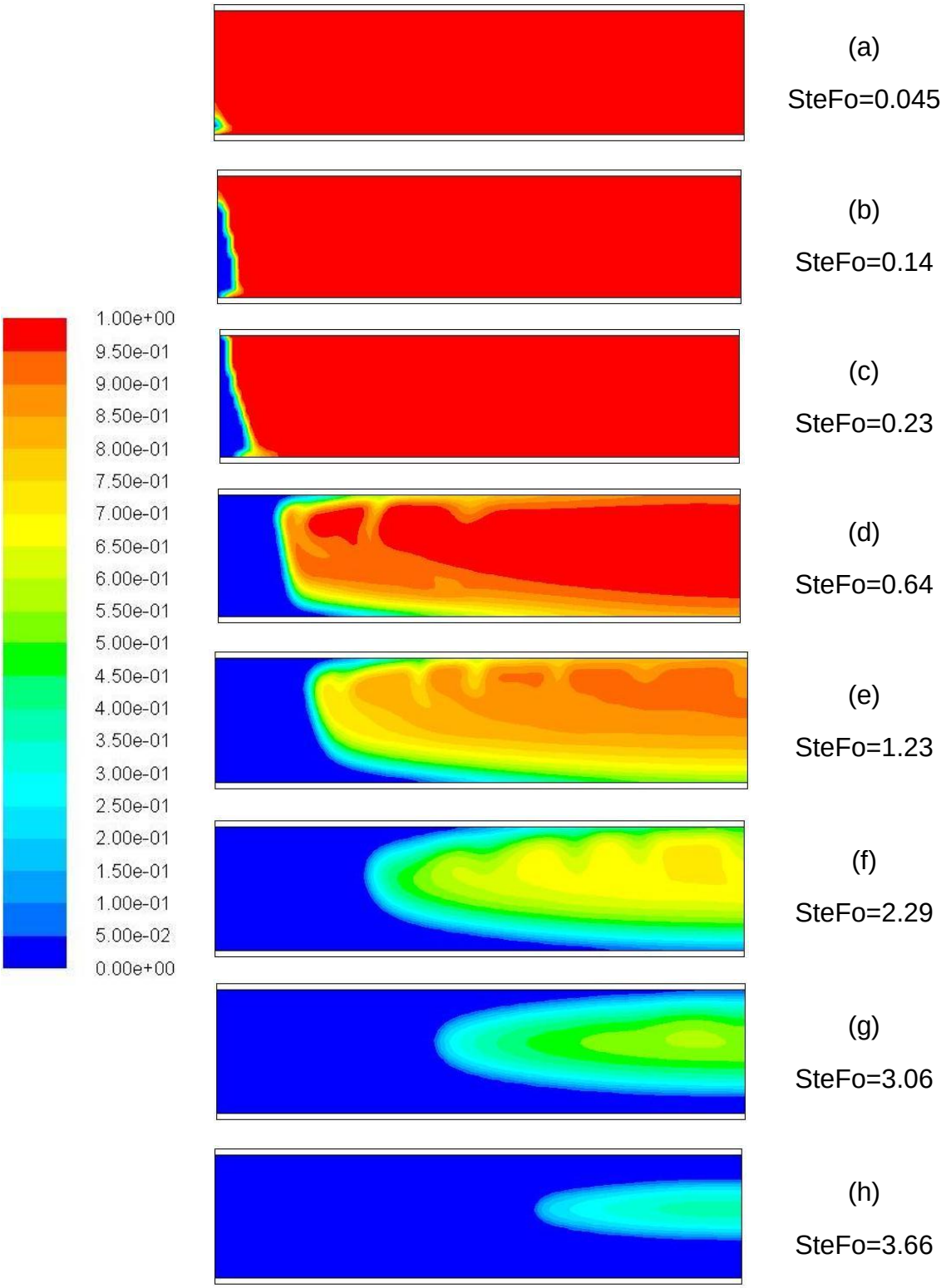

Figure 6.20 Contours of liquid fraction for HTF velocity of 1 m/s and average HTF temperature of 559 K (-20 K), at various times during discharging of a finned segment using $NaNO_3$ PCM.

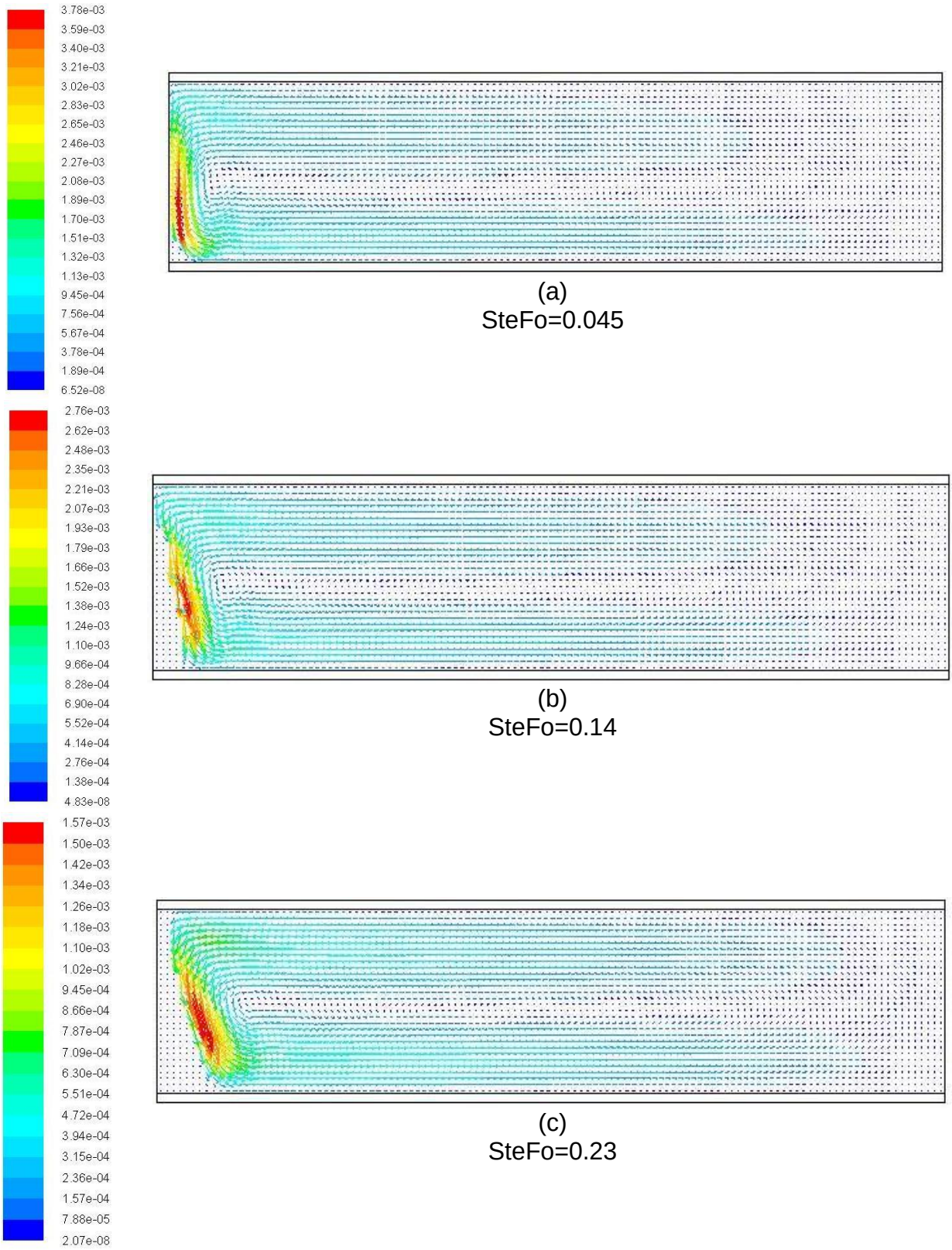

Figure 6.21 Vectors of velocity in the PCM for HTF velocity of 1.0 m/s and HTF average temperature of 559 K at various times for the discharging process using $NaNO_3$ PCM

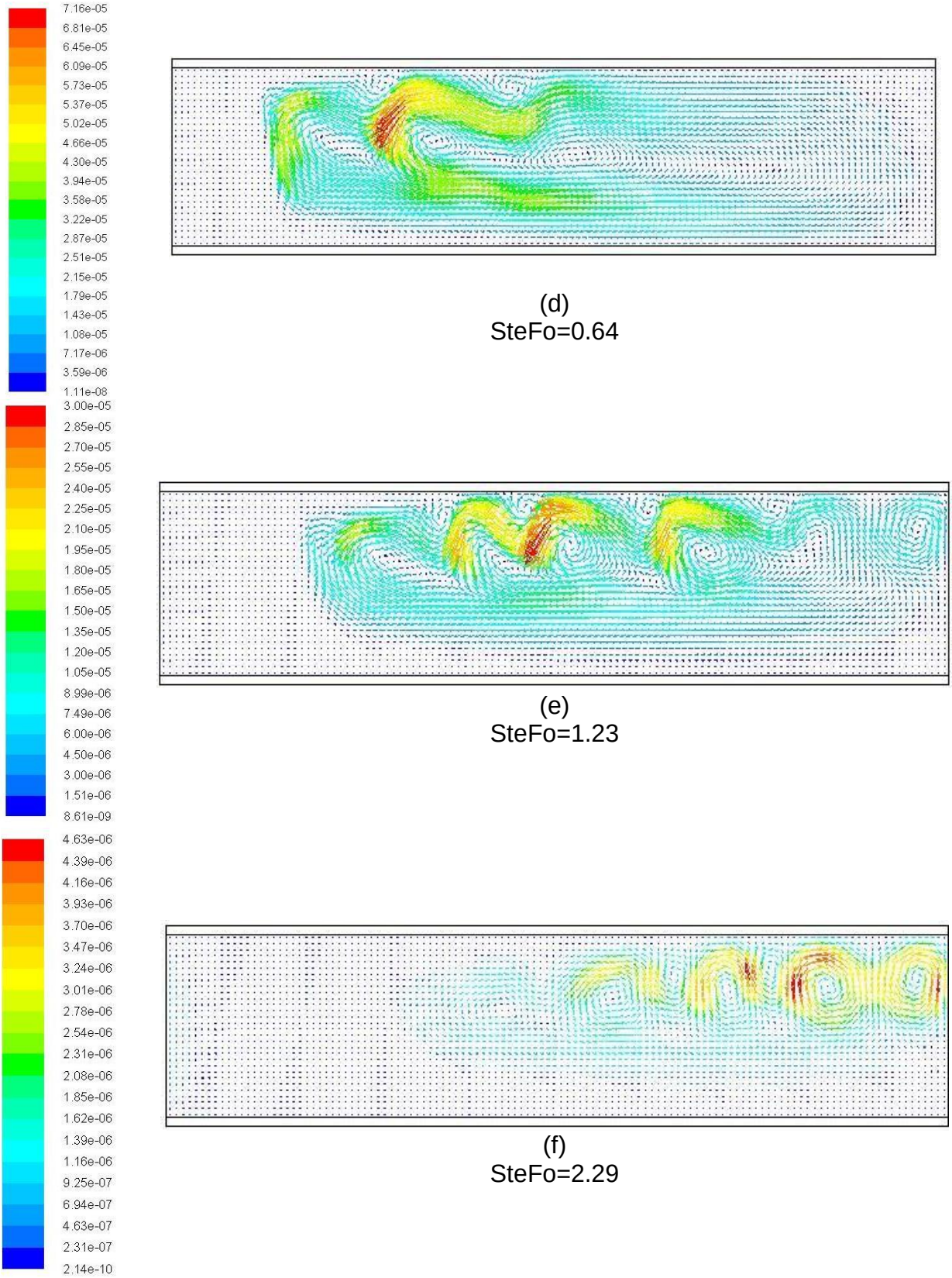

(d)
SteFo=0.64

(e)
SteFo=1.23

(f)
SteFo=2.29

Figure 6.21 Continued

As the process continues the PCM solidifies on the walls in an inverted conical shape as shown in Figure 6.20(b-c). It will also be noticed that as the process progresses many circular fluid flows are formed (Figure 6.21(d)-(f)). This is due to the heat transferred through the fins causing the PCM to cool, becomes heavy and move down. From the velocity magnitudes shown in the left hand side of Figure 6.21, it will be seen that the velocity reduces drastically due to the reduction in space for liquid PCM caused by increasing solid layer on the fin surface. This makes the effect of the natural convection to be negligible and the shape of the melting front becomes symmetrical as for that of pure conduction (see Figure 6.20(f)-(h)). Finally Figure 6.22 presents the temperature distribution at the selected times described above.

In summary, natural convection distorts the shape of the solidification front during solidification with higher impact at the beginning of the process. But looking at the heat flux variation (Figure 6.19a), the effect of natural convection is not so pronounced to affect the heat transfer characteristics during the process and thus the main mode of heat transfer is conduction.

6.6.2.2 Heat Transfer Coefficient during Solidification

From the heat transfer characteristics presented in section 6.6.2.1, the heat flux at the wall depends on the thickness of the solid layer of PCM and thus depends on the liquid fraction. Thus the heat transfer coefficient may depend on the HTF mass flow rate (velocity), wall temperature and the liquid fraction.

In order to determine which of these parameters affect the heat transfer coefficient during solidification two sets of simulations were conducted using HTF velocities of 0.25 m/s and 1 m/s. for each HTF velocity three average HTF temperatures of 20 K, 15 K and 10 K below melting point of the PCM ($NaNO_3$) were considered. The heat transfer coefficient at each time is calculated using equation (6.7) from the time wise average heat flux at the HTF-pipe wall and average HTF-pipe wall temperature.

$$h_s = \frac{\dot{q}_w}{T_w - T_m} \tag{6.7}$$

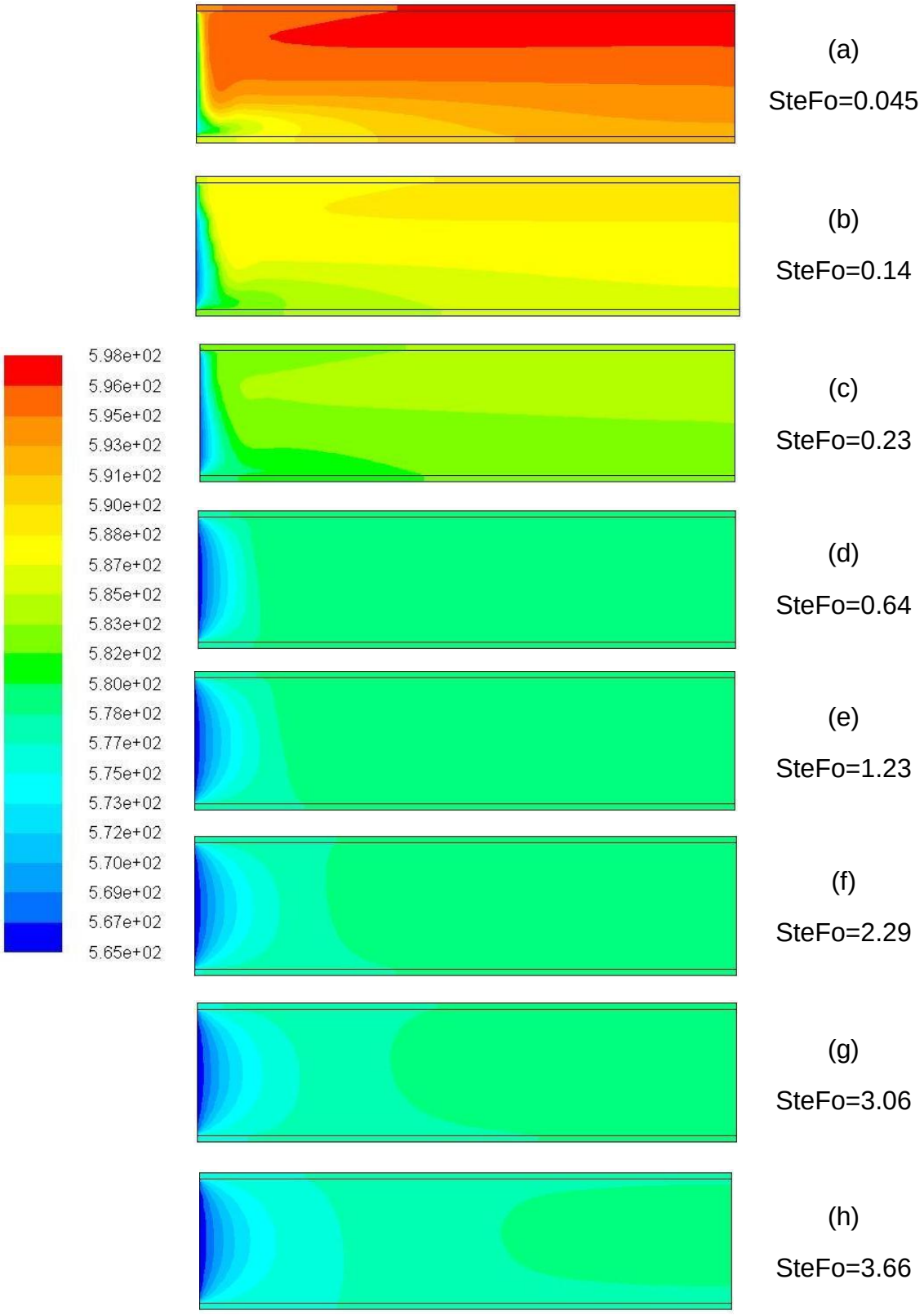

Figure 6.22 Temperature distribution in the PCM for HTF velocity of 1.0 m/s and HTF average temperature of 559 K at various times for the discharging process using $NaNO_3$ PCM

Figure 6.23 presents the heat transfer coefficient as a function of the liquid fraction for HTF velocities of 0.25 m/s and 1 m/s at different average HTF temperatures. Initially the PCM in contact with the surface of the tube is liquid at a temperature above the melting temperature. Thus the heat flux at the surface will be high. The temperature of the PCM layer adjacent to the tube wall reduces reaching the melting point and the PCM starts to solidify. As the phase change interface moves away from the tube wall the heat transfer coefficient decreases almost linearly after the initial transient. Neglecting the initial transient, the heat transfer coefficient is almost a linear function of the liquid fraction and is independent of the HTF-pipe wall temperature. It is a function of the liquid fraction because the main mode of heat transfer is pure conduction and during solidification the solid interface thickness increases. Comparing the values of the heat transfer coefficient in Figure 6.23 (a) and (b), it will be seen that the heat transfer coefficient also depends on the velocity of HTF (HTF mass flow rate) in the pipe (heat sink).

Figure 6.24 presents the heat transfer coefficient as a function of the liquid fraction for HTF mass flow rates from 0.024 to 0.094 kg/s corresponding to HTF velocities of 0.25-1.0 m/s. Neglecting values from 1 to 0.9 liquid fractions, the heat transfer coefficient can be represented as a general linear function having slopes and intercepts dependent on the HTF mass flow rates as shown:

$$h_s = a(LF) + c \tag{6.8}$$

Where:

$$a = 224.04\left(\dot{m}_{htf}\right) + 20.265$$

and

$$c = 1395.4\left(\dot{m}_{htf}\right) + 267.96$$

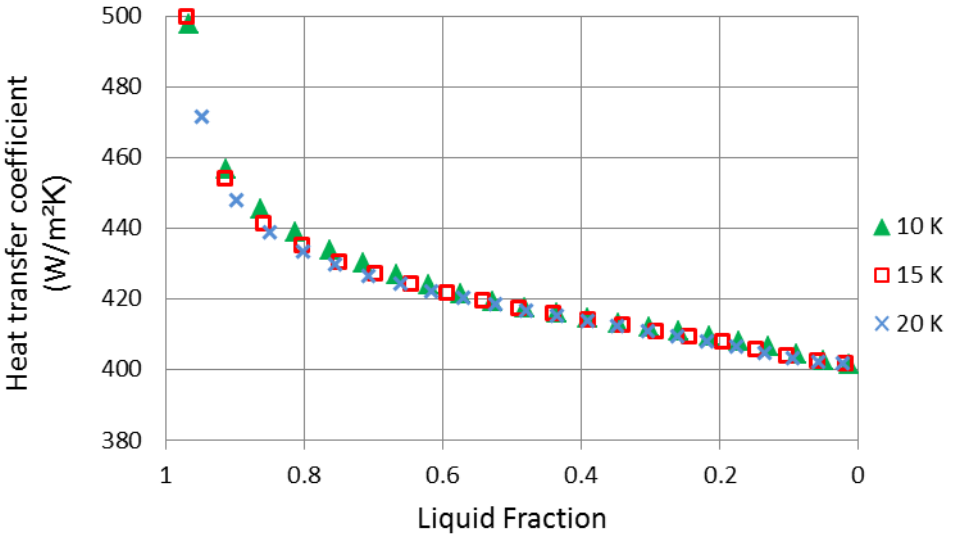

(a)

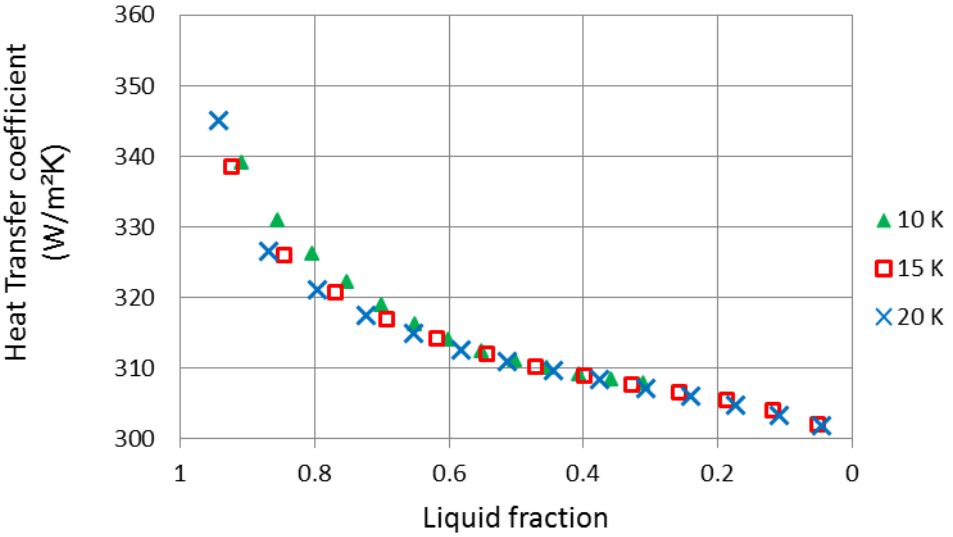

(b)

Figure 6.23 Heat transfer coefficient as a function of Liquid fraction at different HTF average temperatures for HTF velocity of (a) 1 m/s (b) 0.25 m/s

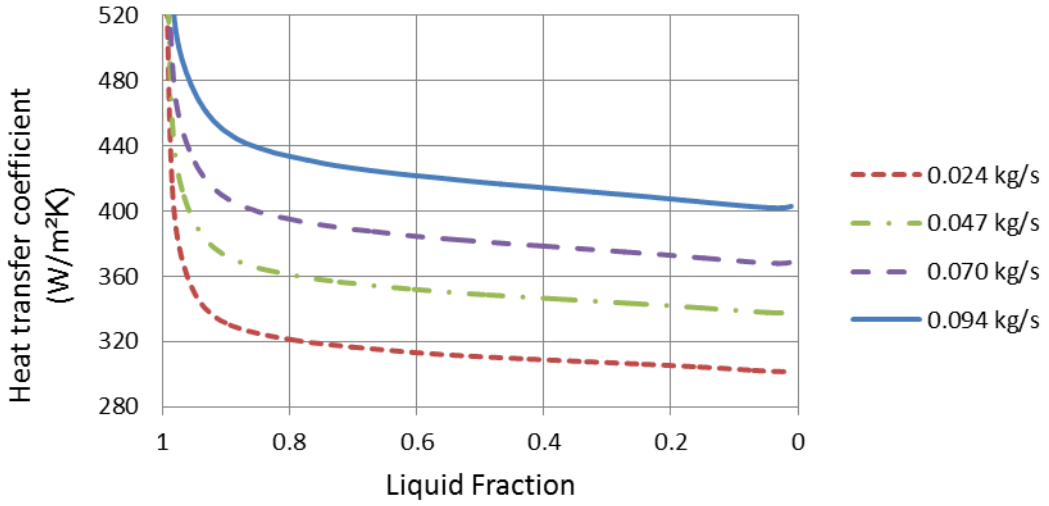

Figure 6.24 Heat transfer coefficient for the solidification process as function of HTF mass flow rate and liquid fraction

6.7 Conclusions

In this Chapter, the various heat transfer enhancement methods suitable for LHS systems for parabolic-trough plants using synthetic oil as HTF were reviewed. It was found out that the use of fins is the most suitable and practical. CFD simulations considering the discharging of a single finned segment showed that increasing the fin outer radius above 48.8 mm does not result into any performance benefit and a fin configuration having distance between fins of 10 mm, fin thickness of 1 mm was found to be the best configuration.

During the charging process convection plays a role in the heat transfer and thus the heat transfer coefficient during the melting and overheating process (after melting) will be PCM dependent. Relationships that can be used for the determination of the heat transfer coefficient during melting (equation (6.4)-(6.6)) were determined for each PCM. Charts from which the heat transfer coefficient during overheating can be obtained were presented.

During the discharging process pure conduction is the main mode of heat transfer and the heat transfer coefficient during solidification depends on the

liquid fraction and the HTF mass flow rate (velocity). A linear function based on liquid fraction was developed for the determination of the heat transfer coefficient (equation (6.8)). The obtained correlations can be used to determine the performance of a complete finned LHS system.

7 ANALYSIS OF A COMPLETE STORAGE SYSTEM

In this chapter the modelling and simulation of the HCSS which consist of three finned LHS and CTR modules arranged in series (Figure 1.2) was conducted. A single HCSS element was considered and the heat transfer coefficients obtained in Chapter 6 were used. The performance of a single storage element was then used for the design of an 875 MWh_{th} capacity system, suitable for 6 hour full load turbine operation of a 50 MW_e plant. The capital cost of the system was also obtained.

The Dymola Simulation environment which is based on the Modelica language was used for the modelling and simulation. The Techthermo library [31] which contains different models for basic processes of heat transfer (conduction and forced convection), control volumes, and pressure drop models was also used in order to reduce the amount of modelling effort required.

7.1 Cascaded Finned Latent Heat Storage (LHS) Element Modelling

A finned LHS module consist of parallel single finned tubes (or elements) of identical performance (Figure 7.1(a)). Thus the capacity of the PCM module can be obtained by multiplying the capacity of the single finned element with the total number of parallel elements in the module. Considering a single finned element (Figure 7.1(b)), the bulk mean temperature of the HTF changes as it flows through the tube. To capture this, the element will be divided into axial segments. In each axial segment the heat transfer is one dimensional. It will be assumed that the fins and the PCM in the annular gap is a composite material or one material with an effective thermal conductivity. Thus the models of finned segments (Figure 7.1(c)) can be placed in series to form a complete model of a finned LHS element. The finned LHS element can be connected to each other in series to form a cascaded finned LHS element, with each cascade having different PCM.

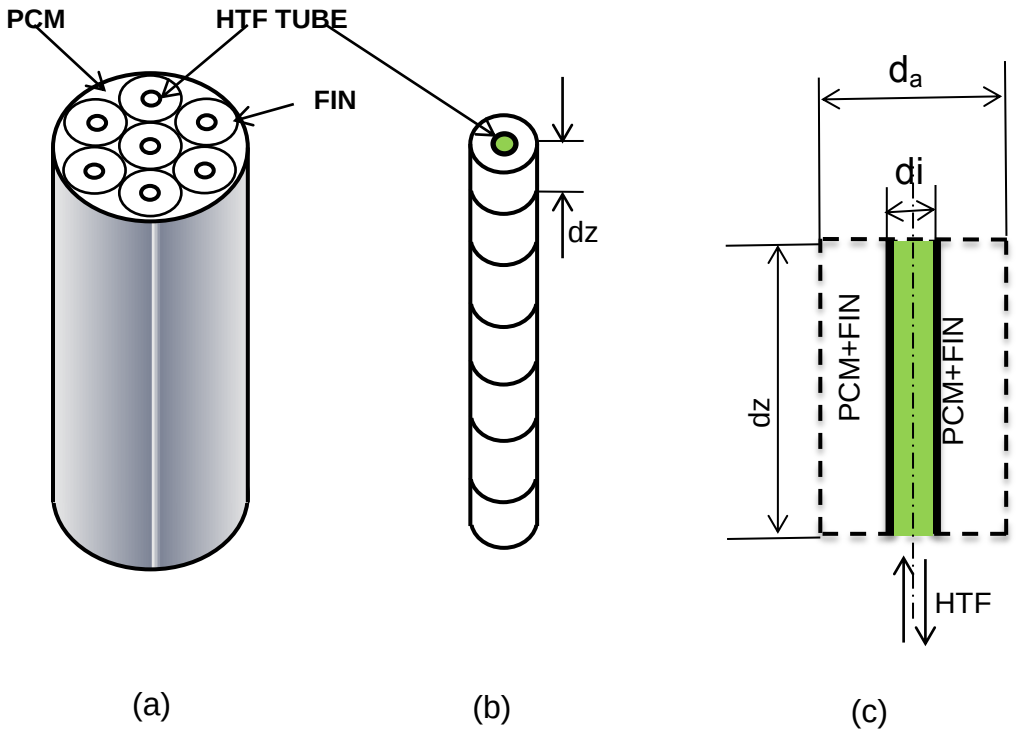

Figure 7.1 Physical model of the finned storage element

7.1.1 Finned Segment Model

The segment model is divided into two sub models:

- The HTF-flow in pipe model
- The finned annular gap model

Dymola allows the building of individual physical models and joined together to form a complete model. Figure 7.2 presents the structure of the finned segment model which can be arranged in series to form a finned-LHS and cascaded finned-LHS element models. The thermo-physical properties of both the HTF and PCM are inputs to the HTF and annular gap models respectively.

7.1.1.1 HTF-Flow in Pipe Model

In the HTF-flow in pipe model, the heat absorbed or released by the HTF and the pressure drop as the HTF flows through the segment is calculated. In the HTF pipe, heat is transferred between the HTF and the pipe inner wall by forced convection causing the change in the temperature of the HTF from the inlet to outlet. The thermal resistance of the HTF pipe wall will then determine the temperature outside the HTF-pipe wall surface in contact with the PCM. Thus energy balance in the HTF is represented in Figure 7.3 and is given by:

$$\dot{m}_{htf}(h_{in} - h_{out}) = \dot{Q}_{to\ PCM} + \dot{m}_{htf}\frac{dh_{mean}}{dt} \tag{7.1}$$

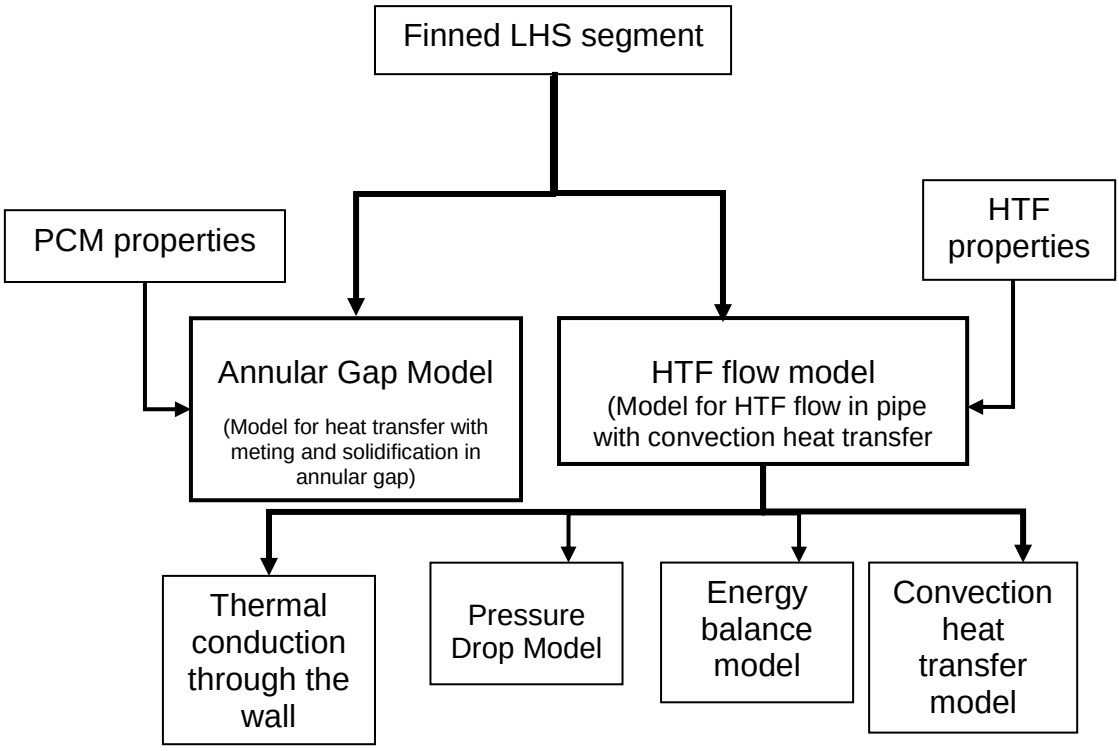

Figure 7.2 Structure of the finned segment model

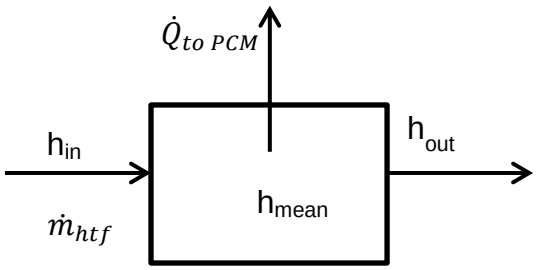

Figure 7.3 Energy Balance for HTF flow in pipe

The second term in the RHS of equation (7.1) represents the heat transferred due to the change in the mean enthalpy (mean HTF temperature) with time and the first term represents the heat transferred through the wall to the PCM given by:

$$Q_{to\ PCM} = h_{fc} 2\pi r dz \left(T_{htf} - T_{wi}\right) = 2\pi dz k_w \left(\frac{T_{wi} - T_{wo}}{ln\left(\frac{r_o}{r_i}\right)} \right) \qquad (7.2)$$

The average HTF temperature in the segment, T_{htf} is obtained from a relationship between the enthalpy and the temperature of the HTF.

The transient second term in equation (7.1), was neglected in order to simplify the model since its effect will cancel out over a complete charging and discharging cycle. Equations (7.1) and (7.2) are solved and the unknown wall temperature, the heat transfer rate and the HTF outlet temperature are determined. It will be observed that these equations cannot be solved without knowing the outside wall temperature T_{wo}. This temperature will be determined when the model is joined with the annular gap model. The enthalpy and other thermo-physical properties (density, specific heat and viscosity) are obtained as functions of temperature from the property table of therminol VP-1 [159].

The “Techthermo” library contains models for the calculation of forced convection heat transfer coefficient, heat transfer through a wall with/without storage. These were used to represent the forced convection heat transfer and

the heat transfer through the wall. A model was built that will provide the required thermodynamic and thermo physical properties of the HTF (HTF property model). In the model the enthalpy is represented as a function of temperature (in ^{o}C) by:

$$h_{htf} = 1.4(T^2) + 1496.8(T) - 18175$$

Alternatively the enthalpy can be calculated from the specific heat capacity thus:

$$h_{htf} = C_p\left(T - T_{ref}\right) + h_{ref}$$

The specific heat capacity and thermal conductivity were assumed to be constant and are calculated at an average temperature before the start of the simulation. This was done to reduce the complexity of the model to prevent numerical instabilities. They are calculated using a four degree polynomial as follows:

$$C_p = 2.414(T) + 5.9591 \times 10^{-3}(T^2) - 2.9879 \times 10^{-5}(T^3) + 4.4172 \times 10^{-8}(T^4)$$

$$k_{htf} = 0.137743 - 8.19477 \times 10^{-5}(T) - 1.92257 \times 10^{-7}(T^2) + 2.5034 \times 10^{-11}(T^3) - 7.2974 \times 10^{-15}(T^4)$$

Other thermo physical properties such as the density, dynamic viscosity can either be assumed constant or calculated as a function of temperature using a linear gradient between two known temperatures or using a function. The function for the density and dynamic viscosity are presented in equations (7.3) and (7.4) respectively. The Modelica code for the HTF property model is presented in section B.1.1 in Appendix B.

$$\rho_{htf} = 1083 - 0.90797(T) + 7.8116 \times 10^{-4}(T^2) - 2.367 \times 10^{-6}(T^3) \qquad (7.3)$$

$$\mu_{htf} = \frac{806.78(t^{-1.438})}{1000} \qquad (7.4)$$

Finally the pressure drop across the segment is calculated by assuming a smooth pipe using the friction coefficient that was obtained using the Blasius equation. This model is already available in the “Techthermo” library and was used for pumping power calculations. Figure 7.4 presents the schematic diagram of the whole HTF-flow in pipe model, with three connectors: The inlet and outlet mass flow connector which has the enthalpy, pressure and mass flow variables. These connectors connect adjacent HTF-flow in pipe models. The third connector is the Heat-flow connector which has the heat flow and temperature variables and is connected to the finned annular gap model.

7.1.1.2 Finned Annular Gap Model

In the modelling of the finned annular gap the fin is assumed to only contribute to the increase in the effective heat transfer (thermal conductivity) into/out of the PCM. Thus it does not contribute to the storage capacity. In Section 6.6, the heat transfer coefficient in the finned annular gap for the selected configuration has been determined. It will be assumed that the PCM occupies the annular gap as a concentrated mass exchanging heat with the HTF flowing through the pipe and there is no heat transfer from one segment to the other (i.e in the axial direction). The difference in the heat transfer mechanisms and characteristics during the charging and discharging as was seen in section 6.6, necessitated the need to consider each process separately so that the peculiarities of the charging and discharging processes are captured effectively.

Keeping in mind that the PCM is assumed to be a lumped mass, initially at the start of charging the PCM is at a temperature lower than the melting point and heat transferred from the HTF causes increase in the temperature of the PCM until the melting temperature is reached. The average PCM temperature remains constant until all the PCM has melted and the average PCM temperature starts to increase until there is no driving temperature difference.

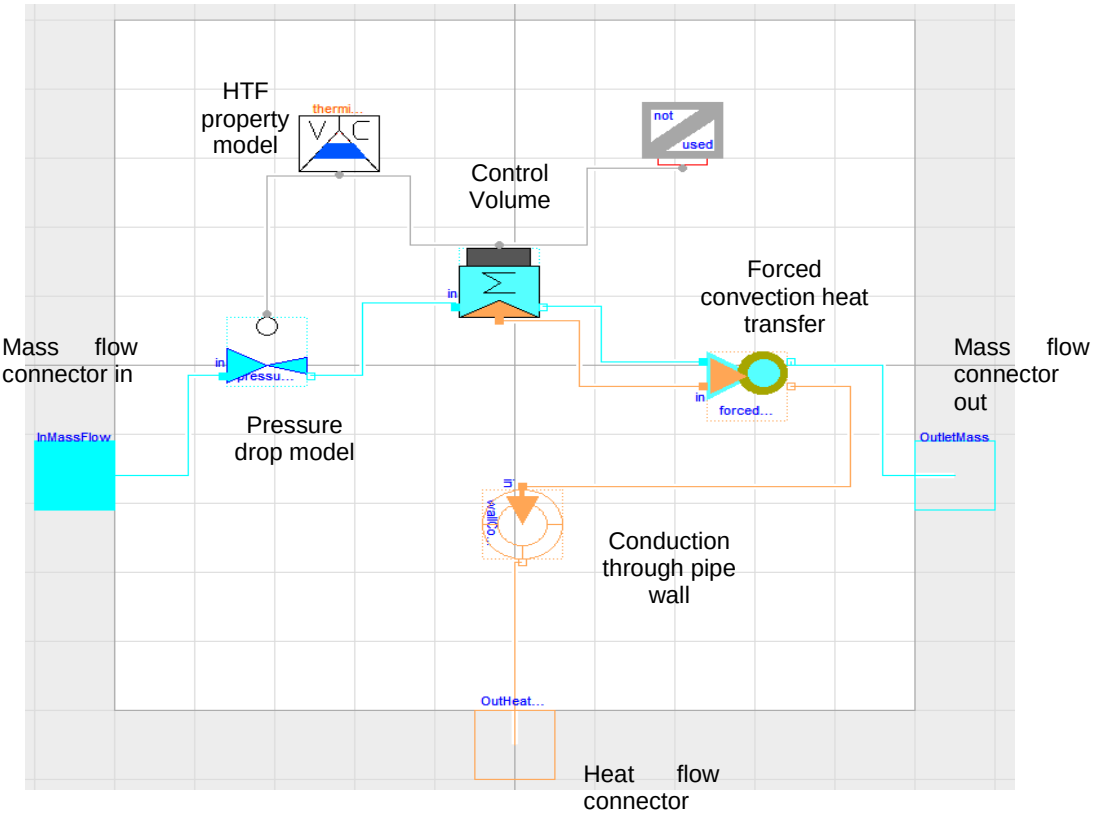

Figure 7.4 Schematic diagram of the HTF flow in pipe model

The discharging process is opposite to the charging process. Figure 7.5 shows this. In order to include the latent heat of fusion, the effective heat capacity method was used by assuming that phase change occurs over a small range of temperature ΔT_m (Figure 7.5). Thus the specific heat capacity during phase change is given by:

$$c_{p,pcm,m} = \frac{\lambda}{\Delta T_m} + \frac{c_{p,pcm,s} + c_{p,pcm,l}}{2}$$

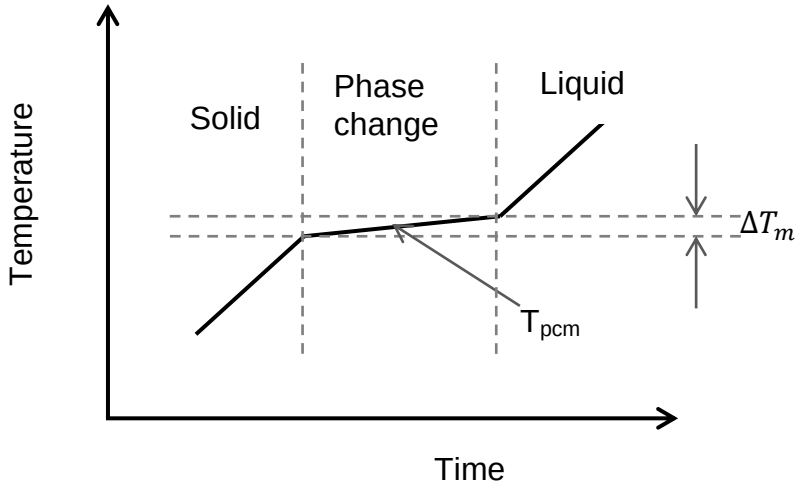

Figure 7.5 The charging and discharging processes

The transient change in temperature of the PCM is calculated using the equation:

$$\dot{Q}_{to\ PCM} = m_{pcm} c_{p,pcm} \frac{dT_{pcm}}{dt}$$

Where $c_{p,pcm}$, is the specific heat capacity of the PCM and is different for the three phases is shown in Figure 7.6. To avoid discontinuities in the specific heat capacities the change in specific heat capacity from one phase to the other is assumed linear (Figure 7.6). The PCM state is tracked using the specific internal energy (u) given by:

$$u = c_{p,pcm} T_{pcm}$$

The heat transfer rate through the wall is calculated using:

$$\dot{Q}_{to\ PCM} = hA_o(T_{wo} - T_{pcm})$$

This heat transfer coefficient in the PCM (h) is different for the charging and the discharging process.

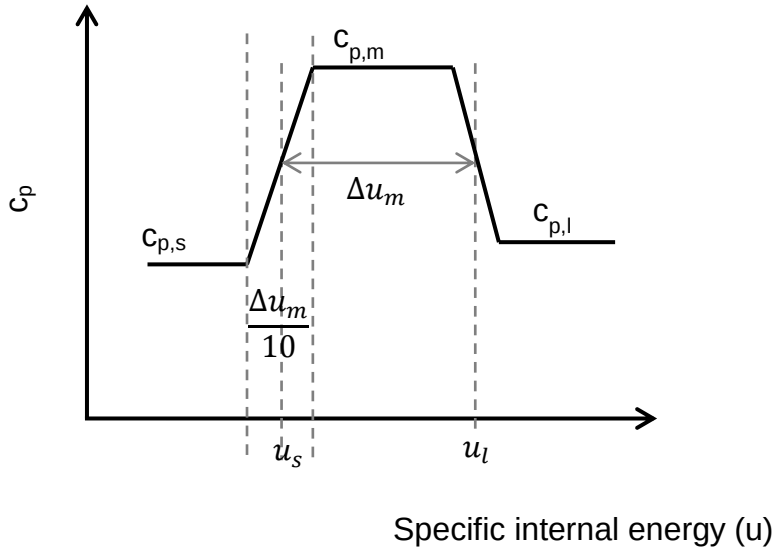

Figure 7.6 Variation of specific heat capacity with specific internal energy

For the charging process the quasi-stationary heat transfer coefficient obtained in equation (6.4)-(6.6) for each PCM was used when the PCM is solid and during melting. When the PCM is liquid the heat transfer coefficient obtained in Figure 6.18 was used. Section A.1 in Appendix A presents how a relationship for this heat transfer coefficient was obtained. For the discharging process the heat transfer coefficient during solidification was found to vary linearly with liquid fraction and was represented in equation (6.8) by a linear function of the liquid fraction for each HTF mass flow rate. Section A.2 in Appendix A presents the equations solved in the annular gap model.

Finally the model was implemented in Dymola having two heat flow ports. One that will be connected to the HTF flow model and the other will be insulated. The thermo-physical properties of the PCM were implemented as a separate data model. In sections B.1.2 and B.1.3 of Appendix B, the Modelica code for the PCM property and annular gap models respectively are presented using $NaNO_3$ PCM as example. To make the other annular gap models the PCM thermo-physical properties are changed in the property model.

7.1.2 The Segment and Developing Cascaded Element Model

Figure 7.7 presents the Dymola segment model consisting of the HTF flow model and the annular gap model joined together. The two green rectangles are data models for the pipe wall thermo-physical properties and the segment geometry. To form the cascaded finned LHS element, segment models for each PCM were developed by using a PCM property model for each PCM. Many segments of each PCM were then joined together to form a finned LHS element model and these elements can be joined in series to form the cascaded finned LHS element. The “Directional Signal” (Blue inverted triangle in Figure 7.7) is an input that determines the charging and discharging processes. In the model the height of each segment (dz) is determined from the total height of the cascaded finned LHS element and the number of axial segments. The Modelica code for the cascaded finned LHS is presented in section B.1.4 of Appendix B.

7.1.3 Validation of the Segment Model with CFD Results

In this section simulation result from the Dymola segment model for a single finned-LHS segment were compared with CFD results obtained in section 6.6 using $NaNO_3$ PCM.

7.1.3.1 Charging

Figures 7.8 and 7.9 presents the comparison of CFD and Dymola model results for a single finned LHS segment for HTF mass flow rate of 0.094 kg/s at different temperature differences between the average HTF temperature and the PCM melting temperature ($T_{htf} - T_m$). Initial PCM temperature of 286.5^oC was used. The heat transfer rate and average PCM temperature are almost the same especially during the melting process and the time to reach end of melting are also very close. From Figure 7.8 the heat transfer rate at the end of melting shoots up. This is due to the discontinuity of the heat transfer coefficient since the coefficient for overheating is different from that of melting during the charging process.

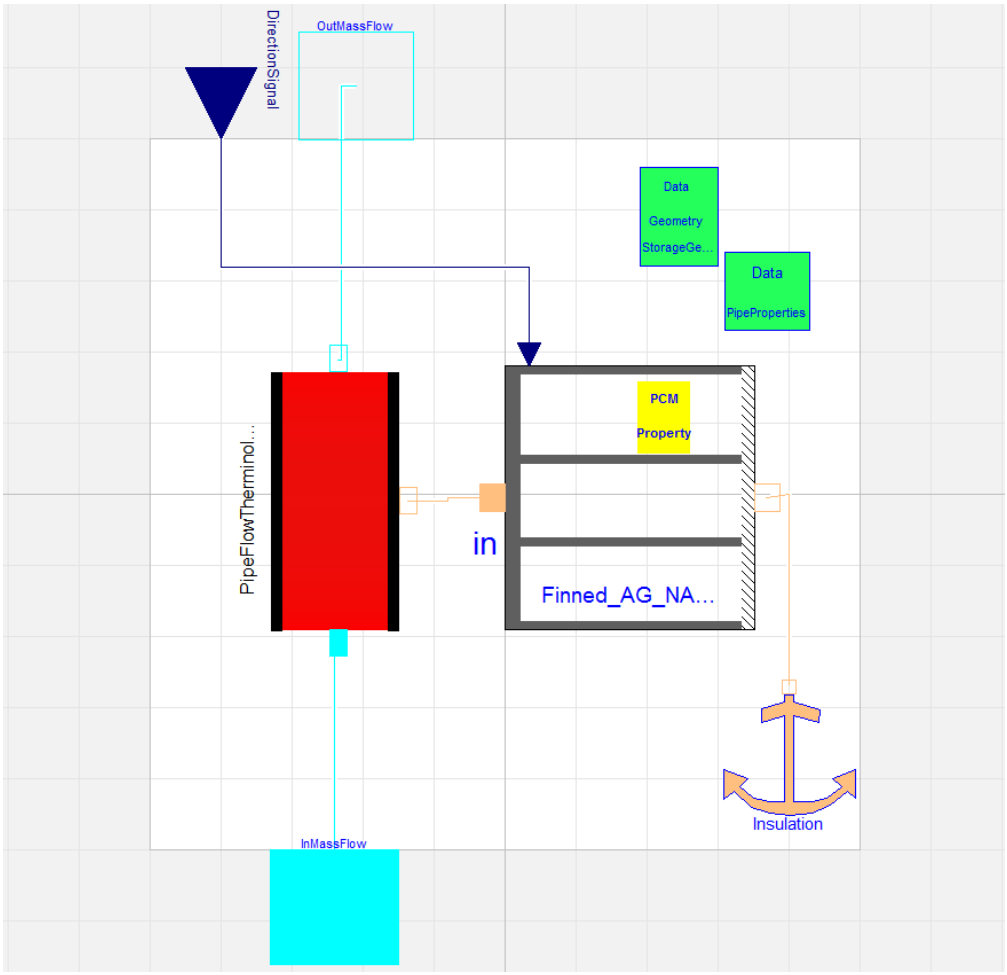

Figure 7.7 Dymola finned LHS segment model

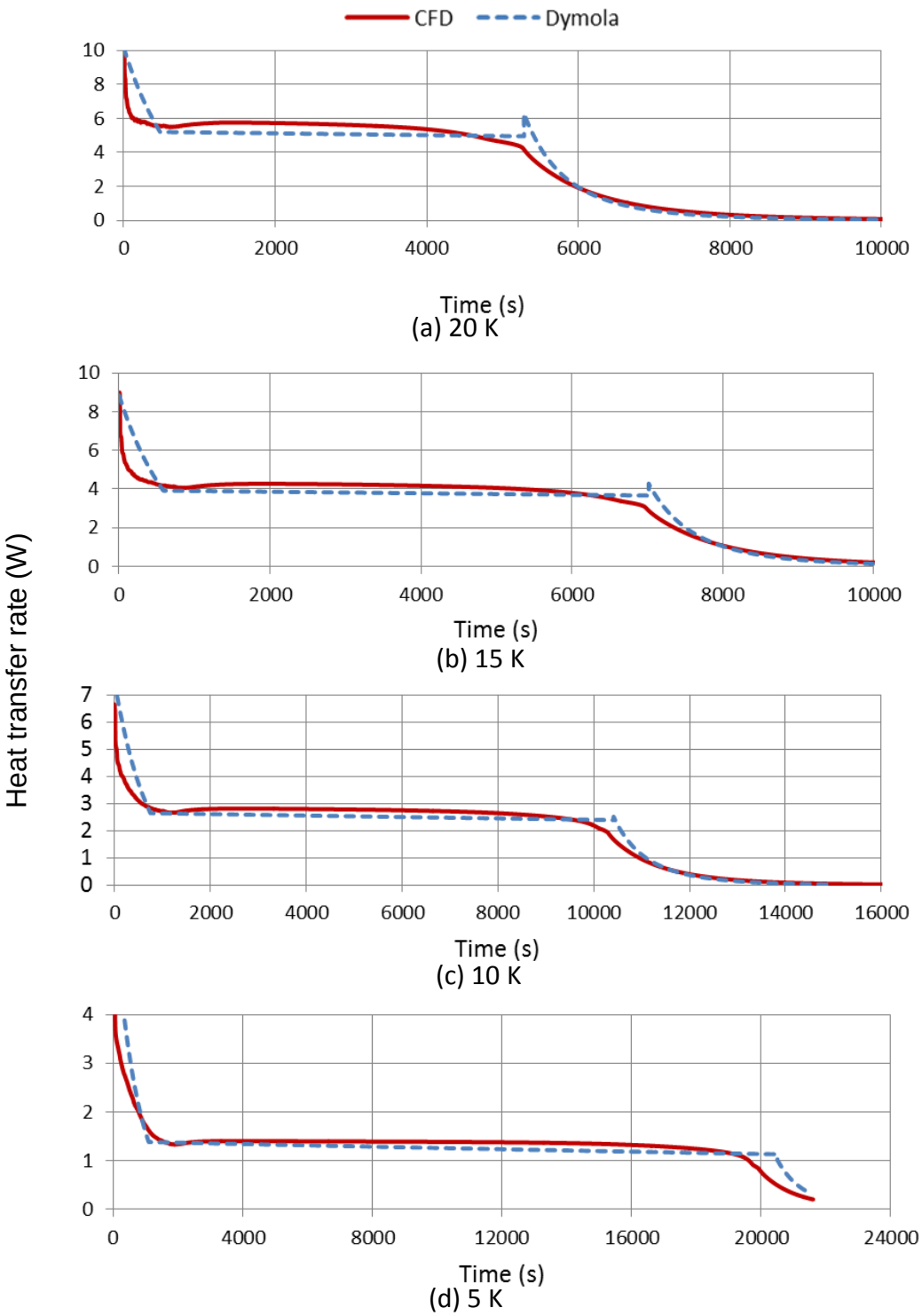

Figure 7.8 Heat transfer rate comparison between CFD and Dymola model result for the charging of a single finned LHS segment at different temperature differences ($T_{htf} - T_m$) for HTF mass flow rate of 0.094 kg/s

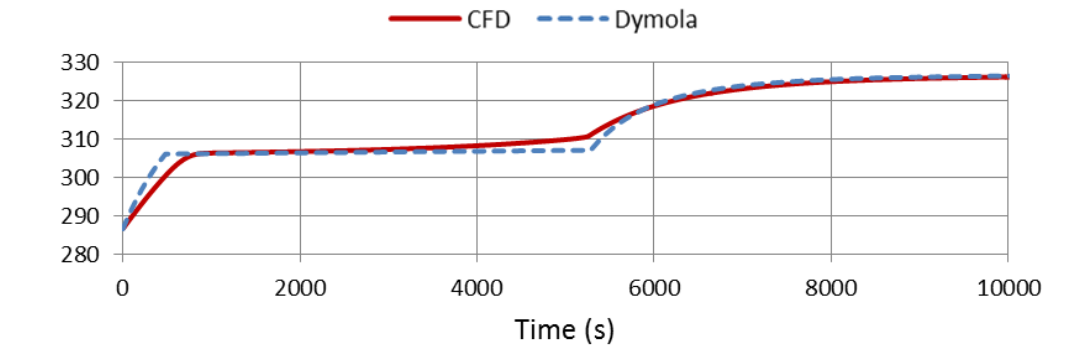

(a) 20 K

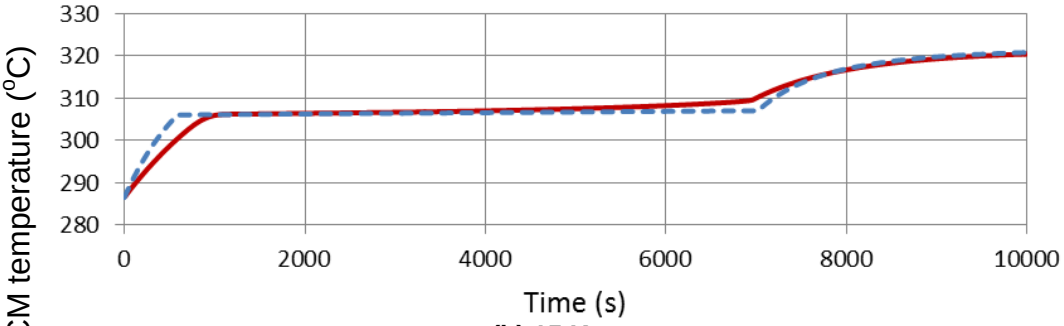

(b) 15 K

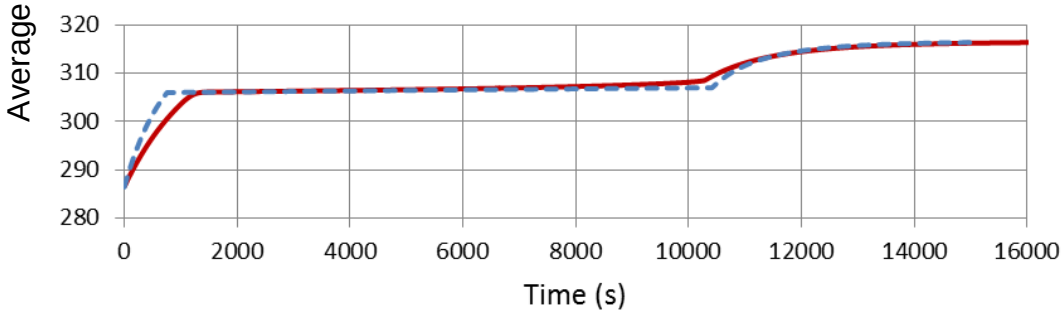

(c) 10 K

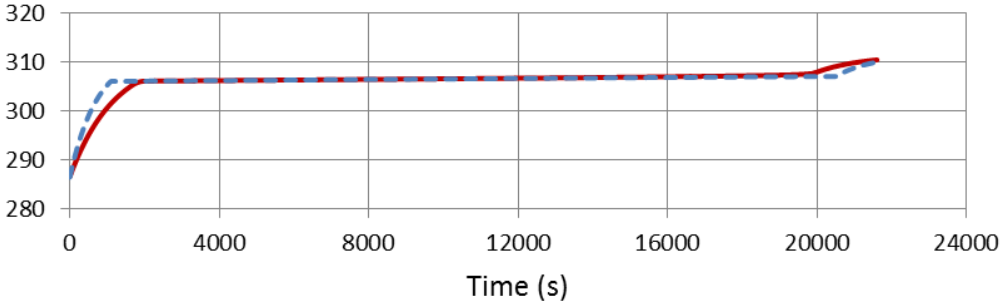

(d) 5 K

Figure 7.9 Average PCM temperature comparisons between CFD and Dymola model result for the charging of a single finned LHS segment at different temperature differences ($T_{htf} - T_m$) for HTF mass flow rate of 0.094 kg/s

7.1.3.2 Discharging

Figures 7.10 and 7.11 presents the heat transfer rate and average PCM temperature comparison respectively, for the CFD and Dymola simulations. Average HTF temperature of PCM of 286.5^{o}C and initial PCM temperature of 327^{o}C were used. There is a very good agreement between the results. Little discrepancies can be observed at the time to complete solidification. The discrepancy in time to complete solidification is 653 s and 1672 s for the 0.094 kg/s and 0.023 kg/s HTF mass flow rates respectively. This is corresponds to an increase in the time to reach the end of solidification of 6.6 % and 10.5 % respectively. This may be due to the high heat transfer rates at the beginning of the discharging process due to contact of the PCM with the HTF-pipe wall which was not captured in the model.

7.2 Concrete Tube Register (CTR) Element Modelling

The CTR is a solid media storage system consisting of an array of tubes embedded in a concrete. The concrete is casted together with the tube array (Figure 7.12). The HTF flows through the tube exchanging thermal energy with the concrete. The feasibility of the CTR as a storage system for parabolic-trough plants have been investigated both at laboratory and pilot scale. A CTR module is thus composed of many storage elements (single tubes surrounded by the storage material) neglecting the storage material in between adjacent elements.

7.2.1 Material Suitable for Concrete Tube Register (CTR) Storage

Among all thermal storage materials, concrete is the cheapest [8]. For parabolic-trough plants, CTRs were first investigated in lab scale in the Centre for Solar Energy and Hydrogen Research (ZSW), Germany [182]. Apart from the requirement of good thermo-physical properties, concrete must have a thermal expansion similar to that of the tube register, cyclic stability with no degradation in performance for thousand cycles, be easy to handle, have good contact with the tube register and low cost.

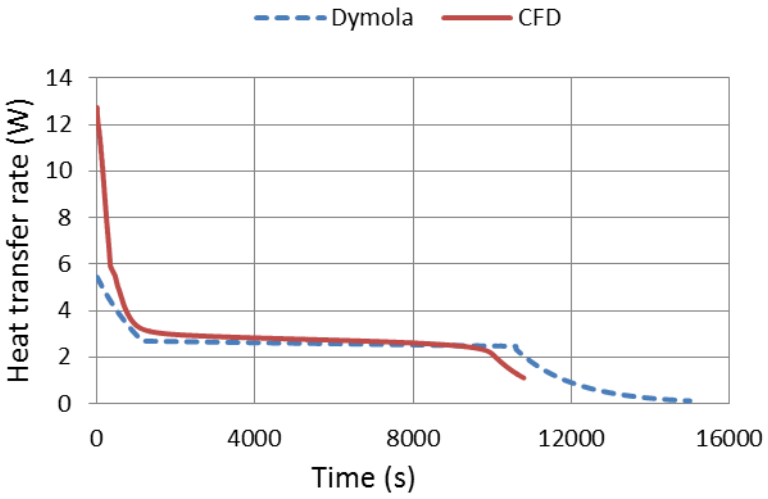

(a) 0.094 kg/s

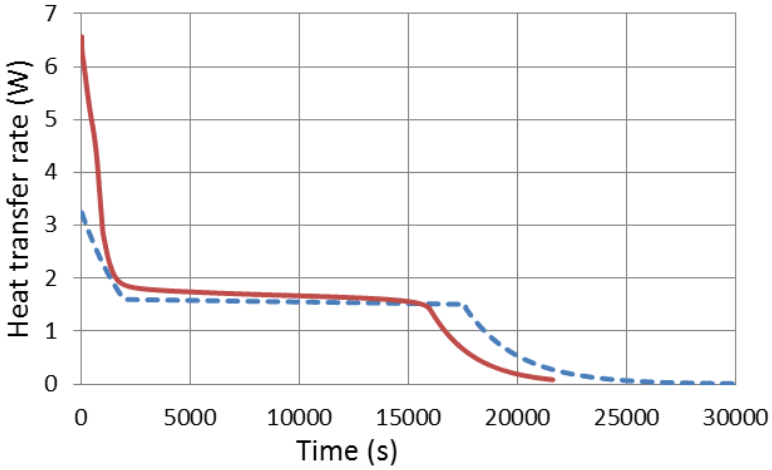

(b) 0.023 kg/s

Figure 7.10 Heat transfer rate comparison between CFD and Dymola model result for the discharging of a single finned LHS segment for HTF mass flow rates of (a) 0.094 kg/s and (b) 0.023 kg/s

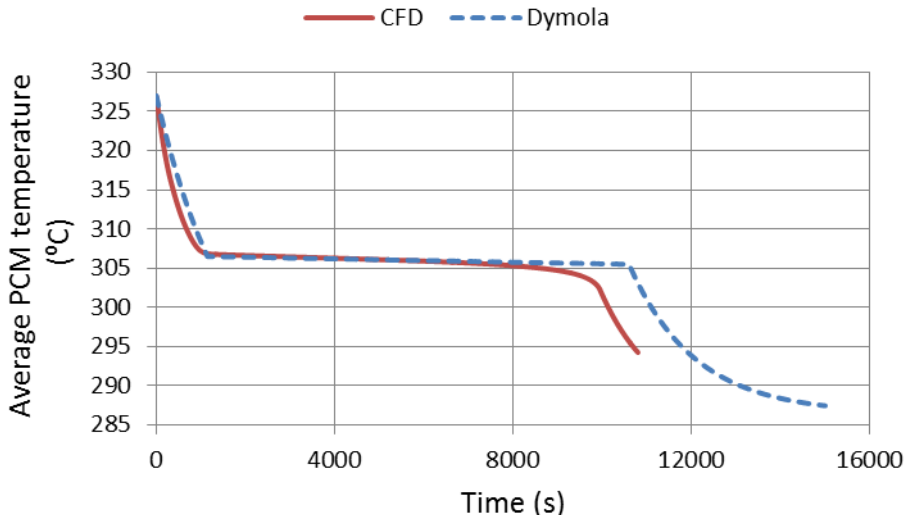

(a) 0.094 kg/s

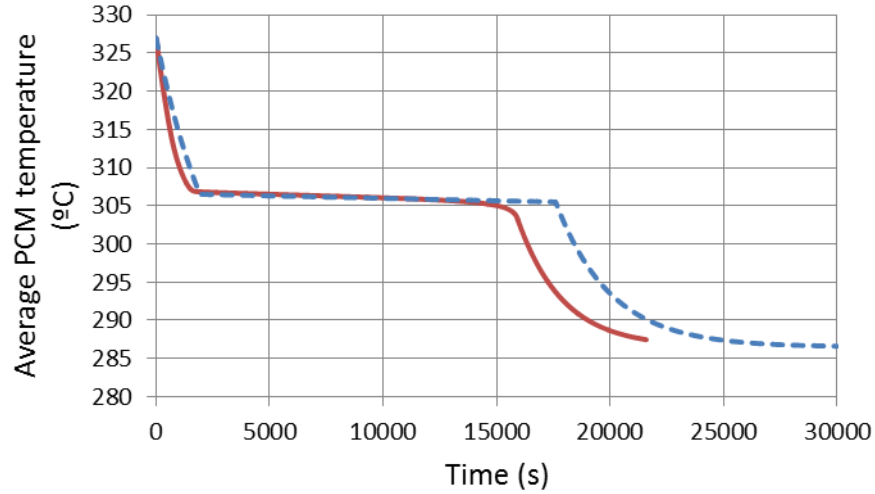

(b) 0.023 kg/s

Figure 7.11 Average PCM temperature comparison between CFD and Dymola model result for the discharging of a single finned segment at HTF mass flow rates of (a) 0.094 kg/s and (b) 0.023 kg/s

Figure 7.12 Picture of CTR storage module [183]

Over the years considerable research has been done in the development of suitable concrete materials for use in CTR. Initially four concrete materials were proposed and investigated at lab scale [94]:

- Basalt concrete
- Sand Concrete
- High-temperature concrete: cement binder, Iron oxide and flue ash as main aggregate and other auxiliary materials
- Castable Ceramic: composed of Al_2O_3 binder with Iron oxide and other material as main aggregates and other auxiliary materials.

Properties of these materials are presented in Table 7.1. Initial tests proved the non-suitability of basalt and sand concrete. This makes castable ceramic and high-temperature concrete as the two possible options. Various compositions of the aggregates in high temperature concrete and castable ceramic have been investigated and densities ranging from 1780-2320 kg/m^3 and 3300-3660 kg/m^3

Table 7.1 Properties of concrete storage materials [94]

Material	Sand concrete	Basalt concrete	Castable ceramic	High temperature concrete
Density (kg/m^3)	2050	2340	3400	2400
Specific heat capacity (J/kgK)	940	920	940	970
Thermal conductivity (W/mK)	1.1	1.4	1.4	1.2
Coefficient of thermal expansion [10^{-5}/K]	8-10	10	12.3	10.5

have been obtained for high temperature concrete and castable ceramic respectively [184]. Live test with storage modules (castable ceramic and high-temperature concrete) having capacities of 350 kWh_{th} have shown that castable ceramic has 20% higher capacity and 35% higher thermal conductivity than high temperature concrete [95]. But the high-temperature concrete is easier to handle and stronger. Both materials are suitable but high-temperature concrete has lower cost and thus is the most suitable. Other factor to consider in the design of CTR is the ability of the concrete to release embedded water (as steam) during operation (thus the concrete should be permeable to steam). This is because at initial start up the concrete will need to be dried.

This led to further test on the high temperature concrete storage units with a storage module having a volume of 20 m^3 called the N4-concrete [92]. The N4-concrete consist of blast furnace cement as binder, temperature resistant gravel and sand, and polyethylene fibre to improve permeability. Test has been conducted for over 370 charging and discharging cycles with no degradation in performance [13; 96]. Table 7.2 presents the thermo-physical properties of the N4-concrete. Py et al. [185] proposed the use of vitrified wastes containing asbestos (recycled industrial ceramic) as solid media storage which can be cheaper than high-temperature concrete.

Table 7.2 Thermo physical properties of N4 concrete and Vitrified ACW [13; 185]

Material	N4 concrete		Vitrified ACW
	Equation	Value range	
Density (kg/m^3)		2250	3120
Specific heat capacity (J/kgK)	$0.7 + 8.75 \times 10^{-4}T(℃)$	720-1050	800-1034
$\rho c_p\ (kJ/m^3K)$		1620-2362	2496-3226
Thermal conductivity	$1.467 - 6.667 \times 10^{-4}T(℃)$	1.45-1.2	2.1-1.4
Coefficient of thermal expansion [10^{-6}/K]	-	11.6	8.8

The material developed has the potential of reducing the cost of the storage and also a means of recycling waste. The cost of the raw industrial ceramic is about 10 times lower than that of concrete. The thermo-physical properties of the material (Vitrified ACW) are also presented in Table 7.2. They also have the potential of eliminating the need for the tube register which forms the major cost of the CTR. Nonetheless there is still much to do in terms of the production and testing of a storage module using this material and thus it is at a primitive research stage. This thus means that high-temperature concrete is the most matured solid media storage material and was used in this research.

7.2.2 Model of Concrete Tube Register (CTR)

The modelling of a CTR storage module can be done by considering only one storage element. Since the storage element is axis-symmetrical, heat transfer in the storage medium will be in two dimensions (radial and axial). The storage element can be divided into smaller axial segments in order to account for the axial heat transfer and change in temperature of the HTF flowing through the pipe. These axial segments can be joined to form a storage element.

The axial segment model consists of the HTF-flow in pipe model (which has been described in detail in section 7.1.1.1) and the annular gap model (concrete annular gap). In order to increase the model's numerical accuracy, the concrete annular gap was divided into radial elements. The transient heat transfer into or out of the concrete is calculated using the one dimensional conduction equation considering the annular gap as a hollow cylinder. Thus energy balance in the annular gap is given by:

$$\dot{Q} = k_{conc} A_o \frac{dT_{conc}}{dr} = m_{conc} c_{p,conc} \frac{dT_{conc}}{dt}$$

Consider a single annular gap, j with n radial discretization (elements) as shown in Figure 7.13 and assuming the average temperature of each radial element to be at the centre of the element. Energy balance for radial element, i (Figure 7.13b) is given by:

$$m_i c_{p,conc} \frac{dT_i}{dt} = \dot{Q}_{j,i-1} - \dot{Q}_{j,i} + \dot{Q}_{j-1,i} - \dot{Q}_{j+1,i}$$

Where:

$$m_i = \rho_{conc} \times \pi dz((r_i + idr)^2 - (r_i + (i-1)dr)^2)$$

The radial heat transfer in and out of the element ($i.e. \dot{Q}_{j-1,i}\ and\ \dot{Q}_{j+1,i}$) can be obtained using the one dimensional conduction equation:

$$\dot{Q}_{j,i} = 2\pi kdz \left(\frac{T_{j,i} - T_{j,i+1}}{ln\left(\frac{r_{i+1}}{r_i}\right)} \right)$$

The outer surface of the storage-element is assumed to be insulated since it is the point where two adjacent storage-elements meet. Thus $\dot{Q}_n = 0$ and the equation for heat flow for the first radial element adjacent to the HTF-pipe wall is given by:

$$\dot{Q}_{in} = 2\pi kdz \left(\frac{T_{j,wo} - T_{j,1}}{ln\left(\frac{r_1}{r_o}\right)} \right)$$

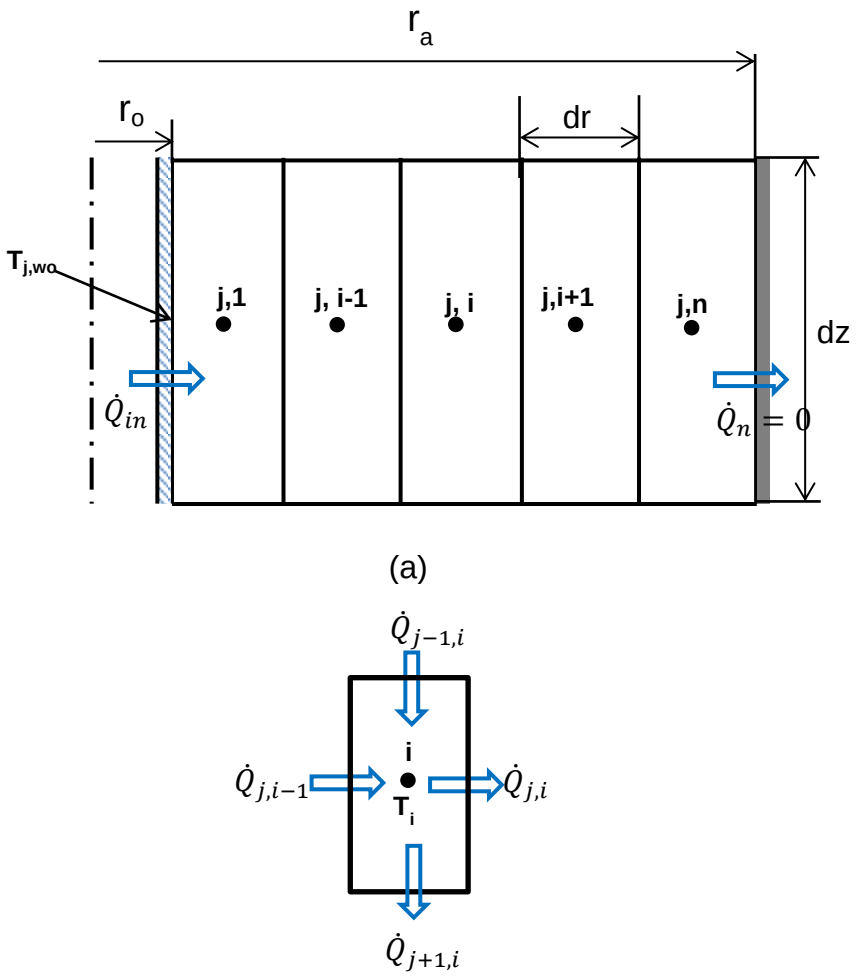

Figure 7.13 Model for a single concrete annular gap segment

The axial conduction heat transfer is calculated using:

$$\dot{Q}_{j,i} = k_{conc}(\pi(r_{i+1}^2 - r_i^2)\left(\frac{T_{j-1,i} - T_{j,i}}{dz}\right)$$

These equations are formulated for each element and solved. The model was implemented in Dymola by modifying the already available cylinder conduction model in the “TechThermo” Library. The annular gap model was connected to the HTF-flow in pipe model to form the segment model. Various axial segment models are then connected to form a CTR storage-element.

7.2.3 Test of Annular Gap Model

A single annular gap model with height (dz) of 0.1 m, outer storage element radius (r_a) of 0.4 m, inner radius of HTF-pipe of (r_i) of 0.01 m, HTF pipe wall thickness of 0.001 m was used for the testing of the annular gap model. The properties of the storage material are that of castable ceramic (density =3500 kg/m^3, specific heat capacity =866 J/kgK, thermal conductivity =1.35 W/mK). A constant wall temperature of 390^{o}C and 350^{o}C were imposed on the HTF pipe wall during charging and discharging respectively with an initial storage temperature of 350^{o}C at the start of charging. Charging and discharging duration of 1 hr each with a break of 1 hr in between charging and discharging were used. The annular gap was divided into five radial elements in order to see the radial temperature gradient in the storage. Figure 7.14 presents the temperature of each radial element for a complete cycle.

It will be observed that at the end of charging there is a radial temperature gradient in the annular gap. During the break period the temperature gradient tries to equalize thus reducing the temperature of the element adjacent to the HTF-pipe wall. Thus the outer radius of the CTR must be chosen in such a way that this effect is minimized.

7.2.4 Concrete Tube Register (CTR) Model Validation

7.2.4.1 Validation with other Similar Model Result

Tamme et al. [97] presented the analysis of a CTR for parabolic-trough plants using a model developed based on the same concept used in this modelling. The CTR analysed has a HTF inner pipe diameter of 0.02 m, thickness of 0.001m, outer storage element diameter of 0.08 m and a length of 500 m. Concrete (density=2,200 kg/m^3, specific heat capacity= 1,000 J/kgK, and thermal conductivity=1.2 W/mK) was used as storage material.

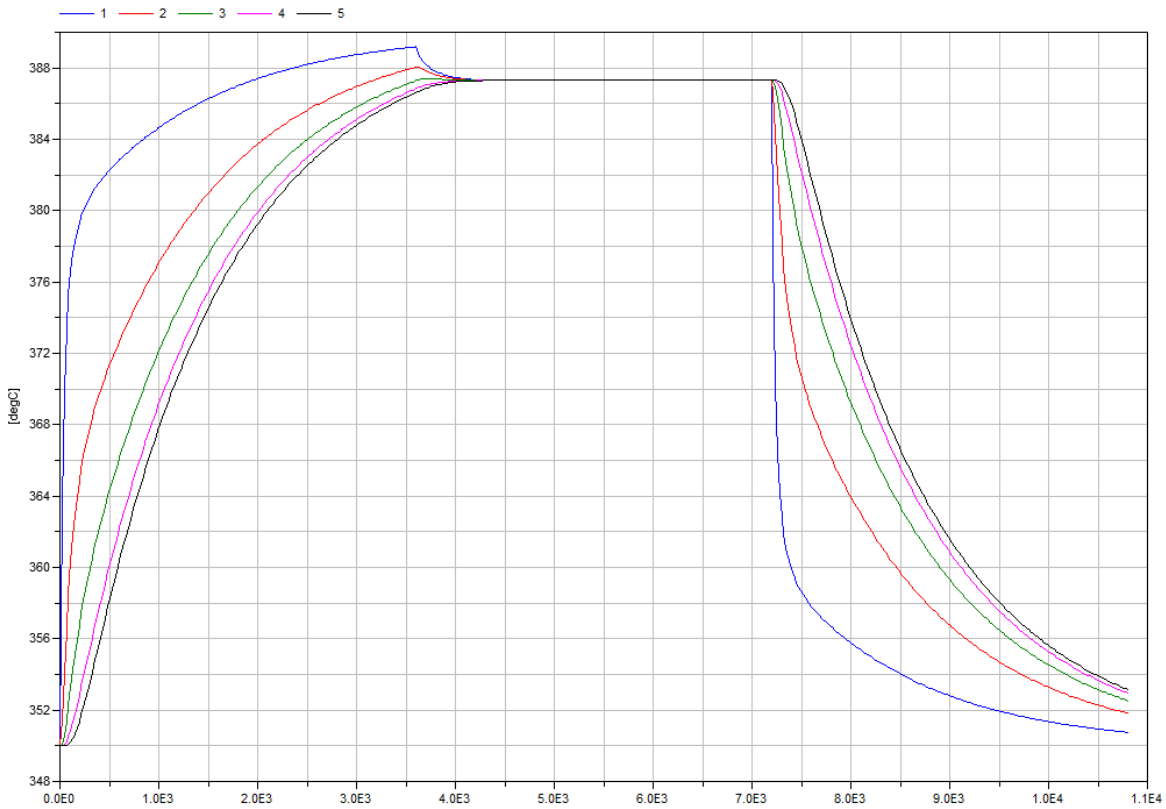

Figure 7.14 Temperature distribution in concrete annular gap using castable ceramic as storage material and considering one axial segment

The HTF inlet temperature of 390^{o}C and 265^{o}C were used during charging and discharging respectively. Charging and discharging duration were 1 hour each with a break of 15 minutes in between. The HTF mass flow rate was adjusted until the storage requirements for parabolic-trough plant were achieved (i.e. maximum HTF outlet temperature of 315^{o}C during charging and minimum HTF outlet temperature of 350^{o}C during discharging).

Several simulations, using different HTF mass flow rates and initial storage temperature of 265^{o}C were conducted to find the HTF mass flow rate that satisfies the above requirements. For each mass flow rate the simulation was run for about 20 cycles in order to have a periodically balanced state. A mass flow rate of 0.25 kg/s was found to satisfy the requirements. Figure 7.15 presents the comparison of the HTF temperature distribution along the storage

length between the results of this model and those of Tamme et al. [97] at the start and end of charging and discharging.

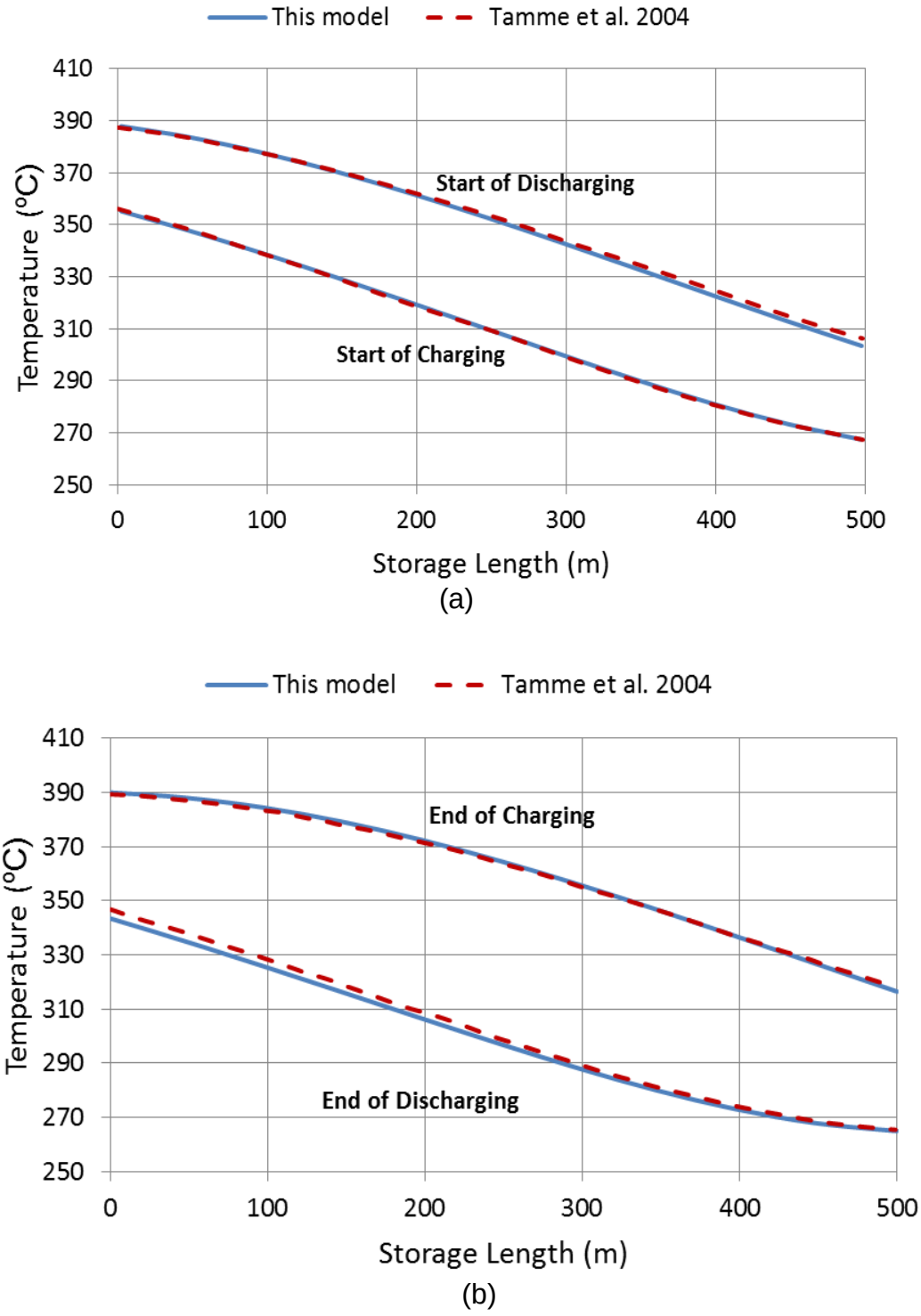

Figure 7.15 Comparison of Temperature distribution of HTF along the length of the storage between this model and that of Tamme et al. [97] at (a) Start (b) End, of charging and discharging.

There is agreement between the two simulation results, thus proving the accuracy of the model. The temperature distribution at the end of charging and discharging are different from that at the start of charging and discharging. This is due to the temperature gradient in the storage material at these times and thus during the break period there is equalization of the temperature in the storage. This means that the temperature gradient at these times must be minimized by choosing a suitable distance between HTF-pipes.

7.2.4.2 Validation with Experimental Results

Experiments have been conducted by Laing et al. [95] for the charging and discharging of a CTR. The tube register contains 36 tubes having inner and outer diameters of 0.021 m and 0.025m respectively in square arrangement of 6 by 6 tubes with distance between tubes of 0.08 m. The CTR storage module has a total dimension of 0.48 x 0.48 x 23 m. Castable ceramic was used as storage material (density=3,500 kg/m^3, specific heat capacity=866 J/kgK, thermal conductivity=1.35 W/mK). The storage was run for two cycles between 150^{o}C and 200^{o}C average storage temperatures. Parameters used are presented in Table 7.3. In the paper [95], the HTF inlet temperatures during charging and discharging were not specified. Thus in the simulation HTF inlet temperature of 210^{o}C and 150^{o}C were used. An initial storage temperature of 130^{o}C was used.

The simulation considering a single storage-element with 46 and 5 axial and radial elements respectively was conducted. Figure 7.16 presents the temperature comparisons at the core (fifth radial element) at a position of 1m from the top and bottom for the simulation and experiment. It will be seen that there is agreement between the two results. Figure 7.17 presents the comparison of the heat transfer rate into and out of the storage for the experiment and simulation.

Table 7.3 Parameters used in experiments by Laing et al. [95]

Cycle	HTF Mass Flow rate (kg/s)		Duration (hrs:mins)	
	Charging	Discharging	Charging	Discharging
First	1.7	1.9	2	1:20
Second	1.7	1.9	1:42	1:30

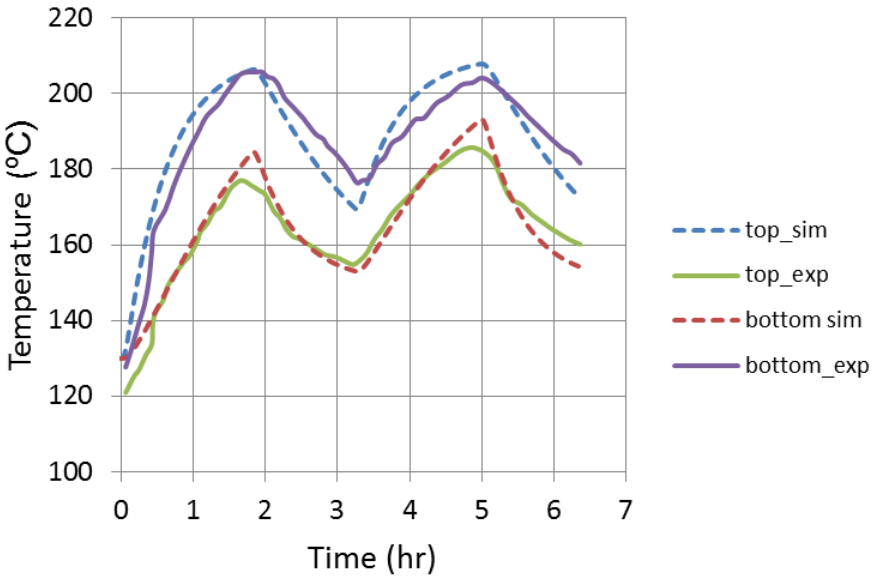

Figure 7.16 Comparison of temperatures at the core (outer element radius) a CTR at a distance of 1m from the top and bottom of the storage module.

Two values of the heat transfer rate were calculated in the experiment: The first was calculated using the measured mass flow rate and the HTF inlet and outlet temperatures using the specific heat capacity of the HTF (Exp:HTF), the second (Exp:Storage) using the average temperature change in the storage and the specific heat capacity of the storage material. In the simulation the heat transfer rate obtained in the single storage element is multiplied by the number of elements to obtain the total heat transfer rate. Considering the way the power was calculated in the experiment and simulation there is a very good agreement between the two results.

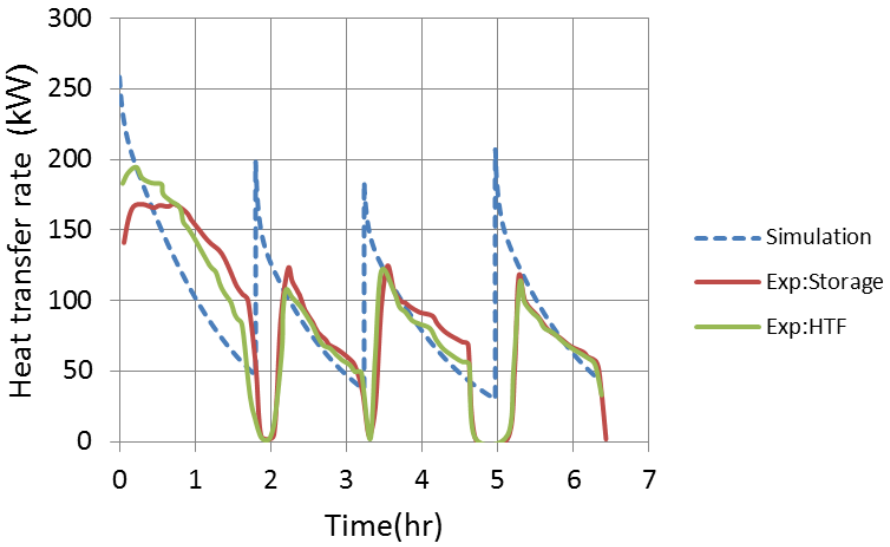

Figure 7.17 Comparison of heat transfer rate to/from concrete storage between experiment and simulation

7.3 Preliminary Design of Cascade and Concrete Tube Register (CTR)

In this section the preliminary design of the cascaded finned-LHS and the CTR was conducted to find the length of each of the finned LHS element that will give the best performance with the least amount of PCM. Also the performance of the CTR needs to be known in order to have an idea of the length required. The HCSS consists of a three stage cascaded finned-LHS and the CTR. The CTR was used to cover the operating temperature range. The boundary conditions of the storage system for the charging and discharging are shown in Figure 7.18.

7.3.1 Cascaded Finned Latent Heat Storage (LHS)

The storage system is connected parallel to the solar field, thus the bottom of the cascaded finned-LHS will be connected to the inlet of the solar field. During charging the inlet temperature of the cascaded finned LHS is determined by the HTF outlet temperature of the CTR.

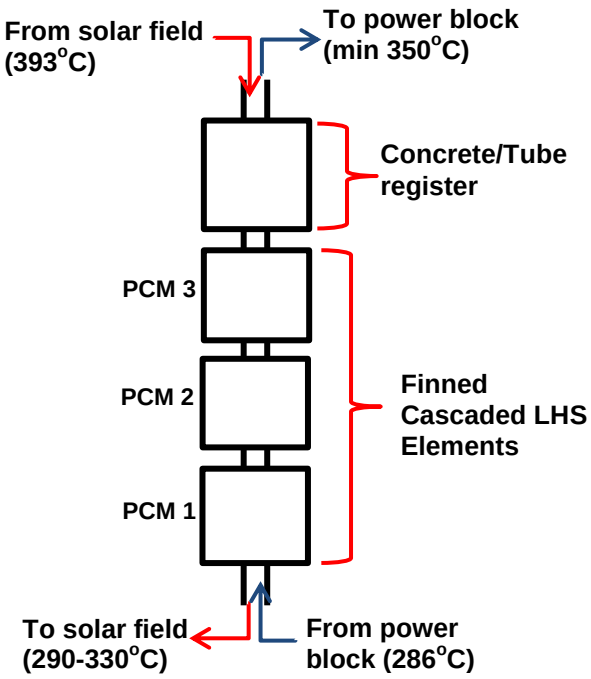

Figure 7.18 Boundary conditions of the storage system

But during discharging the HTF inlet temperature is determined by the HTF outlet temperature of the power block which is 286°C at design point. The length of the cascade and individual finned LHS element was determined considering the discharging process since it is slower.

7.3.1.1 Individual Finned Latent Heat Storage (LHS) Element Length

Considering heat transfer point of view (heat exchanger design) the length of each module must be selected allowing the minimum temperature difference at the end of the cascade (terminal temperature difference) to be very small (1-5°C). The smaller the terminal temperature difference the higher the length of the required heat exchanger (HTF-pipe) and the higher the HTF outlet temperature. A high HTF outlet temperature is required, but it comes with a penalty of higher heat exchanger length meaning higher cost. Thus the length of heat exchanger must be selected by using a compromise between these two variables (i.e terminal temperature difference and length of the heat exchanger). Considering the first PCM ($NANO_3$), HTF inlet temperature of 286°C and HTF

mass flow rate of 0.03 kg/s and initial PCM temperature of 1^{o}C above melting point of the PCM, simulations were conducted considering different length of the HTF-pipe from 5 m to 17.5 m. Figure 7.19 presents the variation of terminal temperature difference and effectiveness with HTF-pipe length. The effectiveness was calculated using the relation:

$$effectiveness = \frac{average\ heat\ transfer\ rate\ during\ phase\ change}{maximum\ posible\ heat\ transfer\ rate}$$

$$effectiveness = \frac{\dot{Q}_{ave}}{\dot{m}_{htf} c_{p,htf} (T_{in,htf} - T_m)}$$

The maximum possible heat transfer rate was calculated considering that the maximum temperature the HTF can reach theoretically is the melting temperature of the PCM during phase change. The terminal temperature difference was obtained from the difference between the melting temperature of the PCM and the time average HTF outlet temperature over the solidification process.

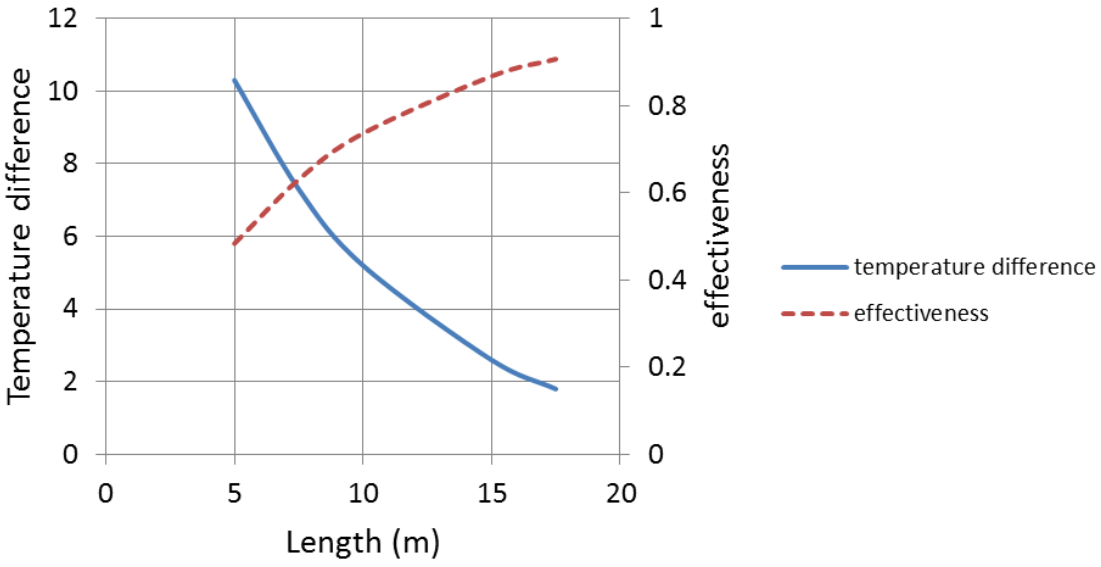

Figure 7.19 Variation of terminal temperature difference and effectiveness with HTF-pipe length for $NANO_3$ PCM.

From Figure 7.19 it will be seen that the temperature difference is an inverse exponential function of the HTF-pipe length and a 4-5^{o} temperature difference can be a compromise with a corresponding heat exchanger effectiveness of 0.75 to 0.8.

Since the main mode of heat transfer during the discharging process is conduction the heat exchanger length for the other two PCMs will thus be expected to be same as that of sodium nitrate. To confirm this similar simulation was conducted using KNO_3/KCl as PCM. Figure 7.20 present the comparison of the terminal temperature difference and effectiveness between the two PCMs. The temperature difference is almost identical. The shapes of the effectiveness graph have similar trends. The small difference in the result can be attributed to the accuracy of the calculation of the effectiveness since the average heat transfer rate, which is a function of liquid fraction, was used. Finally a 5^{o} terminal temperature difference corresponding to finned-LHS element length of 10 m was selected as a good compromise.

7.3.1.2 Cascaded Finned Latent Heat Storage (LHS) Length

Considering a terminal temperature difference of 5^{o} corresponding to a 10 m length for each finned LHS element, simulation was conducted for the 3-stage cascaded finned-LHS for the discharging process using HTF inlet temperature of 286^{o}C and mass flow rate of 0.03 kg/s. Each PCM is assumed to be initially at 20 K above its melting temperature and the length of each axial segment of 0.6 m was used.

Figure 7.21 presents the variation of the HTF outlet temperature at the end of the 3-stage cascaded finned LHS with time. Initially the HTF temperature reduces drastically due to the decrease in the average temperature of the over-heated PCM and then becomes constant for a period of time and start to reduce slowly until the 6 hours discharging time has reached. A minimum HTF temperature of 328^{o}C was obtained for about 3.5 hours from the beginning of discharging after which the temperature begins to fall.

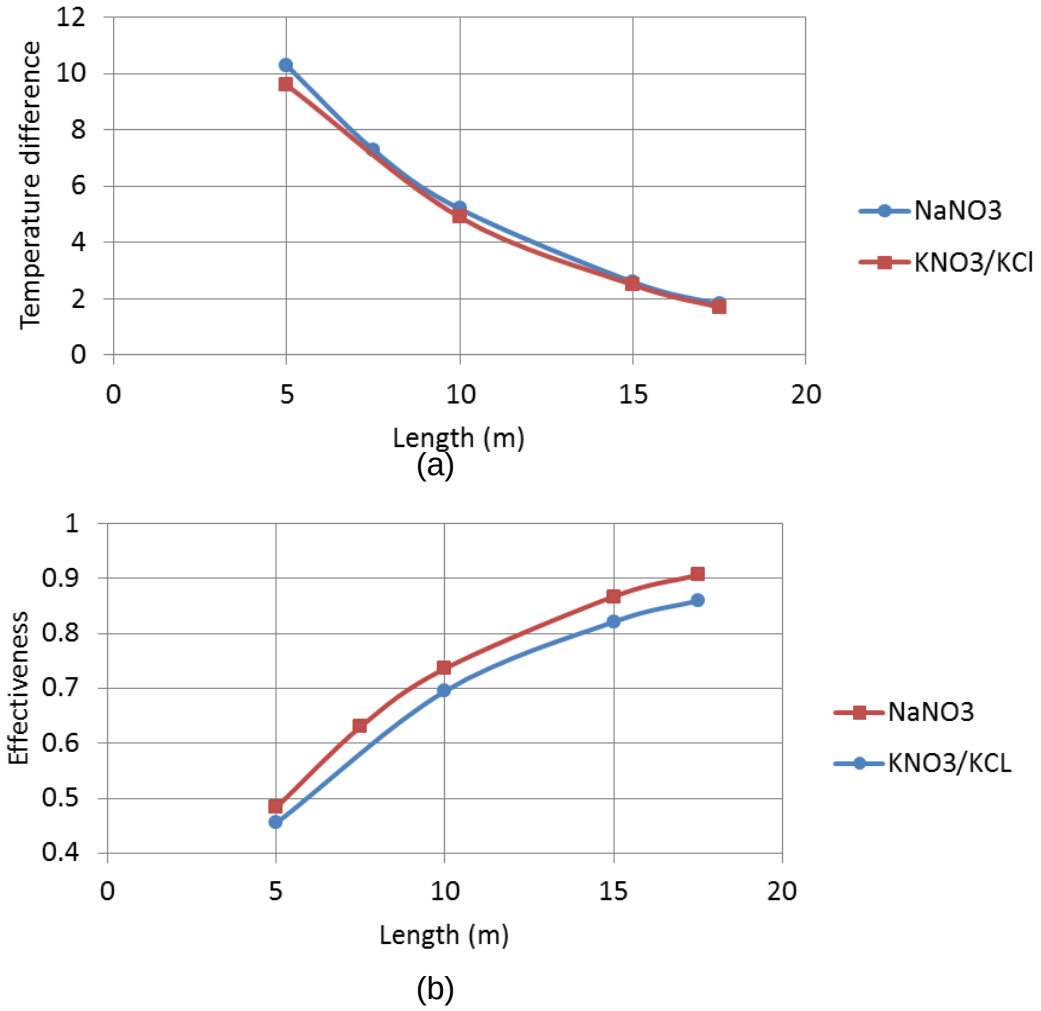

Figure 7.20 Comparison of Terminal temperature difference and effectiveness between $NaNO_3$ and KNO_3/KCl PCMs

The slow reduction in the HTF outlet temperature signifies the reduction in the heat flux as the solidification process progresses. Looking at Figure 7.22, PCMs 2 and 3 solidified faster than PCM 1 with a rate inversely proportional to the latent heat of fusion of the PCM. The liquid fraction for PCM 1($NaNO_3$) is higher due to its higher latent heat of fusion and at the end of discharging (6 hours) there is still remaining 30% unsolidified PCM ($NaNO_3$).

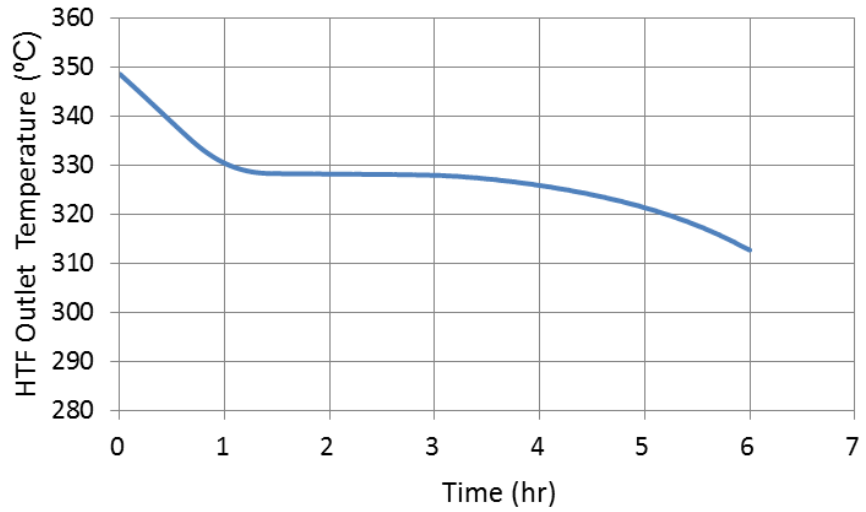

Figure 7.21 HTF outlet temperatures for a complete three stage cascade using equal element length of 10 m for HTF inlet temperature of 286°C.

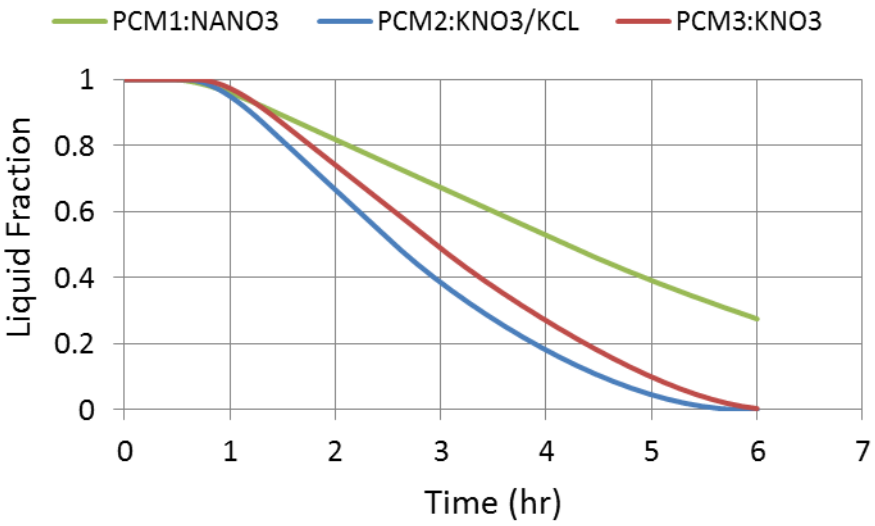

Figure 7.22 Liquid fraction for each PCM in the cascade for three-stage cascaded system

This showed that the latent heat of fusion of each PCM should be considered in the design. The heat transfer point of view resulted into same length of HTF-pipe in each element irrespective of their latent heat of fusion. There is need to consider changing the length of each element based on other criteria, to see

whether there will be more capacity utilization. Thus other methods of dividing the cascade between the PCMs were experimented. Using cascade total length of 30 m, the cascade was then divided using the following criteria:

- Case 1: length proportional to the latent heat of fusion of the PCM ($\lambda \propto A$). Meaning the length of each LHS element is proportional to its PCM latent heat of fusion. This thus results to a cascade with module ratios of 25:11:14 corresponding to $NaNO_3$, KNO_3/KCl and KNO_3 finned LHS elements respectively.
- Case 2: the length is adjusted such that there is same capacity in each element ($m_{pcm}\lambda = constant$). This result to a ratio of 11:22:17 corresponding to $NaNO_3$, KNO_3/KCl and KNO_3 finned LHS elements respectively.

Simulations were then conducted using a total HTF-pipe length of 30 m (same as the total obtained considering the heat exchanger point of view) and the length of the cascade divided based on the criteria described above. Table 7.4 presents the theoretical capacity and the length of each finned LHS element using each of the criteria and that considering the heat exchanger point of view. The theoretical capacity was calculated considering the latent and sensible heat capacity for 20 K temperature difference above and below the melting point of each PCM.

Figure 7.23 presents the HTF outlet temperature, heat discharged comparison of the three cases. It will be seen that, using same capacity in each module produced higher HTF outlet temperatures (Case 2). From Figure 7.23(b) it will be seen that even though Case 2 has the lowest theoretical capacity (Table 7.4), it still has the highest actual capacity (heat discharged) and consequently higher utilization factor. This thus makes distributing the cascade based on same capacity ($m_{pcm}\lambda = constant$) in each module to be the best option in terms of capacity and PCM utilization.

Table 7.4 Theoretical capacity and the length for each cascade corresponding to each criterion.

	Theoretical Capacity (MJ)			Module length (m)		
	Case 1	Case 2	Case 3	Case 1	Case 2	Case 3
PCM1:NaNO3	48.37	21.28	32.25	15	6.6	10
PCM2:KNO3/KCL	12.54	25.08	19.00	6.6	13.2	10
PCM3:KNO3	18.96	23.02	22.57	8.4	10.2	10
Total	79.88	69.39	73.82	30	30	30

Case 1: using length proportional to latent heat of fusion
Case 2: using same capacity in each module
Case 3: using same length (heat exchange point of view)

Figure 7.24 presents the liquid fraction comparison of the three cases for each of the three PCMs. There is no much difference in the liquid fraction for PCM 2 and 3. But for PCM 1, case 2 utilizes more of the PCM with only 8.5% of the PCM unsolidified at the end of 6 hours. Thus the cascade should be divided according to the same capacity in each module.

Finally the following procedure for the design of the cascaded finned LHS is proposed:

- First a terminal temperature difference is selected
- Based on the terminal temperature difference the length of each module can be determined and the total length of the cascade obtained
- The total length of the cascade is then divided based on having the same capacity ($m_{pcm}\lambda = constant$) in each module to obtain the final length of each module.

7.3.2 Concrete Tube Register (CTR)

The dimensions of the CTR especially the length required to fulfil the boundary condition of the charging and discharging, needs to be known. This will give a guide to the initial length of the CTR required. In this preliminary design the HTF

inlet temperature of the CTR during discharging was assumed to be 330^{o}C (5^{o} below the melting point of PCM 3), which is the HTF outlet temperature of the cascaded finned LHS.

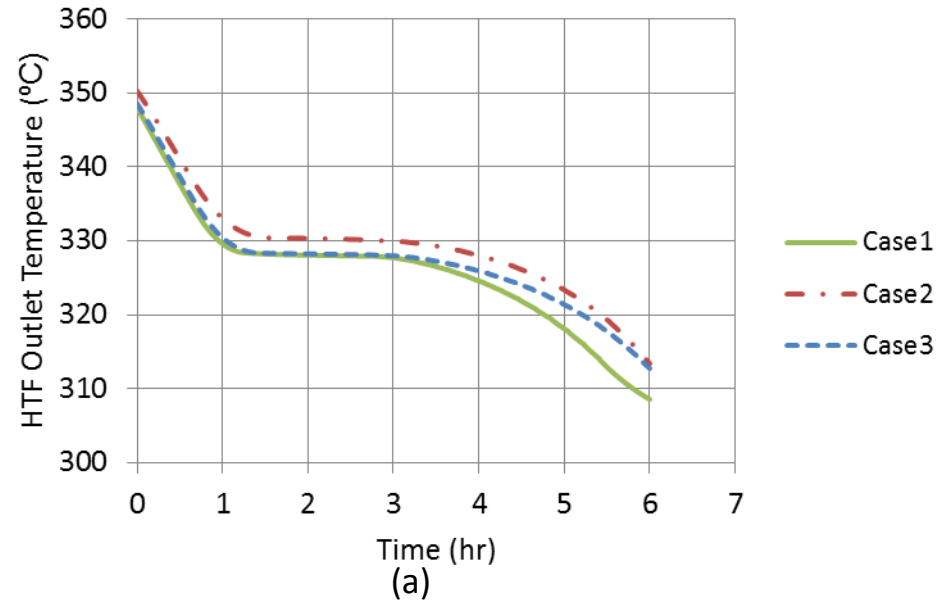

(a)

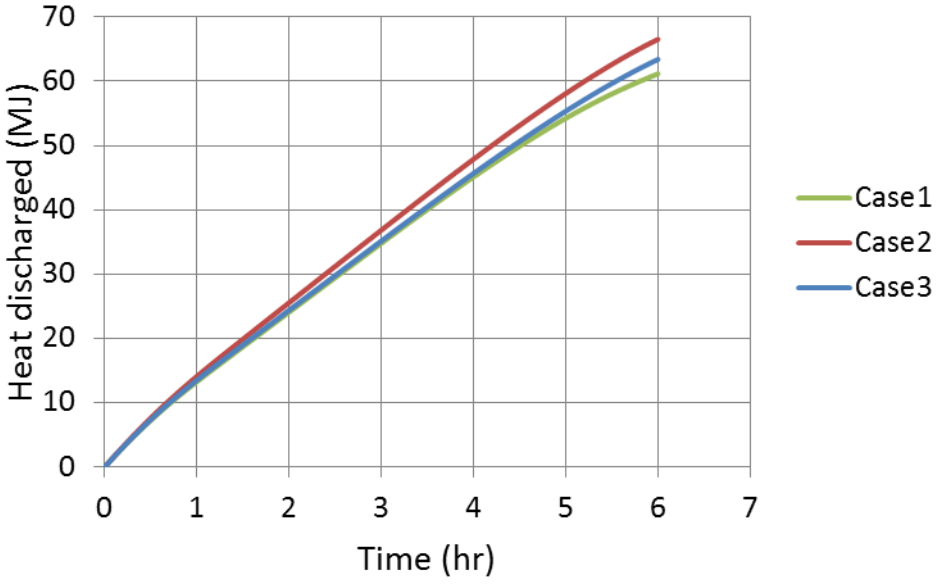

(b)

Figure 7.23 (a) HTF outlet temperature (b) Heat discharged comparisons for case 1, 2 and 3

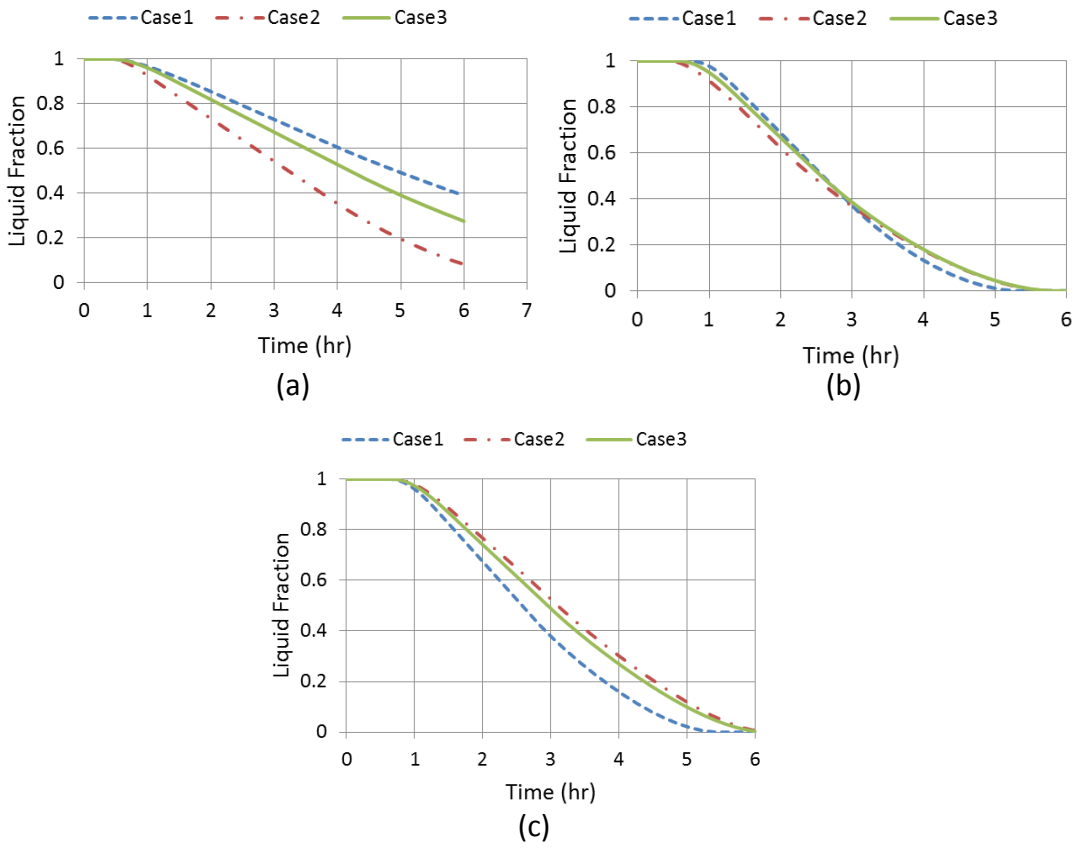

Figure 7.24 Liquid fraction variation with time for the three cases for (a) PCM 1 (b) PCM 2 and (c) PCM 3.

The HTF outlet temperature during discharging is limited to a minimum of 350^{o}C (minimum temperature required for turbine operation). During charging the HTF inlet temperature is 393^{o}C (from solar field). The thermo-physical properties of N4-concrete (Table 7.2) were used. The HTF pipe has same dimensions as that of the cascaded finned LHS and outer diameter of the CTR element of 0.08 m was used to minimize the radial temperature gradient at the end of charging. Storage length of 120 m was used and a 6/6 hr charging and discharging cycle was considered. The total length was divided into 48 axial segments. It should be noted that the determination of the storage capacity must be made at a periodically balanced state. Thus many cycles were simulated in order to ensure a periodically balance state.

Figure 7.25 presents the temperature of the last radial element in the CTR element for the top and bottom axial segments and the average storage temperature for the charging and discharging for 5 cycles and Figure 7.26 presents the HTF outlet temperature during charging and discharging. After two cycles the system has reached a periodically balanced state and that the temperature of HTF at the end of discharging is slightly below 350^{o}C. Thus CTR length of 120 m may fulfil the requirement assuming the cascaded finned LHS will provide HTF temperatures of 330^{o}C for the whole duration of operation.

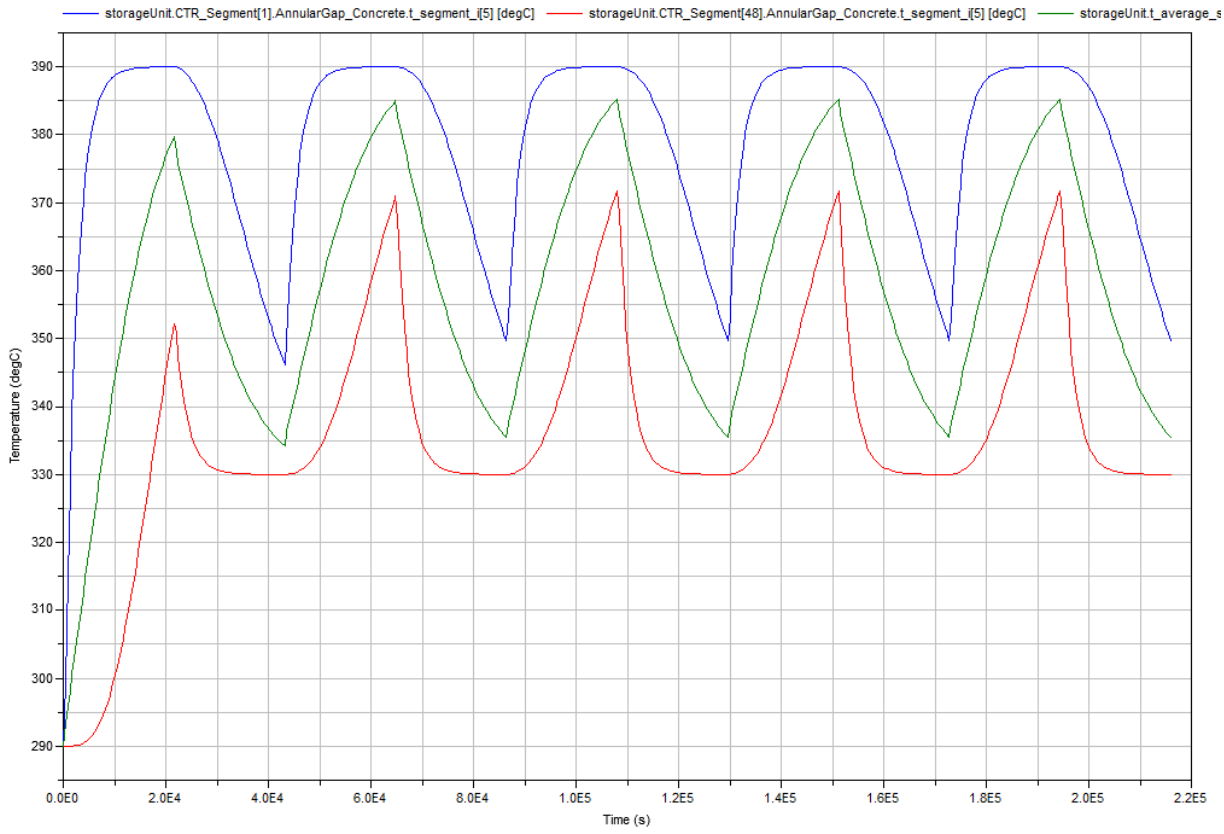

Figure 7.25 Temperature at the core (last radial element) of the CTR element for the top and bottom axial segments and the average storage temperature for both charging and discharging for 5 cycles

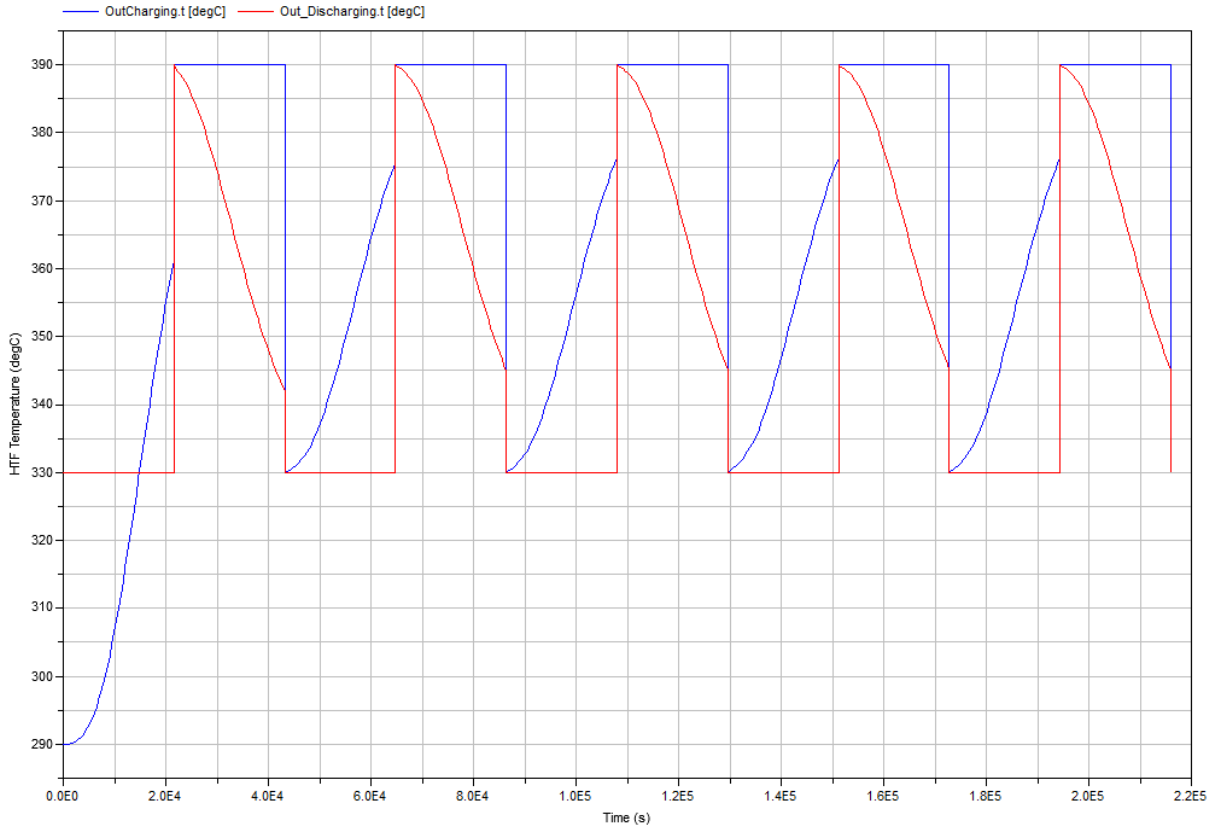

Figure 7.26 HTF outlet temperatures during charging and discharging for a 6h/6h cycle

7.4 Design of the Complete Storage System (or HCSS)

In section 7.3.1 the total length of the cascaded finned LHS of 30 m was obtained, of which each finned-LHS element will have a length as follows based on having same capacity in each module:

$NaNO_3$: 6.6 m, KNO_3/KCL: 13.2 m and KNO_3: 10.2 m.

In section 7.3.2 a CTR of length 120 m almost satisfy the boundary conditions of the parabolic-trough plant using synthetic oil (Therminol VP-1) as HTF and thus gave an idea of the length required. For the HCSS element a CTR length of 130 m was used. The dimensions of the CTR and the cascaded finned LHS elements are as in the preliminary design. The boundary conditions of the

storage system have been presented in Figure 7.18. HTF outlet temperature is limited to a maximum of 330^{o}C and minimum of 350^{o}C during charging and discharging respectively. A 12 hour charging/discharging cycle was considered and simulations were conducted for 10 cycles to ensure a periodically balanced state.

Figure 7.27 presents the HTF outlet temperature during charging and discharging. The green line represents the HTF temperature at the end of the cascaded finned LHS element. Figure 7.28 presents the cumulative heat transferred into the CTR and the cascaded finned LHS element for the 10 cycles. A periodically balanced state has been achieved and the capacity of the CTR is more than that of the cascade.

Considering the periodically balanced state (the 10th cycle), Figure 7.29 presents the variation of cumulative heat transferred with time during charging and discharging for the individual finned-LHS elements, the total for the cascade and the CTR element. The total capacity of the HCSS element is 129.23 MJ out of which 44% (57.26 MJ) is that of the cascaded finned LHS element and the rest (56%) is from the CTR element (Figure 7.30). The cascaded finned LHS element provides less than 50% of the total capacity. This is undesirable as it will limit the potential for reducing the required storage size.

In order to see whether there are possibilities of increasing the capacity ratio, the cascaded finned LHS was examined in detail. From Figure 7.30, PCM 1 provides the smallest capacity, meaning that it has the lowest utilization factor. Looking at Figure 7.31, 70% of the mass of PCM 1 is utilized in the storage, with both PCM 2 and 3 having 90% of PCM undergoing phase change during the 12 hour charging/discharging cycle.

Thus there is need for exploring whether the percentage capacity provided by the cascade can be increased. Increasing the capacity ratio of the cascade can only be beneficial if the capacity per unit length of the cascade (unit volumetric capacity) increases and/or the cost of the increased length is less than the cost of the length decrease of the CTR.

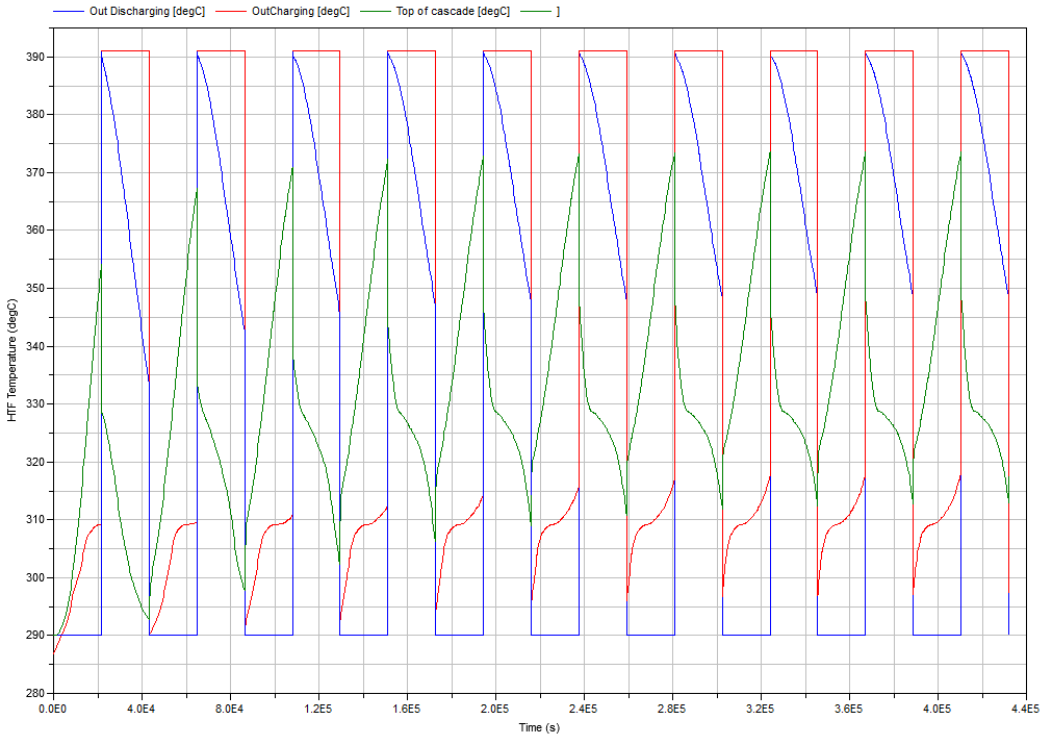

Figure 7.27 HTF temperatures for 10 cycles to reach the periodically balanced state for a complete cascaded finned LHS and CTR elements.

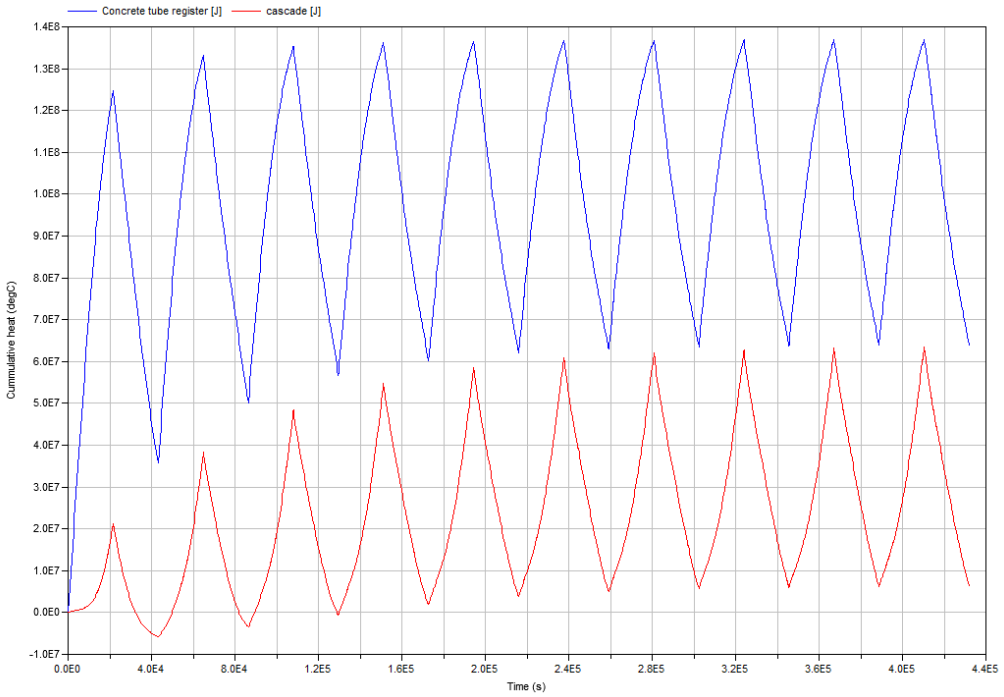

Figure 7.28 Variation of cumulative heat with time for the CTR and the cascaded finned LHS elements for 10 cycles

.

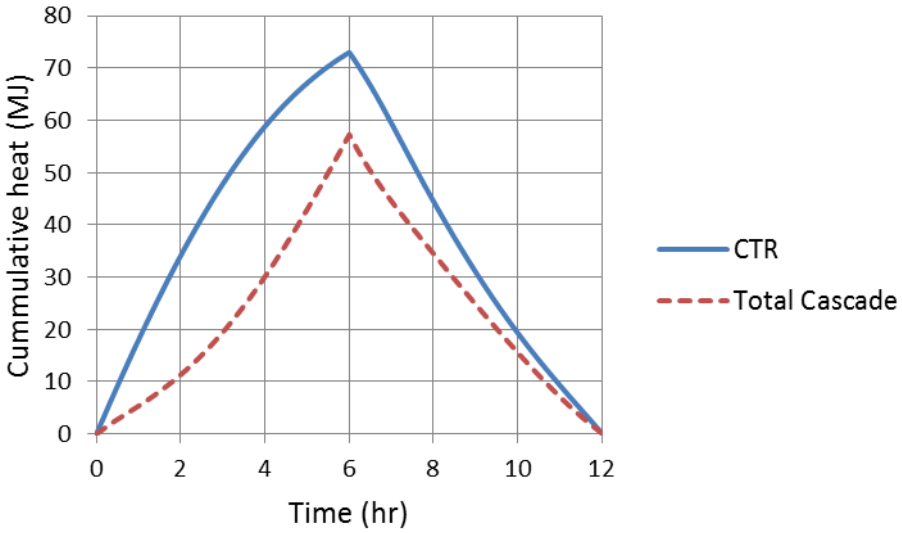

Figure 7.29 Variation of cumulative heat with time for the 10th Cycle

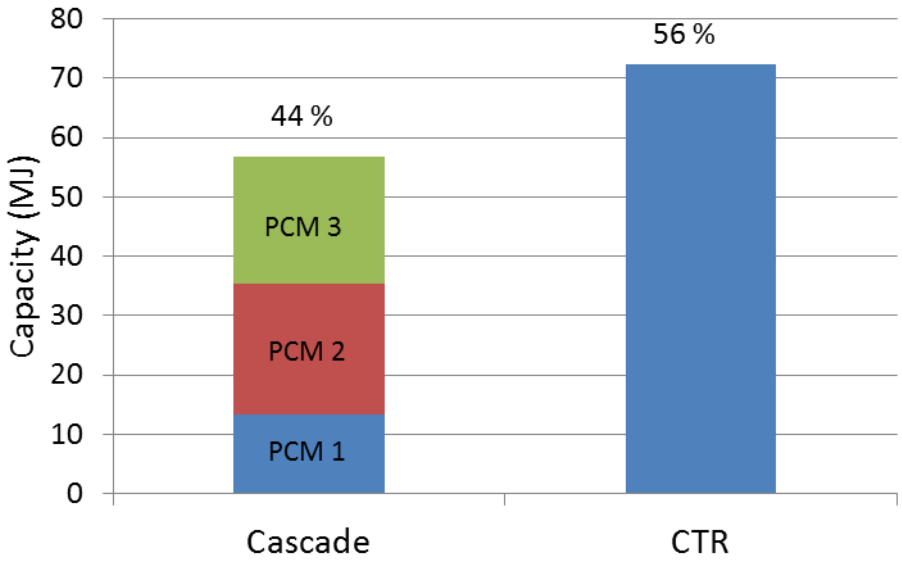

Figure 7.30 Actual capacity of individual storage elements.

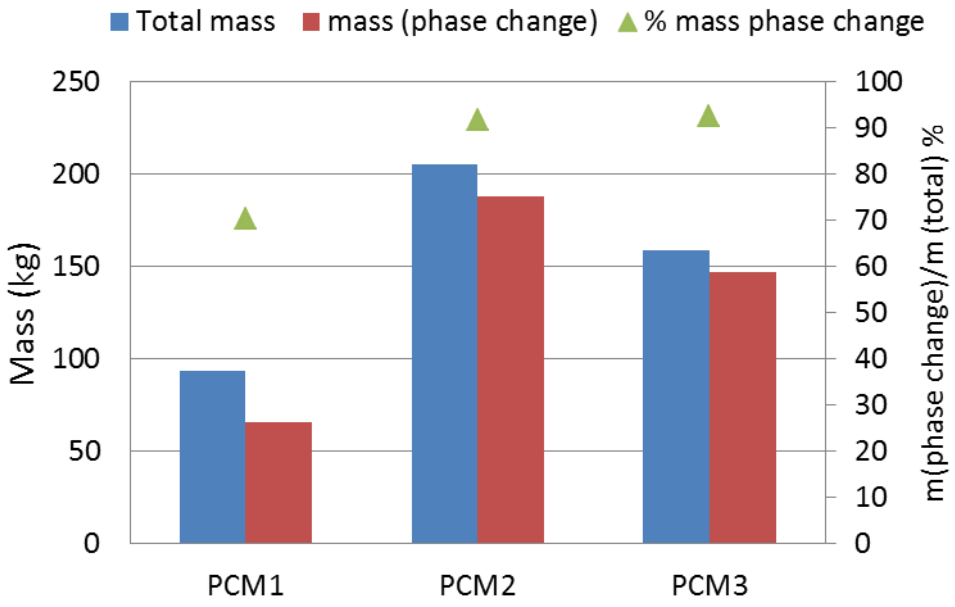

Figure 7.31 Mass of PCM that undergoes phase change for 12 hour charging discharging cycle

7.4.1 Effect of Cascade Length

In this section the effect of increasing the length of the cascade in order to see whether it will result into a beneficial increase in the capacity ratio of the cascade was explored. The length of the cascade was increased to 36 m and the length of each finned LHS element was obtained considering same capacity in each element. The length of the CTR required has to be obtained by trying different lengths. Thus Simulations were conducted with CTR lengths of 80 m, 90 m and 120 m for 12 hour charging/discharging cycle.

Figure 7.32 presents the HTF outlet temperature during charging and discharging at the periodically balanced state for the three CTR lengths. It will be observed that storage of length 120 m satisfy the boundary condition requirements.

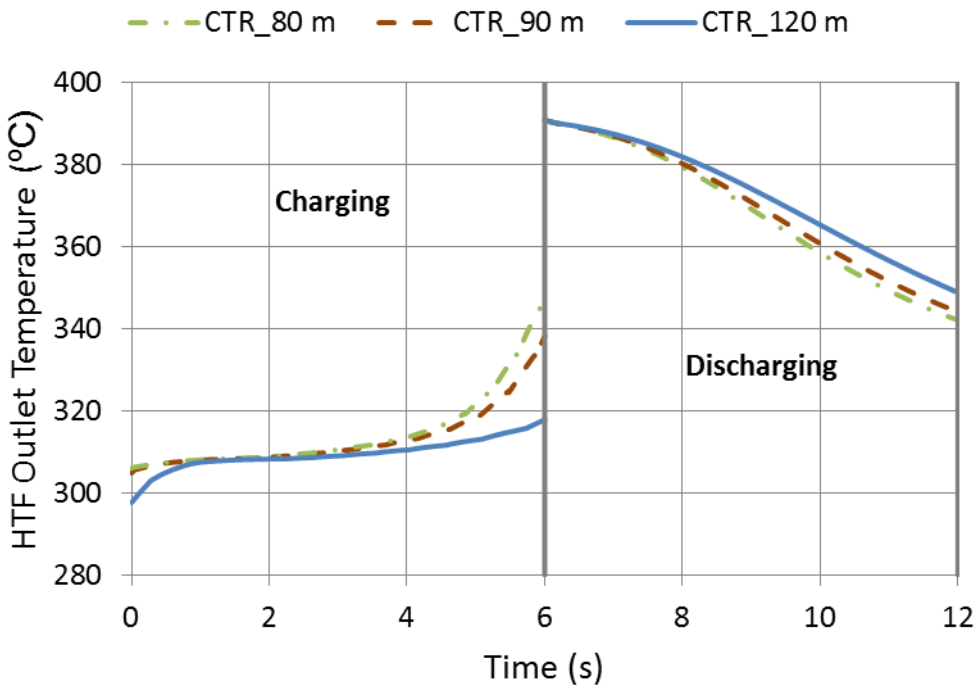

Figure 7.32 HTF outlet temperature during charging and discharging at the periodically balanced state for CTR lengths of 80, 90 and 120 m.

Table 7.5 presents the performance comparisons of a HCSS with cascade and CTR lengths of 30 m and 130 m respectively with that of 36 m and 120 m respectively. The difference in length in the required CTR length is 10 m (a decrease of about 7.6%) and resulted into an increase in the CTR capacity and specific capacity of ~11% and 3.5% respectively. Considering the cascaded finned-LHS section, the storage capacity increases as the length of the cascade was increased from 30 m to 36 m (20% increase in length). However the specific capacity and percentage phase change decreases with increase in the length of the cascade. For the HCSS element, the 36 m length cascade system capacity is greater by only 0.9 MJ.

Thus increasing the length of the cascade does not result into smaller storage size even though the capacity ratio of cascade increased from 44% to 50.4%. As such the cascade of length 30 m is the optimum length of the cascade for the HTF mass flow rate of 0.03 kg/s.

Table 7.5 Performance comparisons for storage system with cascade lengths of 30 m and 36 m.

	30 m		36 m	
	Cascade	CTR	Cascade	CTR
Length (m)	30	130	36	120
Actual capacity (MJ)	56.8	72.4	65.5	64.5
Capacity/Unit length (MJ/m)	1.89	0.557	1.82	0.54
Specific capacity (kJ/kg)	124.01	49.75	119.28	48.02
Mass of storage material (kg)	457.8	1455.6	549.34	1343.6
m (phase change)/m (total) %	87.6		83	
Capacity ratio (%)	44	56	50.4	49.6

7.4.2 Effect of HTF Mass Flow Rate

Up to this stage, HTF mass flow rate of 0.03 kg/s has been used. In this section the effect of HTF mass flow rate on the actual capacity of the HCSS element was investigated. The HTF mass flow rate affects the total length of the storage (in order to satisfy the boundary conditions), thus determines the actual capacity. Thus for each HTF mass flow rate there is a corresponding cascade and CTR length that will give the maximum specific capacity. In view of this, simulations were conducted for cascade lengths ranging from 30 m to 42 m for HTF mass flow rates of 0.025 kg/s to 0.04 kg/s. Table 7.6 presents the result comparisons. Generally there is increase in actual capacity and required CTR length as the HTF mass flow rate increases for a particular cascade length. Figure 7.33 presents a plot of the specific capacities of all the cases simulated. For each HTF mass flow rate the best cascade length was selected based on the one having the highest specific capacity and phase change.

Table 7.6 Cascade length appropriate for each HTF mass flow rate

HTF mass flow rate (kg/s)	**0.025**		**0.03**		**0.035**		**0.04**		
Cascade									
Length of cascade (m)	30	36	30	36	36	42	30	36	42
Actual capacity (MJ)	46.59	53.97	56.8	65.5	69.2	77.48	56.33	75.32	84.6
Specific capacity (kJ/kg)	101.77	98.25	124.01	119.28	126.03	120.89	123.07	137.11	132.02
Phase change mass(total) %	72.2	60.1	87.6	83	88.3	83.8	82.5	92.6	90.6
Capacity ratio %	42.2	48.9	44	50.4	45.5	50.85	32	43.5	48.9
Concrete Tube Register									
Required length of CTR (m)	120	110	130	120	150	140	200	170	160
Actual capacity of (MJ)	63.9	56.34	72.4	64.5	83.04	74.87	119.46	97.79	88.31
Specific capacity (kJ/kg)	47.53	45.74	49.75	48.02	49.45	47.76	53.35	51.36	49.31
Mass of storage material (kg)	1343.6	1231.6	1455.5	1343.6	1679.5	1567.5	2239.3	1903.4	1791.4

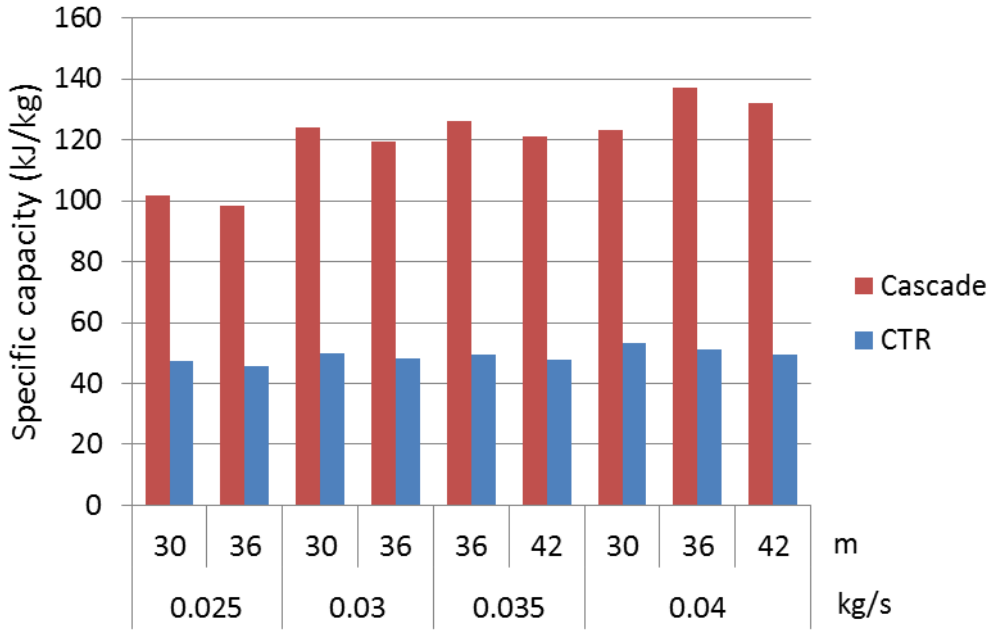

Figure 7.33 Effect of HTF mass flow rate on cascade and CTR specific capacity

7.4.3 Selection of Design Storage Element Mass Flow rate

From section 7.4.2 each HTF mass flow rate has a corresponding length that will give the highest specific capacity. Other factors have to be considered in the selection of the best design mass flow rate. These include: the total storage capacity of the storage system (not a single storage element), the total HTF mass flow rate and the required pumping power through the storage. Generally there is increase in specific capacity as the HTF mass flow rate increases. Thus the selection of design HTF mass flow rate must consider the complete storage system.

For a 50 MWe parabolic-trough plant a thermal storage system with capacity of 875 MWh_{th} is required for 6 hour full load turbine operation. Based on the capacity of a single storage element from Table 7.6 the total HTF mass flow rate required can be obtained by multiplying the single element HTF mass flow rate with the required number of storage-elements to provide the required capacity. Table 7.7 presents the total mass flow rate and the calculated pumping power. Although the single element HTF mass flow rate increase from

0.03 kg/s to 0.04 kg/s, the total required mass flow rate for the 875 MWh_{th} capacity, for 0.035 kg/s and 0.04 kg/s are lower than that for 0.03 kg/s. This is because the single element capacity increases with increase in the HTF mass flow rate, leading to lower number of storage elements required to fulfil the total storage capacity.

To select a design HTF mass flow rate, the required pumping power has to be considered since increase in the HTF mass flow rate lead to increase in the total length of the storage. Thus Figure 7.34 presents the variation of the pumping power and the HCSS element capacity with single element HTF mass flow rate. The capacity change is almost a linear function of the single element HTF mass flow rate but the rate of change of the pumping power increases with increasing mass flow rate. Selection of design mass flow rate cannot be solely based on the pumping power since after all the pumping power may be negligible compared to the electricity produced or the total plant pumping power requirement.

Table 7.7 Calculation of total HTF mass flow rate and pumping power for 875 MWh_{th} capacity HCSS

Storage element HTF mass flow rate (kg/s)	**0.025**	**0.03**	**0.035**	**0.04**
Length of cascade (m)	30	30	36	36
Length of CTR (m)	120	130	150	170
Storage Element Capacity (MJ)	110.49	129.2	152.24	173.11
number storage element for 6h capacity	28,509	24,381	20,691	18,197
Total storage system HTF mass flow rate (kg/s)	713	731	724	728
Total pressure drop (bar)	0.78	1.15	1.75	2.45
pumping power (kW)	71.27	107.84	162.48	228.62

Figure 7.35 presents the percentage capacity and PCM phase change produced by the cascade. HTF mass flow rates of 0.03 and 0.035 kg/s have almost equal percentage phase change and the percentage capacity increase and then decrease with a maximum at HTF mass flow rate of 0.035 kg/s. Single element HTF mass flow rate of 0.035 kg/s will be the best mass flow rate since its percentage capacity is higher than that of the 0.03 kg/s. It was selected as the design HTF mass flow rate.

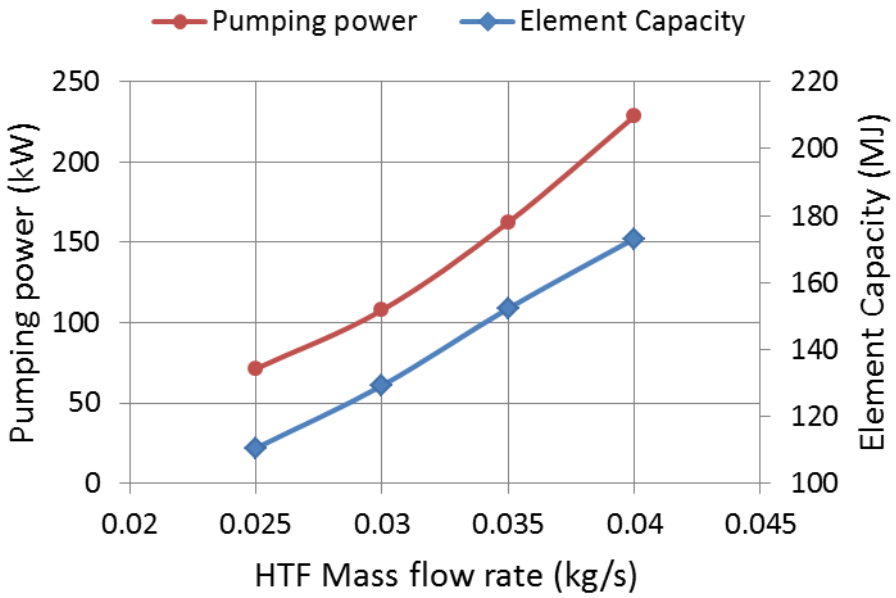

Figure 7.34 Variation of pumping power and storage element capacity with single storage element HTF mass flow rate

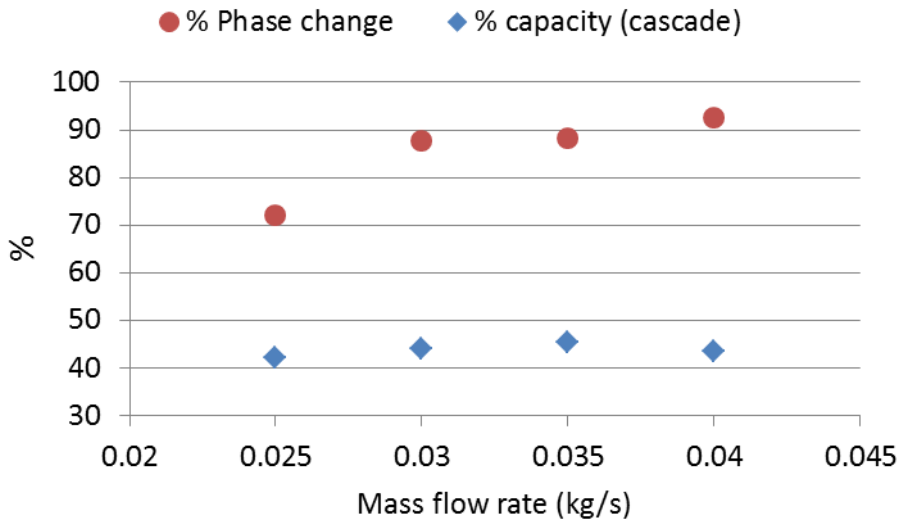

Figure 7.35 Effect of HTF mass flow rate on % phase change and capacity of cascade

7.4.4 Complete Storage (HCSS) Size for 6 Hour Capacity

In section 7.4.3, the cascade and CTR length that can satisfy the boundary conditions of the parabolic-trough plant for charging and discharging and the most suitable design HTF mass flow rate of 0.035 kg/s of a single storage-element were obtained considering a single HCSS element. The capacity required for 6 hours operation of the parabolic-trough plant is 875 MWh_{th}. Considering the capacity of the single HCSS element with cascade length of 36 m, 20,691 HCSS elements in parallel will be required to achieve this required capacity for HTF mass flow rate of 0.035 kg/s.

7.4.4.1 The Cascaded Finned Latent Heat Storage (LHS)

The storage-elements for each finned-LHS module will be arranged in a cylindrical enclosure in a staggered arrangement in order to have compact module. Mathematical calculations were conducted to find the size of the cylindrical enclosure that will contain this number of storage-elements. It was found that 82.5 circular rows of storage-elements are required. Thus the

diameter of the storage must be able to accommodate 83 circular rows. Considering each storage-element has an outer radius of 48.8 mm, the total diameter of each finned LHS module will be 16.30 m. This diameter can accommodate 20,917 pipes which is greater than the required number of pipes (i.e. 20,691). The extra space will thus be used for construction tolerances between adjacent storage-elements.

Table 7.8 presents the dimensions of the cascaded finned LHS element for each PCM. The height of the element for each PCM was calculated considering the solid PCM and the thickness of the fins. Table 7.9 presents the material requirement for each of the modules of the cascaded finned LHS. The net storage material volume was calculated considering the active amount of PCM within the fins while the gross volume of storage material includes the volume between storage-elements. The volume of material that fills the space between storage elements is about 25% of the total gross volume.

Table 7.8 Finned-LHS element configuration

	PCM 1	**PCM 2**	**PCM 3**	**Total**
HTF pipe Inner diameter (m)		0.008		
HTF pipe outer radius (m)		0.012		
Outer diameter of storage element (m)		0.0976		
Fin thickness (m)		0.001		
number of fins/element	792	1584	1224	3600
Length of HTF-pipe considering fin thickness (m)	8.712	17.424	13.464	39.6

Table 7.9 Material requirement for each finned-LHS module

	PCM 1	PCM 2	PCM 3	Total
Number of storage elements required	20,691	20,691	20,691	20,691
PCM volume expansion	0.107	0.141	0.033	
Net volume of storage material (m^3)	1207	2415	1866	5489
Gross volume of storage material (m^3)	1634	3268	2526	7428
density of storage material @20 kg/m3	2261	2100	2109	
Gross mass of storage material (tonnes)	3,694.8	6,863.4	5,326.3	15,884.6

Table 7.10 presents the dimension of each of the finned-LHS modules in the cascade. To obtain the height of each module, PCM expansion and the height of header were considered. Assuming a header of 0.1 m and the volume expansion of each PCM (presented in Table 7.9), the total height of each finned LHS module was calculated. The net volume of each module represents the volume of the storage excluding the header volume and the gross represent that including the header volume. The cascade provides 45.5% of the total capacity of the storage system and the gross volumetric specific capacity is 43.75 kWh/m^3.

7.4.4.2 Concrete Tube Register (CTR)

Table 7.11 presents the calculation for the size and material requirement of the CTR module. A total volume of CTR of ~15,800 m^3 is required (excluding space between adjacent elements) to provide the required 54.5% capacity of the HCSS. Considering that the storage length is 150 m, the cross sectional area of the storage that will fit 20,691 parallel pipes in a staggered arrangement is 4.2 m by 27.6 m. Thus the gross storage volume of the CTR is 17,388 m^3.

Table 7.10 Cascaded LHS module dimensions and capacity

	PCM 1	PCM 2	PCM 3	Total
Length of storage module including volume expansion (m)	9.64	19.88	13.91	43.43
Length of module including header (m)	9.74	19.98	14.01	
Diameter of storage module (m)		16.3		
Net volume of storage module (m^3)	2012.48	4148.57	2902.28	9063.33
Gross volume considering header (m^3)	2022.9	4159	2912.7	9094.6
Capacity (MWh_{th})	94.41	152.18	151.32	397.91
% capacity	10.8	17.4	17.2	45.5
Gross specific capacity (kWh_{th}/m^3)	46.67	36.59	51.95	43.75

Table 7.11 Dimension and storage material requirement of the CTR

Storage Element Dimension	
HTF pipe inner diameter(m)	0.008
HTF-pipe outer diameter (m)	0.012
Outer diameter of storage element (m)	0.08
Length (m)	150
Storage material requirement	
Storage material mass (tonne)	34,750.6
Density of storage material (kg/m^3)	2,250
Storage material volume (m^3)	15,444.69
Storage module dimensions/capacity	
Gross module volume (m^3)	17,388
module dimensions (m)	4.2 x 27.6 x 150
capacity (MWh_{th})	477.294
% capacity	54.5
Specific capacity (Gross) (kWh_{th}/m^3)	27.45

This storage can be built consisting of small modular units since the construction as a single unit is impossible and unreasonable as proposed by Laing et al.[96]. The calculated gross specific capacity of 27.4 kWh/m^3 is similar to that obtained in experiments by Laing et al. [96] (26.6 kWh/m^3).

7.4.5 Heat Lost

In the simulation, heat lost to the surrounding was not considered. Thus in this section, the heat lost from each module will be estimated in order to quantify the amount of heat lost.

7.4.5.1 The Cascaded Finned Latent Heat Storage (LHS)

An empirical heat lost equation was developed by Herrmann et al. [9] for the two-tank system from the result of the test of solar two [186]. This heat loss equation is given by:

$$\dot{q}_{loss} = 0.00017 \times T_{salt} + 0.012\ kW/m^2$$

where T_{salt} is the average temperature in the tank.

This was used in estimating the heat lost from each finned LHS module for a 24 hour period. The surface area of each module is required in calculating the heat lost. Table 7.12 presents the surface area of each module, the maximum storage temperature and the calculated heat lost for a 24 hour period. The total heat loss for the three modules is 5.774 MWh_{th} for 24 hours considering the average tank temperature to be that at the end of charging (maximum average temperature). From the previous section the total capacity of the cascade is 397 MWh_{th}. Thus the percentage heat loss in a 24 hour period is 1.45% of the capacity. This is negligible and will not impact in the performance of the system.

7.4.5.2 Concrete Tube Register (CTR)

Bahl et al. [187] determined a function for the calculation of the heat lost from a CTR module. Results of heat lost were obtained for various mean concrete storage temperatures. Using the empirical approach developed by Schack and Schack [188], the heat lost function is given by:

Table 7.12 Estimation of heat loss for the Cascade

	PCM 1	PCM 2	PCM 3
Average temperature, ^{o}C (end of charging)	315	333	353
Total surface area of module, m^2	916.11	1,440.48	1,134.77
heat loss, kW	60.05	98.83	81.71
heat loss for 24 hour period, kWh	1,441.22	2,371.95	1,961.15

$$\dot{Q}_{loss}(W) = 9.35 \times (T_{\text{conc}} - T_{amb})^{1.201} \quad (7.5)$$

Where T_{conc} is the average temperature in the concrete, and T_{amb} is the ambient temperature and assumed to be 25^{o}C.

The heat lost function presented is not for a unit storage surface area. This means that it is valid for the surface area of the experimental module. To obtain a general function that can be applied for any surface area, the surface area of the studied module must be considered. The module has a surface area of 56.02 m^2. Thus equation (7.5) becomes:

$$\dot{q}_{loss} = 0.1669 \times (T_{\text{conc}} - T_{amb})^{1.201}$$

The maximum and minimum average temperatures in the concrete module are 384^{o}C and 334^{o}C respectively. Table 7.13 presents the calculated maximum, average and minimum heat lost over a 24 hour period. The concrete module total surface area is 9771.84 m^2. The ambient temperature is assumed to be 25^{o}C. The maximum heat lost for a 24 hour period is less than 10% of the whole capacity. This can thus be compensated by increasing the size of the CTR module by 10%.

Table 7.13 Estimation of heat loss for the CTR module

	Average temperature (^oC)	Heat loss		% capacity
		MW_{th}	MWh_{th}/24 hrs	
Minimum	334.49	1.598	38.36	8.0
Average	359.31	1.754	42.09	8.8
Maximum	384.13	1.911	45.87	9.6

7.5 Cost Analysis

In this section the capital cost of the storage system was determined and compared with that of the two-tank system.

7.5.1 The Cascaded Finned Latent Heat Storage (LHS)

The cascaded finned LHS section of the storage system consists of:

- The storage module container (for each PCM)
- The finned HTF tube (the heat exchanger)
- The PCM Inventory

In order to have a basis for comparison with the two-tank system, the unit cost estimates developed by Kelly et al. [11] and Herrman et al., [9] for the two-tank system was used for the cost of common components such as the storage module container and the salt inventory. These costs included the manufacturing and assembly cost of the component. Details of the unit cost are presented in the following section. An overhead of 10% will be added to cover the cost of additional piping, valves, instrumentation e.t.c.

7.5.1.1 Unit Cost Estimation

7.5.1.1.1 The Storage Module Container

Each of the three finned LHS modules will be constructed as standalone tanks connected by a pipe and the dimensions of which have been presented in Table

7.10. As has been stated above the unit cost of the storage tank will be based on publically available unit cost estimate for the commercially available two-tank system.

The storage module container consists of:

i. **The Container Shell**: This is made up of carbon steel with an average wall thickness of 38 mm, floor thickness of 8 mm and roof thickness of 6 mm. The tank shell is assumed to be made of carbon steel with a unit price of 4.40 $/kg. This price includes the cost of material, shop, field fabrication and shipping.

ii. **Insulation**: Insulation of the wall, the bottom and the roof with calcium silicate block covered with corrugated aluminium jacket to protect it from weather. The required insulation thickness was assumed to be a linear function of the temperature in the tank. 300 mm thickness corresponds to 290^{o}C and 500 mm corresponds to 565^{o}C. Also the unit cost of the insulation varies linearly from 160 $/m^2 to 235 $/m^2 corresponding to thicknesses of 300 mm and 500 mm respectively. Thus equation (7.6) presents the equation for calculating the cost of insulation with reference to the average storage temperature.

$$C\left(\frac{\$}{m^2}\right) = 0.2727(T_{pcm}) + 80.909 \qquad (7.6)$$

The average temperature in each of the finned LHS modules at the end of the charging period was used for the determination of the required insulation thickness and the unit cost of insulation. This is presented in Table 7.14.

iii. **Container Foundation**: It will be assumed that the cost of the foundation is similar to that of the commercially available two-tank system. Even though the foundation for the latent heat storage system is different from that of the two-tank system. Robak et al. [28] estimated the cost of the foundation to be 688 $/m^2.

Table 7.14 Required insulation thickness and unit cost

Module	Average temperature at the end of charging (^oC)	Calculated insulation thickness (mm)	Unit cost ($/m^2)
PCM 1	315	318	166.82
PCM 2	333	331	171.73
PCM 3	353	346	177.19

7.5.1.1.2 The PCM Inventory

In Kelly et al. [11], the cost of the molten salt inventory used was 0.5 $/kg including labour and fuel required to melt the salt. This will be used in order to have same basis for comparison with the two-tank system.

7.5.1.1.3 The Finned Heat Exchanger

For temperature applications less than 400^oC and for cyclic operation, the embedded fin is the most suitable fin type. The commonly used fin is the L type wrap on fin, suitable for lower temperature applications of which cost can readily be obtained from heat exchanger tube manufacturers. The capital cost for L type wrap on fin is mostly the same as that of the embedded fin [189]. Thus cost of finned tube with similar characteristics as much as possible to that required was obtained from two manufacturers. The first was 4.18 US$/m length of the finned tube based on the bulk quantity from an international manufacturer in China and the second is 8 US$/m length based on buying small quantity from a manufacturer in the UK. The unit cost of bare tube required to fill up the space at the top of each module to accommodate volume expansion was estimated to be 20% of the unit cost of the finned tube. The cost of installation and welding was assumed to be 10% of the unit cost. Since the cost of the finned tube is not a standard cost, it will thus be assumed to have a lower and higher cost and the capital cost will be estimated based on these separately. Thus the unit cost of the heat exchanger will range from 5.38 $/m to 10.4 $/m with an average of 7.89 $/m length of the heat exchanger.

7.5.1.2 Capital Cost of Cascade

Table 7.15 presents the amount of material for each of the components of the storage system while Table 7.16 presents the corresponding cost of the components calculated form the unit cost provided in section 7.5.1.1. Three capital costs (minimum, average and maximum) were presented. The cost of the HTF inventory was neglected. Figure 7.36 presents a pie-chart showing how the cost is distributed among the components of the cascaded finned LHS based on the minimum and maximum heat exchanger cost. The capital cost of the cascade finned-LHS ranges from $18.5 to $23.5 million.

Table 7.15 Amount of materials required for the cascaded storage system

Item	Unit	PCM 1	PCM 2	PCM 3	Total
Container shell	t	169.42	323.61	233.72	726.75
Insulation (Fire Bricks)	m^2	711.71	1238.53	931.39	2881.63
Container foundation	m^2	210.62	210.62	210.62	631.86
Heat exchanger length	m	199,548	410,993	287,777	898,318
PCM Inventory	t	3,694.82	6,863.439	5,326.30	15,884.55
Over head	%	10	10	10	

Table 7.16 Capital cost estimation based on the maximum, average and minimum cost of the heat exchanger (1000 $)

Item	**Minimum**	**Average**	**Maximum**
Container shell		3,197.71	
Insulation (Fire Bricks)		496.45	
Container foundation		434.72	
Heat exchanger	4,832.95	7,087.72	9,342.50
PCM Inventory		7,942.28	
Over head	1,690.41	1,915.89	2,141.37
Total	18,594.52	21,074.78	23,555.03

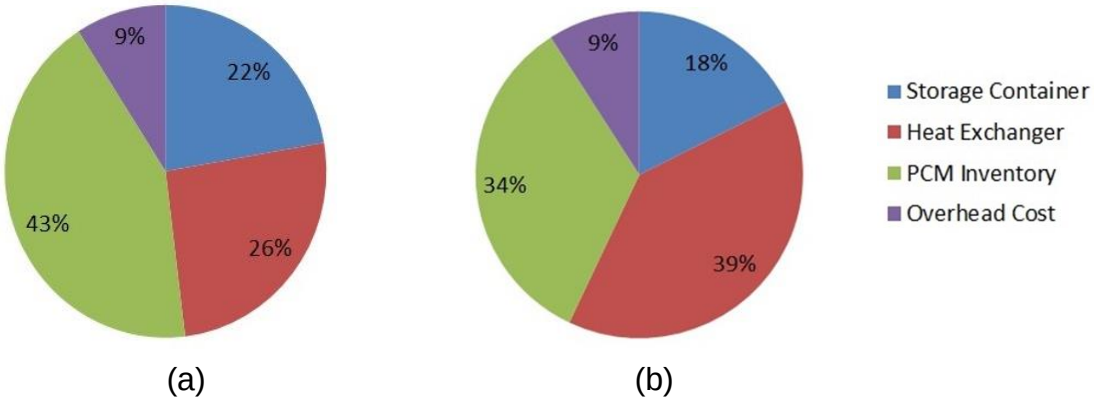

(a) (b)

Figure 7.36 Capital cost distribution of the finned LHS cascade for (a) minimum (b) maximum heat exchanger cost

7.5.2 Concrete Tube Register (CTR)

Using similar approach used in the cascade, the cost of the CTR was estimated based on the unit cost of various components of the storage. The CTR is composed of:

- Heat exchanger (steel pipes)
- The storage concrete
- Insulation
- Foundation

7.5.2.1 Unit Cost Estimation

For the storage material the unit cost of plain concrete provided by Kelly et al. [11] of 0.04 $/kg was used as the minimum cost and the 0.1 $/kg was used as the maximum [concrete network] and a labour cost of 15% was added. The unit cost of the tube register of 2.5 $/kg was also used [11].

The storage foundation will be made of reinforced concrete and is assumed to be similar to the concrete foundation of the two-tank system in which the unit cost of plain concrete and steel reinforcement are 85 $/m^3 and 0.8 $/kg respectively. A concrete slab requires 73 kg/m^3 of reinforced steel. Thus the

cost of the foundation concrete will be 87.48 $/m^2 assuming the height of the foundation to be 0.61 m. The foundation will also consist of 0.3 m thick foam glass [190] as insulation material with a unit price of $356/m^3. Thus the unit price of foam glass Insulation will be will be $106.8/m^2 surface area of insulation. This will thus make the total unit price of foundation to be 194.28 $/m^2.

The walls and the top of the storage module will be insulated with mineral wool with thickness of 0.4 m covered with troughed sheets. Mineral wool suitable for operating temperature range has a density of 100 kg/m^3 [191]. The unit cost of mineral wool was obtained using an average of 46 $/m^2 from two suppliers [192; 193] based on buying small quantity. It was assumed that the bulk price of the insulation will be 25% cheaper than the small quantity price i.e $34.5/m^2.

7.5.2.2 Capital Cost of Concrete Tube Register (CTR)

Table 7.17 presents the calculation of the capital cost of the CTR considering the 10% increase in capacity to compensate for the calculated heat lost. The quantity of each of the component of the CTR was calculated and the total capital cost of the CTR was obtained using the maximum and minimum cost of plain concrete. The labour cost was assumed to be 20% of the material costs and an overhead of 10% was added. The HTF inventory was neglected. Figure 7.37 presents the cost distribution of the various components of the CTR. The storage container refers to the cost of the insulation and the foundation. The heat exchanger has the highest cost of 46% of the CTR capital cost.

7.5.3 Capital Cost of Complete Storage System

Figure 7.38 presents the capital cost of the complete storage system based on the minimum, average and maximum costs. The capital cost ranges from $ 27.79 to 36.18 Million US$ with an average of $31.98 million. In Table 7.18 the cost of the various component of the cascaded finned LHS and the CTR are presented.

Table 7.17 Capital cost estimation of CTR

Item	Unit	Quantity	Unit Cost ($/unit)	Capital Cost ($)	
				Minimum	Maximum
Insulation (roof and wall)	m^2	6069	34.5	209,381	279,175
Foundation	m^2	4554	194	884,751	884,751
Heat exchanger	kg	1,673,169	2.5	4,182,923	4,182,923
Storage material	kg	42,166,539	0.04 – 0.1	1,686,662	4,216,654
Labour	%	20		1,392,743	1,912,701
Over head	%	10		835,646	1,147,620
Total				**9,192,107**	**12,554,031**

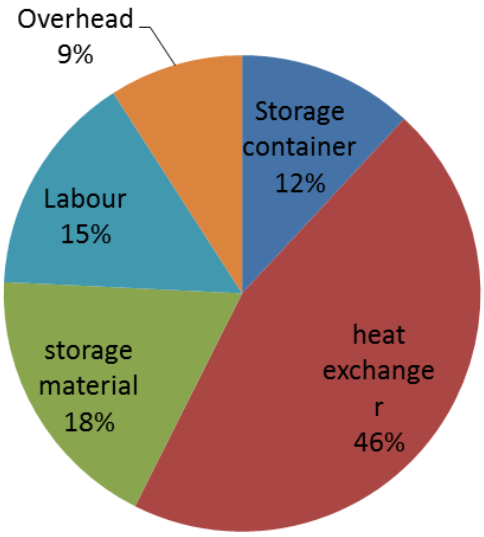

Figure 7.37 Cost distribution of the CTR based on the minimum unit cost

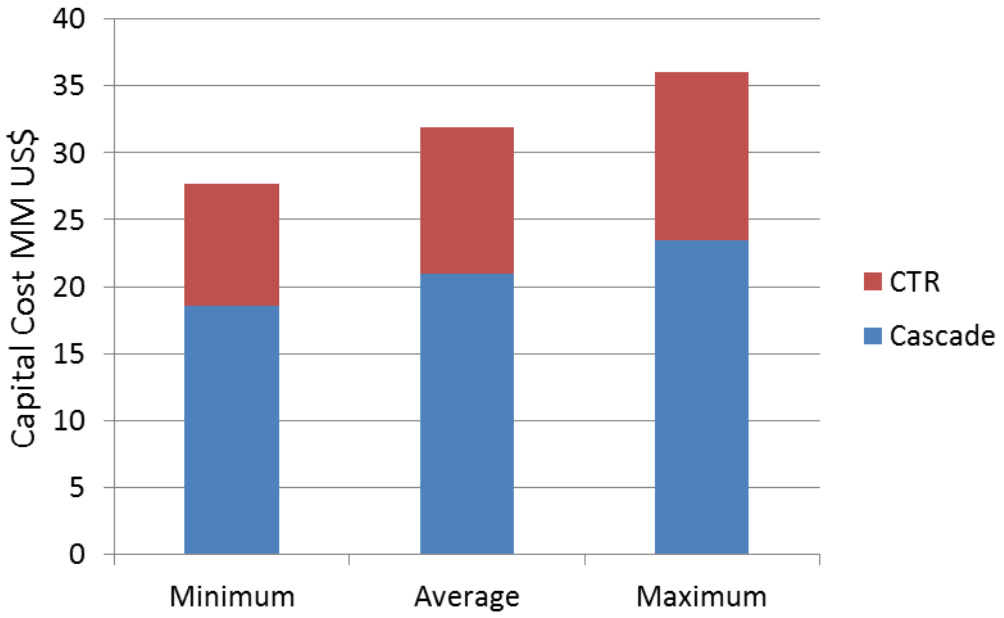

Figure 7.38 Capital cost of complete storage system

Table 7.18 Capital costs of finned cascade and the CTR based on the average unit cost in million US$

	Cascade	CTR
Storage container (including insulation and foundation)	4.13	1.16
Storage material	7.94	2.95
Heat exchanger	7.09	4.18
Labour*	-	1.65
Overhead (10%)	1.92	0.99
Total	**21.08**	**10.90**
Specific cost ($/kWh$_{th}$)	52.95	23.86

*the cost of labour for the cascade finned LHS has been included in individual components

7.5.4 Comparison with the Two-Tank System

For capacity of 875 MWh$_{th}$ (capacity required for 6 hour operation), the two tank system consist of a cold tank having a diameter of 37.2 m and hot tank with

diameter of 37.7 m. Both tanks have a height of 14 m with an active salt inventory of 26,000 tonnes [9; 20]. The total volume of the two tanks is thus 30,847.88 m^3. The volumetric specific capacity of the liquid solar salt was calculated to be 28.36 kWh/m^3. For the cascaded finned LHS and CTR storage system, the volumetric specific capacity was calculated to be 31 kWh/m^3 since the gross volume of the HCSS is 28,221 m^3. Even though the volumetric specific capacity of the CTR which is a solid sensible heat storage, the total specific capacity is greater than that of the two tank system by about 9.3%. This thus shows that the HCSS is a more compact than the two-tank system.

The specific capacity of the three-stage cascaded finned-LHS is ~44 kWh/m^3. This is greater than that of the two-tank system by 15.39 kWh/m^3. This corresponds to an increase in capacity of 54%. This thus shows the potential of the cascaded finned-LHS in reducing the size of the storage system.

Table 7.19 presents the cost comparison of various components of the HCSS with the two-tank system. The average cost of the HCSS was used here. It will be seen that the storage container and material cost for the HCSS is less than that of the two tank system, but the cost of heat exchanger for the HCSS is greater. This is partly due to the amount of steel pipes required in the CTR which forms 46% of the cost of the CTR. For the three-stage cascade the heat exchanger size can be reduced by using PCM with higher latent heat of fusion. This thus shows the need for developing new PCMs with high latent heat of fusion. The minimum capital cost is close to the capital cost of the two-tank system. The average cost is ~12% greater than the cost of the two tank system.

7.5.5 Concrete Tube Register (CTR) Cost Reduction Potential

The heat exchanger forms major part of the cost of the CTR. Thus to reduce the cost of the system ways of reducing the cost of the heat exchanger has to be found.

Table 7.19 Capital cost comparison with the two-tank system

	HCSS (MM$)	Two-tank system (MM$)
Storage container	5.29	8.21
Storage material	10.89	13.03
Heat exchanger	11.27	4.2
Molten salt pump	-	1.38
Labour	1.65	-
Overhead (10%)	2.91	2.59
Total	32.0	28.45
Specific cost ($/kWh$_{th}$)	36.6	32.5

FEM analysis of using pre-cast concrete slabs with horizontal placed high conductivity plates between slabs; and horizontal and vertical plates showed that 47% and 60% reduction in the amount of tube required is obtainable [13]. The benefit of this reduction will only be justified by considering the amount of the high conductivity material used. Potential high conductivity materials are aluminium and graphite.

Considering the use of aluminium plate of 0.5 mm thickness with density of 2700 kg/m^3 and estimated specific cost of 7000 $/m^3 [126]. Table 7.20 presents the cost reduction potential of using horizontal plates; and horizontal and vertical plates. The amount of steel and aluminium required with cost implication are presented. The amount of steel required without high conductivity plates was also presented for comparison. The average heat exchanger cost was used here. The use of horizontal plates resulted into 20% cost reduction while the use of vertical and horizontal plates resulted to about 24 % reduction in the cost of the CTR.

Table 7.20 Cost reduction potential using high conductivity plates

	Unit cost	Quantity			Cost ($)		
		No plates	Horizontal plates	Horizontal and vertical plates	No plates	Horizontal plates	Horizontal and vertical plates
Steel pipe, kg	2.5/kg	1,673,169	886,780	669,268	4,182,923	2,216,949	1,673,169
Aluminium sheets, m^3	7000/m^3		173	227		1,211,364	1,586,214
Total					4,651,061	3,708,053	3,498,785
Cost Reduction (%)					0	20.28	24.77

The use of horizontal plates resulted into 8.7% and 2.9% reduction in the capital cost of the heat exchanger and the overall capital cost of the HCSS respectively. The use of the vertical and horizontal plates resulted into 10.6% and 3.6% reduction in the cost of the heat exchanger and the overall cost of the HCSS respectively. Thus the use of the horizontal only and vertical and horizontal plates results into the decrease in the capital cost of the storage system.

7.6 Conclusions

Models for three-stage cascaded finned LHS and CTR storage-elements were developed and validated. The three-stage cascaded finned-LHS model was based on the heat transfer coefficient obtained in chapter 6. The model result for a single finned segment was compared with the CFD results and reasonable agreements were obtained. The CTR model was based on transient conduction with radial and axial discretization. The model was validated with experimental results and similar model from the literature. High temperature concrete was found to be the most suitable material for CTR storage system.

A procedure for the design of the three-stage cascaded finned-LHS and each cascade was proposed as follows:

- First a terminal temperature difference is selected
- Based on the terminal temperature difference the length of each PCM module is determined and the total length of the cascade obtained
- The total length of the cascade is then divided based on having the same capacity in each module to obtain the final length of each module.

Using this procedure a terminal temperature difference of 5^{o} was found to be a good compromise for the outlet temperature and the length of required heat exchanger. 5^{o} terminal temperature difference corresponds to a total three-stage cascade length of 30 m and based on having same capacity in each cascade, the length of each module is:

$NaNO_3$: 6.6 m, KNO_3/KCL: 13.2 m and KNO_3: 10.2 m.

Considering a 12 hour charging and discharging cycle, A CTR length of 130 m was found to satisfy the maximum charging and minimum discharging boundary conditions using a design mass flow rate of HTF of 0.03 kg/s at a periodically balanced state. The Three-stage cascade provides only 44% of the total capacity. This may be partly due to the fact that the cascade cannot produce temperatures above 335^{o}C which is the melting point of the third PCM. Even though increasing the length of the cascade increased the capacity ration to 50.4% it reduces the specific capacity of the cascade. Thus this is not a viable option.

For Six hours operation of the turbine a storage system capacity of 875 MWh_{th} is required. Design HTF mass flow rate of 0.035 kg/s was found to be the best and for the 6 hour capacity, 20,691 storage elements are required. These elements are arranged in a cylindrical enclosure for the three-stage cascade with each PCM having a separate container and a cuboid for the CTR. The dimension of the storage system is presented in Table 7.10 and Table 7.11 for the three-stage finned cascade and the CTR respectively. The effect of heat lost showed that heat lost can be neglected for the three-stage cascade while for the CTR the heat lost is about 10% of the storage capacity.

The capital cost of the HCSS ranges from $27.79 to $36.18 million. The minimum cost is less than the cost of the two-tank system while the average cost is greater by ~12%. The volumetric specific capacity of the storage system is 9.3% less than that of the two tank system, even though the CTR has a low volumetric specific capacity since it is a solid sensible storage system. The three-stage cascaded finned LHS has a volumetric specific capacity of 15.39 kWh/m^3 greater than that of the two-tank system, corresponding to an increase in capacity of 54%. This thus shows the potential of the finned cascaded LHS to provide a more compact storage system than the existing two tank system. It also points out the need for the development of new PCM's that will cover the whole operating temperature range of the parabolic-trough plant and also having higher latent heat of fusion similar to that of sodium nitrate. This will reduce the required size of the storage thus reducing the cost considerably.

8 CONCLUSIONS AND RECOMMENDATIONS FOR FURTHER WORK

8.1 Conclusions

A review of the various solar thermal power generation technologies showed that the parabolic-dish, parabolic-trough and the power tower are the most advanced solar thermal power generation technologies and have reached commercial status. The parabolic dish has the highest solar to electricity conversion efficiency (about 30%), but is best suited for small scale or standalone applications with capacities up to 25 kW_e. The power tower technology is best suited for large capacities (200-500 MW_e) making it to potentially produce cost effective electricity due to economy of scale. But the large scale means high initial capital investment which makes it less attractive.

Most power tower commercial plants either use water or molten salt as the HTF with 671 MW_e and 420 MW_e capacity using water and molten salt as HTF respectively under construction. The two-tank thermal storage system can easily be integrated with the molten-salt power tower plants making them capable of producing uninterrupted power for 24 hours. Although the use of water as the HTF offers potential cost reductions since a steam generator is not required, the most suitable thermal storage system is the use of pressurized water/steam tanks which are difficult to design and expensive for large scale use. There is need for finding alternative cost effective storage methods for power-tower plants using water as the HTF to be able to produce power uninterrupted for 24 hours.

The parabolic-trough is the most matured technology with most plants in operation utilizing this technology. This is partly due to the experience gained in the operation and maintenance of the 354 MW_e SEGS plants for more than two decades. Three working fluids: water, thermal oil and molten salts have been used in parabolic-trough plants but the use of thermal oil (synthetic oil) is the most matured with most plants in operation (~2.68 GW_e) and under construction (~1.4 GW_e) utilizing this technology. The use of water/steam as HTF has been

demonstrated showing about 11% reduction in LEC [90] for plant without storage but higher LEC was obtained for plants integrated with the existing two-tank system [91]. This showed that using the existing two-tank system with water/steam plant does not result into lower LEC. There is need for developing a thermal storage system specifically suitable for water/steam HTF in order to realise their cost reduction potential. The parabolic-trough technology using synthetic oil (Therminol VP-1) as HTF with operating temperature ranging from 291^{o}C to 391^{o}C [11] is the most matured solar thermal power generation and cost effective in the small and medium scale capacity (<200 MW_e).

There are basically three methods of storing thermal energy: chemical, sensible and latent. Chemical storage is at the developmental stage and very expensive and has not been applied in parabolic-trough power plants. The sensible and latent heat storage methods are the most considered for parabolic-trough plants. Three technologies have been researched over the years under the sensible storage methods: two-tank, single-tank thermocline, and the CTR systems.

The two-tank system is currently the state of the art in thermal storage for parabolic-trough. This technology is expensive due to the amount of storage materials (molten inorganic salt) and two tank requirements. It also has high parasitics, due to the need to keep the storage material above its high melting temperature.

The single tank thermocline system offers lower cost and reduced storage material inventory compared to the two-tank system and has been demonstrated on small scale [99]. Simulations of commercial scale system have shown its capability for producing a smaller and more cost effective (~33% reduction in cost compared to the two-tank system) storage system if the turbine is allowed to operate up to minimum temperature of 300^{o}C during discharging [12]. The main challenge hindering the full utilization of the single-tank thermocline system is thermal ratcheting. There is also need for a complete optimization of the storage system integrated with commercial scale

parabolic-trough solar thermal plant to determine the storage size and capacity that will give the minimum capital and LEC.

The availability and low cost of concrete prompted the development of the CTR system, in order produce a more cost effective system. Various pilot plants were tested and the feasibility of developing a commercial scale system has been conducted successfully [13]. The main issue with CTR is their high volume. There is no plan for the deployment of a CTR for parabolic-trough plants using synthetic oil as the HTF.

LHS systems offer smaller storage sizes due to their higher storage density. Due to the wide operating temperature range (between 300 and 400^{o}C) in parabolic-trough plants, many PCMs, with different melting temperatures, have to be used to realise the potential of LHS systems. Investigation on cascaded LHS have shown that there is need for heat transfer enhancement in the PCM and there is lack of potential PCMs to cover the whole operating temperature range of parabolic-trough plants using synthetic oil as the HTF.

It was shown that the low thermal conductivity of potential PCMs for use in LHS systems and the lack of available PCMs to cover the operating temperature range (between 300 and 400^{o}C) have hindered the capability of producing a more cost effective LHS system than the currently available two-tank system. There are very few PCMs having melting temperature in the operating temperature range of the parabolic-trough plants using synthetic oil as the HTF. Alkali nitrates and nitrites are the most suitable PCMs for use in LHS systems due to their stability, corrosiveness and compatibility with materials of the system. Many eutectic mixtures of materials have potential for use but the main challenge with eutectic mixture is the correctness of the melting temperature and latent heat of fusion reported in the literature. Thus properties of these eutectic mixtures must be confirmed using experiments before a PCM can be termed suitable. Many of the potential eutectic mixtures (Tables 4.3 and 4.4) are chlorides and hydroxides both of which corrode steel, hydroxides attack aluminium and chlorides have high vapour pressure. This has limited their suitability. In view of this only three commercially available PCMs (Table 4.5)

whose properties have been confirmed experimentally, are suitable in the operating temperature range. There is need in finding other PCMs with high latent heat of fusion preferably mixtures containing more of nitrates since they are the most suitable. Thus to cover the operating temperature range a sensible storage stage can be incorporated to form a hybrid system.

Thus, in this study, a hybrid cascaded storage system (HCSS) consisting of a cascaded finned-LHS and a high temperature sensible (CTR) stages was proposed and analysed for use as a thermal storage system in a parabolic-trough solar thermal power plant, using synthetic oil as the HTF, via modelling and simulation. A thorough review of the literature showed that this configuration has not been investigated.

The existence of a phase change model in the commercial CFD software meant that modelling effort will be reduced and design of LHS systems for particular application can be simplified. Although Shmueli et al. [164] validated this model for melting in vertical cylinder with experimental data by comparison of only the liquid fraction, deviations of up to 12% was obtained. Other variables such as the temperature distribution and melt interface in the PCM were not compared. Sciacovelli et al. [194] also compared the temperature distribution in PCM with those obtained experimentally with discrepancies observed at regions below the melting point of the PCM. No comparison of other parameters was conducted.

The Fluent CFD phase change model was thus validated using the well-controlled and documented experimental results of Jones et al. [139] for the melting of paraffin (n-eicosane) in a vertical cylinder. Maximum deviation of the predicted melt fraction of 7.5% was obtained, which is smaller than those obtained by Shmueli et al. [164] by 4.5%. Comparison of temperatures at various locations and the melt interface shape at various times in the domain gave reasonable agreements with the experimental data. The results obtained compared reasonably well with those obtained using other numerical codes. The use of effective heat capacity in the solid PCM, proposed by Wang et al. [140] was found to increase the accuracy of the predicted temperature distribution below melting point but has a negligible effect on the melt fraction.

This showed that the Fluent phase change model is capable for use in modelling of phase change in vertical cylinders.

Most numerical investigation of melting and solidification in cylindrical enclosures are for aspect ratios (L/r_o) of less than 20 and for low temperature applications (i.e. $<100^oC$). In practice, especially for solar thermal power generation applications, very large aspect ratios are used. Also these studies are either for the charging or discharging only but not both. In view of this the validated model was used for the simulation of the charging and discharging of a practical size single shell-and-tube storage element with an aspect ratio (L/r_o) of 153. During charging (melting) the presence of the four heat transfer regimes classified by Jany and Bejan, [160] for rectangular enclosures were also observed for cylindrical annular enclosure. The effect of natural convection cannot be neglected during charging since it plays a big role and the existence of quasi-stationary melting was observed during the charging process. Although various correlations have been developed for the dimensionless quasi-stationary heat transfer coefficient during melting, its dependency on various geometrical configurations such as the radius of the HTF-pipe, the radius of shell, height of cylinder and also the PCM's thermo-physical properties have limited their practical application.

During discharging, conduction was found to be the main mode of heat transfer during most part of the process. This is because as the process progresses the PCM solidified around the tube forming a layer of solid PCM around the HTF-pipe. Although there is convection in the liquid phase, the solid layer makes conduction to be dominant. Thus models that neglect the effect of convection can predict the amount of heat discharged in a LHS system with a maximum discrepancy of 6%. The percentage of PCM that undergoes phase change during a specified time interval, which is a measure of the actual capacity of the LHS system, is lower during discharging and thus design of LHS system must be based on the discharging process.

The low thermal conductivity of potential PCMs necessitates the enhancement of heat transfer in the PCM. Various heat transfer enhancement methods

suitable for parabolic-trough plants using synthetic oil as the HTF that have been studied in the literature, were reviewed. It was concluded that the use of fins is the most suitable and practical technique to be employed. Thus, there is need of finding the best fin configuration, heat transfer characteristics and heat transfer coefficients that can be used for the design of a complete finned LHS system using synthetic oil as the HTF. Although Guo and Zang [180] presented the effect of different fin configurations for finned-LHS module using $KNO_3/NaNO_3$ PCM, their study did not consider the heat transfer process in the HTF flowing in the pipe. Therefore, the study did not give realistic quantitative performance results.

CFD simulations, considering the discharging of a single finned-LHS segment, showed that increasing the fin outer radius above 48.8 mm for HTF-pipe with outer diameter of 0.012 m, does not result into any performance benefit. A fin configuration having distance between fins of 10 mm, fin thickness of 1.0 mm was found to be the best configuration. During the charging process in a finned LHS, convection was found to play a role in the heat transfer and quasi-stationary melting was also observed. The quasi-stationary heat transfer coefficient during the melting and overheating process (after melting) was PCM dependent. Thus convection cannot be neglected during the charging of a finned LHS system. The heat transfer coefficient during melting was found not to be a strong function of the driving temperature difference. Correlations that can be used for the determination of the heat transfer coefficient during melting – equations (6.4) to (6.6) – were determined for each PCM as functions of the HTF mass flow rate. Charts for the heat transfer coefficient during overheating were also obtained.

During the discharging process pure conduction is the main mode of heat transfer. Although convection distorts the shape of the melt interface especially at the beginning of the process, it has negligible impact in the heat transfer rate over most part of the process. The heat transfer coefficient during solidification depends on the liquid fraction and the HTF mass flow rate (or velocity). This is not surprising since as solidification progresses, the solid PCM layer around the

fin and the HTF pipe increases. A linear function based on liquid fraction was developed for the determination of the heat transfer coefficient (equation (6.8)). These obtained correlations can be used to determine the performance of a complete finned LHS system suitable for parabolic-trough plant using synthetic oil as HTF. The finding of the best finned configuration and correlations that can be used for design of finned LHS system for parabolic-trough plants has not appeared in the literature.

Models for the cascaded finned-LHS and CTR storage-elements were developed in the Dymola simulation environment. The heat transfer coefficients obtained in Chapter 6, for the charging and discharging were used. Comparison between the Dymola model and CFD results for a single finned-LHS segment gave reasonable agreements. Using the model and considering the discharging of a cascaded finned LHS element, a procedure for the design of the cascade (length of each finned LHS element and total length of the cascaded finned LHS) was obtained as follows:

- First a terminal temperature difference is selected (i.e. 5^oC).
- Based on the terminal temperature difference the length of each PCM module is determined and the total length of the cascade obtained.
- The total length of the cascade is then divided based on having the same capacity ($m_{pcm}\lambda = constant$) in each finned LHS element to obtain the final length of each element.

Using this procedure a terminal temperature difference of 5^o was found to be a good compromise for the HTF outlet temperature and the length of required heat exchanger. 5^o terminal temperature difference corresponds to a cascaded finned-LHS element length of 30 m and based on having same capacity in each cascade, the length of each finned LHS element is:

$NaNO_3$: 6.6 m, KNO_3/KCl: 13.2 m and KNO_3: 10.2 m.

The CTR model was based on transient conduction with radial and axial discretization. Validation of the CTR model with experimental and similar model

from the literature showed reasonable agreements. Preliminary investigation considering only the CTR showed that a length of ~120 m is required.

A model for the complete HCSS element was formed by joining the cascaded finned LHS and the CTR models in series. Simulations were then conducted for a 12 hour charging and discharging cycle using a HTF mass flow rate of 0.03 kg/s with the length of the CTR adjusted until the required boundary conditions of the parabolic-trough plant for a 12 hour charging and discharging cycle. A CTR length of 130 m was found to satisfy the boundary condition at a periodically balanced state. The cascaded finned-LHS provides only 44% of the total capacity. This may be partly due to the fact that the cascade cannot produce temperatures above 335^{o}C which is the melting point of the third PCM. Increasing the length of the cascaded finned LHS to 36 m, was found to increase the capacity ratio of the cascade to 50.4% but it reduces the specific capacity of the cascade.

The effect of HTF mass flow rate on the element capacity was then investigated. For each HTF mass flow rate the best cascade length and CTR lengths were obtained that give the highest specific capacity and percentage capacity of cascade. It was found out that a design mass flow rate of 0.035 kg/s is the best considering specific capacity and total required number of storage elements in an 875 MWh_{th} capacity system. This corresponds to a HCSS element capacity of 42.29 kWh_{th}, cascade and CTR lengths of 36 m and 150 m respectively.

For six hours full load operation of a 50 MW_e power block, a storage system capacity of 875 MWh_{th} is required. For an 875 MWh_{th} capacity HCSS, 20,691 HCSS elements are required (considering each HCSS-element capacity of 42.29 kWh_{th}). The dimension of the HCSS is presented in Tables 7.10 and 7.11 for the cascaded finned-LHS and the CTR modules respectively. The effect of heat lost showed that heat lost can be neglected for the cascade while for the CTR the heat lost is about 10% of the storage capacity. This means the size of the CTR must be increased by 10% to cater of the heat lost.

The capital cost of the HCSS ranges from $27.79 million to $36.18 million. The minimum cost is less than the cost of the commercially available two-tank system while the average cost is greater by ~12%. The volumetric specific capacity of the storage system is 9.3% less than that of the two-tank system, even though the CTR has a low volumetric specific capacity since it is a solid sensible storage system. The cascaded finned-LHS stage has a volumetric specific capacity which is greater than that of the two-tank system by 15.39 kWh/m^3, corresponding to an increase in capacity of 54%. This thus shows the potential of the cascaded finned-LHS system in providing a more compact storage system than the existing two-tank system. It also points out the need for the development of new PCMs that can cover the whole operating temperature range of the parabolic-trough plant and also those with latent heat of fusion similar to that of sodium nitrate. This will reduce the required size of the storage thus reducing the cost considerably.

The use of horizontal; and horizontal and vertical heat transfer enhancement plates in CTR in order to reduce the amount of steel pipe required in the CTR showed a decrease in the CTR cost of 20 and 24% respectively equivalent to a total reduction in the 2.9% reduction for horizontal plates and 3.6% reduction for vertical and horizontal plates in the capital cost of the HCSS. The impact of the potential cost reduction in the CTR was small in the complete HCSS since the cost of the system is dominated by the cost of the cascaded finned-LHS.

The proposed HCSS is a passive storage system that does not require the flow of storage material meaning the cost of operation and maintenance will be lower than the two-tank system. The development of a suitable PCM especially with melting temperature between 350 and 400^oC will make the system not to require the CTR module making it more compact and the performance of the system when integrated with the plant will be enhanced. This can result into lower LEC. The cost of a two-tank system is almost proportional to the size of the system. But a higher storage capacity HCSS system (e.g. 9 hours) can be realised by increasing the fin height and the length of the CTR. There will be no

need of increasing the number of HTF-pipes. This means that the HCSS has potential of even lower capital cost at higher capacity.

However, the heat transfer coefficient obtained for the charging processes, in Chapter 6, may only be valid for the particular fin configuration and HTF-pipe radius of 6 mm. This is due to its high dependence on the geometrical configuration of the system. That obtained for the discharging is also only valid for the distance between fins and fin thickness of the best selected configuration. This can limits the applicability of the developed model for the design of storage system considering other fin configurations. Nonetheless changing the HTF-pipe radius may not give high discrepancies considering that the design is mostly determined by the slower discharging process. But it will affect the dynamic performance of the system when incorporated with the solar thermal power plant.

8.2 Recommendations for Further Work

The following are recommended future work that can improve upon the work presented in this thesis:

- Since the design of a LHS must be based on the slower discharging process a general correlation for the heat transfer coefficient as a function of liquid fraction and other geometrical parameters such as fin thickness, fin height, HTF pipe radius, distance between fins, thermal conductivity of PCM and forced convection heat transfer coefficient in HTF pipe can be obtained. This can be used for the design of any finned LHS system. This can be done by conducting several simulations and finding the effect of each on the heat transfer coefficient. From this work it has been established that the heat transfer coefficient during discharging does not depend on the driving temperature difference.

- The integration of the designed HCSS with models of the solar field and the power block in order to determine the dynamic performance of the system and the annual performance and economics considering solar radiation of a particular place can be conducted. Thus the LEC can be determined for the

whole system. Also an optimization study of various storage capacities (> 6 hours) using LEC as the objective function can be conducted to determine the optimum storage capacity.

- The PCM screening conducted in Chapter 4 has shown that there is need for finding materials with high latent heat, especially eutectic mixtures of nitrates and nitrites with melting temperatures between 300 and 400^{o}C with more emphasis on materials having melting temperature between 335 and 400^{o}C in order to cover the operating temperature range.

- The capacity of the cascade was limited by the melting temperature of the top PCM (335^{o}C). Considering that in the Rankine power cycle (maximum pressure of 100 bar) about 88.4% of the thermal energy required is at a temperature level below 311^{o}C (pre-heating and evaporation of feed water). The HCSS can be designed in such a way that during discharging the cascaded finned-LHS section is used for the pre-heating and evaporation of the feed water while the CTR can be used for the superheating of the steam. This concept can increase the percentage capacity of the cascaded finned-LHS thus increasing the volumetric specific capacity of the system and performance. Also the annual performance can be conducted and the LEC determined.

- The single tank thermocline storage system has been proved to offer potential cost reduction in terms of capital cost. There is still the need for optimization of the system integrated with the solar thermal power plant to determine the capacity that will give the minimum LEC.

REFERENCES

[1] WEC (2010), *Solar Energy. In: 2010 Survey of energy resources,* , WEC, London.

[2] Denholm, P., Drury, E., Margolis, R. and Mehos, M. (2009), Solar Energy: The largest Energy Resource, in Sioshansi, F. B. (ed.) *Generating Electricity in a Carbon Constrained World,* Academic Press, Burlington, USA, pp. 271-302.

[3] De Laquil, P., Kearney, D., Geyer, M. and Diver, R. (1993), Solar-Thermal Electric Technology, in *Renewable energy: sources for fuels and electricity,* Earthscan, London, pp. 213-296.

[4] SolarPACES (2010), *CSP Technology*, available at: www.solarpaces.org (accessed 12/09).

[5] Müller-Steinhagen, H. and Trieb, F., (2004), *Concentrating solar power: A review of the technology*, Quarterly of the Royal Academy of Engineering Ingenia.

[6] NREL (2014), *Concentrating solar power projects*, available at: www.nrel.gov (accessed 02/21).

[7] Gil, A., Medrano, M., Martorell, I., Lázaro, A., Dolado, P., Zalba, B. and Cabeza, L. F. (2010), State of the art on high temperature thermal energy storage for power generation. Part 1-Concepts, materials and modellization, *Renewable and Sustainable Energy Reviews,* vol. 14, no. 1, pp. 31-55.

[8] Pilkington (2000), *Survey of thermal storage for parabolic trough power plants,* NREL/SR-550-27925, National Renewable Energy Laboratory, Colorado, USA.

[9] Herrmann, U., Kelly, B. and Price, H. (2004), Two-tank molten salt storage for parabolic trough solar power plants, *Energy,* vol. 29, no. 5-6, pp. 883-893.

[10] Aringhoff, R., Brakmann, G., Geyer, M. and Teske, S. (2005), Concentrated solar thermal power - Now! *Report of Greenpeace International, the European Solar Thermal Industry Association (ESTIA) and IEA SolarPACES Programme,* .

[11] Kelly, B., Kearney, D. and Price, H. (2006), *Thermal Storage commercial plant design study for a 2- tank indirect molten salt system,* NREL/SR-550-40166, National Renewable Energy Laboratory, Colorado, USA.

[12] Kolb, G. J. (2011), Evaluation of annual performance of 2-tank and thermocline thermal storage systems for trough plants, *Journal of Solar Energy Engineering, Transactions of the ASME,* vol. 133, no. 3.

[13] Laing, D., Bahl, C., Bauer, T., Fiss, M., Breidenbach, N. and Hempel, M. (2012), High-temperature solid-media thermal energy storage for solar thermal power plants, *Proceedings of the IEEE,* vol. 100, no. 2, pp. 516-524.

[14] Roeb, M., Neises, M., Monnerie, N., Sattler, C. and Pitz-Paal, R. (2011), Technologies and trends in solar power and fuels, *Energy and Environmental Science,* vol. 4, no. 7, pp. 2503-2511.

[15] Nomura, T., Okinaka, N. and Akiyama, T. (2010), Technology of latent heat storage for high temperature application: A review, *ISIJ International,* vol. 50, no. 9, pp. 1229-1239.

[16] Shabgard, H., Robak, C. W., Bergman, T. L. and Faghri, A. (2012), Heat transfer and exergy analysis of cascaded latent heat storage with gravity-assisted heat pipes for concentrating solar power applications, *Solar Energy,* vol. 86, no. 3, pp. 816-830.

[17] Dinter, F., Geyer, M. A. and Tamme, R. (eds.) (1991), *Thermal energy storage for commercial applications,* Springer-Verlag, New York.

[18] Michels, H. and Hahne, E. (1996), Cascaded latent heat storage for solar thermal power stations, *Proceedings of 10th International Solar Forum,* Freiburg, Germany, EuroSun, Germany.

[19] Michels, H. (2006), *Kaskadierte Speicher latenter Wärme für Parabolrinnen-Solarkraftwerke* (PhD thesis), VDI Verlag, Dusseldorf, Germany.

[20] Michels, H. and Pitz-Paal, R. (2007), Cascaded latent heat storage for parabolic trough solar power plants, *Solar Energy,* vol. 81, no. 6, pp. 829-837.

[21] Steinmann, W. D., Laing, D. and Tamme, R. (2010), Latent heat storage systems for solar thermal power plants and process heat applications, *Journal of Solar Energy Engineering, Transactions of the ASME,* vol. 132, no. 2, pp. 0210031-0210035.

[22] Steinmann, W. D., Laing, D. and Tamme, R. (2009), Development of PCM storage for process heat and power generation, *Journal of Solar Energy Engineering, Transactions of the ASME,* vol. 131, no. 4, pp. 0410091-0410094.

[23] Steinmann, W. D. and Tamme, R. (2008), Latent heat storage for solar steam systems, *Journal of Solar Energy Engineering, Transactions of the ASME,* vol. 130, no. 1, pp. 0110041-0110045.

[24] Tamme, R., Bauer, T., Buschle, J., Laing, D., Müller-Steinhagen, H. and Steinmann, W. D. (2008), Latent heat storage above 120°C for applications in the industrial process heat sector and solar power generation, *International Journal of Energy Research,* vol. 32, no. 3, pp. 264-271.

[25] Pincemin, S., Py, X., Olives, R., Christ, M. and Oettinger, O. (2008), Elaboration of conductive thermal storage composites made of phase change materials and graphite for solar plant, *Journal of Solar Energy Engineering, Transactions of the ASME,* vol. 130, no. 1, pp. 011005-0110055.

[26] Pincemin, S., Olives, R., Py, X. and Christ, M. (2008), Highly conductive composites made of phase change materials and graphite for thermal storage, *Solar Energy Materials and Solar Cells,* vol. 92, no. 6, pp. 603-613.

[27] Laing, D., Bauer, T., Ehmann, D. and Bahl, C. (2010), Development of a thermal energy storage system for parabolic trough power plants with direct steam generation, *Journal of Solar Energy Engineering, Transactions of the ASME,* vol. 132, no. 2, pp. 0210111-0210118.

[28] Robak, C. W., Bergman, T. L. and Faghri, A. (2011), Economic evaluation of latent heat thermal energy storage using embedded thermosyphons for concentrating solar power applications, *Solar Energy,* vol. 85, no. 10, pp. 2461-2473.

[29] Shabgard, H., Bergman, T. L., Sharifi, N. and Faghri, A. (2010), High temperature latent heat thermal energy storage using heat pipes, *International Journal of Heat and Mass Transfer,* vol. 53, no. 15-16, pp. 2979-2988.

[30] Agyenim, F., Hewitt, N., Eames, P. and Smyth, M. (2010), A review of materials, heat transfer and phase change problem formulation for latent heat thermal energy storage systems (LHTESS), *Renewable and Sustainable Energy Reviews,* vol. 14, no. 2, pp. 615-628.

[31] Steinmann, W. D. and Zunft, S. (2002), TechThermo-A library for modelica applications in technical thermodymics, in Otter, M. (ed.), *2nd International Modelica Conference,* 18-19 March, Germany, The Modelica Association, pp. 217.

[32] El-Wakil, M. M. (1985), *Powerplant technology,* McGraw-Hill, New York.

[33] Trieb, F., Langniß, O. and Klaiß, H. (1997), Solar electricity generation - A comparative view of technologies, costs and environmental impact, *Solar Energy,* vol. 59, no. 1-3, pp. 89-99.

[34] Holl, R. J. (1989), *Status of solar-thermal electric technology,* EPRI GS-6573, Electric Power Research Institute.

[35] Schiel, W. and Keck, T. (2012), Parabolic dish concentrating solar power (CSP) systems, in Lovegrove, K. and Stein, S. (eds.) *Concentrating Solar Power Technology: Principles, development and applications,* Woodhead Publishing Ltd, Oxford, pp. 284-322.

[36] Lovegrove, K., Zawadski, A. and and Coventy, J. (2006), Taking the ANU Big Dish to commercialization, *Proceedings of ANZSES the Annual Conference, Solar 2006,* 13-15 September, Canberra, .

[37] Lovegrove, K. and Dennis, M. (2006), Solar thermal energy systems in Australia, *International Journal of Environmental Studies,* vol. 63, no. 6, pp. 791-802.

[38] Lovegrove, K., Burgess, G. and Pye, J. (2011), A new 500m2 paraboloidal dish solar concentrator, *Solar Energy,* vol. 85, no. 4, pp. 620-626.

[39] Jaffe, L. D. (1988), A review of test results on solar thermal power modules with dish mounted Stirling and Brayton cycle engines, *Journal of Solar Energy Engineering, Transactions of the ASME,* vol. 110, pp. 275-281.

[40] Lopez, C. W. and Stone, K. W. (1992), Design and performance of the Southern California Edison Stirling Dish, *ASME International Solar Energy Conference,* March, Maui, Hawaii, .

[41] Koshaim, B. (1986), *Fifty KW solar membrane concentrator,* , The SOLERAS Program, Saudi Arabian National Centre for Science and Technology.

[42] Bean, J. R. and Diver, R. B. (1995), *Technical Status of the Dish Stirling Joint Venture,* 95-202, Cummins Power Generation Inc. and US Department of Energy, New Mexico.

[43] Andraka, C., Diver, R., Adkins, D., Rawlinson, S., Cordeiro, P., Dudley, V. and Moss, T. (1993), Testing of the Stirling engine solar reflux heat-pipe receivers, *Proceedings of the 28th Intersociety Energy Conversion Conference (IECEC),* August, Atlanta, GA, .

[44] IEA (2010), *Technology roadmap: Concentrating solar power,* , IEA, OECD, Paris.

[45] Ho, C. K. and Iverson, B. D. (2014), Review of high-temperature central receiver designs for concentrating solar power, *Renewable and Sustainable Energy Reviews,* vol. 29, pp. 835-846.

[46] Siegel, N. P. (2010), Solar thermal power generation in the United States, *Nihon Enerugi Gakkaishi/Journal of the Japan Institute of Energy,* vol. 89, no. 4, pp. 322-330.

[47] Baker, A. F. (1988), *10 MWe Solar Thermal Central Receiver Pilot Plant Receiver Performance Final Report,* SAND 88-8000, Sandia National laboratories, New Mexico, USA.

[48] Radosevich, L. G. and Skinrood, A. C. (1989), Power production operation of Solar One, the 10 MWe Solar Thermal Central Receiver Pilot Plant, *Journal of Solar Energy Engineering, Transactions of the ASME,* vol. 111, no. 2, pp. 144-151.

[49] Solúcar (2006), *10 MW solar thermal power plant for southern spain: Final technical progress report*, available at: ec.europa.eu/energy/res/sectors/doc/csp/ps10_final_report.pdf (accessed 12/12).

[50] EC (2007), *Concentrating solar power: From research to implementation,* , EC, Brussels.

[51] Abengoa Solar (2012), *Our plants: Operating facilities Spain*, available at: www.abengoasolar.com (accessed 01/01).

[52] Meduri, P. K., Hannemann, C. R. and Pacheco, J. E. (2010), Performance Characterization and Operation of eSolar's Sierra Suntower Power Tower Plant, *Proceedings of the 2010 SolarPACES Conference,* 21-24 September, Perpignan, France, .

[53] eSolar (2011), *Sierra Sun Tower: A blueprint for solar energy*, available at: www.esolar.com (accessed 11/27).

[54] Vant-Hull, L. L. (2012), Central Tower Concentrating Solar Power, in Lovegrove, K. and Stein, S. (eds.) *Concentrating Solar Power Technology: Principles, development and applications,* Woodhead Publishing, Oxford, pp. 240-283.

[55] Reilly, H. E. and Pacheco, J. E. (2000), *Solar Two: A succesful power tower demonstration project,* SAND2000-0559C, Sandia National Laboratories, New Mexico, USA.

[56] Pacheco, J. E., Reilly, H., Kolb, G. and Tyner, C. E. (2000), Summary of the Solar Two test and evaluation program, *Proceedings of the 2000 SolarPACES Conference,* 8-10 March, Sydney, Australia, .

[57] Reilly, H. E. and Kolb, G. J. (2001), *An evaluation of molten-salt power towers including results of the Solar Two project,* SAND2001-3674, Sandia National Laboratory (SAND), New Mexico, USA.

[58] SENER (2011)*, Gemasolar solar power plant reaches 24 hours of uninterrupted production*, available at: www.sener-power-process.com (accessed 11/30).

[59] IEA (2009), *Renewable energy essential: Concentrating solar power,* , IEA, Paris.

[60] Kribus, A., Zaibel, R., Carey, D., Segal, A. and Karni, J. (1998), A solar-driven combined cycle power plant, *Solar Energy,* vol. 62, no. 2, pp. 121-129.

[61] Fricker, H. W. and Meinecke, W. (1988), PHOEBUS results of the system comparison of the 30 MWe European feasibility study, *In the proceedings of the 4th International Symposium on Research, Development and Applications of Solar Thermal Technology,* Santa Fe, New Mexico, Hemisphere Publishing Company, New York, pp. 265-277.

[62] Koll, G., Schwarzbozi, P., Hennecke, K., Hartz, T. H., Schmitz, M. and Hoffschmidt, B. (2009), The solar thermal tower julich-A research and demostration plant for central receiver systems, *In Proceedings of the 2009 SolarPACES Conference,* 15-18 September 2009, Berlin, Germany, .

[63] Grasse, W. (1991), PHOEBUS: international 30 MWe solar tower plant, *Solar Energy Materials,* vol. 24, no. 1-4, pp. 82-94.

[64] Meinecke, W., Kiera, M. and Wehowsky, P. (1991), 30 MWe PHOEBUS feasibility study: results of system engineering, *Solar Energy Materials,* vol. 24, no. 1-4, pp. 95-107.

[65] Klaiß, H., Köhne, R., Nitsch, J. and Sprengel, U. (1995), Solar thermal power plants for solar countries - Technology, economics and market potential, *Applied Energy,* vol. 52, no. 2-3, pp. 165-183.

[66] Hennecke, K., Schwarzbözl, P. and Koll, G. (2007), The solar tower Julich- A solar thermal power plant for test and demonstration of air receiver technology, *In the Proceedings of ISES World Congress 2007: Solar Energy and Human Settlement,* 18-21 September, Beijing, China, Springer Verlag, pp. 1749-1753.

[67] EC (2005), *SOLGATE Solar hybrid gas turbine electric power system; Final publishable report,* EUR21615, Directorate-General for Research, EC, Brussels.

[68] Rabl, A. (1976), Optical and thermal properties of compound parabolic concentrators, *Solar Energy,* vol. 18, no. 6, pp. 497-511.

[69] Kribus, A., Doron, P., Rubin, R., Karni, J., Reuven, R., Duchan, S. and Taragan, E. (1999), A multistage solar receiver: The route to high temperature, *Solar Energy,* vol. 67, no. 1-3, pp. 3-11.

[70] Karni, J., Kribus, A., Doron, P., Rubin, R., Fiterman, A. and Sagie, D. (1997), The DIAPR: A high-pressure, high-temperature solar receiver, *Journal of Solar Energy Engineering, Transactions of the ASME,* vol. 119, no. 1, pp. 74-78.

[71] Mokri, A., Aal Ali, M. and Emziane, M. (2013), Solar energy in the United Arab Emirates: A review, *Renewable and Sustainable Energy Reviews,* vol. 28, pp. 340-375.

[72] Kalt, A., Loosme, M. and Dehne, H. (1981), *Distributed Collector System Plant Construction Report,* IEA-SSPS-SR-1, IEA, Cologne.

[73] Schraub, F. A. and Dehne, H. (1983), Electric generation system design: Management, startup, and operation of IEA distributed collector solar system in Almeria, Spain, *Solar Energy,* vol. 31, no. 4, pp. 351-354.

[74] Fernández-García, A., Zarza, E., Valenzuela, L. and Pérez, M. (2010), Parabolic-trough solar collectors and their applications, *Renewable and Sustainable Energy Reviews,* vol. 14, no. 7, pp. 1695-1721.

[75] Gee, R. C. and Hale, M. J. (2005), Solargenix Energy Advanced Parabolic Trough Development, *Presented at the 2005 DOE Solar Energy Technologies Program Review Meeting,* 7-10 Novemeber, Denver, Colorado, .

[76] Canada, S., Cable, R. and Price, H. (2005), Status of APS 1-MWe parabolic trough project, *2005 DOE Solar Energy Technologies Program Review Meeting,* 7-10 November, Denver, Colorado, .

[77] Jones, J. (2007), Concentrating solar power, CSP lifts off, 2007, *Renew Energy World,* vol. 10, no. 3, pp. 36-38.

[78] EurObserv'ER (2013), *The state of renewable energies in Europe: The 13th EurObserv'ER Report,* , EurObserv'ER, Paris.

[79] ENEA (2011), *Renewable Energy Sources*, available at: www.enea.it (accessed 12/05).

[80] Marquez, C. (2008), *An Overview of CSP in Europe, North Africa and the middle East,* , CSP Today.

[81] Price, H., Lüpfert, E., Kearney, D., Zarza, E., Cohen, G., Gee, R. and Mahoney, R. (2002), Advances in parabolic trough solar power technology, *Journal of Solar Energy Engineering, Transactions of the ASME,* vol. 124, no. 2, pp. 109-125.

[82] Zarza, E., Valenzuela, L., León, J., Hennecke, K., Eck, M., Weyers, H. -. and Eickhoff, M. (2004), Direct steam generation in parabolic troughs: Final results and conclusions of the DISS project, *Energy,* vol. 29, no. 5-6, pp. 635-644.

[83] Eck, M. and Zarza, E. (2006), Saturated steam process with direct steam generating parabolic troughs, *Solar Energy,* vol. 80, no. 11, pp. 1424-1433.

[84] Zarza, E., Rojas, M. E., González, L., Caballero, J. M. and Rueda, F. (2006), INDITEP: The first pre-commercial DSG solar power plant, *Solar Energy,* vol. 80, no. 10, pp. 1270-1276.

[85] Zarza, E., Lopez, C. W., Camara, A., Martinez, A., Burgaleta, J. I., Martin, J. C. and Fresneda, A. (2008), Almeria GDV- The first solar power plant with direct steam generation. *14th Biennial CSO SolarPACES (Solar Power and Chemical Energy Systems) Symposium,* 4-7 March, Las Vegas (USA), .

[86] PSA (2009), *Plataforma Solar de Almeria-Biannual Report 2008-2009,* , PSA, Spain.

[87] Mills, D. R. and Morrison, G. L. (2000), Compact linear fresnel reflector solar thermal powerplants, *Solar Energy,* vol. 68, no. 3, pp. 263-283.

[88] DLR (German Aerospace Centre) (2007), *Inauguration of new Fresnel Collector at Plataforma Solar de Almería in Spain*, available at: www.dlr.de (accessed 12/20).

[89] AREVA Solar (2011), *AREVE Solar: Projects*, available at: www.areva.com (accessed 12/20).

[90] Feldhoff, J. F., Benitez, D., Eck, M. and Riffelmann, K. -. (2010), Economic potential of solar thermal power plants with direct steam generation compared with HTF plants, *Journal of Solar Energy Engineering, Transactions of the ASME,* vol. 132, no. 4.

[91] Feldhoff, J. F., Schmitz, K., Eck, M., Schnatbaum-Laumann, L., Laing, D., Ortiz-Vives, F. and Schulte-Fischedick, J. (2012), Comparative system analysis of direct steam generation and synthetic oil parabolic trough power plants with integrated thermal storage, *Solar Energy,* vol. 86, no. 1, pp. 520-530.

[92] Laing, D., Lehmann, D. and Bahl, C. (2008), Concrete Storage for Solar Thermal Power Plants and Industrial Process Heat, *3rd International Renewable Energy Storage Conference (IRES III),* 24-25 November, Berlin, .

[93] Laing, D., Steinmann, W. D., Fiß, M., Tamme, R., Brand, T. and Bahl, C. (2008), Solid media thermal storage development and analysis of modular storage operation concepts for parabolic trough power plants, *Journal of Solar Energy Engineering, Transactions of the ASME,* vol. 130, no. 1, pp. 0110061-0110065.

[94] Tamme, R., Steinmann, W. D. and Laing, D. (2003), High temperature thermal energy storage technologies for power generation and industrial process heat, *Proceedings of 9th International conference on thermal storage,* 1-4 September, Warsaw, Poland, .

[95] Laing, D., Steinmann, W. D., Tamme, R. and Richter, C. (2006), Solid media thermal storage for parabolic trough power plants, *Solar Energy,* vol. 80, no. 10, pp. 1283-1289.

[96] Laing, D., Lehmann, D., Fi, M. and Bahl, C. (2009), Test results of concrete thermal energy storage for parabolic trough power plants, *Journal of Solar Energy Engineering, Transactions of the ASME,* vol. 131, no. 4, pp. 0410071-0410076.

[97] Tamme, R., Laing, D. and Steinmann, W. D. (2004), Advanced thermal energy storage technology for parabolic trough, *Journal of Solar Energy Engineering, Transactions of the ASME,* vol. 126, no. 2, pp. 794-800.

[98] Laing, D., Steinmann, W. D., Viebahn, P., Gräter, F. and Bahl, C. (2010), Economic analysis and life cycle assessment of concrete thermal energy storage for parabolic trough power plants, *Journal of Solar Energy Engineering, Transactions of the ASME,* vol. 132, no. 4.

[99] Pacheco, J. E., Showalter, S. K. and Kolb, W. J. (2002), Development of a molten-salt thermocline thermal storage system for parabolic trough plants, *Journal of Solar Energy Engineering, Transactions of the ASME,* vol. 124, no. 2, pp. 153-159.

[100] Herrmann, U., Geyer, M. and Kearney, D. (2002), Overview on thermal storage systems, *Workshop on Thermal Storage System for Trough Power Systems,* 20-21 February, Golden, CO, .

[101] Steinmann, W. D. and Eck, M. (2006), Buffer storage for direct steam generation, *Solar Energy,* vol. 80, no. 10, pp. 1277-1282.

[102] Brosseau, D., Kelton, J. W., Ray, D., Edgar, M., Chisman, K. and Emms, B. (2005), Testing of thermocline filler materials and molten-salt

heat transfer fluids for thermal energy storage systems in parabolic trough power plants, *Journal of Solar Energy Engineering, Transactions of the ASME,* vol. 127, no. 1, pp. 109-116.

[103] Burolla, V. P. and Bartel, J. J. (1979), *The High temperature compatibility of Nitrate Salts, Granite rock and Pelletized Iron ore,* SAND79-8634, Sandia National Laboratories, USA.

[104] Yang, Z. and Garimella, S. V. (2010), Thermal analysis of solar thermal energy storage in a molten-salt thermocline, *Solar Energy,* vol. 84, no. 6, pp. 974-985.

[105] EPRI (2010), *Solar thermocline storage systems-preliminary design study,* 1019581, EPRI, California, USA.

[106] Watanabe, T., Kikuchi, H. and Kanzawa, A. (1993), Enhancement of charging and discharging rates in a latent heat storage system by use of PCM with different melting temperatures, *Heat Recovery Systems and CHP,* vol. 13, no. 1, pp. 57-66.

[107] Watanabe, T. and Kanzawa, A. (1995), Second law optimization of a latent heat storage system with PCMs having different melting points, *Heat Recovery Systems and CHP,* vol. 15, no. 7, pp. 641-653.

[108] Gong, Z. X. and Mujumdar, A. S. (1996), Finite element analysis of a multistage latent heat thermal storage system, *Numerical Heat Transfer; Part A: Applications,* vol. 30, no. 7, pp. 669-684.

[109] Gong, Z. X. and Mujumdar, A. S. (1997), Thermodynamic optimization of the thermal process in energy storage using multiple phase change materials, *Applied Thermal Engineering,* vol. 17, no. 11, pp. 1067-1083.

[110] Aceves, S. M., Nakamura, H., Reistad, G. M. and Martinez-Frias, J. (1998), Optimization of a class of latent thermal energy storage systems with multiple phase-change materials, *Journal of Solar Energy Engineering, Transactions of the ASME,* vol. 120, no. 1, pp. 14-19.

[111] Mehling, H. and Cabeza, L. F. (2007), Phase change materials and their basic properties, in Paksoy, H. O. (ed.) *Thermal energy storage for sustainable energy consumption: Fundermentals, case studies and design,* Springer, Netherlands, pp. 257-277.

[112] SERI (1989), *Phase change thermal energy storage,* SERI/STR-250-3516, Solar Energy Research Institute (SERI), Colorado, USA.

[113] Gomez, J. C. (2011), *High-temperature phase change materials (PCM) candidates for thermal energy storage (TES) applications,* NREL/TP-5500-51446, NREL, Colorado.

[114] Hoshi, A., Mills, D. R., Bittar, A. and Saitoh, T. S. (2005), Screening of high melting point phase change materials (PCM) in solar thermal concentrating technology based on CLFR, *Solar Energy,* vol. 79, no. 3, pp. 332-339.

[115] Gardner, P. J. and Preston, S. R. (1991), The high temperature heat capacities of indium(i) bromide and indium(III) bromide by differential scanning calorimetry, *Thermochimica Acta,* vol. 180, no. 0, pp. 281-287.

[116] Glatzmaier, G. C., Gomez, J., Starace, A., Turchi, C. and Ortega, J. (2011), High temperature phase change materials for thermal energy storage applications, *SolarPaces Symposium,* 20-23 September, Granada, Spain, .

[117] Takahashi, Y., Kamimoto, M., Abe, Y., Sakamoto, R., Kanari, K. and Ozawa, T. (1987), Investigation of latent heat-thermal energy storage materials. IV. Thermoanalytical evaluation of binary eutectic mixtures of NaOH with LiOH or KOH, *Thermochimica Acta,* vol. 121, no. C, pp. 193-202.

[118] Vargel, C., (2004), *Corrosion of aluminium*, 1st ed., Elsevier, Amsterdam ; Boston.

[119] Janz, G. J., Allen, C. B., Bansal, N. P., Murphy, R. M. and Tomkins, R. P. T. (eds.) (1979), *Physical properties data compilations relevant to energy storage- 2, Molten salts: Data on Single and Multi-component salt systems.* Part 2 ed, National Bureau of Standards.

[120] Janz, G. J. and Tomkins, R. P. T. (eds.) (1981), *Physical properties data compilations relevant to energy storage-4, Molten salts: Data on Additional single and multi-component salt systems.* Part 4 ed, National Bureau of Standards.

[121] Hunold, D., Ratzesberger, R. and Tamme, R. (1992), Heat transfer mechanisms in latent-heat thermal energy storage for medium temperature applications, *Proceedings Of The 6th International Symposium on Solar Thermal Concentrating Technologies,* Majocar, Spain, pp. 475.

[122] Lumsden, J. (1966), *Thermodynamics of Molten Salt Mixtures,* Academic Press, New York.

[123] Jriri, T., Rogez, J., Bergman, C. and Mathieu, J. C. (1995), Thermodynamic study of the condensed phases of NaNO3, KNO3 and CsNO3 and their transitions, *Thermochimica Acta,* vol. 266, no. C, pp. 147-161.

[124] Bader, R. G., Schawe, J. E. K. and Höhne, G. W. H. (1993), A new method of purity determination from the shape of fusion peaks of eutectic systems, *Thermochimica Acta,* vol. 229, no. C, pp. 85-96.

[125] Bauer, T., Laing, D., Kröner, R. and Tamme, R. (2009), Sodium nitrate for high temperature latent heat storage, *The 11th International Conference on Thermal Energy Storage- Effstock,* 14-17 June, Stockholm, Sweden.

[126] Laing, D., Bauer, T., Steinmann, W. D. and Lehmann, D. (2009), Advanced temperature latent heat storage system- Design and test results, *The 11th International Conference on Thermal Energy Storage,* 14-17 June, Stockholm, Sweden.

[127] Takahashi, Y., Sakamoto, R. and Kamimoto, M. (1988), Heat capacities and latent heats of LiNO3, NaNO3, and KNO3, *International Journal of Thermophysics,* vol. 9, no. 6, pp. 1081-1090.

[128] Kenisarin, M. M. (2010), High-temperature phase change materials for thermal energy storage, *Renewable and Sustainable Energy Reviews,* vol. 14, no. 3, pp. 955-970.

[129] Geyer, M. A. (1991), Thermal storage for solar power plants, in Winter, C. J., Sizmann, L. L. and Vant-Hull, L. L. (eds.) *Solar Power Plants,* Springer-Verlag, New York.

[130] Kemink, R. G. and Sparrow, E. M. (1981), Heat transfer coefficients for melting about a vertical cylinder with or without subcooling and for open or closed containment, *International Journal of Heat and Mass Transfer,* vol. 24, no. 10, pp. 1699-1710.

[131] Souza Mendes, P. R. and Pinho Brasil Jr., A. C. (1987), Heat transfer during melting around an isothernal vertical cylinder, *Journal of Heat Transfer,* vol. 109, no. 4, pp. 961-964.

[132] El-Dessouky, H. T., Bouhamra, W. S., Ettouney, H. M. and Akbar, M. (1999), Heat transfer in vertically aligned phase change energy storage systems, *Journal of Solar Energy Engineering, Transactions of the ASME,* vol. 121, no. 2, pp. 98-109.

[133] Pal, D. and Joshi, Y. K. (2000), Melting in a side heated tall enclosure by a uniformly dissipating heat source, *International Journal of Heat and Mass Transfer,* vol. 44, no. 2, pp. 375-387.

[134] Subrahmaniyam, S., Kumar, A. P. S. and Namuduri, D. (2005), Natural convection effects on freezing in vertical cylinders, *International Solar Energy Conference,* pp. 193.

[135] Sparrow, E. M., Patankar, S. V. and Ramadhyani, S. (1977), Analysis of melting in the presence of natural convection in the melt region, *Journal of Heat Transfer,* vol. 99 Ser C, no. 4, pp. 520-526.

[136] Okada, M. (1985), Heat transfer during melting around vertical cylinder (1st report, analysis and experiments of the melting without subcooling), *Bulletin of the JSME,* vol. 28, no. 243, pp. 2007-2013.

[137] Ismail, K. A. R. and Melo, C. A. (1998), Convection-based model for a PCM vertical storage unit, *International Journal of Energy Research,* vol. 22, no. 14, pp. 1249-1265.

[138] Ismail, K. A. R. and Gonçalves, M. M. (1999), Thermal performance of a pcm storage unit, *Energy Conversion and Management,* vol. 40, no. 2, pp. 115-138.

[139] Jones, B. J., Sun, D., Krishnan, S. and Garimella, S. V. (2006), Experimental and numerical study of melting in a cylinder, *International Journal of Heat and Mass Transfer,* vol. 49, no. 15-16, pp. 2724-2738.

[140] Wang, S., Faghri, A. and Bergman, T. L. (2012), Melting in cylindrical enclosures: Numerical modeling and heat transfer correlations, *Numerical Heat Transfer; Part A: Applications,* vol. 61, no. 11, pp. 837-859.

[141] Lacroix, M. (2002), Modelling of latent heat storage systems, in Dincer, I. and Rosen, M. (eds.) *Thermal Energy Storage: Systems and Applications,* 1st Edition ed, John Wiley, England, pp. 303-335.

[142] Eckert, E. R. and Drake, R. M. (1987), *Analysis of Heat and Mass Transfer,* Hemisphere Publishing Corporation, London.

[143] Dincer, I. and Rosen, M. A. (2002), *Thermal energy storage: systems and applications,* Wiley, Chichester.

[144] Nedjar, B. (2002), An enthalpy-based finite element method for nonlinear heat problems involving phase change, *Computers and Structures,* vol. 80, no. 1, pp. 9-21.

[145] Eyres, N. R., Hartree, D. R., Ingham, J., Jackson, R., Sarjant, R. J. and Wagstaff, J. B. (1946), The calculation of variable heat flow in solids, *Philosophical Transactions of the Royal Society of London. Series A: Mathematical and Physical Sciences,* vol. 240, pp. 1-57.

[146] Hunter, L. W. and Kuttler, J. R. (1989), Enthalpy method for heat conduction problems with moving boundaries, *Journal of Heat Transfer,* vol. 111, no. 2, pp. 239-242.

[147] Cao, Y. and Faghri, A. (1990), Numerical analysis of phase-change problems including natural convection, *Journal of Heat Transfer,* vol. 112, no. 3, pp. 812-816.

[148] Swaminathan, C. R. and Voller, V. R. (1993), On the enthalpy method, *International Journal of Numerical Methods for Heat and Fluid Flow,* vol. 3, no. 3, pp. 233-244.

[149] Dutil, Y., Rousse, D. R., Salah, N. B., Lassue, S. and Zalewski, L. (2011), A review on phase-change materials: Mathematical modeling and simulations, *Renewable and Sustainable Energy Reviews,* vol. 15, no. 1, pp. 112-130.

[150] Furzeland, R. M. (1980), A comparative study of numerical methods for moving boundary problems, *IMA Journal of Applied Mathematics (Institute of Mathematics and Its Applications),* vol. 26, no. 4, pp. 411-429.

[151] Voller, V. R., Swaminathan, C. R. and Thomas, B. G. (1990), Fixed grid techniques for phase change problems. A review, *International Journal for Numerical Methods in Engineering,* vol. 30, no. 4, pp. 875-898.

[152] Voller, V. R. and Prakash, C. (1987), A fixed grid numerical modelling methodology for convection-diffusion mushy region phase-change problems, *International Journal of Heat and Mass Transfer,* vol. 30, no. 8, pp. 1709-1719.

[153] Voller, V. R., Cross, M. and Markatos, N. C. (1987), Enthalpy method for convection/diffusion phase change, *International Journal for Numerical Methods in Engineering,* vol. 24, no. 1, pp. 271-284.

[154] Fluent (2011), *ANSYS Fluent user's guide,* Release 14.0 ed, ANSYS Inc., USA.

[155] Stryker, P. C. and Sparrow, E. M. (1990), Application of a spherical thermal conductivity cell to solid n-eicosane paraffin, *International Journal of Heat and Mass Transfer,* vol. 33, no. 9, pp. 1781-1793.

[156] Himran, S., Suwono, A. and Mansoori, G. A. (1994), Characterization of alkanes and paraffin waxes for application as phase change energy storage medium, *Energy Sources,* vol. 16, no. 1, pp. 117-128.

[157] Yaws, C. L. (1999), *Chemical properties handbook,* McGraw-Hill, New York.

[158] Frenkel, M. (2003), *TRC Thermodynamic Tables-Hydrocarbons,* US Government Printing Office, Washington.

[159] Solutia (2008), *Therminol VP-1: Vapour Phase/Liquid Phase Heat Transfer Fluid,* Technical Bulletin 7239115C, Solutia.

[160] Jany, P. and Bejan, A. (1988), Scaling theory of melting with natural convection in an enclosure, *International Journal of Heat and Mass Transfer,* vol. 31, no. 6, pp. 1221-1235.

[161] Lim, J. S. and Bejan, A. (1992), Prandtl number effect on melting dominated by natural convection, *Journal of Heat Transfer,* vol. 114, no. 3, pp. 784-787.

[162] Bareiss, M. and Beer, H. (1984), Experimental investigation of melting heat transfer with regard to different geometric arrangements, *International Communications in Heat and Mass Transfer,* vol. 11, no. 4, pp. 323-333.

[163] Kalhori, B. and Ramadhyani, S. (1985), Studies on heat transfer from a vertical cylinder, with or without fins, embedded in a solid phase change medium, *Journal of Heat Transfer,* vol. 107, no. 1, pp. 44-51.

[164] Shmueli, H., Ziskind, G. and Letan, R. (2010), Melting in a vertical cylindrical tube: Numerical investigation and comparison with experiments, *International Journal of Heat and Mass Transfer,* vol. 53, no. 19-20, pp. 4082-4091.

[165] Zalba, B., Marín, J. M., Cabeza, L. F. and Mehling, H. (2003), Review on thermal energy storage with phase change: Materials, heat transfer analysis and applications, *Applied Thermal Engineering,* vol. 23, no. 3, pp. 251-283.

[166] Jegadheeswaran, S. and Pohekar, S. D. (2009), Performance enhancement in latent heat thermal storage system: A review, *Renewable and Sustainable Energy Reviews,* vol. 13, no. 9, pp. 2225-2244.

[167] Bauer, T., Tamme, R., Christ, M. and Oettinger, O. (2006), PCM-Graphite composites for high temperature thermal energy storage, *Proceedings of the 10th International Conference on Thermal Energy Storage (ECOSTOCK 2006),* 31 May - 2 June, Stockton, New Jersey.

[168] Yin, H., Gao, X., Ding, J. and Zhang, Z. (2008), Experimental research on heat transfer mechanism of heat sink with composite phase change materials, *Energy Conversion and Management,* vol. 49, no. 6, pp. 1740-1746.

[169] Elgafy, A. and Lafdi, K. (2005), Effect of carbon nanofiber additives on thermal behavior of phase change materials, *Carbon,* vol. 43, no. 15, pp. 3067-3074.

[170] Zhang, Y., Ding, J., Wang, X., Yang, R. and Lin, K. (2006), Influence of additives on thermal conductivity of shape-stabilized phase change material, *Solar Energy Materials and Solar Cells,* vol. 90, no. 11, pp. 1692-1702.

[171] Chen, C., Wang, L. and Huang, Y. (2007), Electrospinning of thermo-regulating ultrafine fibers based on polyethylene glycol/cellulose acetate composite, *Polymer,* vol. 48, no. 18, pp. 5202-5207.

[172] Morisson, V., Rady, M., Palomo, E. and Arquis, E. (2008), Thermal energy storage systems for electricity production using solar energy direct steam generation technology, *Chemical Engineering and Processing: Process Intensification,* vol. 47, no. 3, pp. 499-507.

[173] Laing, D., Eck, M., Hempel, M., Johnson, M., Steinmann, W. D., Meyer-Grünefeldt, M. and Eickhoff, M. (2012), High temperature PCM storage for DSG solar thermal power plants tested in various operating modes of water/steam flow, *Proceedings of SolarPACES Conference,* 11-14 September, Marrakech, Morrocco.

[174] Laing, D., Bauer, T., Breidenbach, N., Hachmann, B. and Johnson, M. (2013), Development of high temperature phase-change-material storages, *Applied Energy,* vol. 109, pp. 497-504.

[175] Faghri, A. (1995), *Heat pipe science and technology,* Taylor and Francis, New York.

[176] Lee, W. S., Chen, B. R. and Chen, S. L. (2006), Latent heat storage in a two-phase thermosyphon solar water heater, *Journal of Solar Energy Engineering, Transactions of the ASME,* vol. 128, no. 1, pp. 69-76.

[177] Liu, Z., Wang, Z. and Ma, C. (2006), An experimental study on heat transfer characteristics of heat pipe heat exchanger with latent heat storage. Part I: Charging only and discharging only modes, *Energy Conversion and Management,* vol. 47, no. 7-8, pp. 944-966.

[178] Robak, C. W. (2012), *Latent heat thermal energy storage with embeded heat pipes for concentrating solar power applications* (unpublished MSc thesis), University of Connecticut.

[179] Adinberg, R., Zvegilsky, D. and Epstein, M. (2010), Heat transfer efficient thermal energy storage for steam generation, *Energy Conversion and Management,* vol. 51, no. 1, pp. 9-15.

[180] Guo, C. and Zhang, W. (2008), Numerical simulation and parametric study on new type of high temperature latent heat thermal energy storage system, *Energy Conversion and Management,* vol. 49, no. 5, pp. 919-927.

[181] Incropera, F. P. and DeWitt, D. P. (2002), *Fundermentals of Heat and Mass Transfer,* 5th Edition ed, John Wiley, New York.

[182] Ratzesberger, R., Beine, B. and Hahne, E. (1994), Regeneratoren mit Beton und Phasenweschselmaterial als Speichermasse, *VDI-GET Tagung,* Leipzig.

[183] Tamme, R. (2003), Cocrete Storage: Update on the German concrete TES program, *Workshop on Thermal Storage for Trough Power Systems,* 20-21 February, Golden CO, USA.

[184] Tamme, R., Laing, D., Steinmann, W. D. and Zunft, S. (2002), 'Innovative thermal energy storage technology for parabolic trough concentrating solar power plants', *Proceedings of the 4th ISES Europe Solar Congress (EuroSun 2002),* 23-26 June, Bolagna.

[185] Py, X., Calvet, N., Olives, R., Meffre, A., Echegut, P., Bessada, C., Veron, E. and Ory, S. (2011), Recycled material for sensible heat based thermal energy storage to be used in concentrated solar thermal power plants, *Journal of Solar Energy Engineering, Transactions of the ASME,* vol. 133, no. 3.

[186] Pacheco, J. E. and Gilbert, R. (1999), Overview of recent results of the Solar Two test and evaluation program, *Proceedings of the 1999 ASME International Solar Energy Conference,* 11-14 April, Maui, HI.

[187] Bahl, C., Laing, D., Hempel, M. and Stuckle, A. (2009), Concrete Thermal Energy Storage for Solar Thermal Power Plants and Industrial Process Heat, *Proceedings of SolarPACES Symposium,* 15-18 September, Berlin. Germany.

[188] Schack, A. and Schack, K. (1983), *Der industrielle Wärmeübergang,* Verlag Stahleisen mbH, Düsseldorf.

[189] McHugh, S. and Chappel, S.E., (1999), *Specifying the right fin type for air cooled heat exchangers*, September ed., Hydrocarbon Processing, Houston, TX.

[190] Laing, D., Bahl, C., Bauer, T., Lehmann, D. and Steinmann, W. D. (2011), Thermal energy storage for direct steam generation, *Solar Energy,* vol. 85, no. 4, pp. 627-633.

[191] RockWool (2014), *ProRox SL 960 UK (RW5)*, available at: http://www.rockwool-rti.co.uk/ (accessed 16/09).

[192] Condell (2014), *RockWool Prorox Slabs*, available at: http://www.condell-ltd.com/ (accessed 01/06).

[193] Just Insulation (2014), *Insulation Price List*, available at: http://www.just-insulation.com/005-info/prices-pricelist.html (accessed 01/06).

[194] Sciacovelli, A., Verda, V. and Colella, F. (2011), Numerical model for storage systems based on phase-change materials, *ASME 2011 International Mechanical Engineering Congress and Exposition,* Vol. 4, 11-17 November, Denver, Colorado, pp. 237.

APPENDICES

Appendix A

A.1 Implementation of the heat transfer coefficient during overheating in Dymola model

Figure A.1 presents the heat transfer coefficient during over heating neglecting temperature difference of less than 2 K. it will be seen that they can be represented by a linear function of the temperature difference. For each PCM each of the curves is represented by a linear function having intercept and slope. Then the slopes and intercepts were then plotted as a function of the mass flow rate (Figure A.2). The slopes were represented by a polynomial function and the intercept with a linear function as shown in Table A.1 from which the heat transfer coefficient can be obtained using:

$$h_o = slope\left(T_w - T_{pcm}\right) + intercept$$

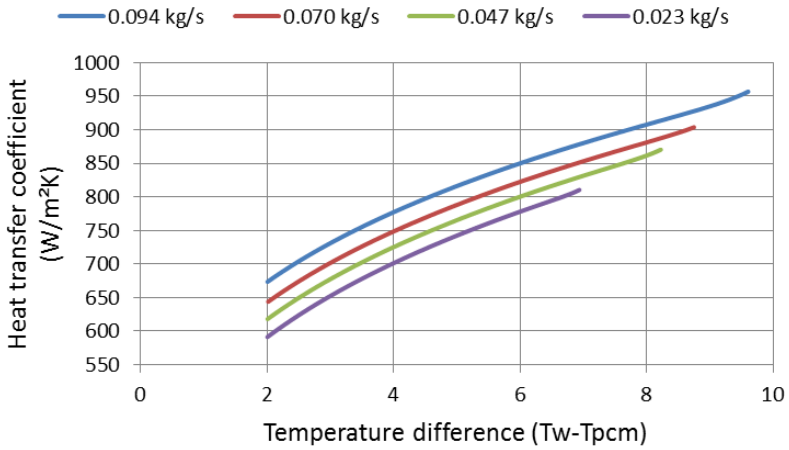

(a)

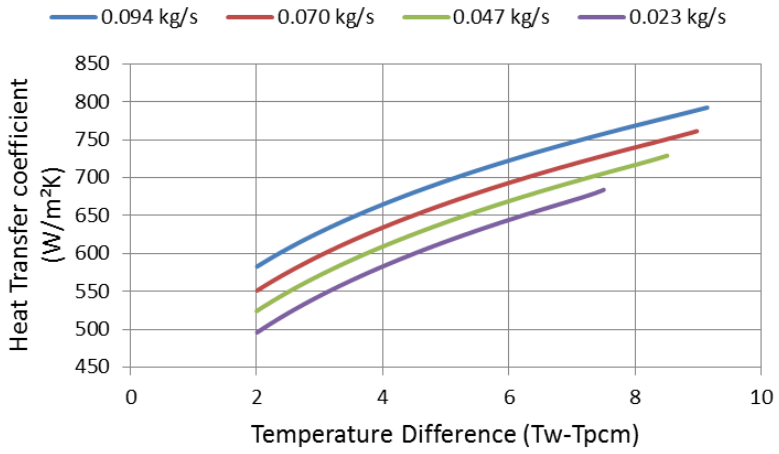

(b)

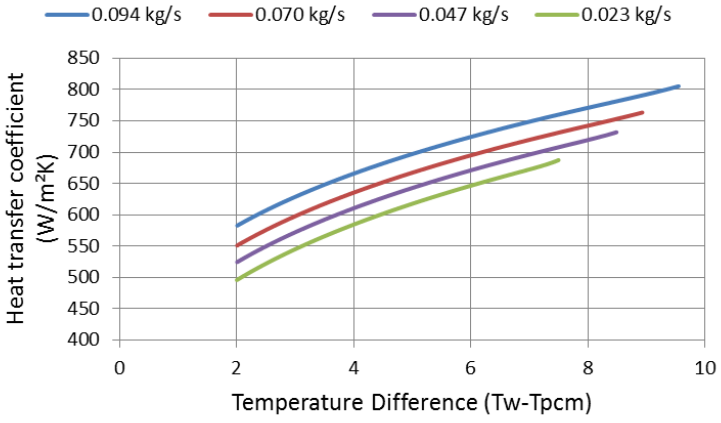

(c)

Figure A.1 Heat transfer during overheating of the PCM for (a) $NaNO_3$ (b) KNO_3/KCl and (c) KNO_3 for the charging process

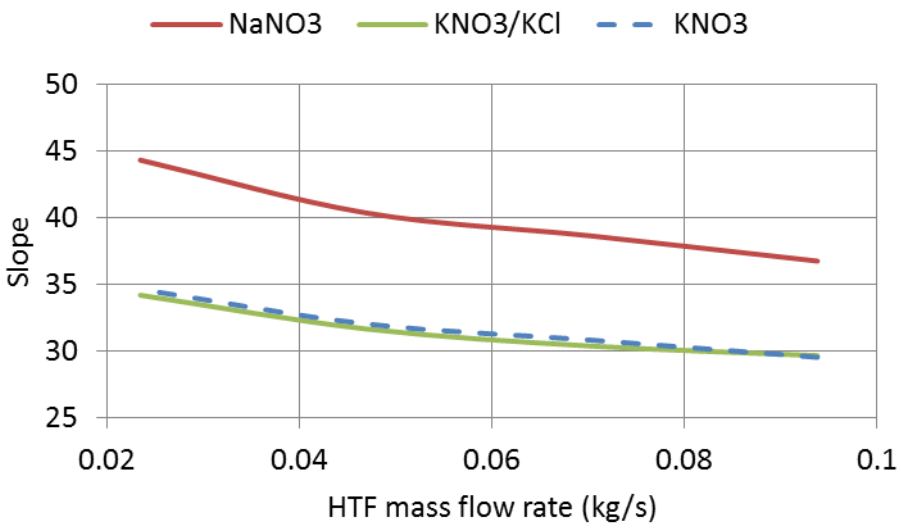

(a)

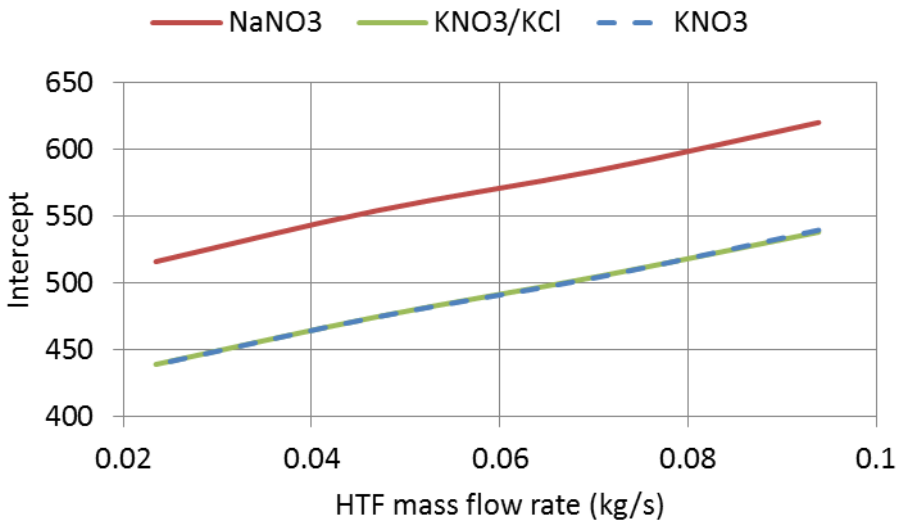

(b)

Figure A.2 (a) Slope (b) Intercept functions for the heat transfer coefficient during overheating

Table A.1 Slope and intercept functions for the three PCM's

PCM	Slope (A1)	Intercept (A2)
$NaNO_3$	$945.6\dot{m}_{htf}^2 - 215.2\dot{m}_{htf} + 48.77$	$1459.7\dot{m}_{htf} + 483.31$
KNO_3/KCl	$822.57\dot{m}_{htf}^2 - 159.9\dot{m}_{htf} + 37.49$	$1395\dot{m}_{htf} + 407.58$
KNO_3	$594.2\dot{m}_{htf}^2 - 140.1\dot{m}_{htf} + 37.55$	$1415.1\dot{m}_{htf} + 406.56$

A.2 Equations for the complete finned annular gap model

The PCM state is tracked using the internal energy (U) given by:

$$u_{pcm} = c_p T_{pcm}$$

A.2.1 Charging

1. Set of equations solved when PCM is solid melting

$$Q_{in} = 2\pi r_o dz h_m (T_{wi} - T_{pcm})$$

$$Q_{in} = m_{PCM} C_p \frac{dT_{pcm}}{dt}$$

$$\frac{du_{PCM}}{dt} = \frac{Q_{in}}{m_{PCM}}$$

$$LF = 0$$

$$m_{melt} = LF \times m_{pcm}$$

$$h_m = 1391.6\dot{m}_{htf} + 933.64$$

2. Set of equations solved during melting

$$Q_{in} = 2\pi r_o dz h_m (T_{wi} - T_{pcm})$$

$$Q_{in} = m_{PCM} C_p \frac{dT_{PCM}}{dt}$$

$$\frac{du_{PCM}}{dt} = \frac{Q_{in}}{m_{PCM}}$$

$$LF = \frac{u_{PCM} - u_s}{\Delta u_m}$$

$$m_{melt} = LF \times m_{pcm}$$

$$h_m = 1391.6\dot{m}_{htf} + 933.64$$

3. Set of equations solved during overheating

$$Q_{in} = 2\pi r_o dz h_o (T_{wi} - T_{PCM})$$

$$Q_{in} = m_{PCM} C_p \frac{dT_{PCM}}{dt}$$

$$\frac{du_{PCM}}{dt} = \frac{Q_{in}}{m_{PCM}}$$

$$LF = 1$$

$$m_{melt} = LF \times m_{PCM}$$

$$h_o = A1(T_{wi} - T_{PCM}) + A2$$

Where A1 and A2 are the slopes and intercept presented in Table A.1.

A.2.2 Discharging

During discharging the heat transfer coefficient during the whole process is calculated as a function of liquid fraction using:

$$h_s = a(LF) + c$$

Where:

$$a = 224.04\left(\dot{m}_{htf}\right) + 20.265$$

and

$$c = 1395.4\left(\dot{m}_{htf}\right) + 267.96$$

The following equations are solved at each phase.

$$Q_{in} = 2\pi r_o dz h_s (T_{wi} - T_{pcm})$$

$$Q_{in} = m_{pcm} C_p \frac{dT_{pcm}}{dt}$$

$$\frac{du_{PCM}}{dt} = \frac{Q_{in}}{m_{pcm}}$$

$$LF = 1$$

$$m_{melt} = LF \times m_{PCM}$$

Appendix B

B.1 Finned Segment Model

B.1.1 Code for HTF property model (Model 'Therminol VP-1')

```
model TherminolVP1
"Model for the properties of therminol VP-1 for temperature ranging from 250 to 400 deg. C."
/* In the model the specific heat capacity and thermal conductivity are asumed constant and
calculated using a four degree polynomial function. Enthalpy can be calculated from
temperature either using linear gradient with Cp or using a polynomial function.
Density and dynamic viscosity can be assumed constant, linear or using a polynomial
or power function.*/
extends TechThermo.Interface.ThermalState.PropertyPort;
//-----Start Documentation-----------------------------------------------
// parameters for finding the enthalpy
parameter Integer option_h_correlations=1
"option for calculation of h: 1- using gradient (CpT), 2: using a polynomial correlation";
parameter Integer option_rho_correlations=1
"option for calculation of density(rho): 0 for constant density, 1 for linear and 2 for poly";
parameter Integer option_eta_correlations=1 "option for calculation of dynamic viscosity (eta):
0 for constant (using eta_const): 1 for linear interpolation: 2 for power function";
parameter Modelica.SIunits.Temp_C t_average=290 "average temperature for the calculation
of the specific heat capacity and thermal conductivity in deg. C";
parameter Modelica.SIunits.Density rho_const=790
"const. value of density, used when option_rho_correlations is 0";
parameter Modelica.SIunits.DynamicViscosity eta_const=0.0001977
"constant dynamic viscosity used when option_eta_correlation=0";
parameter Modelica.SIunits.Temp_C t0=250
"first reference temperature for the calculation of enthalpy by using option_h_correlation=1";
parameter Modelica.SIunits.SpecificEnthalpy h0=442200
"measured enthalpy in J/kg at reference temperature ie t0";
// Calculation of specific heat
parameter Modelica.SIunits.SpecificHeatCapacity c_heat=(1.498 +
0.002414*t_average + (5.9591*10^(-6))*(t_average)^2 - (2.9879*10^
(-8))*(t_average)^3 + (4.4172*10^(-11))*(t_average)^4)*1000
"const. value for cp calculated using corrlation with a polynomial of degree four";
// Calculation of thermal conductivity (W/mK)
parameter Modelica.SIunits.ThermalConductivity k_therm = 0.137743 - (8.19477*10^(-5))*(t_average)
- (1.92257*10^(-7))*(t_average)^2 + (2.5034*10^(-11))*(t_average)^3 -
(7.2974*10^(-15))*(t_average)^4 "Thermal conductivity at average temperature over the
whole range of operting temperature calculated using polynomial";
// Reference temperatures for calculation of density and dynamic viscosity using linear gradient
parameter Modelica.SIunits.Temp_C t1=250 "Lower reference temperature";
parameter Modelica.SIunits.Temp_C t2=350 "Higher reference temperature";
//Density values at reference temperatures
parameter Modelica.SIunits.Density rho1=867 "Density at t1";
parameter Modelica.SIunits.Density rho2=761 "density at t2";
parameter Real t_grad_rho=(rho2 - rho1)/(t2 - t1)
"gradient density dependant on temperature, needed if option_rho_correlations==1";
// parameters for calculation of dynamic viscosity
parameter Modelica.SIunits.DynamicViscosity eta_1=0.000288
"dynamic viscosity at temperature t1";
parameter Modelica.SIunits.DynamicViscosity eta_2=0.000177
"dynamic viscosity at temperature t2";
parameter Real t_grad_eta=(eta_2 - eta_1)/(t2 - t1)
"gradient dynamic viscosity dependant on temperature, needed if option_eta_correlations=1";
//Variables
Modelica.SIunits.DynamicViscosity eta(start=eta_1) "dynamic viscosity";
Modelica.SIunits.SpecificEnthalpy h(start=430000) "enthalpy of HTF";
Modelica.SIunits.Temp_C t(start=250) "temperature at h";
equation
// calculation of enthalpy
//assert(h< 430000 or t <250,
//"model not defined for temperatures less than 250 deg C.");
//assert( h>810000 or t > 400,
// "model not defined for temperatures greater than 400 deg C.");
// using linear gradient
if option_h_correlations == 1 then
h = c_heat*(t - t0) + h0;
// using polynomial
elseif option_h_correlations == 2 then
h = (0.0014*(t)^2 + 1.4968*(t) - 18.175)*1000;
end if;
// calculation of density
//constant density
if option_rho_correlations == 0 then
StateCut.rho = rho_const;
elseif option_rho_correlations == 1 then
```

```
// interpolation of density rho dependant on temperature
StateCut.rho = rho1 + t_grad_rho*(t - t1);
elseif option_rho_correlations == 2 then
// density calculation using correlations for therminol vp-1
StateCut.rho = 1083 - 0.90797*(t) + 0.00078116*(t)^2 - (2.367*10^(-6))
*(t)^3;
end if;
// calculation of dynamic viscosity
// constant dynamic viscosity
if option_eta_correlations == 0 then
eta = eta_const;
elseif option_eta_correlations == 1 then
//linear gradient
eta = eta_1 + t_grad_eta*(t - t1);
elseif option_eta_correlations == 2 then
//power function
eta = (806.78*(t^(-1.438)))/1000;
end if;
StateCut.h = h;
StateCut.t = t;
;
end TherminolVP1;
```

B.1.2 PCM property model (Model 'PCM property')

```
model PCM_Property
  "Thermal physical properties of PCM (Sodium Nitrate default)"
  // Material specific properties
  parameter Modelica.SIunits.Temp_C tm=306.5
    "Melting temperature of PCM in Deg. C";
  parameter Modelica.SIunits.SpecificEnthalpy Delta_hm=172000
    "Specific enthalpy of melt PCM [J/kg]";
  parameter Modelica.SIunits.SpecificHeatCapacity cp_s=1780
    "Specific heat capacity of solid at melting temp. [J/kgK]";
  parameter Modelica.SIunits.SpecificHeatCapacity cp_l=1560
    "Specifc heat capacity of liquid at melting point";
  parameter Modelica.SIunits.Density rho_s=2261
    "Density of solid PCM at 20 deg C";
  parameter Real dV_melt=0.107 "Volume change during melting";
  parameter Modelica.SIunits.ThermalConductivity k_s=0.58
    "Thermal conductivity of solid PCM at melting point W/mK";
  parameter Modelica.SIunits.ThermalConductivity k_l=0.6
    "Thermal conductivity of liquid at melting point W/mK";
  parameter Modelica.SIunits.Temp_C tm_Delta=2
    "Temperature difference to calculate cp_m";
  // variables
  Modelica.SIunits.Temp_C tm_s=tm - 0.5*tm_Delta "Theoretical start of melting";
  Modelica.SIunits.Temp_C tm_l=tm + 0.5*tm_Delta "Theoretical end of melting";
  Modelica.SIunits.SpecificHeatCapacity cp_m=(Delta_hm/tm_Delta) + (cp_s +
      cp_l)/2 "Theoretical specific heat capacity during melting";
  Modelica.SIunits.SpecificHeatCapacity cp;
  Modelica.SIunits.ThermalConductivity k;
  Modelica.SIunits.Density rho;
  Modelica.SIunits.SpecificInternalEnergy u
    "the specific internal energy of PCM with base at 0 deg. C";
  Modelica.SIunits.SpecificInternalEnergy u_ms
    "specific internal energy at begining of melting";
  Modelica.SIunits.SpecificInternalEnergy u_ml
    "specific internal energy at end of melting";
  Modelica.SIunits.SpecificInternalEnergy u_mDelta
    "specific internal energy difference between melting";
equation
  rho = rho_s;
  u_ms = tm_s*cp_s;
  u_ml = u_ms + Delta_hm + (0.5*tm_Delta*cp_s) + (0.5*tm_Delta*cp_l);
  u_mDelta = u_ml - u_ms;
 // calculation of varying thermo-physical properties
 if u <= u_ms - 0.5*u_mDelta then
     cp = cp_s;
     k = k_s;
 elseif u <= u_ms + 0.5*u_mDelta then
     cp = cp_s + (u - (u_ms - 0.5*u_mDelta))/u_mDelta*(cp_m - cp_s);
```

```
    k = k_s + (u - (u_ms - 0.5*u_mDelta))/u_mDelta*(k_l - k_s);
 elseif u <= u_ml + 0.5*u_mDelta then
   cp = cp_m - (u - (u_ms + 0.5*u_mDelta))/u_mDelta*(cp_m - cp_l);
   k = k_l;
 else
   cp = cp_l;
   k = k_l;
 end if;
end PCM_Property;
```

B.1.3 Finned Annular Gap model (Model 'Finned_AG_NANO3')

```
model Finned_AG_NANO3

  //it uses a model "PCM_property for material data
  extends TechThermo.Interface.HeatFlow.TwoPort(final switch_q_dot_const=false,
      final switch_t_const=false);
  // parameters
parameter Modelica.SIunits.Length r_i=0.003 "outer radius of HTF pipe";
parameter Modelica.SIunits.Length r_o=0.0325 "Inner radius of shell or point of symmetry";
  parameter Modelica.SIunits.Length dz=0.227
    "height of annular segment or element";
  parameter Modelica.SIunits.Temp_C t_initial=300 "Initial temperature in Deg. C";
  constant Real PI=Modelica.Constants.pi;
  parameter Modelica.SIunits.MassFlowRate m_HTF "mass flow rate of HTF";
 // parameters for the calculation of heat transfer coefficient during solidification. This is valid for all PCM's
  parameter Modelica.SIunits.CoefficientOfHeatTransfer h_solidificationA1= 244.56*(abs(m_HTF))+22.112
"This factor is to be multiplied by Liquid fraction";
  parameter Modelica.SIunits.CoefficientOfHeatTransfer h_solidificationA2= 1387.8*(abs(m_HTF))+267.55
    "Intercept";
  //parameters for the calculation of heat transfer coefficient during overheating after melting
parameter Modelica.SIunits.CoefficientOfHeatTransfer h_overheatingA1= -
30578*((abs(m_HTF))^3)+ 6327.6*((abs(m_HTF))^2)
-496.43*((abs(m_HTF))^3)+52.923 "This factor is to be multiplied by temperature difference";
  parameter Modelica.SIunits.CoefficientOfHeatTransfer h_overheatingA2= 1459.7*(abs(m_HTF))+483.31
    "Intercept";
  // Variables
  Modelica.SIunits.Temp_C t_PCM "PCM temperature";
  Modelica.SIunits.SpecificInternalEnergy u_PCM "Internal energy of PCM";
  Modelica.SIunits.Mass m_PCM "mass of PCM in annular gap";
  Modelica.SIunits.Mass m_melt "mass of molten PCM";
  Modelica.SIunits.CoefficientOfHeatTransfer h_intoPCM
    "coefficient of heat transfer obtained from CFD at the various processes occuring during charging and discharging";
  Modelica.SIunits.Energy Q_cum(start=0, fixed=true) "total energy transfered";
  Real LF "Liquid fraction";
  //components
  F_LHS_Concrete_Cascade.Finned_LHS_Cascade.PCM_Property props(
    tm=306.5,
    dV_melt=0,
    k_s=0.53,
    k_l=0.53,
    tm_Delta=1,
    u=u_PCM,
    rho_s=1910,
    cp_s=1297.5)
  Modelica.Blocks.Interfaces.RealInput DirectionSignal
    "Either charging (positive) or discharging (negative)"
equation
  m_PCM = PI*(r_o^2 - r_i^2)*dz*props.rho;
  // check if initial parameters are senseful
  assert(t_initial < props.tm or t_initial > props.tm,
    "you cant start this simulation with t_initial = t_melting! it couldnt be clear if it is the beginning or end of");
```

```
  assert(t_initial >= 0 and t_PCM >= 0,
    "model not defined for temperatures less than 0 deg C.");

  if initial() then
    t_PCM = t_initial;
    if t_initial <= props.tm then
      u_PCM = props.cp_s*t_initial;
    else
      u_PCM = props.u_ml + (props.cp_l*(t_initial - props.tm));
    end if;
  end if;
// CHARGING
if DirectionSignal >=0 then
// Average PCM temperature is less than the melting temperature
    if (u_PCM <= props.u_ms) then
      if t_in <t_PCM then
      q_in_dot=0;
      else
        q_in_dot = 2*PI*r_i*dz*h_intoPCM*(t_in - t_PCM);
    end if;
      q_in_dot = m_PCM*props.cp*der(t_PCM);
      der(u_PCM) = q_in_dot/m_PCM;
      LF=0;
      m_melt=LF*m_PCM;
      h_intoPCM = 1391.6*(abs(m_HTF))+933.64;
//PCM temperature is at the melting range
    elseif (u_PCM < props.u_ml) and (u_PCM > props.u_ms) then
       if t_in <t_PCM then
      q_in_dot=0;
      else
        q_in_dot = 2*PI*r_i*dz*h_intoPCM*(t_in - t_PCM);
    end if;
     h_intoPCM = 1391.6*(abs(m_HTF))+933.64;
     q_in_dot = m_PCM*props.cp*der(t_PCM);
     der(u_PCM) = q_in_dot/m_PCM;
     LF = (u_PCM - props.u_ms)/(props.u_ml - props.u_ms);
     m_melt = LF*m_PCM;
//Average PCM temperature is above melting point and the PCM is totally liquid
    else
      if t_in <t_PCM then
       q_in_dot=0;
       else
        q_in_dot = 2*PI*r_i*dz*(1 + props.dV_melt)*h_intoPCM
        *(t_in - t_PCM);
    end if;
     // obtained from CFD
     h_intoPCM =  h_overheatingA1*(t_in - t_PCM)+ h_overheatingA2;
     q_in_dot = m_PCM*props.cp*der(t_PCM);
     der(u_PCM) = q_in_dot/m_PCM;
     LF = 1;
     m_melt = LF*m_PCM;
   end if;
// DISCHARGING
else
    h_intoPCM =  h_solidificationA1*(LF)+ h_solidificationA2;
  if (u_PCM >= props.u_ml) then
     if t_in > t_PCM then
       q_in_dot=0;
       else
       q_in_dot = 2*PI*r_i*dz*(1 + props.dV_melt)*h_intoPCM
   *(t_in - t_PCM);
     end if;
     LF=1;
     q_in_dot = m_PCM*props.cp*der(t_PCM);
     der(u_PCM) = q_in_dot/m_PCM;
    m_melt = LF*m_PCM;
 //Solidfication
  elseif (props.u_ml > u_PCM) and (u_PCM > props.u_ms) then
```

```
   if t_in > t_PCM then
     q_in_dot=0;
     else
    q_in_dot = h_intoPCM*2*PI*r_i*dz *(t_in - props.tm);
   end if;
   LF = (u_PCM - props.u_ms)/(props.u_ml - props.u_ms);
   q_in_dot = m_PCM*props.cp*der(t_PCM);
   der(u_PCM) = q_in_dot/m_PCM;
   m_melt = LF*m_PCM;
  else
   if t_in > t_PCM then
     q_in_dot=0;
     else
   q_in_dot = 2*PI*r_i*dz*h_intoPCM*(t_in - t_PCM);
   end if;
   q_in_dot = m_PCM*props.cp*der(t_PCM);
   der(u_PCM) = q_in_dot/m_PCM;
   LF=0;
   m_melt=LF*m_PCM;
  end if;
end if;
  q_in_dot = der(Q_cum);
  t_out = t_PCM;
end Finned_AG_NANO3;
```

B.1.4 Finned Cascaded Storage Element (Model 'FStorageCascade')

```
model FStorageCascade
  "model for a complete storage cascade with three PCM's"
  extends TechThermo.Interface.MassFlow.TwoPort;
  parameter Modelica.SIunits.Distance total_length_PCM=2.76
    "total length of pipe for the three cascaded Finned LHS";
  parameter Modelica.SIunits.Distance r_out_storage=0.065
"outer radius of of shellor symetry point)";
parameter Modelica.SIunits.Diameter di_pipe=0.008 "Inner diameter of HTF pipe";
parameter Modelica.SIunits.Thickness t_wall_pipe=0.002 "HTF Pipe thickness";
  parameter Real n_pipe_storage=100 "number of paralle pipe in storage unit";
  parameter Modelica.SIunits.MassFlowRate m_HTF "mass flow rate of HTF";
    //parameter TechThermo.Component.SIunits.Temp_C t_initial=286
  //  "initial temperature of PCM";
  parameter TechThermo.Component.SIunits.Temp_C t_average=290
    "Average temperature of HTF in storage unit for the calculation of specific heat and thermal conductivity";
  parameter Integer n_axial_PCM1=6
    "number of storage segments in axial direction for PCM1:NANO3";
  parameter Integer n_axial_PCM2=9
    "number of storage segments in axial direction for PCM2:KNO3/KCL";
  parameter Integer n_axial_PCM3=11
    "number of storage segments in axial direction for PCM3:KNO3";
  parameter Integer n_axial=n_axial_PCM1+n_axial_PCM2+n_axial_PCM3
    "total number of storage segments in axial direction in the LHS cascade (three stage)";
  parameter Modelica.SIunits.Distance dz=total_length_PCM/n_axial
    "Length of each segment in a storage cascade";
  Modelica.SIunits.Energy Q_cum_PCM1
    "cummulative heat transfered by storage module 1";
  Modelica.SIunits.Energy Q_cum_PCM2;
  Modelica.SIunits.Energy Q_cum_PCM3;
  Modelica.SIunits.Energy Q_cum_total_PCM;
  // total Heat transfered to/from the storage
  Modelica.SIunits.HeatFlowRate Q_dot_PCM1;
  Modelica.SIunits.HeatFlowRate Q_dot_PCM2;
  Modelica.SIunits.HeatFlowRate Q_dot_PCM3;
  Modelica.SIunits.HeatFlowRate Q_dot_total;
  Modelica.SIunits.Mass m_PCM1;
```

```
  Modelica.SIunits.Mass m_PCM2;
  Modelica.SIunits.Mass m_PCM3;
  Modelica.SIunits.Mass m_PCM_total;
  Modelica.SIunits.Mass m_melt_PCM1;
  Modelica.SIunits.Mass m_melt_PCM2;
  Modelica.SIunits.Mass m_melt_PCM3;
  Modelica.SIunits.Mass m_melt_total;
  F_LHS_Concrete_Cascade.Finned_LHS_Cascade.GeometryParameterCascade StorageGeometry(
    r_out_storage=r_out_storage,
    di_pipe=di_pipe,
    t_wall_pipe=t_wall_pipe,
    dz=dz,
    total_length=total_length_PCM)
  F_LHS_Concrete_Cascade.Concrete_Tube_Register.PipeWallParameter PipeProperties
F_LHS_Concrete_Cascade.Finned_LHS_Cascade.LHSSegment_VP1_NaNO3[n_axial_PCM1] FSegment_PCM1(
    each StorageGeometry=StorageGeometry,
    each PipeProperties=PipeProperties,
    each t_initial=286,
    each t_average=t_average,
    each m_HTF=m_HTF,
    each DirectionSignal=DirectionSignal);
F_LHS_Concrete_Cascade.Finned_LHS_Cascade.LHSSegment_VP1_KNO3_KCL[n_axial_PCM2]
    FSegment_PCM2(
    each StorageGeometry=StorageGeometry,
    each PipeProperties=PipeProperties,
    each t_initial=300,
    each t_average=t_average,
    each m_HTF=m_HTF,
    each DirectionSignal=DirectionSignal);
F_LHS_Concrete_Cascade.Finned_LHS_Cascade.LHSSegment_VP1_KNO3[n_axial_PCM3] FSegment_PCM3(
    each StorageGeometry=StorageGeometry,
    each PipeProperties=PipeProperties,
    each t_initial=315,
    each t_average=t_average,
    each m_HTF=m_HTF,
    each DirectionSignal=DirectionSignal);
  Modelica.Blocks.Interfaces.RealInput DirectionSignal
equation
  // first connection with the inlet mass flow
  connect(FSegment_PCM1[1].InMassFlow, InMassFlow);
  for i in 1:(n_axial_PCM1 - 1) loop
    connect(FSegment_PCM1[i].OutMassFlow, FSegment_PCM1[i + 1].InMassFlow);
  end for;
  connect(FSegment_PCM1[n_axial_PCM1].OutMassFlow, FSegment_PCM2[1].InMassFlow);
  for i in 1:(n_axial_PCM2 - 1) loop
    connect(FSegment_PCM2[i].OutMassFlow, FSegment_PCM2[i + 1].InMassFlow);
  end for;
  connect(FSegment_PCM2[n_axial_PCM2].OutMassFlow, FSegment_PCM3[1].InMassFlow);
  for i in 1:(n_axial_PCM3 - 1) loop
    connect(FSegment_PCM3[i].OutMassFlow, FSegment_PCM3[i + 1].InMassFlow);
  end for;
  connect(FSegment_PCM3[n_axial_PCM3].OutMassFlow, OutMassFlow);
  // cummulative heat transfered in or out of the storage
  Q_cum_PCM1 = sum(FSegment_PCM1.Finned_AG_NANO3.Q_cum);
  Q_cum_PCM2 = sum(FSegment_PCM2.Finned_AG_KNO3_KCL.Q_cum);
  Q_cum_PCM3 = sum(FSegment_PCM3.Finned_AG_KNO3.Q_cum);
  Q_cum_total_PCM = Q_cum_PCM1 + Q_cum_PCM2 + Q_cum_PCM3;
  // total Heat transfered to/from the storage
  Q_dot_PCM1 = sum(FSegment_PCM1.Finned_AG_NANO3.q_in_dot);
  Q_dot_PCM2 = sum(FSegment_PCM2.Finned_AG_KNO3_KCL.q_in_dot);
  Q_dot_PCM3 = sum(FSegment_PCM3.Finned_AG_KNO3.q_in_dot);
  Q_dot_total = Q_dot_PCM1 + Q_dot_PCM2 + Q_dot_PCM3;
  m_PCM1 = sum(FSegment_PCM1.Finned_AG_NANO3.m_PCM);
  m_PCM2 = sum(FSegment_PCM2.Finned_AG_KNO3_KCL.m_PCM);
  m_PCM3 = sum( FSegment_PCM3.Finned_AG_KNO3.m_PCM);
  m_PCM_total = m_PCM1 + m_PCM2 + m_PCM3;
  m_melt_PCM1 = sum(FSegment_PCM1.Finned_AG_NANO3.m_melt);
  m_melt_PCM2 = sum(FSegment_PCM2.Finned_AG_KNO3_KCL.m_melt);
```

```
m_melt_PCM3 = sum( FSegment_PCM3.Finned_AG_KNO3.m_melt);
m_melt_total = m_melt_PCM1 + m_melt_PCM2 + m_melt_PCM3;
//LF_total = m_melt_total/m_PCM_total;
end FStorageCascade;
```